UNIVERSITÉ DE SHERBROOKE
Faculté de génie
Département de génie mécanique

Comprendre les auto-oscillations dans le caloduc pulsé mono-branche

Understanding Self-Oscillations in the Single-Branch Pulsating Heat Pipe

Thèse de doctorat
Specialité: génie mécanique

Albert Tessier-Poirier

Sherbrooke (Québec) Canada

Janvier 2022

JURY MEMBERS

Luc G. Fréchette

Supervisor

Martin Brouillette

Examiner

Julien Sylvestre

Examiner

Richard H. Rand

Examiner

Marco Marengo

Examiner

RÉSUMÉ

Dans cette thèse, des contributions scientifiques sur la compréhension des auto-oscillations dans le caloduc auto-oscillant mono-branche (SBPHP) et le moteur fluidique auto-oscillant (SOFHE) sont présentées. Le SBPHP est un tube de faible diamètre fermé à l'une des extrémités, dans lequel une bulle de vapeur est suivie d'une colonne de liquide. Étonnamment, chauffer l'extrémité fermée au-delà d'un certain seuil mène à des oscillations de la colonne de liquide qui peuvent être maintenues indéfiniment. Ces auto-oscillations peuvent être utilisées pour refroidir, pomper ou pour récupérer de l'énergie lorsque couplées à un transducteur électromécanique (SOFHE). Toutefois, parce que la dynamique est mal comprise, il est difficile de contrôler les auto-oscillations et de comprendre comment concevoir des dispositifs performants. Dans cette thèse, des réponses à des questions fondamentales sur la dynamique sont obtenues, par une approche théorique et des validations expérimentales, pour mieux comprendre le phénomène et guider la conception. Nous nous demandons d'abord d'où proviennent les oscillations et pourquoi leur amplitude augmente durant le démarrage. Nous montrons que l'inertie de la colonne de liquide couplée à la compression/dilatation de la vapeur produit un système masse-ressort. Nous révélons ensuite l'existence d'un mécanisme d'instabilité, dû à l'interaction du changement de phase qui agit comme force de rétroaction positive et à la friction visqueuse, qui dissipe de l'énergie. Le démarrage se produit lorsque le coefficient du changement de phase est supérieur au coefficient de friction. Le système masse-ressort et le mécanisme d'instabilité sont validés expérimentalement. Nous nous demandons ensuite : pourquoi l'amplitude sature durant le démarrage ? Nous montrons, à l'aide de techniques de dynamique non linéaire, que cela s'explique par l'existence d'un mécanisme limitant produit par les non-linéarités. Le système atteint un cycle limite, produit par une bifurcation de Poincaré-Andronov-Hopf. En contrôlant le changement de phase et la friction, il est possible d'augmenter l'instabilité et de réduire la limitation et ainsi, d'augmenter l'amplitude des oscillations. Nous poussons l'étude de la dynamique plus loin, de faibles à grandes amplitudes. Pour ce faire, nous utilisons la continuation numérique d'abord, puis obtenons des solutions analytiques précises. Nous nous intéressons ensuite au comportement du SOFHE. Nous montrons comment la dynamique, la puissance et l'efficacité sont influencées par le transducteur électromécanique. Des récupérateurs auto-oscillants (comme SOFHE) diffèrent qualitativement de récupérateurs forcés. Finalement, nous revisitons nos résultats selon une approche énergétique générale. Nous montrons que le mécanisme d'instabilité et le mécanisme limitant peuvent être expliqués en fonction du travail produit par le changement de phase et par la friction. Il est possible d'augmenter significativement l'amplitude, la puissance ou l'efficacité en augmentant le travail fait par le changement de phase ou en réduisant celui fait par la friction. Nous concluons en suggérant que contrôler l'amplitude et le synchronisme du changement de phase par des tubes modifiés semble être une avenue très prometteuse pour améliorer la performance des dispositifs.

Mots-clés : dynamique nonlinéaire, cycle limite, bifurcation de Hopf, mécanique des fluides, microfluidique, refroidissement, récupération d'énergie, transducteur

ABSTRACT

In this thesis, scientific contributions on the understanding of the self-oscillations in the Single-Branch Pulsating Heat Pipe (SBPHP) and on the Self-Oscillating Heat Engine (SOFHE) are presented. The SBPHP is a tube of small diameter closed at one end in which a vapor bubble is followed by a liquid plug. Surprisingly, heating the closed end over a threshold leads to oscillations of the liquid plug which can be maintained indefinitely. Those self-oscillations can be used for cooling, pumping or energy harvesting when coupled to an electromechanical transducer (SOFHE). However the lack of understanding of the dynamics makes it difficult to control the self-oscillations and to understand how to design good devices. In this thesis, some fundamental questions on the dynamics are answered by a theoretical approach and experimental validation, in order to better understand the phenomenon and to provide guidelines for the design of effective devices. We first look at where the oscillations come from and why the amplitude grows during the startup. We show that the compression and expansion of the vapor coupled with the liquid plug inertia leads to a spring-mass system. We then uncover the existence of an instability mechanism due to the interplay of phase-change which acts as a positive feedback and viscous friction, which dissipates energy. The startup occurs when the phase-change coefficient is greater than the friction coefficient. Both the spring-mass system and the instability mechanism are validated experimentally. We then ask: why does the amplitude saturate during the startup? We show, using nonlinear dynamical techniques, that this is explained by a limiting mechanism produced by the nonlinearities . The system reaches a limit cycle, created through a Poincaré-Andronov-Hopf bifurcation. By controlling the phase-change and the friction, one can promote the instability mechanism and reduce the limiting mechanism such that the oscillations amplitude increases. We also study the dynamics further, from small to large oscillations amplitude. To do so, we use numerical continuation first, and then obtain accurate analytical solutions. We then consider the behavior of a SOFHE. We show how the dynamics, the power output and the efficiency are impacted by the electromechanical transducer. We find that self-oscillating harvesters (as SOFHE) differs qualitatively from forced-oscillating harvesters. Finally, we review our results from a general energy perspective. We show that the instability mechanism and the limiting mechanism can be explained by the phase-change and the friction work rate. One can increase the oscillations amplitude or the power output and the efficiency significantly by increasing the phase-change work rate or reducing the friction work rate. We conclude by suggesting that controlling the magnitude and the timing of the phase-change by engineered tubes seems a promising approach to increase the performance of devices.

Keywords: nonlinear dynamics, limit cycle, hopf bifurcation, fluid mechanics, microfluidic, cooling, energy harvesting, transducer

the science knowledge only adds
to the excitement, the mystery
and the awe of a flower

Richard P. Feynman

REMERCIEMENTS

Je voudrais d'abord exprimer toute ma reconnaissance à mon directeur de recherche, Luc Fréchette, pour ses généreux conseils, pour toute la latitude qu'il m'a offerte dans l'orientation de mes travaux et enfin, pour son enthousiasme contagieux qui a grandement alimenté mon intérêt pour la science.

I am also deeply grateful to Richard Rand, who accepted with enthusiasm to share with us both his knowledge and passion for nonlinear dynamics. Over the years, he offered me not only scientific guidance but also advice and support for professional development.

I would also like to thank the other jury members, Martin Brouillette, Julien Sylvestre and Marco Marengo for accepting to read and evaluate my thesis. I am proud to be evaluated by researchers of such a high caliber. Je remercie tout spécialement Martin Brouillette et Julien Sylvestre qui m'ont suivi tout au long de mon doctorat en tant que membre de mon comité de thèse.

J'aimerais ensuite remercier mes collègues du groupe de recherche Micros. Avec Thomas Monin, j'ai partagé les difficultés, les succès et les rires. Tout au long de mon doctorat, Étienne Léveillé a été une ressource indispensable, autant sur le plan des idées que dans le laboratoire. Quant à Alexandre Juneau-Fecteau, il m'a inspiré par ses vastes connaissances, sa générosité et son attitude en recherche. Un merci tout spécial à Nooshin Karami qui me suit dans le projet et avec qui j'ai partagé d'innombrables discussions enrichissantes. Merci aussi à Alihossein Nikkhah avec qui j'ai eu le plaisir de collaborer. Je remercie également Fabien Formosa qui, comme coauteur, a contribué très positivement à mes travaux.

Durant mon doctorat plusieurs auteurs ont été une source d'inspiration inestimable. À travers le temps et l'espace, j'ai eu la chance de faire leur connaissance de par leurs écrits. J'aimerais entre autres remercier Cornelius Lanczos, Stephen Wiggins, Henk W. De Regt, Dennis Dieks, et Steven Strogatz.

Finalement je souhaite remercier mes parents, Cécile et Alain pour leur support, encouragements et curiosité envers ma recherche. Je réserve mes derniers remerciements à Corinne, ma complice de toujours. Elle a été d'un appui sans faille, à l'écoute dans les moments plus difficiles comme dans les moments heureux. Ses connaissances sur les cycles limites dépassent maintenant largement ses champs d'intérêt.

TABLE OF CONTENTS

LIST OF SYMBOLS

A	inner section area of the tube
a_0	nonlinear coefficient in the normal form
c	dimensional friction coefficient
c_P	pressure nonlinearity coefficient
c_T	phase-change nonlinearity coefficient
d	coefficient in the normal form
E	energy (sum of kinetic and potential)
F	force
g	gravitational acceleration
H_v	enthalpy of vaporization
K	kinetic energy
L	length
m	mass
P	pressure
$\hat{P}_e$	effective external pressure (augmented by gravity)
$\dot{Q}_g$	heat transfer between the walls and the vapor
q_1	dimensionless position
q_2	dimensionless velocity
q_3	dimensionless mass of vapor
R	inner radius of the tube
r	radius in phase-space
Re_ω	kinetic Reynolds number
R_g	gas constant
r_{LC}	radius on the limit cycle
t	time
T_g	temperature of the vapor (spatially averaged)
$\left\|T'_{w,0}\right\|$	absolute value of the axial wall thermal gradient
T_H	temperature of the heat source
T_{HL}	dimensionless phase-change limit
T_L	temperature of the heat sink
U	potential energy
$\mathcal{V}_g$	gas (vapor) volume
W	work
x_i	position of the meniscus relative to the equilibrium
z_i	phase-space variables in the normal form

Greek Letters

$\widetilde{\alpha}$	dimensionless oscillation growth rate
γ_{th}	ratio of the specific heat c_p/c_v
δ	bifurcation parameter, $\delta = \sigma - \zeta_f$
$\widetilde{\varepsilon}$	dimensionless phase change constant due to variations of saturation temperature
λ_1	dimensionless growth rate of the first exponential
μ	dynamic viscosity
ν	kinematic viscosity
ω	angular frequency
ω_n	natural angular frequency
Π	instability number, $\Pi = \sigma/\zeta_f$
φ	constant of the linearized solution
ψ	measure of the asymmetry of the arctangent
ρ	density
σ	phase-change coefficient
τ	dimensionless time
θ	angle of the tube relative to the horizontal
ζ_f	dimensionless friction coefficient

Subscripts

0	equilibrium value, or for $\delta = 0$ in normal form
α	component in phase with position
β	component in phase with velocity
e	external (on the air side)
f	viscous friction
g	gravity or gas (vapor)
ℓ	liquid
m	produced by change of vapor mass
r, res	resonator
sat	at saturation condition
sys	system
v	produced by change of vapor volume
ω	which relates to the oscillating flow regime
w	wall

Mathematical notation

$\bar{\cdot}$	averaged quantity
Δ	difference between a property and the equilibrium value
$\dot{\cdot}$	time derivative (dimensional or dimensionless, according to the variable)
$\widetilde{\cdot}$	dimensionless quantity

⋆ Note that there are some minor differences in the choice of symbols from one chapter to the other (e.g. we initially used $\widetilde{\sigma}$ to for the *dimensionless* phase-change coefficient, but later dropped the $\widetilde{\cdot}$ and used only σ for simplicity). Refer to the text in each chapter.

CHAPTER 1

INTRODUCTION

1.1 Context

The Pulsating Heat Pipe (PHP) is a device in which a vapor-liquid plug system self-oscillates. Various PHP configurations are possible. One such configuration is the Single-Branch Pulsating Heat Pipe (fig. 1.1) which consists of one straight small tube (a diameter of 1 mm is typical), closed at one end and open at the other . First, the tube is partially filled with liquid. The closed-end is then heated while a heat sink maintains the mid-section at room temperature. A vapor bubble eventually appears at the closed-end and expands until an equilibrium is reached. At this point, the volume of vapor is fixed and the liquid plug does not move (t_0 in fig. 1.1). If the temperature of the heat source is further increased above some threshold, the liquid plug starts oscillating. The oscillation amplitude increases and then stabilizes, the system reaching a steady-state oscillating regime (see fig. 1.2). These oscillations can be maintained indefinitely.

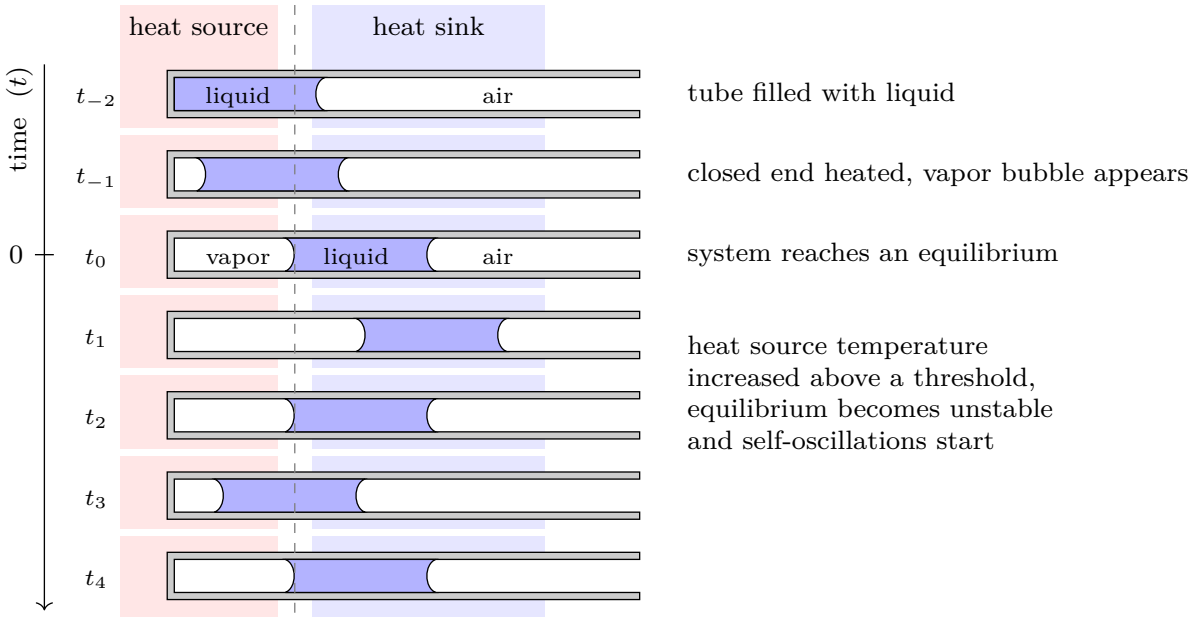

Figure 1.1 Schematic of the Single-Branch Pulsating Heat Pipe (SBPHP), with oscillations starting at t_0. Figure adapted from [112], in accordance with the APS copyright policy.

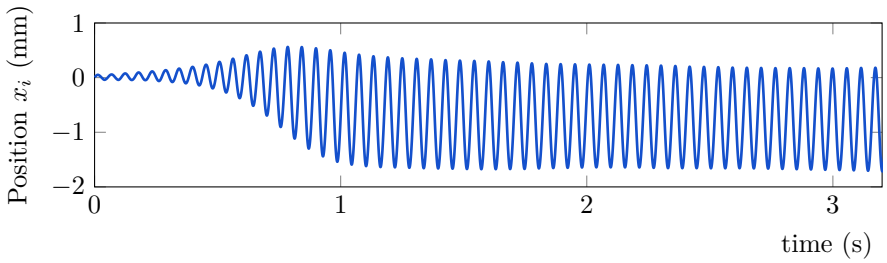

Figure 1.2 Experimental measurement of the meniscus (at the vapor - liquid plug interface) during the startup of the oscillations. The oscillation amplitude grows and then saturates, as the system reaches a steady-state oscillating regime. Figure adapted from [112], in accordance with the APS copyright policy.

This phenomenon has been considered for a number of applications, including cooling, pumping and energy harvesting. The PHP considered as a cooling technology was first described by Akachi [3]. The self-oscillations transfer heat from the heat source to the heat sink by both evaporation and condensation (latent heat) and convection in the liquid plug (sensible heat), effectively cooling down the heat source. For cooling purposes, the device considered is usually a multi-branch Pulsating Heat Pipe (MBPHP) as shown in fig. 1.3. In a MBPHP, the tube follows a closed serpentine path, and has multiple vapor bubbles and liquid plugs. The term Pulsating Heat Pipe (PHP) describes a family of devices, including both the SBPHP and the MBPHP.

There are numerous cooling applications where the PHP could be a relevant cooling solution [72, 48]. One major application is for electronics cooling [13]. Data centers represent today 1% of the global electricity consumption, with approximately 50% of that consumption used for cooling only [63, 54]. According to the International Technology Roadmap for Semiconductors 2015 (ITRS) [49], the energy consumption is expected to increased by a factor of 2.6 from 2015 to 2029. Improved cooling strategies would help to limit the energy consumption. At the chip level, according to the ITRS, the current cooling solutions will no longer meet the requirements by 2030: “The high junction-to-ambient thermal resistance resulting from a thermal management device such as a heat sink provides inadequate heat removal capability at the necessary junction temperatures for ITRS projections at the end of this roadmap” [49]. A major challenge for cooling technologies is the presence of hot spots (high thermal flux on a small surface). Currently, the heat generated in the chip is transferred by heat conduction through several layers until it reaches the fins of the heat sink and can be removed by air convection. Higher heat transfer rates could be obtained by using either forced liquid convection or phase-change rather than heat conduction. This is why, according to ITRS: “New passive and forced liquid and

phase change (liquid to gas) active heat sinks [...] hold the promise of decreased thermal resistance and improved heat spreading capability to address the effect of hot spots"[49]. The various heat pipes (either conventional, pulsating or as vapor chambers) are promising technologies that could address those issues. Because they are based on phase-change, they allow for very small thermal resistances. Heat pipes are also passive: they do not need an external source of energy to activate a pump.

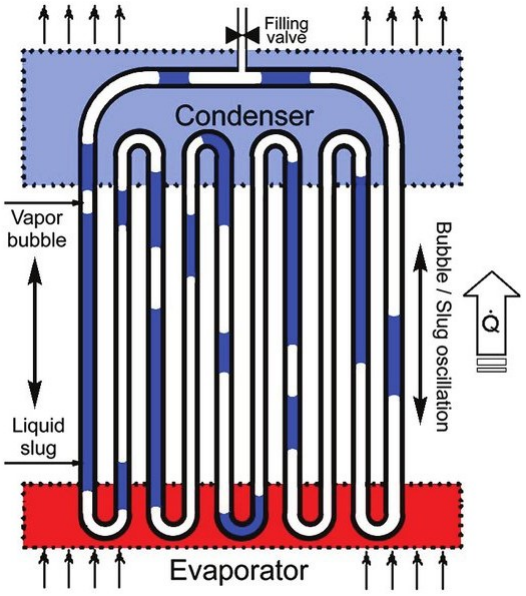

Figure 1.3 Schematic of the multi-branch Pulsating Heat Pipe. Figure reproduced from [61], in accordance with the license CC BY 3.0 [19].

The PHP self-oscillations can also be used as a pump when combined with a valve [25, 26]. In a PHP, heat is converted into mechanical energy (liquid plug oscillations). Part of this mechanical energy can thus be used to pump another fluid. A related application is for propulsion. Indeed, the PHP self-oscillations are at the heart of a toy called the putt-putt boat [32, 33, 52] (more details in section 2.4.1).

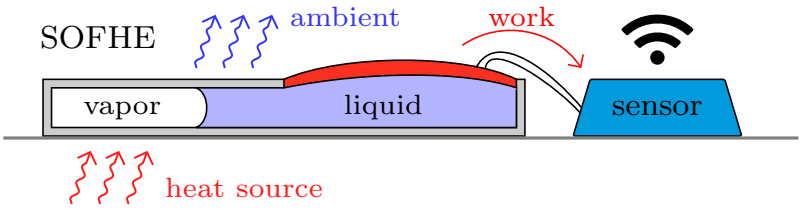

Figure 1.4 Schematic of energy harvesting from the SBPHP self-oscillations, using a piezoelectric membrane as the electromechanical transducer.

Finally, another application of the PHP self-oscillations is for energy harvesting. By coupling a SBPHP to an electromechanical transducer (see fig. 1.4), part of the mechanical

energy can be converted into electrical energy. We coined this device the Self-Oscillating Fluidic Heat Engine (SOFHE) [78, 111]. Others have studied energy harvesting by coupling a MBPHP to an electromechanical transducer [79, 125, 80, 81, 104]. This technology can harvest energy from a heat source, to power a wireless sensor for example.

Various energy harvesting approaches are expected to facilitate the deployment of the Internet of Things (IOT). The Internet of Things consists in the idea of a network of sensors distributed in the environment communicating through the internet. As a result of the deployement of the IOT, the number of sensors in our environment is expected to grow tremendously. These sensors would make it possible to gather much more information from our surroundings, enabling new technologies, products and services. Applications are envisioned for smart home, smart health, transportation, cities, energy production, factories and other domains [76]. In some cases, the information would be gathered locally and then transmitted to the cloud to be analyzed. In other cases, it might be preferable to analyze the information and take decisions locally (the sensor + cloud approach might be too slow, too energy-hungry or impossible due to internet connection issues). The sensor would then be coupled to a microcontroller and possibly to an actuator. This would allow for distributed intelligence in the environment. Within the IOT paradigm, the distributed sensors must be supplied in energy in some way. They could be connected to the power grid, but this would be impractical or too costly in many applications: there is a need for autonomous sensors. Energy can be supplied by a battery, but this limits the lifetime of the device as battery replacement is also impractical. With a battery, there is a tradeoff between the capabilities of the sensor/actuator (more capabilities meaning higher power consumption), the life time of the device and the size and cost of the battery. If however energy can be harvested from the environment, the sensor can be made truly autonomous and the battery size can be kept to a minimum.

1.2 Problem Statement

In the Micros research group, directed by Luc Fréchette, waste heat recovery approaches based on phase-change have been studied for close to ten years. The first device built by Léveillé et al. [68] was a chamber made of a silicon substrate and a piezoelectric membrane, filled with water. The chamber was continuously supplied in water via an external pump. The bottom of the chamber was heated, leading to repetitive explosive evaporation in the chamber with corresponding pulses of voltage at the piezoelectric membrane. After each pulse, the vapor exited the chamber via an outlet and the chamber was filled again with liquid via the inlet so that the cycle could repeat. Later on, self-oscillations, as in a SBPHP, were observed in one of the device. The group was unaware of the literature

on PHP at that point. The main advantage of the self-oscillating mode of operation is that no external pump is needed. The energy harvesting device based on self-oscillations was dubbed the Self-Oscillating Fluidic Heat Engine (SOFHE) in subsequent publications [78, 111]. At the start of my PhD in the Micros Group, we had difficulties reproducing the self-oscillations experiment. We also had no idea what were the conditions required to generate those self-oscillations and how to control them.

Given this starting point, it is useful to discuss what should we aim for in the long term: what would be a good SOFHE? To power wireless sensors, the SOFHE must be able to produce the required power output, be as small as possible, have a low cost, have a predictable behavior and be reliable. The performance of the SOFHE can be quantified by combining the power, volume and cost in two figures of merits, the power density [1] (in W/m^3) and the power divided by the cost (in W/\$), to be maximized. There is a range of environments offering low to large thermal gradients. There is also a range of sensors, from low energy consumption to high energy consumption. Increasing the SOFHE power density extends the range of sensors that can be used for a given thermal gradient and extends the range of thermal gradients for which a given sensor can be used. The question now becomes: What would be a good SOFHE design (geometry, surface treatments, wall materials, working fluid, etc.) such that it can be controlled, works reliably and performs well based on the metrics identified above?

1.3 Research Strategy

In this section, I will explain what my research strategy is. I will first describe my research philosophy (section 1.3.1), describing the research process in engineering, discussing scientific understanding as a key step in that process and finally discussing how I approached my project as part of the engineering research process. I will then present my research questions and objectives (section 1.3.2).

1.3.1 Research Philosophy

Given the starting point described in section 1.2, how can we develop a good SOFHE design? We could do a parametric study experimentally: vary one parameter at a time (e.g. length of the liquid plug) and see the effect on the behavior and the performance. However, I think that taking this approach alone is shortsighted. There are too many parameters and those might be interrelated. Also, we would like to control not just the obvious parameters but the overall design (e.g. there is a very large number of ways to

1. In some applications where the height does not matter as much, the surface power density (in W/m^2) might be a better figure of merit. The height might be a constraint (e.g. less than 1 cm).

modify the internal surface of the tube). In my opinion, it is not enough to simply shoot in the dark. *To reach the desired level of control, we need a theoretical framework to reach a basic understanding of the self-oscillating phenomenon.*

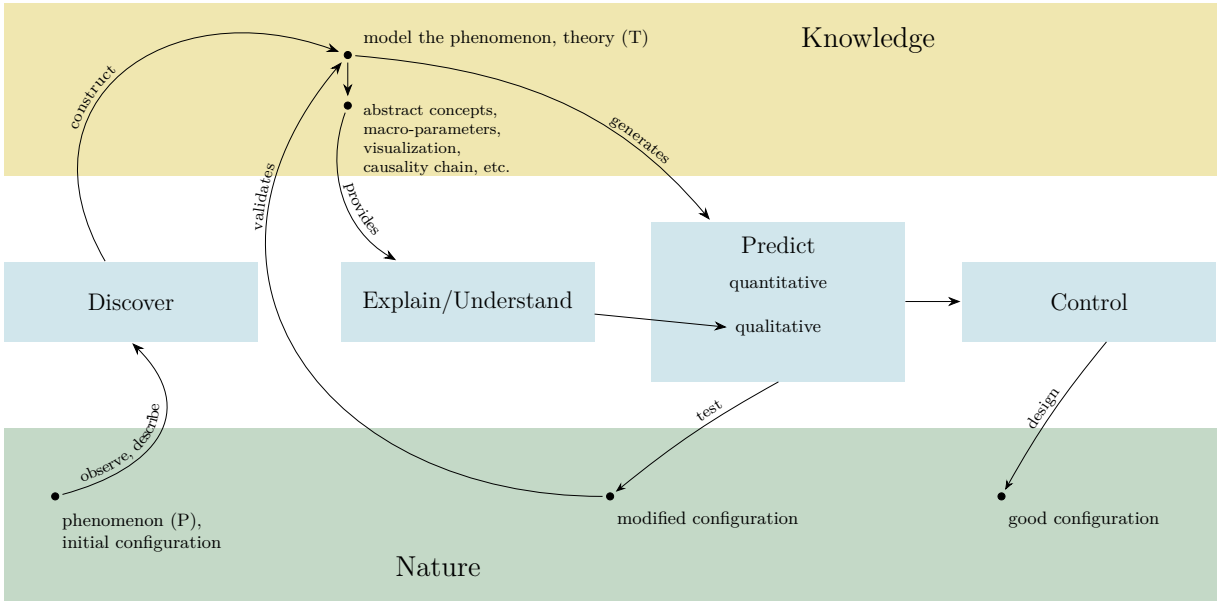

Figure 1.5 Research from an engineering point of view, from the discovery of a phenomenon to the control, leading to the design of a good configuration.

A Representation of Research in Engineering

My advisor, Luc Fréchette, suggested to me the structure shown in fig. 1.5 to describe the research from an engineering point of view. Starting from a *discovered* phenomenon, the engineer wants to *control* it in order to build a good configuration, from which a technology or a product can be produced. First, in the *discover* step, one needs to sufficiently observe and describe the phenomenon. Then, one must construct a theoretical framework, expressed as a mathematical model, to *explain* what one observes. Explanations can be defined as answers to qualitative questions about the observed phenomenon. In the explanation step, one must also be able to carry out retrodictions, which are predictions about already known events, behavior, data, etc. From that, one wishes to know how the system would behave outside the known conditions. The model should allow to *predict* that behavior by tuning its parameters. Those predictions can be tested experimentally, which increases the confidence into the model. Once the model is validated, the engineer can use the qualitative and quantitative predictive power to *control* the phenomenon. The engineer can use the model as a guide towards a good design. For example, one might find the set of parameters maximizing a given performance metric. As the research progress, the theoretical framework gets refined, leading to an increase in the precision and the span of the explanations, predictions and control. The research also progresses from qualitative

to quantitative inquiries. Along the way, one might use not one, but various mathematical models, each being adapted to the state of the research. For example, in the development of the gas turbine, the Brayton thermodynamic cycle can be used to understand the main processes occuring in the engine, to find a limit to the efficiency and to evaluate if there is room for improvement in a given design. However, to predict the mechanical constraints on the various parts accurately, highly detailed numerical simulations are needed.

Scientific Understanding

I would like to linger now on the explanation/understanding step, since it will occupy most of my thesis. A major goal of the theoretical framework is to establish a scientific understanding of the phenomenon. To reach that objective, proper choices must be made in the research strategy, both in terms of modeling and in terms of experiments. So, what exactly do we mean by scientific understanding? In my view, understanding is about building intuitions about the physics. One must be able to make qualitative predictions about the system without having to solve/simulate the equations each time. This point of view has been expressed by several scientists in the past. Werner Heisenberg starts his famous paper introducing the Heisenberg's uncertainty principle in those terms:

> *We believe we understand the physical content of a theory when we can see its qualitative experimental consequences in all simple cases and when at the same time we have checked that the application of the theory never contains inner contradictions.* [53] (english translation of [44])

Richard Feynman describes what it means to understand in those terms, citing Dirac:

> *What it means really to understand an equation—that is, in more than a strictly mathematical sense—was described by Dirac. He said: "I understand what an equation means if I have a way of figuring out the characteristics of its solution without actually solving it." So if we have a way of knowing what should happen in given circumstances without actually solving the equations, then we "understand" the equations, as applied to these circumstances. A physical understanding is a completely unmathematical, imprecise, and inexact thing, but absolutely necessary for a physicist.* [31]

John Hopfield notice the following about understanding in an discussion about artificial intelligence:

> *There is the question of what do you mean by understand? When I taught freshman physics, I used to say I wanted to get students to understand the subject, to understand Newton's laws. I didn't want them to simply memorize a set of examples to which*

> *they knew the equations, to write down to generate the answers. I had this nebulous idea of understanding so if you looked at a situation you can say: I expect the bowl to make that trajectory for example. So, I mean an intuitive notion of understanding. I do not know how to express that very well, I have never known how to express it well and you run smack up against it when you choose these simple neural networks, feed-forward neural networks, which do amazing things and yet you know contain nothing of the essence of what I would have felt was understanding. Understanding is more than just an enormous lookup table.* [36] (adapted for writing)

Insights about the notion of understanding can be found in the philosophy of science. De Regt and Dieks [21] studied what scientific understanding is in a very careful manner. They proposed the following definition for scientific understanding in two criteria:

> *1) Criterion for Understanding Phenomena (CUP): A phenomenon P can be understood if a theory T of P exists that is intelligible (and meets the usual logical, methodological and empirical requirements)*
>
> *2) Criterion for the Intelligibility of Theories (CIT): A scientific theory T is intelligible for scientists (in context C) if they can recognise qualitatively characteristic consequences of T without performing exact calculations* [21].

Thus, there is a distinction between understanding a phenomenon and understanding a theory [2]. According to the CUP criterion, a theory is required to establish an understanding of a phenomenon. This theory must be intelligible (one must be able to understand it). A theory is intelligible if it meets the CIT. We see that the CIT shares similarities with the definitions above, by putting emphasis on qualitative predictions and those being possible without having to solve equations.

I would like to suggest a geometrical viewpoint of scientific understanding, by considering the configuration space, the space of parameters required to described a phenomenon (the following discussion is based on the generic example is shown in fig. 1.6). The phenomenon may exhibit qualitatively different behavior within the configuration space (behavior 1, 2 and 3), each separated by frontiers. We may also be interested in some quantitative property, function of those parameters (a performance metric for example). Let's say the system is at a point A, in a non-desirable behavior (behavior 1, performance=0). If we possess scientific understanding, we can recognize that increasing the parameter p_1 so that the system moves to B will lead to a change of behavior. Furthermore, we recognize from point B that a proper change in p_1 and p_2 will lead to an increase in the performance.

2. Insights on that subject can be found elsewhere in the philosophy of science [37, 14].

More generally, if we possess scientific understanding, we would be aware of the possible behaviors and that a positive performance is obtained in behavior 2. Ideally, we would know that the performance has a single maximum value. Let's give concrete examples. Example 1: two-dimensional linear systems described by the equation $\dot{\boldsymbol{x}} = A\boldsymbol{x}$, where A is a 2×2 matrix, containing four parameters. Qualitatively different behaviors can be classified according to the determinant and the trace of the matrix A as shown in fig. 1.7 (see [107, Chap.5] for the theory). There, scientific understanding of the mathematical system is achieved, as we are able to 1) recognize the possible behaviors, 2) predict the behavior based on two macro-parameters, 3) understand how the behavior can be modified by tuning the properties of the system. Example 2: Mitcheson et al. [73] studied energy harvesting for forced oscillators, for which they were able to obtain analytical solutions. Figure 1.8 shows various behaviors and the dimensionless power output as a function of dimensionless parameters. Here, scientific understanding is achieved because a theory of the phenomenon exists and the theory enables us to 1) recognize the possible behaviors, 2) predict the behavior based on two macro-parameters, 3) qualitatively predict how the performance behaves in terms of those parameters and 4) understand how the behavior and the performance can be modified by tuning those parameters.

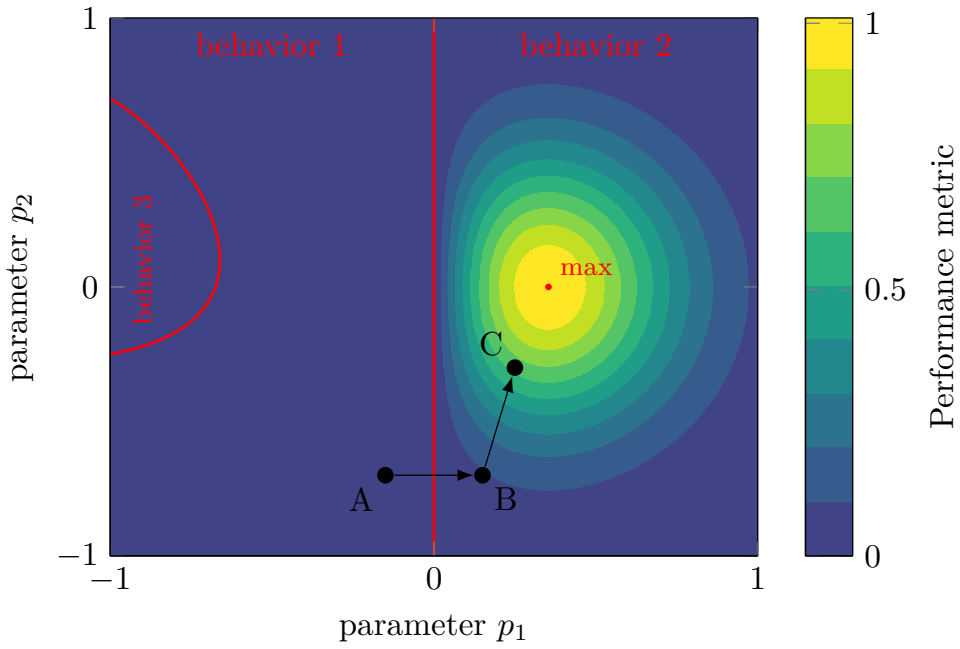

Figure 1.6 Geometrical representation of scientific understanding; qualitative properties (e.g. different behaviors) and quantitative properties (e.g. oscillations amplitude, oscillations frequency, a performance metric) can be shown as functions of the position within the configuration space (only 2 parameters are shown here, but the space could obviously have many more dimensions).

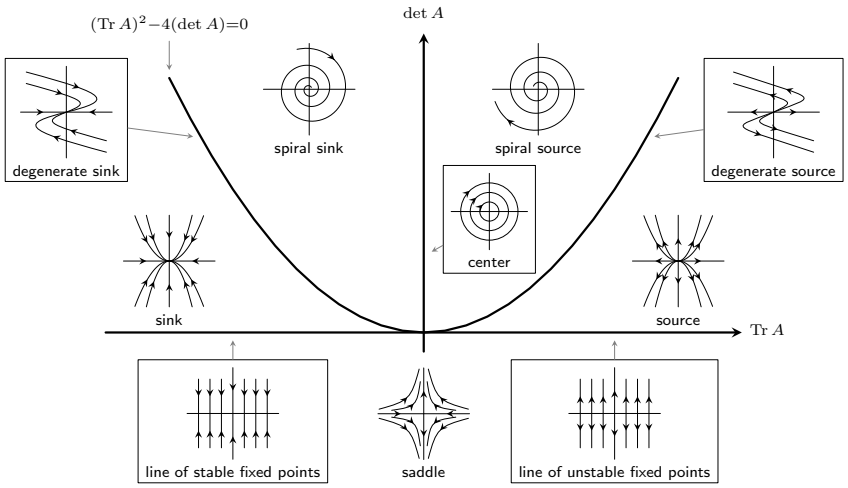

Figure 1.7 Classification of two-dimensional systems described by the equation $\dot{\boldsymbol{x}} = A\boldsymbol{x}$; The figure is slightly modified from the original work of Gernot Salzer (`https://tex.stackexchange.com/a/347401`) in accordance with the license CC BY-SA 3.0 (`https://creativecommons.org/licenses/by-sa/3.0/`).

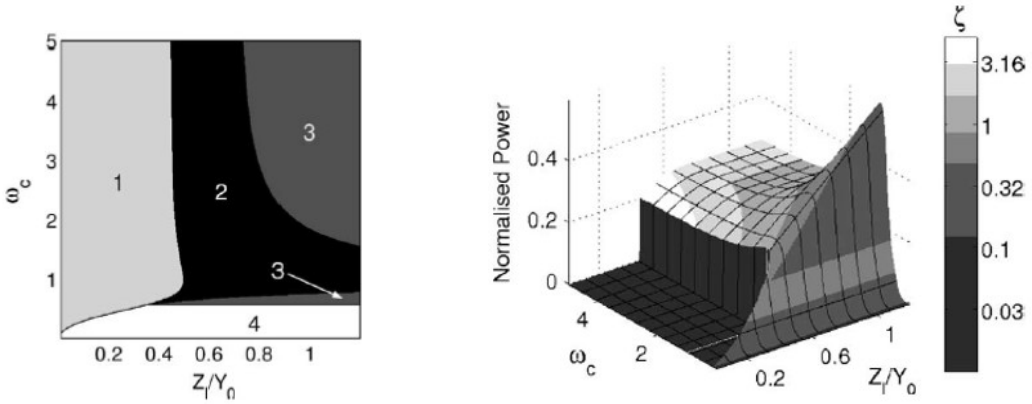

(a) (b)

Figure 1.8 Energy harvesting for a specific configuration of a forced oscillator, called velocity-damped resonant-generator (VDRG), with a electromagnetic transducer and where some practical constraints are considered; (a) operating map with various behaviors (1. unable to operate, 2. operate at the displacement limit, 3. optimal operation, 4. more power available if the damping factor can be increased above ζ_{max}), (b) normalized power (defined by a dimensionless number). The axis are given by $\omega_c = \omega/\omega_n$ with ω the forcing angular frequency and ω_n the natural frequency, and Z_l/Y_0, with Z_l the maximum possible amplitude (internal size of the device) and Y_0 the amplitude of the motion of the device (from an external excitation). Figure from Mitcheson et al. [73, Fig.8,9], in accordance with IEEE license ©2004 IEEE.

A useful point to make is that it might be easier to understand a phenomenon within one configuration space than in another, such that a change of basis might be useful. We see

that in the two examples above. For the two-dimensional linear systems (fig. 1.7), there was originally four parameters (the elements of the matrix A). The behavior of the system can however be completely described by only two parameters, the determinant and the trace of the matrix A. For the energy harvesting example (fig. 1.8), the oscillator is described by numerous physical parameters (the mass, the stiffness, the friction coefficient, etc.). However, the behavior and the dimensionless power output can be described as functions of only two dimensionless numbers ω_c and Z_l/Y_0. The change of basis reduces the number of dimensions, making understanding easier to achieve but more abstract. An additional step is required if one ask what is the effect of a single physical parameter (e.g. the mass of the resonator). This especially occurs when nondimensionalizing a problem.

According to De Regt and Dieks [21], scientists use various toolkits to achieve scientific understanding as defined by the CUP and CIT, such as: causality chain, visualization, abstract reasoning (general behavior of solutions of mathematical equations). Such tools make it possible to get the intuition required to predict the behavior of the system. De Regt and Dieks also mention the importance of skills: understanding is available only if one possesses the required skills to apply the toolkits adapted to the problem.

What it Means For my Project

I would like now to discuss how the desire to reach scientific understanding, with the ultimate goal of guiding the design of devices, influenced my approach. First of all, I identified early on fundamental research questions about the physics of the SBPHP, to guide the modeling approach (see section 1.3.2). Answering those uncovers fundamental causal mechanisms leading to the observed dynamics and thus enables scientific understanding. To find those answers, I made key choices in the modeling approach (ODEs, continuously differentiable) such that classical mathematical approaches could be applied (linear stability analysis, normal forms, averaging, numerical continuation).

Throughout the research, I insisted on taking analytical approaches as much as possible, as opposed to numerical techniques. With an analytical solution, we see explicitly the effects of the parameters in the solution, such that we can naturally see how the behavior changes within the configuration space. The analytical solution makes it easy to build intuitions about the physics, to internalize the dynamics. The analytical approaches are especially useful to find frontiers delimiting qualitatively different behaviors (bifurcations). They also make it possible to find the key parameters of the problem, defining the minimal configuration space to study. In contrast, a numerical solution is much narrower, being only valid for the specified values of the parameters; a large number of simulations might be required to characterize the dynamics and definitive answers are more difficult to reach.

Furthermore, it is (relatively) easy with an analytical solution to follow the impact of the physics (at the differential equations level) on the solution's characteristics (amplitude, frequency, etc.). Numerical approaches on the other hand works more like black boxes, we do not really know what happens between the differential equations and the final solution. Of course, when highly accurate results are required, one typically has to resort to numerical approaches, but this is usually beyond the understanding step.

The contrast between my vision and the literature is particularly apparent with regards to the phase-change modeling. I restricted my analysis to a simple, but highly relevant phase-change expression, whereas in the literature, there is a strong tendency towards more and more sophisticated models to describe the phase-change as accurately as possible. I personally do not care as much about making highly accurate predictions. Keeping in mind that we might want to control the phase-change, those accurate models could quickly become obsolete [3]. I prefer to first understand clearly the role of the phase-change in the dynamics. I want to know if we should tune the phase-change in order to improve the performance, if the effect would be significative and if so, based on which principles the phase-change should be tuned.

Finally, my experimental approach consisted mostly in targeted experiments, to validate the theoretical model and our scientific understanding. I preferred that approach to a large blind parametric study without any prior understanding of the dynamics. Of course, this is not to say that exploratory experiments do not have their place.

1.3.2 The Research Questions and Objectives

Going back to the basic question (section 1.2):

Q0) *What would be a good SOFHE design (geometry, surface treatments, wall materials, working fluid, etc.) such that it can be controlled, works reliably and performs well in terms of power density and power per cost?*

I suggested above that, in order to reach the desired level of control, we must first establish a theoretical framework to produce a basic understanding of the self-oscillations. To guide the theoretical and experimental approaches, and to verify if scientific understanding is achieved, I identify below key qualitative questions about the physics.

The oscillating phenomenon shown in fig. 1.2 is surprising because boundary conditions are constant (heat source and heat sink temperatures, external pressure) but we obtain a periodic motion nonetheless. One may thus ask:

3. Those models should remain useful though for the design of MBPHP, in the cases where one prefers not to control the phase-change and prefer to stick to plain internal surfaces.

Q1) *Where do the oscillations come from?*

A related question is what defines the oscillation frequency. From the small oscillations at the early stage of the startup, one could expect that friction would introduce damping in the system and that the oscillation amplitude would decrease. On the contrary, during the SBPHP startup, the oscillation amplitude grows exponentially. One may then ask:

Q2) *Why does the oscillations amplitude increase during the startup and what are the required conditions for the startup to occur?*

The oscillation amplitude eventually saturates at the end of the startup, the system reaching a steady-state oscillating regime. One may ask:

Q3) *Why does the oscillations amplitude saturate and what defines the oscillation amplitude in the steady-state regime?*

By answering these questions, a better scientific understanding of the SBPHP dynamics should be achieved. Indeed, these questions are chosen to highlight the causal mechanisms leading to the observed behavior (causal explanations being a key tool for scientific understanding as explained above). From the answers to these questions, we should better understand how to control the self-oscillations (startup conditions, frequency, amplitude, etc.). At this point, one may ask the following question regarding energy harvesting from SBPHP self-oscillations:

Q4) *How does an energy harvesting device based on SBPHP oscillations behave?*

More specifically, one would like to understand how to maintain the self-oscillations despite the dissipative effect of the electromechanical transducer, how the oscillation dynamics is impacted by the transducer and how one can increase the power output or the efficiency.

This PhD project aims at answering these questions. The objectives can be directly translated from the research questions above.

1.4 Thesis Plan and Original Contributions

Here, I briefly present the plan of the thesis. I will first review the state of the art (chapter 2), ending with the current knowledge on the research questions identified above (section 2.5). I will conclude that the current answers are incomplete which led me to investigate these questions myself. In the following chapters (chapters 3 to 6), I present my efforts at answering those questions, which constitute original contributions to scientific knowledge. I present each chapters in more details below. This thesis is by article: Chapters 3, 4 and 6 are based on articles published or submitted to scientific journals.

Chapter 3. Why it oscillates and what leads to the startup. In this chapter, we answer the questions of where the oscillations come from, why the oscillations increase during the startup and what are the required conditions for the startup to occur. To do so, a mathematical model is proposed, which is then linearized and solved. We show that the oscillations are explained by the coupling of the spring effect of the vapor and the inertia of the liquid, which leads to a spring-mass system. The startup is explained by an instability mechanism: the phase-change acts as a positive feedback and the viscous friction dissipates the energy. The startup occurs when the phase-change coefficient is greater than friction coefficient. This understanding is validated experimentally.

Chapter 4. What leads to the steady-state regime. In this chapter, we answer the question of why the oscillations amplitude saturates and what defines the oscillation amplitude in the steady-state regime. We first show that, in the startup experiment, the trajectory in phase-space converges towards a limit cycle (corresponding to the steady-state). We obtain an analytical approximation of the dynamics (normal form) which includes the effect of the nonlinearities. We show that the amplitude initially grows due to the instability mechanism and then saturates due to a limiting mechanism, produced by the nonlinearities. We then prove the existence of the limit cycle, which is created via a Poincaré-Andronov-Hopf bifurcation. Finally, based on our mathematical results, we explore how to increase the oscillations amplitude.

Chapter 5. Accurate solution for the steady-state. In this chapter, I first explore the dynamics in more details (waveform, spectral analysis), over a large range of the parameters, by numerical continuation. I then obtain precise analytical approximations valid over that range, using averaging.

Chapter 6. How an energy harvesting device behaves. In this chapter, we answer the question of how an energy harvesting device based on the SBPHP would behave. A load (a dissipative force representing a velocity-damped transducer) is added to the model. Based on the analytical expressions of chapter 5, we study the effect of the load on the dynamics, the power output and the efficiency. We then discuss the design of SOFHE based on our results. We highlight how energy harvesting from a self-oscillator differs from a forced oscillator.

Chapter 7. Energy persective. In this chapter, I revisit the analysis of the dynamics and the energy harvesting by taking an energy perspective. I show how we can analyze the device by considering the energy stored in the resonator, the energy injected by the

phase-change and the energy dissipated by friction. This description enables a general understanding valid for most configurations and provide clear guidelines for the design.

CHAPTER 2

STATE OF THE ART

In this state of the art, I will present important results and approaches in the PHP, focusing mostly on the SBPHP. I will first present a very basic result for PHP, a criterion ensuring the formation of liquid plugs in the PHP (as opposed to the liquid resting at the bottom of the tube), based on the Bond number (section 2.1). I will then briefly summarize the experimental results in MBPHP (section 2.2). The research on MBPHP aims mostly at characterizing, predicting and improving the thermal performance, such that it can be a reliable and performant technology for cooling applications. I will then focus on the SBPHP dynamics. I will start by discussing detailed experimental observations in the SBPHP (section 2.3). I will follow by discussing various approaches to model and understand the dynamics (section 2.4). Finally, I will describe the state of the art on my research questions (section 2.5).

2.1 Criterion for the Formation of Liquid Plugs

One important result in the PHP literature is the existence of a critical diameter to ensure the formation of liquid plugs in the PHP [127, 39]. In the static case, a liquid plug is subject to both gravitational force and surface tension on both ends (on the capillaries). For a large enough tube, the gravitational force would dominates and the liquid would simply rest to the bottom of the tube. For a small enough tube, the surface tension is strong enough such that liquid plugs forms, as seen on fig. 1.1. The ratio between the gravitational force and the surface tension is given by the dimensionless Bond number [72] (often called the Eötvös number):

$$\mathrm{Bo} = \frac{g\left(\rho_\ell - \rho_g\right) D^2}{\gamma} \ , \tag{2.1}$$

where g is the gravitational acceleration, ρ_ℓ and ρ_g are respectively the density of the liquid and the surrounding gas (vapor here), D is the inner diameter and γ is the surface tension. A generally accepted upper limit to ensure the formation of liquid plug is $\mathrm{Bo} = 4$ [127, 39, 72]. Solving for D, we obtain a critical diameter:

$$D_{crit} = 2\sqrt{\frac{\gamma}{g\left(\rho_\ell - \rho_g\right)}} \ . \tag{2.2}$$

We must have $D < D_{crit}$ to ensure the formation of liquid plugs. For water at 20 °C, we get $D_{crit} = 5.5\,\text{mm}$.

2.2 Experimental Results for MBPHP

Since Akachi's patent [3], most of the research on PHP has focused on Multi-branch Pulsating Heat Pipes (MBPHP, fig. 1.3), with cooling applications in mind. Two important research themes in MBPHP are 1) the measurement of the thermal performance, as parameters of the system are varied and 2) the visualization and characterization of the flow within the MBPHP. PHP with thermal conductivity of 10 to 15 times the conductivity of pure copper have been measured [71]. It is found that, as the heat input at the evaporator is increased, the thermal resistance of the MBPHP generally decreases (meaning the thermal performance increases) until the device reaches dry-out [60, 71, 106]. Experimental evidence suggests that the thermal performance of MBPHP is related to the flow regimes inside the MBPHP [59, 39, 71, 106]. Typically, as the heat input is increased, one successively observe no oscillations (static regime), small amplitude oscillations, large amplitude oscillations, circulation with flow reversal and, finally, stable circulation. Those regimes are associated with a gradual increase in thermal performance. In the circulation regime, the flow is annular (instead of vapor bubbles and liquid plugs) in some portions of the tube. Beside the heat input, numerous parameters have been shown to impact the flow regimes and the thermal performance of the MBPHP, including the filling ratio, the inclination angle (relative to the gravitational field), the number of turns and the choice of the working fluid. The effects of the parameters are complex and interrelated. It is generally accepted that there exist an optimal filling ratio (depending on the working fluid, a ratio between 20% and 80% is recommended [127, 39]). MBPHP are found to perform better in a vertical orientation than horizontal orientation. However, the effect of the orientation reduces as the number of turns is increased [127, 39]. Various working fluids have been used in MBPHP, including water, water with nano particles, acetone, ethanol, methanol, FC-72, HFE-7000, R-245fa and R-134a [127]. Which working fluid performs the best varies according to the device configuration.

2.3 Experimental Observations of the SBPHP

It is useful to first go back to the description of the oscillations in the SBPHP. On that subject, important contributions were made by Das et al. [20] and Rao et al. [92, 93]. I will briefly review only Rao et al. [93] here, since it builds upon the previous publications and constitute the most refined experiment. The experimental setup is a glass tube oriented vertically, heated at the top by a transparent evaporator and cooled at the bottom by a

transparent condenser (see fig. 2.1). The working fluid is FC-72. The glass tube has an internal diameter of 2 mm and the evaporator and condenser lengths are both 20 cm. The position of the meniscus is tracked by a high speed camera and synchronized with pressure measurements of the vapor. In a similar setup, Das et al. [20] explain that there are no oscillations for a low temperature of the evaporator. As the evaporator temperature is increased above a threshold, self-oscillations start and are maintained over time.

It is observed in the experiment that the meniscus oscillates between the evaporator and the condenser sections, as shown in fig. 2.2. A thin liquid film left on the wall is also observed. This liquid film is believed to be responsible for a large part of the evaporation, since it has a low thermal resistance. In the experiments of Rao et al. [93] measurements were made at a fixed temperature of the evaporator of $T_e = 46\,°C$ and at several temperature of the condenser, T_c: 28 °C, 24 °C, 20 °C and 16 °C. For $T_c = 28\,°C$, oscillations of constant amplitude (approximately 10 cm peak-to-peak) with a frequency of 1.2 Hz were observed. For $T_c = 24\,°C$, $T_c = 20\,°C$ and $T_c = 16\,°C$, it was observed that the meniscus makes a large oscillation, going into the evaporator, followed by a smaller oscillation, which remains in the condenser (as seen in fig. 2.2). This cycle then repeats itself. The authors suggest that the meniscus is unable to go back into the evaporator during the small oscillation because of the lasting presence of the liquid film into the evaporator, which is still evaporating.

Rao et al. [93] also measured the temperature of the vapor during the oscillations, with a small thermocouple located in the vapor. It was found that the vapor was superheated

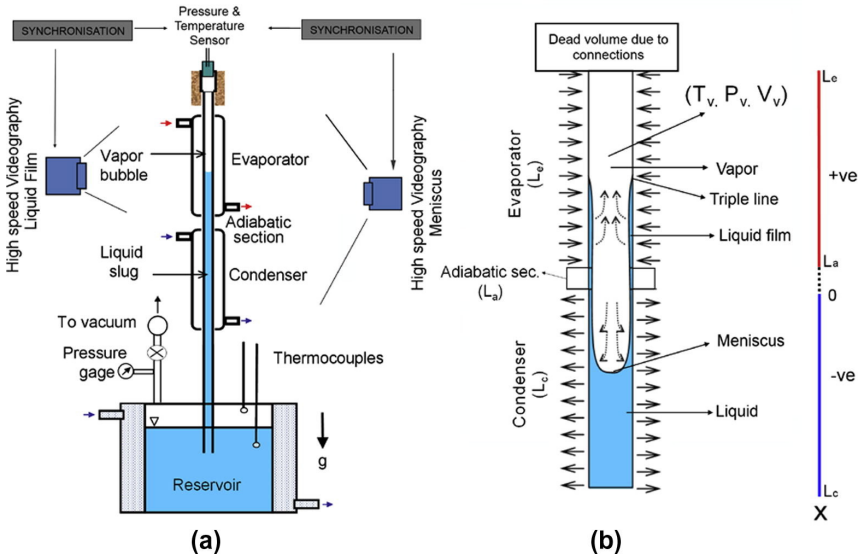

Figure 2.1 Experimental setup in Rao et al. [93]. Figure reproduced with the authorization of Elsevier.

at all time and close to the evaporator temperature (between 44 °C and 46 °C). Furthermore, the temperature of the vapor does not vary much during the oscillations (although variations could be underestimated due to the frequency response of the thermocouple). Similar results were obtained by Gully et al. [41] where a SBPHP was tested in cryogenic conditions to avoid radiation between the thermocouple and the environment, to obtain precise measurements of the vapor temperature.

Rao et al. [93] explains that the pressure in the vapor varies due to both change of volume and changes of mass (due to evaporation and condensation). Measurements shows that the maximum peak of pressure does not occur at the upmost position of the meniscus, but shortly after (during the downward motion). This is explained by the evaporation of the liquid film. The mass of vapor can be obtained indirectly using the ideal gas law: $m_v = P_v V_v/(R_v T_v)$, where P_v, V_v and T_v vary over time and are measured experimentally.

2.4 Modeling and Understanding in UPHP and SBPHP

In order to better understand the dynamics in the MBPHP, researchers have investigated simpler devices which still exhibit the same basic phenomenon of self-oscillations (see fig. 2.3). Those includes the U-shaped Pulsating Heat Pipe (UPHP) which is a MBPHP with only two branches, with only two vapor bubbles and one liquid plug and the Single-branch Pulsating heat pipe (SBPHP) which has only one branch open to the ambient, with only one vapor bubble and one liquid plug. The UPHP and the SBPHP cannot exhibit all the behaviors observes in the MBPHP (for example, no circulation is possible). Nonetheless, they both exhibit self-oscillations.

2.4.1 Putt-Putt Boat

The putt-putt boat is a toy, with a propulsion mechanism based on the same principle as the PHP (see fig. 2.4). A water circuit, comprising a chamber and a channel connected to the surrounding water, is filled with water. The water in the chamber is heated by a candle, vapor is generated and leads to pulsations of the water in the channel, producing thrust. The physics of the PHP has been studied by Finnie and Curl [33, 32] in 1963 and revised later on by Jenkins [52] in 2013. There is no reference to those publications in the PHP literature. I suspect that, if they have been known, they would have greatly influenced the modeling of the PHP and the understanding of its physics.

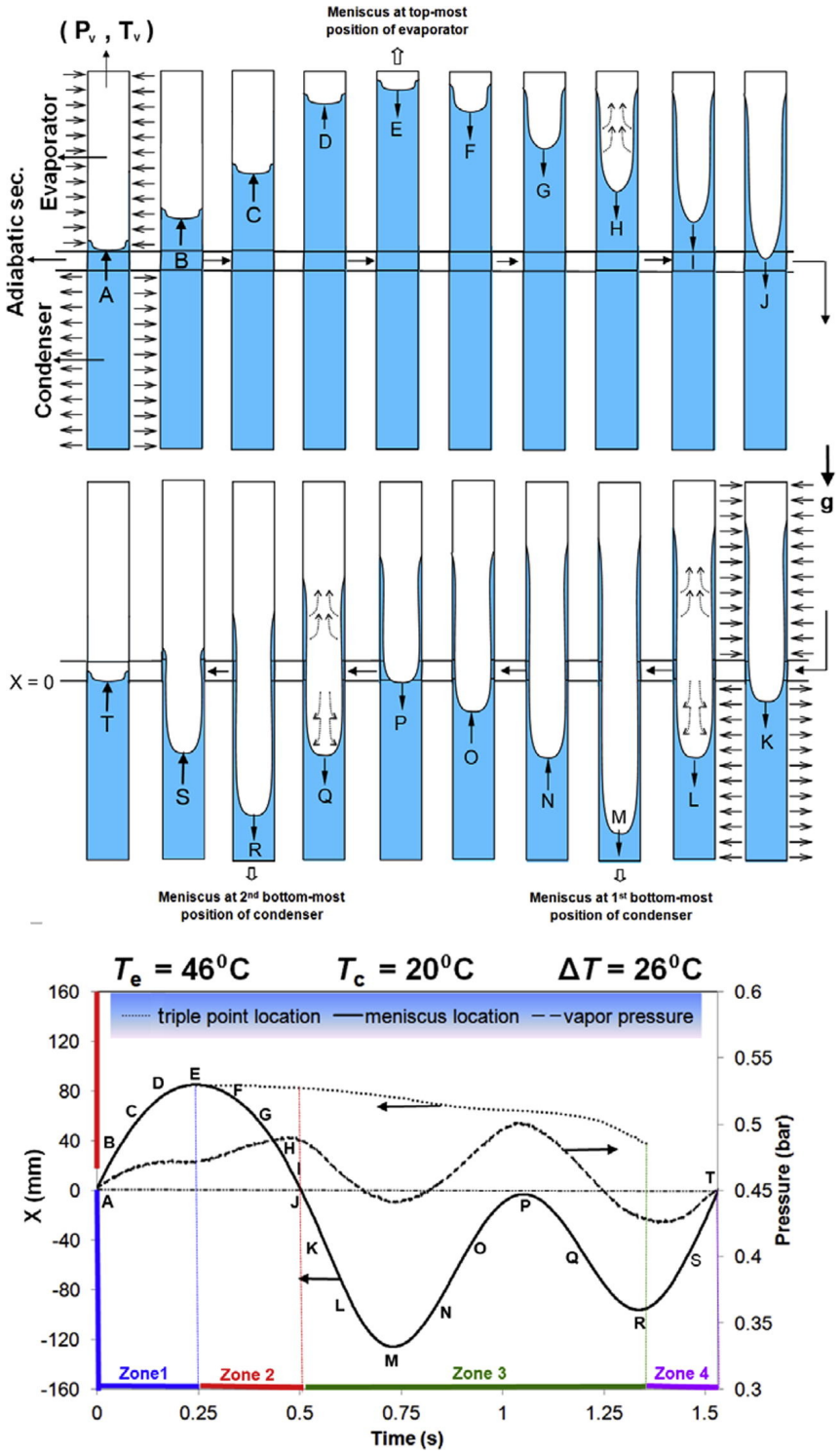

Figure 2.2 Schematic of the oscillations and measurements of the meniscus position and pressure of the vapor, from Rao et al. [93]. Figure reproduced with the authorization of Elsevier.

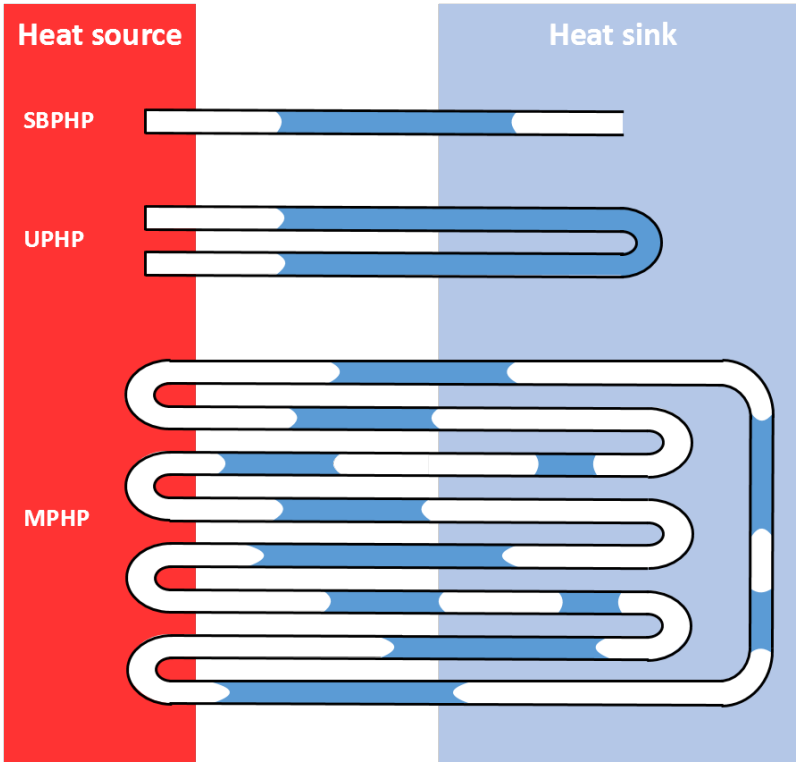

Figure 2.3 Various types of PHP, of increasing complexity: Single-branch Pulsating Heat Pipe (SBPHP) on top, U-shaped Pulsating Heat Pipe (UPHP) in the middle and Multi-branch Pulsating Heat Pipe (MBPHP) at the bottom.

Modeling

Jenkins explains the modeling approach as follow. The ideal gas law is applied to the vapor, leading to:

$$P = \frac{C\,(N_0 + S)}{V_0 - Ay}\ , \tag{2.3}$$

where P is the vapor pressure, C is a constant ($C = RT$ with R the universal gas constant and T the temperature), $N_0 + S$ is the total quantity of vapor (in moles) with N_0 the quantity at equilibrium and S the quantity generated by phase-change ($S = 0$ at equilibrium), V_0 is the volume of vapor at equilibrium, A in the cross-sectional area and y is the displacement of liquid relative to the equilibrium. The temperature of the vapor is assumed constant. To study the startup, one may consider small oscillations around the equilibrium, and linearize the pressure [1]using a Taylor expansion for both y and S close to 0:

$$P \approx P_0 + (P_0/N_0)\,S + k_1 y\ , \tag{2.4}$$

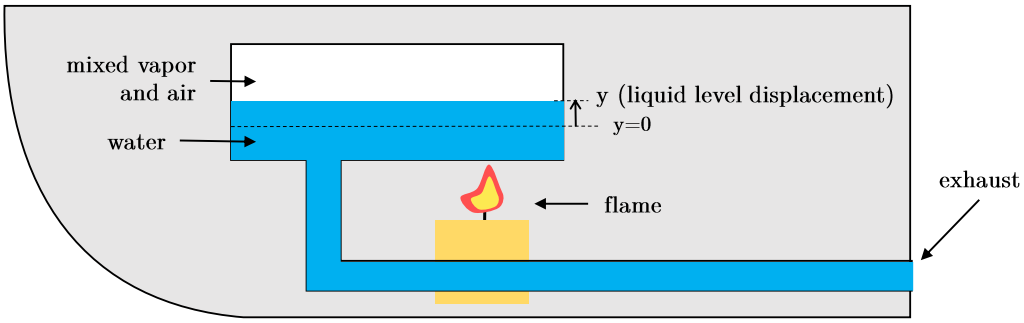

Figure 2.4 Schematic of the putt-putt boat; figure inspired by [52, Fig.9].

where $P_0 = CN_0/V_0$ and $k_1 = AP_0^2/(CN_0)$. The quantity of vapor S must now be found, it varies according to the phase-change. It is assumed that there is a constant evaporation rate in the reservoir. As the liquid moves in the chamber, condensation occurs on the cold walls. The condensation is assumed proportional to the available surface, and is thus proportionnal and opposite to y. Assuming that $y = 0$ corresponds to the equilibrium where the evaporation and condensation balance, the net evaporation rate is:

$$\dot{S} = k_2\, y \ , \tag{2.5}$$

where k_2 is a positive constant. Here, the dependency over the position y does not come from the evaporation (which is constant) but from the condensation rate, which is proportional to the position.

The (linearized) momentum balance is then applied to the liquid, considering the pressure difference (with P_0 the external pressure) and a friction force F_f:

$$\sum F = m_\ell\, \ddot{y} = (P_0 - P)\, A + F_f \ . \tag{2.6}$$

Considering a friction force proportional to the velocity (with $F_f = -c\dot{y}$ and $\gamma = c/m_\ell$) and considering eqs. (2.4) and (2.5), we get:

$$\ddot{y} + \gamma\dot{y} + {\omega_n}^2 y = -\left(\frac{k_2 P_0 A}{m_\ell N_0}\right) \int_0^t y\ dt \ . \tag{2.7}$$

Jenkins explains that, for sinusoidal motion, the right-hand-side of eq. (2.7) is in phase with the velocity $\dot{y}$ and thus act as a positive feedback, injecting energy into the oscillations. The

1. I corrected a typographical mistake in the linearized pressure, [52, Eq.(102)].

criterion for instability (for the startup of the oscillations) is given as $(k_2 P_0/m_\ell N_0) > {\omega_n}^2\gamma$. If the criterion is met, the positive feedback term is greater that the friction force, leading to oscillations growing over time after a perturbation of the equilibrium. It is understood that the oscillations amplitude eventually saturates due to nonlinearities.

My Comments

This analysis by Finnie and Curl [33, 32] and Jenkins [52] is in my opinion one of the most insightful on the physics of the self-oscillations. Of course, the model is a simplification of the reality, but the necessary physics required to describe the dynamics are considered. One insightful aspect in the modeling is that the linearization of the pressure, eq. (2.4), allowed to separate the effect of the change of mass (second term) and the effect of a change of volume (third term). In eq. (2.7), we can see that the change of mass leads to the positive feedback while the change of volume produces a spring force. Also, the instability is understood as a balance between the phase-change and the friction terms. Unfortunately, those publications and the understanding of the physics derived from the model do not seem to be known from the PHP community.

A number of modifications to the model and the analysis would be needed to describe the SBPHP (instead of the putt-putt boat) and to reach a more complete understanding. Here are a few:

1. The dynamical equations are not solved, so there is no description of the dynamics over time. This could be useful in order to better understand the dynamics. A sinusoidal motion is suggested by Jenkins, but eq. (2.7) is actually a third-order differential equation, so the solution is more complicated.

2. The validity of the instability criteria is unclear, because it seems to assume sinusoidal motion in Jenkins [52].

3. The saturation of the oscillations amplitude is explained by the nonlinearities, but there is no theoretical analysis of the amplitude of the oscillations (no study beyond the linearized equations). How to controlled the oscillations amplitude thus remained an open question.

4. There is typically no reservoir of liquid maintaining constant evaporation in a SBPHP, so the phase-change expression should be modified.

5. The parameter for phase-change, k_2, is not expressed in terms of physical quantities. Introducing a more precise expression would make it easier to understand and predict the behavior.

6. The friction is not sufficiently described. The expression of γ is not given. The fact that the flow is oscillating and how this impacts the expression of the friction force is not investigated.
7. The evolution of the temperature of the vapor and the saturation temperature are not included.

2.4.2 Zuo Model

Zuo et al. [129, 130] published one of the first attempt at understanding the dynamics of a UPHP through modeling. Here, I first described their approach and then provide my comments.

The Approach

Zuo et al. start by finding expressions for the various forces applied on the liquid plug (pressure on both ends and viscous friction) and then apply momentum balance on the liquid plug, to obtain a differential equation describing the dynamics. The geometry considered is the one shown in fig. 2.5, with the line representing the tube with multiple vapor bubbles and liquid plugs. In the explanations of the model below, we will consider two vapor bubbles and one single liquid plug, for simplicity.

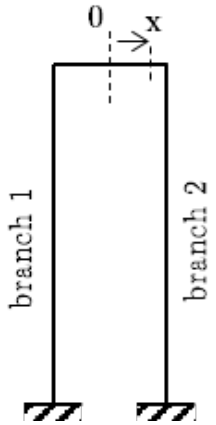

Figure 2.5 Geometry considered by Zuo et al. [129] for the modeling; figure inspired by [129, Fig.6].

The pressure in the vapor in each branch is given by the ideal gas law, $P = mRT/V$. The temperature of the vapor is assumed to always be at saturation, so $T = T_{sat}$. The position of the liquid plug in the device is given by x, defined as the distance from the center of the U-turn to the center of the liquid plug. In the following, A is the tube cross-sectional area, L is the total length of the UPHP, ϕ_0 is the working fluid ratio [2], R is the vapor gas constant, and Q_e is the heat transfer rate. The volume of vapor in the branch 1 is given

2. The filling ratio ϕ_0 is not clearly defined by the authors. According to Ma [70, p.142], the filling ratio is the volume of liquid (at equilibrium, before the oscillations) divided by the total volume, so $\phi_0 = V_\ell/V_t$.

by:

$$V_{v,1} = (L/2)A\rho_\ell(1-\phi_0)/\rho_v + Ax \ . \tag{2.8}$$

Now, the mass of the vapor in the first branch at a time t is given by the mass at time $t = 0$ plus the change of mass due to phase-change from $t = 0$ to t. The mass at time $t = 0$ is given by $m_{v,1}(t = 0) = (L/2)A\rho_\ell(1-\phi_0)$. It is considered here that the heat input Q_e leads to phase-change, with $\dot{m}_{v,1} = Q_e/h_{fg}$, so that the change of mass from $t = 0$ to t is $\int_0^t \dot{m}_{v,1}dt$. This leads to:

$$m_{v,1} = (L/2)A\rho_\ell(1-\phi_0) + \int_0^t \frac{Q_e}{h_{fg}}dt \ . \tag{2.9}$$

We note that the heat input Q_e in the model is fixed (considered positive and constant). Zuo et al. [129] considered $Q_e = 30\,\mathrm{W}$ in their simulations. The pressure in the vapor bubble in the branch 1 is then:

$$P_{v,1} = \frac{m_{v,1}RT_{sat}}{V_{v,1}} = \frac{(L/2)A\rho_\ell(1-\phi_0) + \int_0^t \frac{Q_e}{h_{fg}}dt}{(L/2)A\rho_\ell(1-\phi_0)/\rho_v + Ax}\ RT_{sat} \ . \tag{2.10}$$

Quantities in the branch 2 can be obtained in a similar way, leading to a net force:

$$F = \Delta PA = \frac{-2A^2RT_{sat}}{\left((L/2)A\rho_\ell(1-\phi_0)/\rho_v\right)^2}\left((L/2)A\rho_\ell(1-\phi_0) + \frac{Q_e}{h_{fg}}t\right)x \ . \tag{2.11}$$

The friction force on the liquid plug is obtained by assuming a Poiseuille flow, leading to:

$$F_f = -8\mu_\ell\phi_0^2\,\frac{L\,p}{D}\,\frac{d\,x}{d\,t} \ , \tag{2.12}$$

where p and D are the perimeter of the cross-section and the hydraulic diameter, respectively. Note that, for a circular cross-section, $p/D = \pi D/D = \pi$. With $\phi_0^2 = (L_\ell/L)^2$, this leads to (the following expression does not appear in the original paper):

$$F_f = -8\pi\mu_\ell\left(\frac{L_\ell}{L}\right)^2 L\,\frac{d\,x}{d\,t} = -\,\frac{-8\pi\mu_\ell\,{L_\ell}^2}{L}\,\frac{d\,x}{d\,t} \ . \tag{2.13}$$

Given that the cross-section is constant, we have $\phi_0 = L_\ell/L$, with L the total length. We note that this definition seems to be the one used by Zuo et al., based on the expression of the mass m_ℓ in eq. (2.14): $m_\ell = LA\rho_\ell\phi_0 = \rho_\ell AL(L_\ell/L) = \rho_\ell AL_\ell$, which is indeed the mass of liquid.

The momentum balance on the liquid plug becomes [129, Eq.(5)]:

$$\frac{d^2\,x}{d\,t^2} + \left(\frac{8\mu_\ell p\phi_0}{\rho_\ell DA}\right)\frac{d\,x}{d\,t} + \frac{2A^2RT_{sat}}{(LA\rho_\ell\phi_0)\left((L/2)A\rho_\ell(1-\phi_0)/\rho_v\right)^2}\left((L/2)A\rho_\ell(1-\phi_0)+\frac{Q_e}{h_{fg}}t\right)x = 0, \quad (2.14)$$

=0 missing ►correctedwhich is a second-order differential equation with non-constant coefficients (the stiffness k grows over time without bounds because of the term $(Q_e/h_{fg})t$).

My Comments

The approach of Zuo et al. [129, 130] is the earliest I could find where the momentum balance is applied to the liquid plug and where a differential system of equations is obtained (besides the the putt-putt boat, section 2.4.1). The same basic approach (momentum balance + ideal gas law + expression for phase-change + friction force expression) was used later on by many researchers to model the SBPHP and the UPHP and is now generally accepted as a valid approach by the community.

There is a number of difficulties I could not figure out regarding the model which are worth mentioning. I would expect the volume of vapor at equilibrium ($x = 0$) to be given by[3] $V_{v,1} = (1-\phi_0)(L/2)A$ but Zuo et al. find $V_{v,1} = (L/2)A\rho_\ell(1-\phi_0)/\rho_v$. It is unclear why the ratio ρ_ℓ/ρ_v appears there. Similarly, the mass of vapor $m_{v,1}$ at equilibrium should be $m_{v,1} = \rho_v V_{v,1} = \rho_v(1-\phi_0)(L/2)A$, but Zuo et al. find $V_{v,1} = (L/2)A\rho_\ell(1-\phi_0)$. It is again unclear why the mass of vapor would be proportional to ρ_ℓ. This possible mistake propagates to the final equation. Finally, the friction force F_f in Poiseuille flow is known to be $F_f = -(8\pi\mu_\ell L_\ell)\dot{x}$ (see eq. (3.9a)). Yet, the expression of Zuo et al. for a circular tube is $F_f = -8\pi\mu_\ell({L_\ell}^2/L)\dot{x}$.

Besides those minor points, I find the phase-change representation to be problematic. The phase-change is given by $\dot{m}_{v,1} = Q_e/h_{fg}$ with Q_e a positive constant. This means that the phase-change only includes evaporation (there is no condensation) and the mass of vapor keeps growing over time without bounds. On the contrary, we would expect to have evaporation as well as condensation and the phase-change should not be constant but a function of the dynamics (of the position of the liquid plug for example). Thus, I do not expect the model, a linear second-order differential equation with a stiffness function of time t, to be qualitatively representative of the dynamics in the UPHP. Consequently, I

3. If ϕ_0 is given by $\phi_0 = V_\ell/V_t$, the volume of liquid at equilibrium ($x = 0$) should be $V_\ell = \phi_0 V_t = \phi_0 LA$ (with L the total length). The volume of vapor at equilibrium is then $V_v = V_t - V_\ell = LA - \phi_0 LA = (1-\phi_0)LA$. The volume of vapor in the branch 1 is thus $V_{v,1} = V_v/2 = (1-\phi_0)(L/2)A$.

do not expect the model to correctly predicts the oscillations frequency and the startup behavior.

I conclude that the basic approach in Zuo et al. [129, 130] is useful as a starting point, but there is room for improvement. Possibly because of the final resulting model (eq. (2.14)), which does not seem correct, and maybe because of a lack of details in the model description, the approach by Zuo et al. [129, 130] is unfortunately not recognized as a precursor of the modeling by momentum balance in the PHP litterature.

2.4.3 Ma Model

Here, I will briefly present the modeling approach of Ma et al. [69] (see also Ma [70, Sec.4.4,p.149]). The PHP considered is a loop with multiple bubbles and liquid plugs as shown in fig. 2.6. However, the analysis assumes that "all liquid plugs behave as one liquid plug and all vapor bubbles as one vapor bubble" [70, p.149].

The Approach

Ma et al. assumes the liquid and the vapor to be at saturation at all time. Thus, the pressure in the vapor in the evaporator section is obtained by the Clausius-Clapeyron relation:

$$p_e = p_0 \exp\left[\frac{h_{fg}}{R}\frac{T_e - T_0}{T_e T_0}\right] \tag{2.15}$$

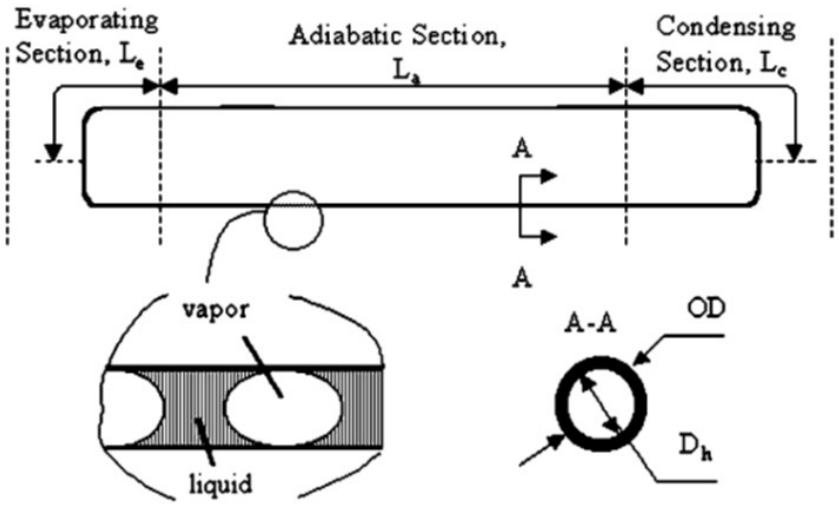

Figure 2.6 Schematic of the PHP model from Ma et al. [69]. Figure reproduced with the authorization of Springer Nature.

as a function of the temperature at the evaporator T_e, assumed to be known. Also, T_0 and p_0 are some temperature and pressure of reference, respectively. The same approach is applied in the condenser, such that a pressure difference between the evaporator and the condenser is given by:

$$\Delta p = p_e - p_c = p_c \left(\exp \left[\frac{h_{fg}}{R} \frac{T_e - T_c}{T_e T_c} \right] - 1 \right) \ . \tag{2.16}$$

This is linearized as:

$$\Delta p = \left(\frac{h_{fg} \rho_{v,c}}{T_e} \right) \Delta T \ , \tag{2.17}$$

with $\Delta T = T_e - T_c$.

Then, it is considered that the oscillations cause compression and expansion of the vapor bubbles, leading to variations of the saturation temperatures in the evaporator and the condenser. Therefore, it is assumed that ΔT oscillates between ΔT_{max} and ΔT_{min} in a sinusoidal fashion:

$$\Delta T = \frac{\Delta T_{max} - \Delta T_{min}}{2} \left(1 + \cos(\omega \tau) \right) \ , \tag{2.18}$$

where ω is the angular frequency of the oscillations. Combining eq. (2.17) and eq. (2.18), a driving force is found:

$$F_d = \Delta p A = \left(\frac{h_{fg} \rho_{v,c}}{T_e} \right) \frac{\Delta T_{max} - \Delta T_{min}}{2} \left(1 + \cos(\omega \tau) \right) \ . \tag{2.19}$$

Starting from the ideal gas law at a time τ, the pressure in the vapor is:

$$p_{v,\tau} = \frac{m_v R T}{L_v A} \ , \tag{2.20}$$

where $L_v A$ is the total volume occupied by the vapor. According to Ma et al., "At a time $\tau + \Delta\tau$, after heat is added to the evaporating section and evaporation occurs, the increase in pressure will result in a decrease in the vapor volume by $-xA$, and the pressure in the vapor space yields":

$$p_{v,\tau+\Delta\tau} = \frac{m_v R T}{(L_v - x) A} \ . \tag{2.21}$$

The resulting variation of pressure is linearized leading to:

$$\Delta p_v = \frac{\rho_v R T}{L_v} x \ . \tag{2.22}$$

Momentum balance is then applied (the mass considered combines the mass of both the vapor bubbles and the liquid plugs) as:

$$m\frac{d^2 x}{d\tau^2} + c\frac{d x}{d\tau} + kx = B\left(1 + \cos\left(\omega\tau\right)\right) \ , \tag{2.23a}$$

where $c(dx/d\tau)$ is the friction force (see Ma et al. [69] for details). The parameters are:

$$m = A\left(\rho_\ell L_\ell + \rho_v L_v\right) \ , \tag{2.23b}$$

$$k = \frac{A\rho_v R T}{L_v} \ , \tag{2.23c}$$

$$B = \left(\frac{h_{fg}\rho_{v,c}}{T_e}\right)\frac{\Delta T_{max} - \Delta T_{min}}{2} \ . \tag{2.23d}$$

The resulting model is an ordinary, non-homogeneous second-order differential equation. It represents a forced harmonic oscillator. Ma et al. concludes that the "model considers the thermal energy from the temperature difference between the evaporator and condenser as the driving force for the oscillating motion, which will overcome both the frictional force and the force due to the deformation of compressible bubbles" [69]. In the model it is assumed that the oscillating frequency corresponds to the natural frequency of the system. It is suggested that, if the forcing frequency can be controlled independently, this could impact the amplitude of the oscillations as well as the heat transfer performance. It is suggested that maximum performance is obtained when the external excitation frequency matches the natural frequency.

My Comments

The work of Ma et al. [69] represents a commendable effort to model a very complicated system (PHP with multiple bubbles and liquid plugs). Combining all the vapor bubbles as one vapor bubble and all the liquid plugs as one liquid plug is an interesting approach. We note that the corresponding natural frequency matched well the observed frequency by Spinato et al. [105, Sec.3.2].

There are a few elements I would like to point out:

1. Saturation conditions are assumed. For the SBPHP, experimental evidences show however that the vapor can be superheated. In that case, the pressure in the vapor is best described by the ideal gas law.

2. Variations ΔT in eq. (2.18) are imposed. A better description would link the saturation temperatures directly to the pressure which itself depends on the volume of the vapor bubbles.

3. The model obtained is a forced system, in contrast with other approaches.

4. I could not understand how the variations of pressure in the vapor due to phase-change is derived (eq. (2.20) to eq. (2.21)). Based on the description, it seems to me that m_v should be modified and the volume should be kept constant but the authors do it the other way around.

5. In the model, it seems that phase-change is not really taken into account (m_v is a constant).

6. It seems like the force from the pressure difference is applied two times, one for F_d due to variation of saturation temperature and one for the spring force. Of course, the pressure force applies only one time. The analysis might still be correct, but the derivation is not obvious. Ideally, a single expression for the pressure would then be split into a number of components.

2.4.4 Film Evaporation-Condensation (FEC) Model

An influential modeling approach on the SBPHP was developed by Dobson and Harms [27], Dobson [25, 26], followed by Zhang and Faghri [126] and Das et al. [20]. This model was coined the Film Evaporation-Condensation (FEC) model by Das et al.. Here, I will focus on the work of Das et al. [20] and then briefly compare the various approaches. I will provide my comments at then end.

The Model

The experimental apparatus of Das et al. [20] is represented in fig. 2.7. The mathematical model used to represent this experiment is shown in fig. 2.8. Momentum balance is applied on the liquid plug as:

$$\frac{d\ (m_\ell \dot{x})}{dt} = (p_v - p_0)\ S - \text{sign}\left[\dot{x}\right] \cdot F_f\ , \tag{2.24}$$

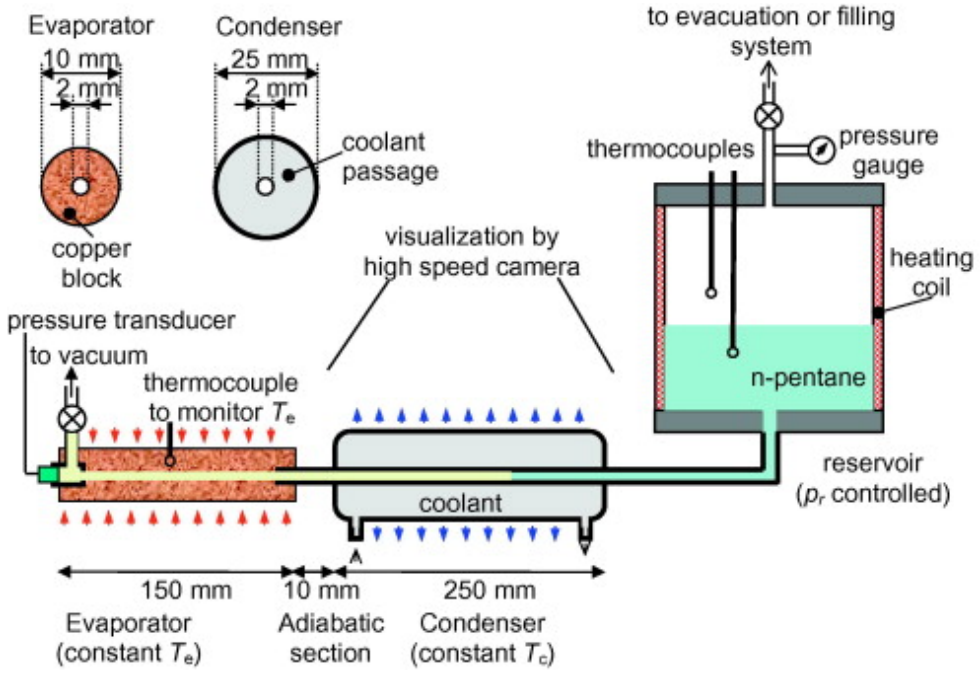

Figure 2.7 Experimental setup from Das et al. [20]. Figure reproduced with the authorization of Elsevier.

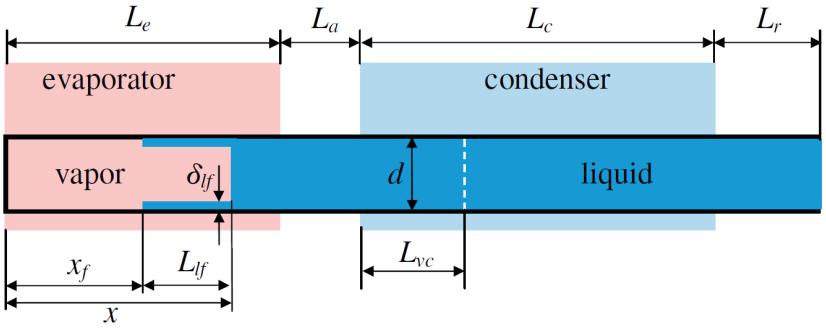

Figure 2.8 SBPHP model from Das et al. [20]. Figure reproduced with the authorization of Elsevier.

with m_ℓ the mass of liquid, x the position of the meniscus relative to the closed end, p_v the pressure in the vapor, p_0 the pressure at the other end, S the cross-sectional area and F_f the absolute value of the friction force. Because the liquid goes in and out of the reservoir (fig. 2.7), the mass m_ℓ varies according to:

$$m_\ell = \rho \left(L_t + L_r - x\right) S \ . \tag{2.25}$$

The friction force is represented as:

$$F_f = \tfrac{1}{2} C_f d \rho \pi \left(L_t + L_r - x\right) \dot{x}^2 \ . \tag{2.26}$$

Here, Das et al. consider $C_f = 0$ for $\mathrm{Re} = 0$, $C_f = 16$ for $\mathrm{Re} < 1$, $C_f = 16/\mathrm{Re}$ for $1 \leqslant \mathrm{Re} < 1180$ and $C_f = 0.078\mathrm{Re}^{-0.25}$ for $\mathrm{Re} \geqslant 1180$, with $\mathrm{Re} = \rho d\dot{x}/\mu$ the Reynolds number. For $C_f = 16/\mathrm{Re}$, the friction force corresponds to the Poiseuille flow:

$$F_f = \tfrac{1}{2} \left(16 \, \frac{\mu}{\cancel{\rho d \dot{x}}}\right) \cancel{d} \cancel{\rho} \pi L_\ell \cancel{\dot{x}^2} = 8 \pi \mu_\ell L_\ell \dot{x} \ , \tag{2.27}$$

with $L_\ell = L_t + L_r - x$ the length of the liquid plug. We will find the same expression later on in eq. (3.9a) (where we include the sign in the expression of F_f).

In the momentum balance eq. (2.24), the pressure in the vapor must be described by an equation. The ideal gas law is used:

$$p_v = \frac{m_v R_v T_v}{S x} \ , \tag{2.28}$$

where R_v is the specific gas constant. In the model of Das et al. [20], the temperature of the vapor T_v is allowed to vary over time and is not required to be at saturation (the vapor can be overheated or subcooled). To find T_v, an energy balance is applied to the vapor, leading to an additional differential equation:

$$m_v c_{v,v} \dot{T}_v = \dot{m}_v R_v T_v + q_{sens} - p_v S \, \dot{x} \ , \tag{2.29}$$

where $c_{v,v}$ is the specific heat at constant volume. The sensible heat exchange between the vapor and the walls is represented as:

$$q_{sens} = U_v \, \pi d \, x_f \left(T_e - T_v\right) \ , \tag{2.30}$$

where the length x_f is the length of the vapor exposed to the wall in the evaporator, given by $x_f = x - L_f$ for $x < L_e$ (meniscus in the evaporator) and by $x_f = L_e - L_{\ell f}$ otherwise (meniscus in the condenser).

Now, an important aspect of the model is to described how the mass of vapor m_v varies. For that, one needs a model of the phase-change. Various contributions to the phase-change are considered. The phase-change from the liquid film is $\dot{m}_e^f$ in the evaporator and $\dot{m}_c^f$ in the condenser. The phase-change at the meniscus is $\dot{m}_e^m$ in the evaporator and $\dot{m}_e^f$ in the condenser. Those phase-change are expressed using simple thermal resistance models and considering the liquid vapor interface at saturation, leading to:

$$h_{\ell v}\dot{m}_e^f = U_e\,\pi d\,L_{\ell f}\,[T_e - T_{sat}(p_v)]\ , \tag{2.31a}$$

$$h_{\ell v}\dot{m}_c^f = U_c\,\pi d\,L_{vc}\,[T_c - T_{sat}(p_v)]\ , \tag{2.31b}$$

$$h_{\ell v}\dot{m}_e^m = U_e^m\,\pi d\,L_e^m\,[T_e - T_{sat}(p_v)]\ , \tag{2.31c}$$

$$h_{\ell v}\dot{m}_c^m = U_c^m\,\pi d\,L_c^m\,[T_c - T_{sat}(p_v)]\ . \tag{2.31d}$$

All those contributions are added up to obtain an expression for the net phase-change [4]:

$$\dot{m}_v = \dot{m}_e^f + \dot{m}_c^f + \dot{m}_e^m + \dot{m}_c^m\ . \tag{2.31e}$$

As can be seen from these expressions, a step profile is considered for the wall temperature: the wall is at $T_w = T_e$ in the evaporator and at $T_w = T_c$ in the condenser. The heat transfer coefficient U_e is given by $U_e = \gamma k_\ell/\delta_{\ell f}$, a function of the liquid thermal conductivity k_ℓ, of the liquid film thickness $\delta_{\ell f}$ and of a correction factor γ. Also, $U_c = U_e$ is considered in the simulations. The other coefficients are fixed. The liquid film thickness $\delta_{\ell f}$ is considered constant and is not predicted by the model but fixed (free parameter).

In eq. (2.31a), the quantity $L_{\ell f}$ is the length of the liquid film in the evaporator only (the name $L_{\ell f}$ is admittedly confusing). The length of the liquid film $L_{\ell f}$ varies based on the phase-change and the motion of the meniscus. A differential equation describing the rate

4. Note that $\dot{m}_v$ was expressed as: $\dot{m}_v = \dot{m}_e^f + \dot{m}_c^f h + \dot{m}_e^m + \dot{m}_c^m$ in [20]. I presume that the h in the term $\dot{m}_c^f h$ was a typographical mistake.

of change of $L_{\ell f}$ is introduced:

$$\frac{dL_{\ell f}}{dt} = \begin{cases} 0 & \text{if } L_{\ell f} = 0,\ \dot{x} < 0 \text{ and } x \leqslant L_e\ , \\ -\dot{m}_e^f / \left(\rho \pi d \delta_{\ell f}\right) & \text{if } x > L_e\ , \\ \dot{x} - \dot{m}_e^f / \left(\rho \pi d \delta_{\ell f}\right) & \text{otherwise.} \end{cases} \tag{2.32}$$

The length L_{vc} is the length of the liquid film in the condenser. It is given by:

$$L_{vc} = \begin{cases} 0 & \text{if } x < L_e + L_a\ , \\ x - (L_e + L_a) & \text{if } L_e + L_a \leqslant x < L_e + L_a + L_c\ , \\ L_c & \text{otherwise.} \end{cases} \tag{2.33}$$

Here, L_{vc} is defined in such a way that it assumes the condenser is covered by the liquid film at all times. Also note that no condensation on the dry wall is allowed/considered.

This concludes the presentation of the model. We omitted the expressions of the lengths L_{ve} and x_f which can be deduced from the geometry (see [20] for details).

I would like to briefly discuss the phase-change from the liquid film described above. Let's first unpack how eq. (2.32) is obtained. The volume of the liquid film in the evaporator is:

$$V_{\ell f} = \left(\pi r^2 - \pi (r - \delta_{\ell f})^2\right) \cdot L_{\ell f}\ .$$

We have that $(r - \delta_{\ell f})^2 = r^2 - 2r\delta_{\ell f} + \delta_{\ell f}^2$. Assuming a thin liquid film, we may neglect the term $\delta_{\ell f}^2$, leading to $(r - \delta_{\ell f})^2 \approx r^2 - 2r\delta_{\ell f}$ and:

$$V_{\ell f} = \left(\pi r^2 - \pi (r - \delta_{\ell f})^2\right) \cdot L_{\ell f} \approx \pi d \delta_{\ell f} L_{\ell f}\ .$$

The change of volume $V_{\ell f}$ due to phase-change at the film in the evaporator, the component $\dot{m}_e^f$. With $m = \rho V$, we can write:

$$dV_{\ell f} = (1/\rho)\,(-\dot{m}_e^f) dt\ ,$$

with ρ the liquid density. Now, from the expression of $V_{\ell f}$ above, the length of liquid $L_{\ell f}$ is:

$$L_{\ell f} \approx \frac{V_{\ell f}}{\pi d \delta_{\ell f}} \ .$$

The rate of change of $L_{\ell f}$ due to phase-change is:

$$\frac{d\,L_{\ell f}}{d\,t} \approx \frac{1}{\pi d \delta_{\ell f}} \frac{d\,V_{\ell f}}{d\,t} = \frac{1}{\pi d \delta_{\ell f}} \left(\frac{-\dot{m}_e^f}{\rho} \right) = -\frac{\dot{m}_e^f}{\pi \rho d \delta_{\ell f}} \ .$$

This is the expression for $x > L_e$ (meniscus outside the evaporator) given by eq. (2.32). Here, the change of length $L_{\ell f}$ is due to the motion of the triple line, at x_f. Because the thickness is fixed, the phase-change model here assumes that the evaporation implies the motion of the triple line. Now, when the meniscus is inside the evaporator, the length $L_{\ell f}$ also varies due to the motion of the meniscus (at x). Adding this component leads to:

$$\frac{d\,L_{\ell f}}{d\,t} \approx -\frac{\dot{m}_e^f}{\pi \rho d \delta_{\ell f}} + \dot{x} \ ,$$

which is the "otherwise" case in eq. (2.32).

In this liquid film model, the condensation on the liquid film in the condenser does not increase the length $L_{\ell f}$ and is instead assumed to increase the mass of the liquid plug.

The Results

Das et al. find an expression for the oscillations period frequency by assuming no phase-change (so that the model can be linearized) [20, Eq.(18,21,25)]:

$$T = 2\pi \ \frac{1}{\sqrt{1 + R_v / c_{vv}}} \sqrt{\frac{\rho \left(L_t + L_r - \langle x \rangle \right) \langle x \rangle}{p_0}} \ , \tag{2.34}$$

where $\langle x \rangle$ is the meniscus position at equilibrium (in fact, this is just the length of vapor at equilibrium) and $L_t = L_e + L_a + L_c$. Thus, $L_t + L_r - \langle x \rangle$ is simply the length of liquid. The angular frequency is $\omega = 2\pi / T$:

$$\omega = \sqrt{\frac{\left(1 + R_v / c_{vv} \right) p_0}{\rho \left(L_t + L_r - \langle x \rangle \right) \langle x \rangle}} \ . \tag{2.35}$$

Das et al. generated numerical simulations of the model above and showed that self-oscillations are produced. The behavior of the model with phase-change and the model without phase-change (called *superheated*) are compared. It is concluded that the model without phase-change is inadequate because it is not able to reproduce the large oscillations amplitude observed experimentally. Thus, the phase-change must be taken into account in the modeling of the SBPHP. The authors find that the model exhibits an instability threshold behavior: "One of the most important features of a PHP model is the existence of the instability threshold. [...] It is sufficient to decrease T_e or increase T_c by 1 K to prevent the oscillations"[20]. In order to compare the model to the experiments, several parameters were fitted. It was found that the model reproduced the experimental measurements qualitatively. They found that the amplitude increased by increasing the difference of temperature $T_e - T_c$. Also, the model was able to reproduce the intermittent behavior (one large oscillation followed by one small oscillation) under some conditions while the amplitude remained constant under some other conditions. Quantitatively, the model was not able to reproduce both the spatial amplitude and the pressure amplitude. The authors believed that the simplified friction expression was responsible for the discrepancy.

Comparison of the Various Approaches

From the original work of Dobson and Harms [27], Dobson [25, 26] to Zhang and Faghri [126] and then Das et al. [20], the modeling approach has evolved. We will mention a few key differences. In the work of Dobson and Harms [27], Dobson [25, 26], the vapor is allowed to be superheated, but the saturation condition at the liquid-vapor interface is not taken into account. In the work of Zhang and Faghri [126], the vapor is assumed to be saturated everywhere [126, Hyp.1, p.757]. Das et al. [20] consider the saturation conditions at the interface and allow the temperature of the bulk of the vapor to vary. The model for phase-change in both Dobson and Harms [27], Dobson [25, 26] and Das et al. [20] is a simple phenomenological model. It assumes a liquid film of constant thickness with a length varying according to a simple expression. In Zhang and Faghri [126], the phase-change model is quite complex. The geometry of the liquid film is derived from hydrodynamics principles. The liquid film thickness varies in both time and space. However, a number of assumptions are considered and there are no experimental validations.

My Comments

The FEC model constitutes a big step in the modeling approach for the SBPHP. It provides a simple model (described by a few ordinary differential equations) that still preserve key features of the physics. Numerical simulations allowed to explore the dynamics and reach some understanding of the physics.

However, no linear stability analysis was carried on because the model cannot be reduced to continuous linearized equations close to the equilibrium. This is due to the modeling approach for the phase-change. This made it impossible to carry on the same insightful analysis used for the putt-putt boat (section 2.4.1). In consequence, the angular frequency is predicted only in the absence of phase-change. It is unclear if the angular frequency prediction still applies in the presence of phase-change. More importantly, the instability mechanism cannot be studied analytically and there is no analytical formula to predict the startup.

I would also like to point out a few minor points:

1. The wall temperature is represented by a step function. This is not physical (axial conduction should smooth the transition between the evaporator and the condenser) but may be considered an acceptable approximation.
2. Das et al. [20] adapted the phase-change expression to consider the saturation condition at the liquid-vapor interface. However, the energy equation eq. (2.29) was taken from Zhang and Faghri [126] and does not take into account the saturation condition at the liquid-vapor interface. Thus, eq. (2.29) is incorrect. I will derived a modified form in appendix A.1.1.
3. The model for phase-change includes a liquid film but still constitutes a simplified approach. The thickness is constant and fixed. The hydrodynamics in the liquid film is not modeled. The phase-change is considered to imply an instantaneous motion of the triple line. The higher phase-change at the triple line is not included (a modification has been proposed by Rao et al. [93]). Also, the thermal resistance should increase for very small thicknesses due to the adhesion force [89], but this is not included.
4. The frequency is obtained by assuming no phase-change. It is unclear if it still applies in the presence of phase-change. There is no experimental validation over a range of the involved parameters.
5. It is unclear why, in the friction force expression (2.26), $C_f = 16$ for $\mathrm{Re} < 1$. Poiseuille flow should still apply there. This condition was not included in the original expression, in [25]. More generally, the friction expression does not include the fact that the flow is oscillating.

2.4.5 Nikolayev's Instability Analysis

Here, I will describe mostly the approach of Nikolayev [84], to study the instability mechanism and the startup in the SBPHP. As stated by Nikolayev, "the simulations [of the FEC

model] cannot give an understanding of the startup criteria for the oscillations or explain the origin of the instability that causes them". There is a need for a deeper understanding of the instability mechanism. Nikolayev [84] tackled this challenge by an analytical study of the FEC model (described in section 2.4.4) using the averaging method. I will also mention the work of Nikolayev [85] who improved the approach by including an axial temperature profile in the wall (instead of a step function). Both approaches were later discussed in details in Nikolayev and Marengo [87] and Nikolayev [86].

The Approach

The model considered is the one described in section 2.4.4. Nikolayev finds the equilibrium of the system, which corresponds to the meniscus located at the interface of the evaporator and the condenser. Deviations from the equilibrium are then considered (e.g. Δx for the meniscus position). The equations are then made dimensionless using the natural angular frequency (for the time) and vapor length at equilibrium (for the lengths) as well as other values at equilibrium. Tilde quantities mean dimensionless deviations from the equilibrium (e.g. $\tilde{x} = \Delta x/\bar{x}$, with $\bar{x}$ the length of the vapor bubble at equilibrium). Finally, the equations are linearized to obtain ([84, Eq.(21)]):

$$\dot{\tilde{x}} = \tilde{v} \ , \tag{2.36a}$$

$$\gamma\dot{\tilde{v}} = \tilde{T} - \tilde{x} + \tilde{m} \ , \tag{2.36b}$$

$$\dot{\tilde{T}} = (\gamma - 1)\left(\dot{\tilde{m}} - \tilde{v}\right) - \varepsilon\tilde{T} \ , \tag{2.36c}$$

$$\dot{\tilde{m}} = \beta \begin{cases} 0 & \text{if } \tilde{x} \leqslant \tilde{L} \ , \\ \alpha_e\left(\tilde{x} - \tilde{L}\right) & \text{if } \tilde{L} < \tilde{x} < 0 \ , \\ -\alpha_e\tilde{L} - \alpha_c\tilde{x} & \text{if } \tilde{x} \geqslant 0 \ , \end{cases} \tag{2.36d}$$

$$\dot{\tilde{L}} = \begin{cases} \tilde{v} & \text{if } \tilde{L} \geqslant \tilde{x}, \tilde{v} < 0, \\ (1/\beta)\dot{\tilde{m}}|_{\alpha_c=0} & \text{otherwise.} \end{cases} \tag{2.36e}$$

Equation (2.36a) and eq. (2.36b) are the momentum balance written as two first-order differential equations. The friction force F_f was neglected here because it was thought to be proportional to v^2 and would thus be nonlinear (I will discuss this further in the comments section). Equation (2.36c) is the energy balance on the vapor bubble required to described the variations of temperature of the vapor. Equation (2.36d) is the phase-change rate equation defined in a piece-wise fashion. Here, $\tilde{L}$ is the dimensionless deviation of L_e^d, which is the distance between the closed end and the triple line ($x - L_e^d$ is the length of the liquid film). Finally, eq. (2.36e) is the rate of change of $\tilde{L}$, describing how the triple

line moves according to phase-change and the motion of the meniscus. In the equations above, four dimensionless numbers are introduced: ε, α_c, α_e and β. ε is given by:

$$\varepsilon = \frac{U_g \pi d L_e \tau}{\bar{m} c_v} \ , \tag{2.37a}$$

which is defined as "the ratio of [the natural period] τ and the time scale that corresponds to the heat exchange of the tube with the gas" [84]. We see that ε is proportional to U_g, the heat transfer coefficient between the vapor and the wall. We expect that for $\varepsilon \to \infty$, the heat transfer between the vapor and the walls ensures that the temperature of the vapor equals the temperature of the walls (isothermal case). We can see that from eq. (2.36c), where the term $-\varepsilon\tilde{T}$ tends to stabilize $\tilde{T}$ close to $\tilde{T} = 0$. For $\varepsilon = 0$, there is no heat transfer between the walls and the vapor (adiabatic walls) so the temperature of the vapor varies as a function of the phase-change and the motion of the liquid plug, according to eq. (2.36c). The dimensionless parameter α_c is given by:

$$\alpha_c = \frac{U\tau \left(T_{sat}(p_r) - T_c\right)}{\rho \delta_f h_{lv}} \tag{2.37b}$$

and characterizes "the film condensation in the condenser" [84], while the parameter α_e:

$$\alpha_e = \frac{U\tau \left(T_e - T_{sat}(p_r)\right)}{\rho \delta_f h_{lv}} \tag{2.37c}$$

characterizes "the film evaporation in the evaporator" [84]. The dimensionless number β:

$$\beta = \frac{\pi d \delta_f L_e \rho}{\bar{m}} \tag{2.37d}$$

is "the ratio of the film mass and the gas bubble mass provided they are the same length" [84]. The reader is referred to the original publication [84] for all the definitions and details.

Now, Nikolayev wishes to study the instability in the system analytically. Classical linear stability analysis cannot be applied because the equations are piecewise (and not continuously differentiable). Nikolayev thus uses averaging instead to obtain an analytical solution. The function:

$$\frac{(\gamma - 1)\,\varepsilon}{\beta} = \frac{1}{\pi}\left[\alpha_e \left(\psi - \xi - \sin\psi\cos\psi + \sin\xi\cos\xi\right) + \alpha_c \left(\psi - \sin\psi\cos\psi\right)\right] \tag{2.38}$$

is obtained [84, Eq. B.5b] and provides an approximation for the instability threshold. The quantities ψ and ξ are new quantities defined along the way [84, Eq. A.5,A.6,A.7]. The approximation is believed to be valid for small α_e and α_c.

The Analysis

The function eq. (2.38) is represented as a surface in fig. 2.9a. A set of parameters can be represented as a point in that space. The system is stable above the surface and unstable below. Nikolayev concludes that the system can be made unstable by increasing the evaporation or the condensation, by increasing α_e or α_c, respectively. Also, increasing the heat exchange between the walls and the vapor, by increasing ε tends to stabilize the system. From this analysis, it seems that an isothermal vapor (with the vapor temperature equal to the walls temperature) is necessary stable.

Finally, Nikolayev compares the analytical threshold formula to the threshold obtained numerically, as show in fig. 2.9b. These curves are obtained for the special case of $\alpha_c = \alpha_e$ (it is a cross-section along the diagonal of the space in fig. 2.9a). One can clearly see that the averaging solution does not match the numerical values exactly. The averaging is believed to provide a lower bound for the instability threshold. The exact instability threshold is a function of all the dimensionless parameters and cannot be represented as a surface in a 3D space as in fig. 2.9a.

Based on the analysis, Nikolayev explains the self-oscillations as follows: "The origin of the self-sustained oscillations is now evident. The evaporation in the evaporator causes the gas

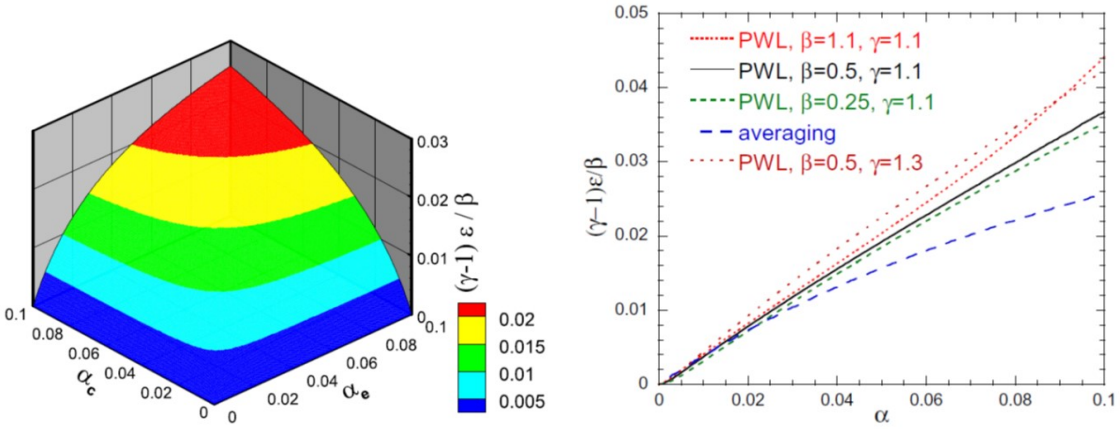

(a) (b)

Figure 2.9 Instability threshold from Nikolayev [84]; (a) surface representing eq. (2.38) (stable above the surface and unstable below), (b) instability threshold obtained numerically versus the analytical formula eq. (2.38). Figures reproduced with the authorization of Elsevier.

pressure increase that propels the meniscus towards the condenser where the condensation causes the pressure decrease and the meniscus returns back to the evaporator". Also, the heat exchange between the walls and the vapor is identified as the energy dissipation in the system.

An Update - the Effect of Axial Heat Conduction in the Wall

Nikolayev [85] improves the approach above by including the axial heat conduction in the wall. This results in a temperature profile in the wall, in the axial direction, that is not a step profile but is instead continuous. The approach is also described by Nikolayev and Marengo [87], Nikolayev [86].

A few results differ from the approach with a stepwise temperature profile. Nikolayev finds that the thermal gradient at equilibrium is a key parameter affecting the instability. Increasing it increases the instability. Also, he finds that the instability is independent of the liquid film and depends only on the phase-change at the meniscus [85, p.479,482]. In addition, in the new approach the friction force is included but expected to be negligible except for tubes of very small diameter. A new instability threshold criterion is obtained [87, Eq. 76]:

$$-\frac{d\bar{T}_w}{dx}\bigg|_{x=\bar{X}_m}^{\text{start-up}} = \left(\frac{\bar{X}_m}{\gamma p_r}\frac{d\bar{p}}{dT}\bigg|_{sat}\right)^{-1} + \frac{U_v h_{lv}}{U_m L_m R_v}\frac{(\gamma-1)^2}{\gamma} + \frac{8\nu p_r h_{lv}}{d_i \bar{T} U_m L_m R_v}\,, \tag{2.39}$$

which gives the minimal value of the thermal gradient at equilibrium to start the oscillations. On the right-hand-side, the first term relates to the slope of the saturation curve, the second term relates to energy dissipated by heat conduction between the walls and the vapor and the third term relates to viscous friction losses.

My Comments

Nikolayev [84] is the first (and only, as far as I know, apart from the putt-putt boat studies) to tackle the question of the instability in the SBPHP and to obtain an analytical criterion. This is a very important question which has not received enough attention in my opinion. The approach of Nikolayev is interesting but, because the model is piecewise, no classical linear stability analysis could be applied. This made the instability analysis quite complicated. In my opinion, a better understanding of the instability mechanism could be reached with a simpler approach.

Here are a few elements I would like to point out:

1. The friction force is incorrectly neglected. Nikolayev [84] neglects the friction force, given by $F_f = \frac{1}{2} C_f d\rho\pi L_\ell \dot{x}^2$, because it is thought to be nonlinear (because proportional to $\dot{x}^2$). However, if the force F_f is written explicitly, by taking $C_f = 16/\text{Re} =$

$16\mu/(\rho d\dot{x})$ as in eq. (2.27), then the friction force becomes proportional to velocity ($F_f = 8\pi\mu_\ell L_\ell \dot{x}$) and is therefore linear. The friction force should be included in the linearized equation and in the stability analysis. The improved approach of Nikolayev [85] includes the friction force.

2. The comments on the FEC model (section 2.4.4) still applies here because the stability analysis is based on that model. In particular, the energy equation does not take into account the fact that the liquid-vapor interface is at saturation.

3. Validity of the averaging method. The averaging technique is classically applied to continuous systems. Within this constraint and the other requirements, the averaging theorem guarantees that the solution found is asymptotically valid. It is unclear to me if the averaging method can apply to the piecewise system described here and if so, what is the impact on the validity of the solution. Those questions are not addressed by Nikolayev [84].

4. Validity of the instability analysis. In a classical stability analysis, the criterion for stability is exact. Here, because of the model or the approach, the criterion is only an approximation. The range of validity of this approximation is unclear. The range of validity for the predicted trends (effects of the parameters) is also unknown.

5. The instability threshold has a lower bound. The averaging approximation for the instability threshold from averaging is considered to be a lower bound by Nikolayev [84]. This is not rigorously demonstrated however. In fact, some numerical results seem to be lower than the averaging results for low α in fig. 2.9b. The discrepancy could be larger for other values of the parameters.

2.4.6 Comparison of the Models

It is useful at this point to highlight the mathematical properties of the different models found in the state of the art.

The putt-putt boat model obtained by Finnie and Curl [33, 32], Jenkins [52] (section 2.4.1) is a third-order ordinary linearized homogeneous differential equation. The mass is the mass of liquid, the spring comes from compression and expansion of the vapor bubble, friction leads to a damping term and the phase-change appears as a positive feedback term.

The Zuo model ([129, 130], section 2.4.2) is an ordinary linearized second-order homogeneous differential equation, with one non-constant coefficient. The mass is the mass of liquid, the spring comes from compression and expansion of the vapor bubble as well as

phase-change (which leads to the non-constant coefficient, a stiffness varying over time). Friction leads to a damping term and there is no positive feedback term.

The Ma model ([69, 70], section 2.4.3) is an ordinary linearized nonhomogeneous second-order differential equation. The mass includes both the mass of vapor and the mass of liquid, the spring comes from the compression and expansion of the vapor bubble and friction leads to a damping term. The phase-change does not lead to a positive feedback but to a forcing term, making the equation nonhomogeneous.

The FEC model ([20], section 2.4.4) is a system of five first-order ordinary homogeneous differential equations (analogous to one fifth-order differential equation). Starting from the basic second-order system described by the momentum balance, the system becomes third-order by adding phase-change, fourth-order by adding varying liquid film length and fifth order by adding varying vapor temperature. The system is piecewise and not continuously differentiable. In the model, the mass is the mass of liquid and friction leads to a damping force. There is a spring effect produced by compression and expansion of the vapor bubble as can be seen from the linearized equations without phase-change. It is difficult to deduce the role of the phase-change from the system of equations only.

The mass is the same in all models except for the Ma model where the vapor mass is included. All models include a spring component due to compression and expansion of the vapor bubble. The Zuo model includes another spring component due to phase-change and, in the FEC model, phase-change might produce a spring component but this is not obvious. In all models, the friction leads to a damping force proportional to velocity, although the coefficients used differ. Models mostly differ by how the phase-change is described. In the putt-putt boat model and in the FEC model, the phase-change is described by a differential equation (increasing the order of the system) and leads to a positive feedback (presumably, in the FEC model). By contrast, the phase-change leads to a varying stiffness in the Zuo model, so that the differential equation has a non-constant coefficient and still no positive feedback. In the Ma model, the phase-change leads to a forcing term so that the differential equation is nonhomogeneous and still does not have a positive feedback. How the behaviors of a forced system and a system with a positive feedback differ will be discussed in section 3.6 and section 6.5.1.

2.5 State of the Art on my Research Questions

Based mostly on the literature described above, I will now briefly review the state of the art on the research questions I identified in section 1.3.2. In short, I find that there has been major progress in experimental measurements and in the theoretical modeling, but

little progress on the understanding of the self-oscillations. The theoretical work focuses today on models of increased complexity to make more accurate predictions, but the basic behavior is not well understood yet.

Q1) *Where do the oscillations come from?*

On one hand, oscillations in the SBPHP are often explained by the coupling of the compression and expansion of the vapor acting as a spring, to the mass of the liquid plug, thus leading to a spring-mass system (or resonator). As described in section 2.4.4, Das et al. [20] were able to find an expression for the oscillations frequency, where they assumed no phase-change. The formula was found to match well the experiments, but not study over a large range of the parameters has been carried on so far. On the other hand, one also finds explanation for the oscillations in the literature based solely on the phase-change. Those explanations take the following form:

> *The first question one can ask about the PHP is "why it oscillates?". One can explain the functioning mechanism of the single branch PHP as follows. When the meniscus situates in the evaporator, evaporation occurs. The vapor expands and the meniscus is pushed into the condenser. The condensation occurs, and the vapor bubble contracts so the meniscus returns back into evaporator.* Nikolayev [86, p.20]

To definitively settle the question, we will improve upon the analysis of Das et al. by including the phase-change, such that the role of each physical components in the system can be clarified. We will also carry out an experimental validation over a large range of the relevant parameters. Those results can be found in chapter 3.

Q2) *Why does the oscillations amplitude increase during the startup and what are the required conditions for the startup to occur?*

It is often said that the phase-change acts as a driving force in the PHP, but there is little theoretical or experimental work though to substantiate that claim and to make it more precise. One important result is the work of Das et al. [20] with the FEC model, that showed numerically that including phase-change allowed for large oscillations amplitudes (section 2.4.4). Nikolayev [84, 85] analyzed the instability mechanism in that model analytically (section 2.4.5). Because the model is piecewise (and not continuously differentiable), no classical linear stability analysis could however be used. This led to a quite complicated approach to analyze the instability. Also, a number of questions can be raised: friction is surprisingly neglected in [84], the validity of the approach is unclear, the instability criterion is approximate but we do not know the range of validity, etc. (see end of section 2.4.5).

One consequence of the absence of a rigorous theoretical description of the instability is that there is also no established knowledge on the effects of the parameters on the startup. Also, there is no consensus on the type of mathematical system that correctly describe the oscillations. The oscillations have been described mathematically by a second-order differential equation with non-constant coefficients ([129, 130], section 2.4.2), by a second-order differential equation with a forcing term ([69, 70], section 2.4.3) and by differential equations without forcing (third-order [33, 32, 52], section 2.4.1 or fifth-order [20], section 2.4.4). Identifying the correct type of mathematical system is important as different types lead to different behaviors. Also, how to control the behavior differs, according to which type the system belongs.

To address the question we will consider a continuously differentiable mathematical model so that we can apply linear stability analysis. We will clarify the role of the different physical components in the startup and clarify what is the correct mathematical system to consider. We will also perform an experimental validation to verify our results. This is described in chapter 3.

Q3) *Why does the oscillations amplitude saturate and what defines the oscillation amplitude in the steady-state regime?*

This question has received very little interest so far. In fact, to my knowledge, it has not even been asked. At most, the effect of some parameters on the amplitude are reported (e.g. [20]). What leads to the steady-state is not however well understood. This situation might be due to the fact that the PHP community is more interested about heat transfer than by the oscillations amplitude per say. On the other hand, recent results show that increasing the oscillations amplitude increases the heat transfer [56]. Another reason might be that the circulation mode (possible only with MBPHP) is considered favorable and there is no more amplitude in that case (section 2.2). We will address the question of the amplitude in chapter 4.

Q4) *How does an energy harvesting device based on SBPHP oscillations behave?*

There has been several attempts to build an energy harvesting device based on the self-oscillating behavior of the PHP, with various types of transducers to convert energy from the PHP to electrical energy [79, 125, 80, 81, 104]. All these attempts are based on the MBPHP, however. These devices are usually described as for cooling with energy harvesting capabilities, instead of being solely dedicated to energy harvesting. The question remains open about how an energy harvester based on the SBPHP oscillations (such as SOFHE) behaves. We will consider this question in chapter 6.

For the research questions mentioned above, a number of intuitive explanations exist, which turn out to be wrong upon close scrutiny. One may mention the oscillations explained solely by phase-change, incorrect expectations on the role of some parameters on the startup ($(dp/dT)_{sat}$, L_ℓ), the idea that the phase-change should be in phase with the velocity or assuming one should aim for impedance matching (between the electromechanical transducer load and the thermofluid system) for the energy harvesting. These explanations are based on limited analyses and analogies. They often do not work because the the physical mechanisms are very much interrelated in the SBPHP. A more thorough theoretical approach is needed. The state of knowledge on the self-oscillations is pre-paradigmatic (in the Kuhnian sense [65]). The goal here is to establish a paradigm.

CHAPTER 3

WHY IT OSCILLATES AND WHAT LEADS TO THE STARTUP

Avant-propos

Auteurs et affiliation:

Albert Tessier-Poirier: étudiant au doctorat à l'Université de Sherbrooke (1,2).

Thomas Monin: étudiant au doctorat à l'Université de Sherbrooke et à l'Université Savoie Mont-Blanc (1,2,3,4).

Étienne Léveillé: professionnel de recherche à l'Université de Sherbrooke (1,2).

Stéphane Monfray: responsable chez STMicroelectronics (4).

Fabien Formosa: Maître de conférences à l'Université Savoie Mont-Blanc (3).

Luc G. Fréchette: professeur à l'Université de Sherbrooke (1,2).

1) Institut Interdisciplinaire d'Innovation Technologique (3IT), Université de Sherbrooke, Sherbrooke, QC, Canada, 2) Laboratoire Nanotechnologies Nanosystèmes (LN2), CNRS UMI-3463, Université de Sherbrooke, Canada, 3) SYMME, Université Savoie Mont-Blanc, 74944 Annecy-le-Vieux, France, 4) STMicroelectronics, 38920 Crolles, France.

Date de soumission: 2019-01-11.

Date de l'acceptation: 2019-09-10.

Date de publication: 2019-10-09.

État d'acceptation: version finale publiée.

Revue: Physical Review Fluids.

Référence: [112].

Titre français: Comment l'évaporation-condensation mène aux auto-oscillations dans le caloduc pulsé monobranche.

Titre anglais: How Evaporation and Condensation Lead to Self-Oscillations in the Single-Branch Pulsating Heat Pipe.

Contribution au document: J'ai mené et réalisé l'ensemble des travaux expérimentaux et théoriques présentés dans cet article à l'exception des mesures expérimentales présentées à l'annexe A.2.2, réalisées par Thomas Monin. Aussi, Thomas Monin et Étienne Léveillé ont fabriqué la majeure partie du montage expérimental. Les coauteurs ont contribués par des conseils et suggestions lors de la recherche et lors de la rédaction du document.

Résumé français: Les auto-oscillations observées dans le caloduc pulsé mono-branche (SBPHP) sont expliquées en démontrant l'existence d'un résonateur mécanique excité par une force de rétroaction positive, par une analyse de stabilité linéaire et des validations expérimentales. Le SBPHP est un tube fermé à l'une des extrémités qui est d'abord rempli d'eau. L'extrémité fermée est ensuite chauffée et une bulle de vapeur s'y forme qui augmente en longueur puis atteint un équilibre. Depuis cet équilibre, augmenter la température de la zone chaude au-delà d'un certain seuil mène à des oscillations de la colonne de liquide qui se maintiennent dans le temps. Nous souhaiterions comprendre l'origine de ces oscillations et pourquoi elles ne s'atténuent pas dans le temps dû à la présence de friction. Un modèle mathématique est construit, puis linéarisé et résolu analytiquement. La solution dans le temps montre que le couplage entre l'inertie de la colonne de liquide et l'effet ressort de la vapeur produit un système masse-ressort, qui peut osciller après une faible perturbation. L'évaporation et la condensation qui se produisent alors que la colonne de liquide oscille mènent à des changements de pression dans la vapeur. La force qui en résulte est une force de rétroaction positive, qui injecte de l'énergie dans le système masse-ressort et rend le système instable, lorsque supérieure à la friction visqueuse. Un critère pour le démarrage est obtenu, basé sur un nombre adimensionnel dérivé du modèle. Un dispositif expérimental est ensuite utilisé pour valider les prédictions théoriques. L'effet sur l'instabilité du gradient thermique axial dans les parois (déstabilisant), de la résistance thermique liée au changement de phase (stabilisant) et de la pression externe (stabilisant) sont validés. La masse de la vapeur et la force de friction sont mesurées durant le démarrage et leurs rôles comme force de rétroaction positive et comme force dissipative, respectivement, sont validés. En conclusion, le mécanisme physique responsable de l'instabilité dans le SBPHP est maintenant bien compris. Les travaux présentés ici constituent des fondations théoriques solides qui contribueront au développement des caloducs auto-oscillants, pour le refroidissement et la récupération d'énergie.

Résumé anglais: The self-oscillations observed in the single-branch pulsating heat pipe (SBPHP) are explained by showing the existence of a mechanical resonator excited by a

self-driving force (feedback) through linear stability analysis, with experimental validation. The SBPHP is a tube closed at one end which is initially filled with water. The closed end is heated and a vapor bubble forms and reaches an equilibrium size. From this stable state, increasing the temperature of the heater temperature beyond a threshold leads to oscillations of the liquid plug sustained over time. We would like to understand where these oscillations come from and why they do not vanish over time due to the friction. A model of this system is formulated such that it can then be linearized and solved analytically for the motion over time. The solution shows that the coupling of the spring effect of the vapor and the inertia of the liquid plug leads to a spring-mass system, which can oscillate after a small perturbation. The evaporation and condensation taking place as the oscillations occur produce a change of the vapor pressure. The resulting force on the liquid plug is positive feedback; it injects energy into the spring-mass system and makes the oscillations unstable (startup) if greater than the friction. A criterion for startup is formally provided in the form of a dimensionless instability number derived from the model. An experimental apparatus is used to validate the theoretical prediction. The predicted effects of the tube's axial temperature gradient (destabilizing), of a thin film thermal resistance (stabilizing), and of the external pressure (stabilizing) are validated. The mass of the vapor and the friction force are measured during the startup and are shown to act as feedback and dissipation, respectively, as predicted by the theory. It is concluded that the main physical mechanism behind the instability in the SBPHP is now well understood. This provides a theoretical basis for the further development of pulsating heat pipes increasingly used for thermal management of electronics and harvesting of waste heat.

Note: pour satisfaire aux exigences de l'Université de Sherbrooke, la version de l'article présentée dans cette thèse diffère de la version officielle.

3.1 Introduction

One major limitation in electronics is the capacity to reject heat produced by the components [49]. Without enough heat dissipation, computation power must be limited to prevent overheating. To operate at higher power and maintain the same reliability, various cooling techniques have been studied, such as heat pipes. Due to phase change, the heat pipe thermal conductivity can be up to 100 times the thermal conductivity of a same size copper rod [30]. The pulsating heat pipe (PHP), proposed by Akachi [3], is a special type of heat pipe consisting of a tube bent into a given number of turns with the two ends connected to each other in the close-loop version, filled with vapor and liquid plugs. When a thermal difference is imposed on the PHP, the fluid may start to oscillate, transferring

heat from the hot section to the cold section by evaporation and condensation, and by convection. The PHP could become an advantageous solution for thermal cooling applications but the limited understanding of its pulsating dynamics hinders proper design. In an effort to understand the basic mechanism behind the oscillations, a simpler device, called a single-branch PHP (SBPHP) has been studied (see fig. 3.1). The SBPHP can also be used as a waste heat harvesting device called the Self-Oscillating Fluidic Heat Engine (SOFHE) [78]. In this paper we focus on the physics of the SBPHP. The behavior in the SBPHP is best described by the following experiment (see Das et al. [20]). A tube of small diameter (∼1 mm), sealed at one end and open at the other, is filled with a working fluid. The tube is heated at the sealed end and cooled at the other. A single vapor bubble (occupying the entire cross-section area) eventually forms at the sealed end, separated from the liquid plug by a meniscus. The vapor bubble increases in size until the meniscus reaches a stable equilibrium position between the hot and the cold end (t_0 in fig. 3.1). From this equilibrium, a small change of a parameter (such as an increase of the heat source temperature) may lead to oscillations of the liquid plug at a given amplitude and frequency for an indefinite amount of time.

Some fundamental questions naturally arise from the observations of the oscillations in the SBPHP, about the frequency of the oscillations and the self-oscillating nature of the system. Such questions have been answered for other self-oscillators by making use of linear stability analysis [52, 107]. We may first ask why the system exhibits an oscillatory behavior and what defines its frequency. Using linear stability analysis, assuming no phase

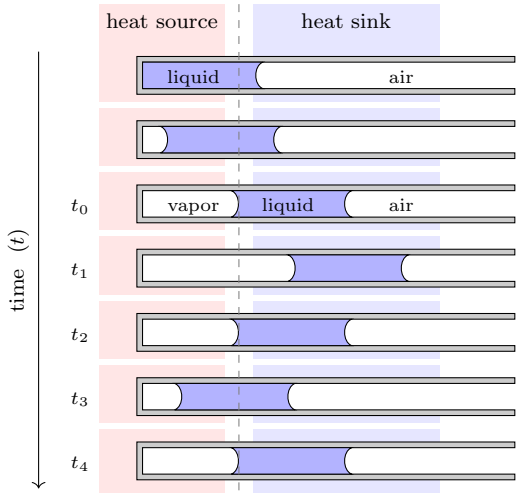

Figure 3.1 Schematic representation of the oscillations, starting at t_0, in the single-branch pulsating heat pipe (SBPHP).

change, Das et al. [20] showed that the SBPHP behaves like a spring-mass system. The process of compression and expansion of the vapor produces a spring effect which leads to a resonator when coupled with the liquid plug's inertia. A corresponding frequency was predicted and matched well with experiments, leading to a well-accepted spring-mass representation [69, 70, 105]. Experimental validation for a large range of gas spring and liquid mass values was previously reported by Monin et al. [77] and is included herein for completeness (see appendix A.2.2). Considering a damped harmonic oscillator, we might expect the amplitude to decrease, following an initial perturbation. On the contrary, experimental evidence shows that the amplitude of the oscillations can be self-sustained [20, 92].

One may then ask why the meniscus does not stabilize at an equilibrium position. The literature on this second question is more elusive. Several researchers believe that phase change drives the oscillations in some way [127]. Das et al. [20] showed by numerical simulations that including phase change can make the system unstable, leading to self-oscillations. The startup conditions were further studied by Nikolayev [85]. It was found that the startup depends heavily on the thermal gradient along the wall at the equilibrium position. However, there is still no clear understanding to this day of how the phase change sustains the oscillations.

Linear stability analysis applied to the complete system (including phase change) should reveal the instability mechanism in the SBPHP, just like it revealed the resonator. However, this analysis has been impractical to use so far, because phase change has been represented by noncontinuous functions (while continuously differentiable functions are required). Finnie and Curl [32, 33] used linearization to achieve a good understanding of a system similar to the PHP, the putt-putt boat (later reviewed by Jenkins [52]). Here we modify their analysis to describe the SBPHP and extend their work both theoretically and experimentally. In this paper we construct a continuously differentiable model derived from conservation laws, which we then linearize and solve (section 3.3). The process confirms the resonator representation. More importantly, the linearization allows us to show that evaporation and condensation produce a positive feedback force, which makes the system unstable and leads to self-sustained oscillations. We derive an analytical instability (startup) criterion. This understanding of the SBPHP self-oscillations is then validated experimentally (section 3.5). We measure the force from phase change and show that it acts as positive feedback while the measured friction force acts as dissipation. In section 3.6, we discuss how our results compare with the literature.

3.2 Models

A model describing the SBPHP dynamics is obtained by first applying a momentum balance on the liquid plug and energy conservation on the vapor bubble (see fig. 3.2), similarly to the models in [126, 20]. The momentum balance on the liquid plug according to fig. 3.2b results in

$$\ddot{x}_i = \frac{1}{m_\ell}\left(P_g\,A - \hat{P}_e\,A + F_f\right), \tag{3.1}$$

where x_i refers to the position of the meniscus relative to the equilibrium (defined later in fig. 3.3) and $\dot{x}_i$ and $\ddot{x}_i$ are respectively the velocity and the acceleration of the liquid plug. The mass of liquid m_ℓ is assumed constant, because the specific volume of vapor is much larger that the one of liquid [1]. The forces considered are those produced by the vapor pressure P_g, the external pressure [2] P_e, and the friction force F_f between the wall and the liquid plug. Gravity is included in the effective external pressure expression $\hat{P}_e \equiv P_e + \rho_\ell\,L_\ell\,g\,\sin\theta$, following the notation of [123]. Capillary forces on each meniscus are assumed to be equal and opposite, resulting in no net capillary force. Energy conservation on the vapor bubble,

$$\dot{T}_g = \frac{1}{c_v\,m_g}\left[\dot{m}_g\left(c_p T_{g,sat} - c_v\,T_g\right) - P_g A\,\dot{x}_i + \dot{Q}_g\right] \tag{3.2}$$

includes energy added by phase change (term in $\dot{m}_g$), the rate of mechanical work done by the liquid plug (term in P_g) and heat transfer from the wall $\dot{Q}_g$. In this equation, T_g is the averaged temperature of the vapor bubble, which is usually overheated ($T_g > T_{g,sat}$). At the meniscus, conditions are at saturation, so the temperature is always $T_{g,sat}$. Also, m_g is the mass of vapor and $\dot{m}_g$ is the net evaporation rate. The energy conservation is used to describe the evolution in time of the temperature of the vapor. We will consider two limiting cases: the isothermal case, where $\dot{Q}_g$ is such that $\dot{T}_g = 0$, and the adiabatic case, where $\dot{Q}_g = 0$. This equation is similar to the literature [126, 20] but, instead of assuming the temperature at the meniscus to be equal to the averaged vapor temperature (which can be overheated), the meniscus is considered to be at saturation conditions (see appendix A.1.1 for a derivation). The pressure of the vapor P_g in eqs. (3.1) and (3.2) is

1. A more detailed analysis shows that the resulting force due to change of the mass m_ℓ is many orders of magnitude smaller than the other forces: for reasonable values of the parameters, we found the ratio of the additional force to each one of the other forces to be about 0.0006%.

2. In the SBPHP, the pressure at the open end, P_e, is a constant. This is unlike the closed MBPHP where for each liquid plugs, the pressures at both ends may vary. Also, the volume of the vapor bubble and the liquid plug varies in the SBPHP whereas the total volume (of the vapor bubbles and the liquid plugs) of the closed MBPHP is constant.

described by the ideal gas law, where $L_{g,0}$ is the vapor bubble length at equilibrium,

$$P_g = \frac{m_g\, R_g\, T_g}{\mathcal{V}_g} = \frac{m_g\, R_g\, T_g}{(x_i + L_{g,0})\; A} \tag{3.3}$$

3.2.1 Phase Change Modeling

The mass of vapor m_g changes due to evaporation or condensation, so we must include an equation describing this process. Finding an expression for the net evaporation rate $\dot{m}_g$ is however a complex problem. A precise predictive model would have to take into account the phase change from a thin liquid film laid on the wall by the oscillating liquid plug [92, 34]. To study the system dynamics, we instead adopt a global representation of the phase change physics by representing it as a heat transfer mechanism defined from a thermal resistance R_{th}, so the heat transfer rate producing evaporation and condensation can be expressed as: $\dot{Q} = [T_w(x_i) - T_{g,sat}]\,/R_{th}$ (see fig. 3.3). We assume here that the meniscus is maintained at saturation (so $T_g = T_{g,sat}$ at the meniscus). This is a common approximation in PHP modeling (see, for example, [20]), which assumes local thermodynamic equilibrium at the interface [117]. The heat transfer $\dot{Q}$ leads to a net evaporation rate $\dot{m}_g$, given by the energy balance on the meniscus control volume

$$\dot{m}_g = \frac{\dot{Q}}{H_v} = \frac{T_w(x_i) - T_{g,sat}}{H_v R_{th}}. \tag{3.4}$$

Although this approach might seem oversimplified, it will be shown to be insightful later on. In section 3.6.3, we discuss how a more realistic phase change (from a liquid film for example) would influence the dynamics. Here, we consider the thermal resistance R_{th} as a single parameter, including the conduction resistance in the wall, the conduction resistance through the liquid and the liquid-vapor interfacial resistance [89]. A more detailed analysis could describe R_{th} in terms of the thermal conductivities, the meniscus

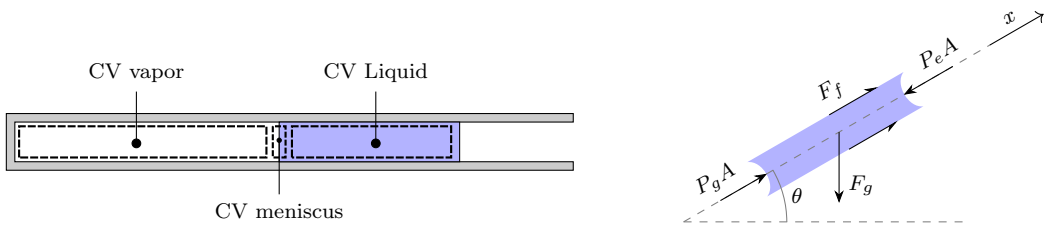

(a) (b)

Figure 3.2 (a) Control volumes and (b) forces (liquid control volume) applied.

geometry and other parameters. Alternatively, R_{th} could be estimated experimentally, by measuring the phase-change rate.

3.2.2 Wall Temperature Profile and Equilibrium

The wall temperature T_w decreases from the heat source to the heat sink because of the axial heat transfer along the tube. We represent it qualitatively by an arctangent function

$$T_w(x) = \frac{T_{HL}}{\pi} \arctan\left[\frac{-\pi\ |T'_{wc}|}{T_{HL}}\ (x - x_c)\right] + \frac{T_H + T_L}{2} \tag{3.5a}$$

as shown in fig. 3.3. Axial heat conduction along the wall smooths the temperature profile such that it must be continuous (and continuously differentiable) to be physically possible. This arctangent profile is thus closer to reality than the step function often use and, additionally, allows linearization. Also, such an S-shaped temperature profile was observed experimentally [74]. The arctangent profile eq. (3.5a) is characterized by high and low temperatures T_H and T_L, respectively,

$$T_{HL} \equiv T_H - T_L, \tag{3.5b}$$

as well as the temperature gradient T'_{wc},

$$|T'_{wc}| \equiv \left(\frac{-dT_w}{dx}\right)_{x=x_c}, \tag{3.5c}$$

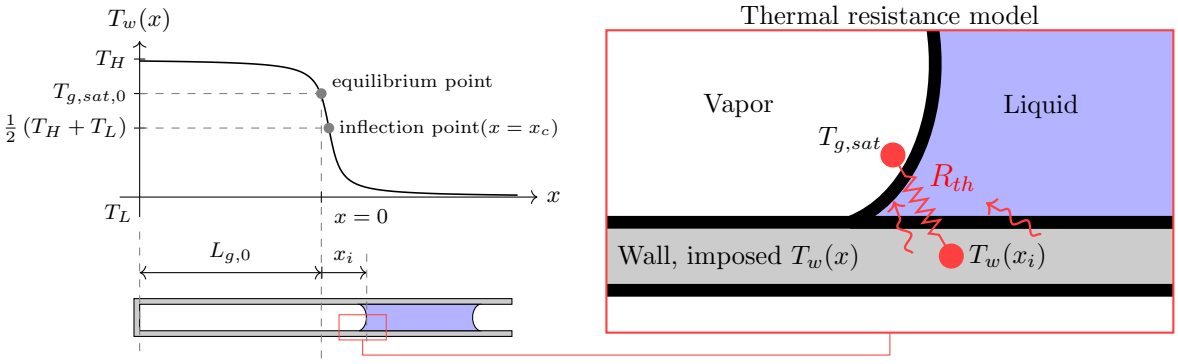

Figure 3.3 Wall temperature profile along the x axis and thermal resistance model for the heat transfer leading to evaporation and condensation.

at the inflection point x_c,

$$x_c \equiv \frac{T_{HL}}{\pi\ |T'_{wc}|}\ \tan\left[\frac{\pi\left[T_{g,sat,0} - \frac{1}{2}\left(T_H + T_L\right)\right]}{T_{HL}}\right], \tag{3.5d}$$

which may differ from the equilibrium point, $x = 0$. One can easily deduce the absolute value of the temperature gradient at the equilibrium point, $\left|T'_{w,0}\right|$,

$$\left|T'_{w,0}\right| \equiv \left(\frac{-dT_w}{dx}\right)_{x=0} = \frac{|T'_{wc}|}{1 + \left(x_c\,\pi|T'_{wc}|/T_{HL}\right)^2}, \tag{3.6}$$

which will turn out to be an important parameter. The temperature profile eq. (3.5a) can then be used in the $\dot{m}_g$ expression eq. (3.4), leading to

$$\dot{m}_g(x_i) = \frac{T_{HL}}{\pi\, H_v R_{th}}\ \arctan\left[\frac{-\pi\ |T'_{wc}|}{T_{HL}}\ (x_i - x_c)\right] + \frac{\frac{1}{2}\left(T_H + T_L\right) - T_{g,sat}}{H_v R_{th}}, \tag{3.7}$$

The saturation temperature $T_{g,sat}$ in eq. (3.7) can be expressed as a function of the vapor bubble pressure according to the Clausius-Clapeyron relation [15], as

$$T_{g,sat} = \left[\left(\frac{1}{T_{g,sat,0}}\right) - \frac{R_g}{H_v} \cdot \ln\left(\frac{P_g}{P_{g,0}}\right)\right]^{-1}. \tag{3.8}$$

3.2.3 Friction Force

A viscous friction force is experienced by the liquid plug along the tube wall. To predict that force, one must find the velocity profile in the liquid. For the idealized case of an infinite liquid column in the laminar regime, subjected to sinusoidal oscillations of the pressure gradient, the flow differs from the Poiseuille parabolic velocity profile but can still be solved analytically [123]. The behavior of the flow depends on the kinetic Reynolds number ($\mathrm{Re}_\omega \equiv \omega R^2/\nu$), a ratio of the oscillating inertial force to the viscous force. For a SBPHP filled with water, with a diameter of 1 mm and for a frequency ranging between 1 and 25 Hz, Re_ω is comprised between 1.6 and 40. Since $\mathrm{Re}_\omega < 2000$, the flow is considered laminar [123]. For $\mathrm{Re}_\omega \ll 4$, the quasistatic Poiseuille profile is a good approximation and the friction is well described by

$$F_f = -\ 8\pi\,\mu\,L_\ell\ \dot{x}_i = \ c\ \dot{x}_i, \tag{3.9a}$$

with $c \equiv -8\pi\,\mu\,L_\ell$. This expression is the simplest form of a dissipative friction force, completely opposed to velocity. It is also the expression commonly used in the PHP literature to date. However, for a laminar flow with $\mathrm{Re}_\omega > 4$, inertial effects are important and the Poiseuille parabolic velocity profile is not valid anymore. From the velocity profile given by White [123], we derived an accurate expression for the friction force given by

$$F_f \approx -\sqrt{\frac{2}{\mathrm{Re}_\omega}}\,\Delta P_g A + \left(\sqrt{\frac{2}{\mathrm{Re}_\omega}} - \frac{1}{\mathrm{Re}_\omega}\right)\frac{\Delta \dot{P}_g\,A}{\omega} \tag{3.9b}$$

valid for $4 < \mathrm{Re}_\omega < 2000$ (see appendix A.1.2 for derivation). We will refer to this case as the oscillating regime in opposition to the quasistatic (Poiseuille) case. In the oscillating regime, the velocity gradient at the wall and the resulting friction force are in advance relative to the average liquid plug velocity $\dot{x}_i$. As a result, the friction force will lead to not only a dissipative effect, but also an inertial one. It should be noted that none of these relations take into account the effect of the meniscus on the flow field. Nonetheless, A. Nikkhah et al. [1] found those analytical expressions to be accurate when compared to CFD as long as the liquid plug is long enough (A ratio $L/D > 10$ was recommended). The experiment below also confirms their validity.

3.2.4 Equilibrium and Complete Dimensionless System of Equations

At equilibrium, the liquid plug is static ($\dot{x}_i = \ddot{x}_i = 0$) so the friction force $F_f(\dot{x}_i = 0) = 0$ and therefore $P_g = \hat{P}_e$ according to eq. (3.1). Also, the mass of vapor m_g is constant ($\dot{m}_g = 0$), so the equilibrium corresponds to the position where $T_w = T_{g,sat,0}$, according to eq. (3.4), which is $x_i = 0$, according to eq. (3.5a). The thermal gradient at the equilibrium is given by eq. (3.6) for the arctangent profile. Equations (3.1) to (3.3) and (3.7) to (3.9) can be solved for the position of the meniscus as a function of time. Since we care about the dynamics about the equilibrium, we replace the quantities m_g, T_g, $T_{g,sat}$ and P_g by their perturbations Δm_g, ΔT_g, $\Delta T_{g,sat}$ and ΔP_g (e.g., $\Delta P_g = P_g - P_{g,0}$ where the 0 subscript refers to the equilibrium value). The equations are then made dimensionless using the quantities at equilibrium (e.g., $\widetilde{\Delta P_g} = \Delta P_g / P_{g,0}$) and the natural angular frequency ω_n (eq. (3.15e), which will be derived in section 3.3). We present this full set of dimensionless equations (eqs. (A.21) and (A.22)) in appendix A.1.3, and the associated dimensionless

quantities eqs. (A.23) and (A.24). A simplified set of equations

$$\ddot{\widetilde{x_i}} = \widetilde{\Delta P_g} + \widetilde{F_f} = \underbrace{-\left(\frac{1}{1+\widetilde{x_i}}\right)\widetilde{x_i}}_{\widetilde{F_\mathcal{V}}} \underbrace{+\left(\frac{1}{1+\widetilde{x_i}}\right)\widetilde{\Delta m_g}}_{\widetilde{F_m}} \underbrace{-\,2\,\zeta_f\,\dot{\widetilde{x}}_i}_{\widetilde{F_f}}, \tag{3.10a}$$

$$\dot{\widetilde{\Delta m_g}} = \widetilde{T_{HL}}\,\arctan\left[\,-\left|\widetilde{T'_{wc}}\right|\,(\widetilde{x_i}-\widetilde{x_c})\,\right] + \widetilde{C_{th}}, \tag{3.10b}$$

is studied, considering the following assumptions: constant saturation temperature, constant temperature of the vapor, and Poiseuille flow. This simpler case allows us to focus on the primary physics responsible for self-oscillations. The momentum balance is given by eq. (3.10a), where the dimensionless pressure $\widetilde{\Delta P_g}$ can be split into two distinct components: a change of volume of the vapor (compression-expansion) $\widetilde{F_\mathcal{V}}$ and a change of mass (evaporation and condensation) of vapor $\widetilde{F_m}$. It will later be shown that $\widetilde{F_\mathcal{V}}$ acts as a spring and is responsible for the oscillations, while $\widetilde{F_m}$ is feedback, responsible for the instability. The dimensionless friction force is $\widetilde{F_f}$, where ζ_f is the dimensionless friction coefficient, based on Poiseuille flow (note that $\zeta_f > 0$). The mass of vapor varies according to the evaporation rate eq. (3.10b), with dimensionless time derivatives in τ and with the definitions

$$\tau \equiv \omega_n\, t, \tag{3.11a}$$

$$\zeta_f \equiv -\,\frac{c}{2\,m_\ell\;\omega_n}, \tag{3.11b}$$

$$\widetilde{T_{HL}} = \left(\frac{1}{\pi\;m_{g,0}\,\omega_n\;H_v\,R_{th}}\right)\;T_{HL}, \tag{3.11c}$$

$$\left|\widetilde{T'_{wc}}\right| = \left(\frac{\pi\;L_{g,0}}{T_{HL}}\right)\;|T'_{wc}|, \tag{3.11d}$$

$$\widetilde{x_c} = \left(\frac{1}{L_{g,0}}\right)\;x_c, \tag{3.11e}$$

$$\widetilde{C_{th}} \equiv \frac{\frac{1}{2}\,(T_H+T_L)-T_{g,sat,0}}{m_{g,0}\,\omega_n\;H_v R_{th}}. \tag{3.11f}$$

In appendix A.1.3, we provide equations and solutions for the general case, which includes non-Poiseuille friction ($\mathrm{Re}_\omega > 4$), variations of vapor temperature and variations of saturation temperature. These effects were found to be secondary; they provide a more accurate physical representation of the problem but are not required to produce self-oscillations. In appendix A.1.3, we also discuss how these affect the dynamics and when they can be neglected.

3.3 Oscillations Startup - Linear Theory

The set of differential equations eq. (3.10) is nonlinear and is therefore difficult to solve analytically. When studying nonlinear dynamical systems, it is common to look for insight into the physics by studying the linearized equations [107]. The linearization of eq. (3.10) leads to

$$\ddot{\widetilde{x}}_i \approx \underbrace{-\widetilde{x}_i}_{\widetilde{F_\mathcal{V}}} + \underbrace{\widetilde{\Delta m_g}}_{\widetilde{F_m}} \underbrace{-2\,\zeta_f\,\dot{\widetilde{x}}_i}_{\widetilde{F_f}}, \tag{3.12a}$$

$$\dot{\widetilde{\Delta m_g}} \approx -2\,\widetilde{\sigma}\,\widetilde{x}_i, \tag{3.12b}$$

where

$$\widetilde{\sigma} \equiv \frac{1}{2}\,\frac{\widetilde{T_{HL}}\left|\widetilde{T'_{wc}}\right|}{1+\left(\widetilde{x_c}\left|\widetilde{T'_{wc}}\right|\right)^2} = \frac{L_{g,0}\left|T'_{w,0}\right|}{2\,m_{g,0}\,\omega_n\,H_v\,R_{th}}. \tag{3.13}$$

The coefficient $\widetilde{\sigma}$ expresses the rate of phase change due to motion of the meniscus along the wall temperature profile and is referred to as the phase-change coefficient (note that $\widetilde{\sigma} \geqslant 0$). The solution of eq. (3.12) is given by eq. (A.28). The system behavior, which depends only on $\widetilde{\sigma}$ and ζ_f, is shown in fig. 3.4.

Let us first consider the case where there is no phase change by taking the phase-change coefficient $\widetilde{\sigma} = 0$. We get $\dot{\widetilde{\Delta m_g}} = 0$ and the mass of vapor is at equilibrium, so $\widetilde{\Delta m_g} = 0$. Equation (3.12a) becomes simply $\ddot{\widetilde{x}}_i = -\widetilde{x}_i - 2\,\zeta_f\,\dot{\widetilde{x}}_i$ which is the well-known universal oscillator equation. For $0 < \zeta_f < 1$, the system is underdamped and the position $\widetilde{x}_i$ oscillates after a perturbation due to the interplay of the inertial term $\ddot{\widetilde{x}}_i$ and the spring term $-\widetilde{x}_i$, but the amplitude decreases over time due to the friction term $-2\,\zeta_f\,\dot{\widetilde{x}}_i$. For $\zeta_f > 1$, the system is overdamped and the position $\widetilde{x}_i$ decreases exponentially towards the equilibrium without oscillating.

Now let us introduce the phase change by considering $\widetilde{\sigma} > 0$ and see how it affects the dynamics. The mass of vapor $\widetilde{\Delta m_g}$ changes according to the phase change eq. (3.12b); $\widetilde{\Delta m_g}$ introduces a dimensionless force $\widetilde{F_m}$ to the classical harmonic oscillator eq. (3.12a) which can change the qualitative nature of the oscillations. Except for the overdamped region (in the lower right corner of fig. 3.4), the solution for the position $\widetilde{x}_i$ reduces to

sinusoidal motion (eq. (A.30a) also gives the velocity and the mass of vapor)

$$\widetilde{x}_i(\tau) = \underbrace{a_1\, e^{\lambda_1 \tau}}_{\text{mean value growth}} + \underbrace{a_2\, e^{\widetilde{\alpha}\tau}\, \sin\left(\widetilde{\omega}\tau + \varphi\right)}_{\text{oscillations growing or not}}, \tag{3.14}$$

where (approximations are given for small $\widetilde{\sigma}$ and ζ_f)

$$\lambda_1 \approx -2\,\widetilde{\sigma}, \tag{3.15a}$$

$$\widetilde{\omega} \approx 1 \tag{3.15b}$$

$$\widetilde{\alpha} \approx \widetilde{\sigma} - \zeta_f = \zeta_f\left(\Pi - 1\right), \tag{3.15c}$$

$$\Pi \equiv \frac{\widetilde{\sigma}}{\zeta_f} = \frac{\rho_\ell\, R_g\, T_{g,0}\, \left|T'_{w,0}\right|}{8\pi\, \mu\, H_v R_{th}\, \hat{P}_e}, \tag{3.15d}$$

$$\omega_n = \sqrt{\frac{k}{m_\ell}} = \sqrt{\frac{P_{g,0}}{\rho_\ell L_\ell L_{g,0}}}. \tag{3.15e}$$

The constants a_1, a_2 and φ are defined by the initial conditions. The sinusoidal part in eq. (3.14) produces oscillations. For small $\widetilde{\sigma}$ and ζ_f, the dimensionless frequency $\widetilde{\omega}$ approaches 1, meaning that the dimensional frequency is ω_n given by eq. (3.15e), as predicted by Das et al. [20]. However, for larger values of $\widetilde{\sigma}$ and ζ_f, $\widetilde{\omega}$ can differ significantly from 1(see fig. A.2d in the appendix and related text for more details).

The oscillations grow or decay due to the exponential $e^{\widetilde{\alpha}\tau}$. The growth rate $\widetilde{\alpha}$ approaches $\widetilde{\sigma} - \zeta_f$ for small $\widetilde{\sigma}$ and ζ_f (eq. (3.15c)). Therefore, the friction ζ_f still tends to make the equilibrium stable (damps the oscillations) as in the universal oscillator equation. However, the phase change $\widetilde{\sigma}$ has the opposite effect; it tends to make the equilibrium unstable (leading to growing oscillations). Phase change can make the equilibrium unstable ($\widetilde{\alpha} > 0$) when greater than friction ($\widetilde{\sigma} > \zeta_f$), leading to the startup of the oscillations after a small perturbation from the equilibrium (see fig. 3.4). The ratio $\widetilde{\sigma}/\zeta_f$, defined here as the dimensionless instability number Π (eq. (3.15d)), can thus be used to assess the system's linear stability (stable for $\Pi < 1$ and unstable for $\Pi > 1$). The Π number suggests that to promote the instability, one may increase the thermal gradient at the equilibrium position $\left|T'_{w,0}\right|$, decrease the external pressure $\hat{P}_e$, or decrease the thermal resistance (by promoting evaporation, for example). Changing the fluid also affects Π. For large value of $\widetilde{\sigma}$ and ζ_f, Π is still valid as a criterion for the startup. The growth rate $\widetilde{\alpha}$ can however change significantly from the approximation (see gray isolines in fig. 3.4 or fig. A.2c for more details).

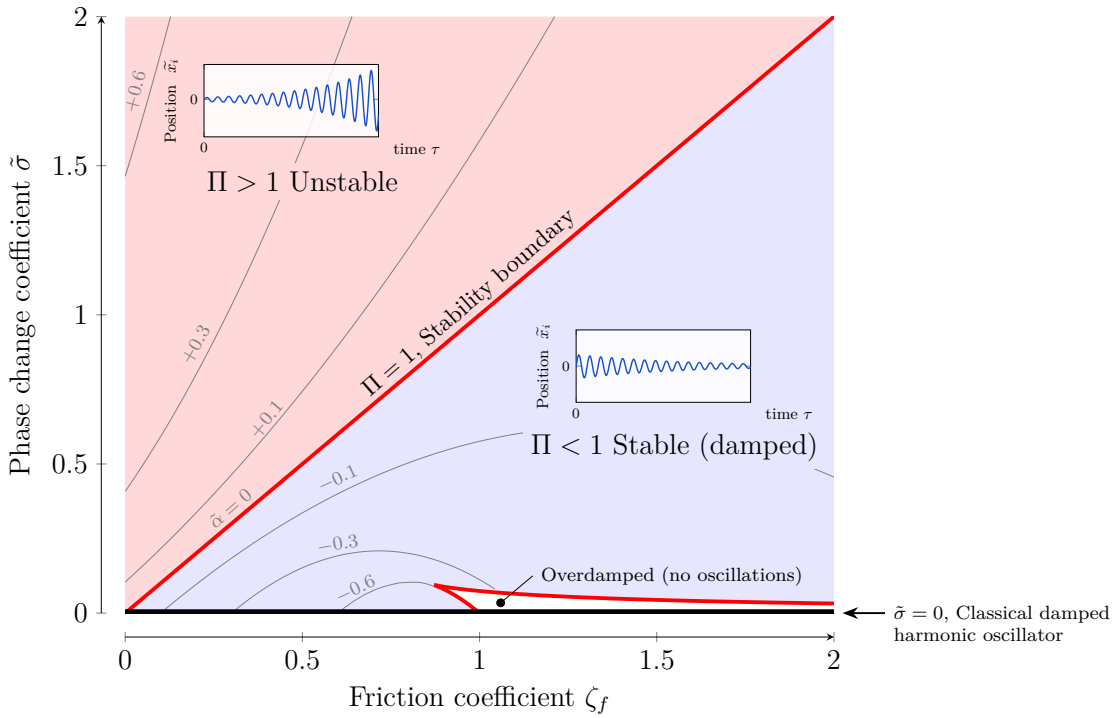

Figure 3.4 The equilibrium state of the SBPHP (based on eq. (3.12)) can be stable (small perturbation leading to either overdamped or damped oscillation) for $\Pi < 1$ or unstable (small perturbation leading to sustain oscillations) for $\Pi > 1$, with the dimensionless number $\Pi = \widetilde{\sigma}/\zeta_f$, where $\widetilde{\sigma}$ is the phase-change coefficient and ζ_f is the friction coefficient.

The first exponential in eq. (3.14) describes the oscillation mean value which decreases in time toward 0 since $\lambda_1 \leqslant 0$ (see fig. A.2b). The approximation of small $\widetilde{\sigma}$ and ζ_f mentioned in this section is usually valid. For example, for a SBPHP filled with water, of a diameter of 1 mm, at atmospheric pressure and with lengths of vapor and liquid of 10 cm, the friction coefficient is $\zeta_f = 0.16$. For a system close to startup, $\widetilde{\sigma}$ is close to ζ_f and both values are therefore small; the system is in the lower left corner of fig. 3.4.

3.4 Understanding the Physics

To understand the physics leading to the solution eq. (3.14), let us analyze the forces applied to the liquid plug, specifically the components of the pressure ($\widetilde{F_v}$ and $\widetilde{F_m}$) and the friction force ($\widetilde{F_f}$) after a small perturbation of the equilibrium and for small $\widetilde{\sigma}$ and ζ_f at first for simplicity (see section 3.4.3 for more general considerations). Figure 3.5 shows the oscillating part of the meniscus position, of the forces and of other components of interest. In the following, we will also make use of an energetic point of view, which is especially useful to study the evolution of the system from one oscillation cycle to another.

A single quantity (the work over a cycle) indicates if the net effect of a force is to increase or decrease the energy (related to the oscillation amplitude) over a cycle. Importantly, this framework remains valid when the dynamics becomes nonlinear. The energy framework introduced here will also be used to analyze experimental data in section 3.5.4.

3.4.1 Resonator (Spring effect from the Vapor Coupled to the Liquid Inertia)

Compression and expansion of the vapor bubble produce a restoring force $\widetilde{F_{\mathcal{V}}}$, which is proportional and opposite to the position $\widetilde{x_i}$ (eq. (3.12a) and fig. 3.5b). It acts as a spring and, coupled with the liquid plug inertia, produces a resonator which explains the oscillations. This resonator representation was already described in the works of Das et al. [20] and Ma et al. [69]. Here we confirm those findings (for small $\widetilde{\sigma}$ and ζ_f) by a more general approach, without neglecting the phase change. We use $\widetilde{K}$ to denote the kinetic energy

$$\widetilde{K} = \frac{K}{P_{g,0} A L_{g,0}} \qquad = \frac{1}{2}\, \dot{\widetilde{x}_i}^2. \tag{3.16a}$$

The force $\widetilde{F_{\mathcal{V}}}$ is conservative, so the work it produces leads to potential energy $\widetilde{U}_r$,

$$\widetilde{U}_r = \frac{U_{res}}{P_{g,0} A L_{g,0}} \qquad = \widetilde{x_i} - \ln\left[1 + \widetilde{x_i}\right] \approx \frac{1}{2}\, \widetilde{x_i}^2. \tag{3.16b}$$

The sum of $\widetilde{U}_r$ and the kinetic energy $\widetilde{K}$ of the liquid mass constitutes the energy of the resonator $\widetilde{E}_r$,

$$\widetilde{E}_r = \widetilde{K} + \widetilde{U}_r \qquad \approx \frac{1}{2}\, r^2(\tau_i), \tag{3.16c}$$

with $r(\tau) \equiv a_2 e^{\widetilde{\alpha}\tau}$. From an energetic viewpoint, the resonator stores energy. In the absence of friction and phase change, $\widetilde{E}_r$ is conserved and the energy is exchanged between the kinetic and the potential forms over a cycle. Considering the linear solution, we obtain the approximation $\widetilde{E}_r \approx \frac{1}{2}\, r^2(\tau_i)$, where the quantity $r(\tau_i)$ is the oscillation amplitude $a_2 e^{\widetilde{\alpha}\tau}$ in the linear solution, at the time $\tau = \tau_i$. We conclude from this expression that energy and oscillation amplitude are linked: what leads to an increase (decrease) of energy $\widetilde{E}_r$ also leads to an increase (decrease) in oscillation amplitude.

3.4.2 Instability Mechanism (Mass of Vapor Versus Friction)

The friction force $\widetilde{F_f}$ produces work $\widetilde{W_f}$,

$$\widetilde{W_f} = \frac{W_f}{P_{g,0} A L_{g,0}} = \int_{\tau_0}^{\tau_1} \widetilde{F_f} \cdot \dot{\widetilde{x}}_i d\tau, \tag{3.17a}$$

on the liquid plug, while the phase change produces a force $\widetilde{F_m}$, which in turn produces a work $\widetilde{W_m}$,

$$\widetilde{W_m} = \frac{W_m}{P_{g,0} A L_{g,0}} = \int_{\tau_0}^{\tau_1} \widetilde{F_m} \cdot \dot{\widetilde{x}}_i d\tau, \tag{3.17b}$$

on the liquid plug. The net work $\widetilde{W_m} + \widetilde{W_f}$ corresponds to energy injected into (dissipated from, if negative) the resonator, leading to an increase (decrease) in the oscillation amplitude.

We obtain the works produced over a cycle at a time τ_i,

$$\widetilde{W}_{f,\text{cycle}} = \int_{\tau_i - \pi/\widetilde{\omega}}^{\tau_i + \pi/\widetilde{\omega}} \widetilde{F_f} \cdot \dot{\widetilde{x}}_i d\tau \quad \approx \quad -\frac{2\pi}{\widetilde{\omega}} \zeta_f \, r^2(\tau_i), \tag{3.18a}$$

$$\widetilde{W}_{m,\text{cycle}} = \int_{\tau_i - \pi/\widetilde{\omega}}^{\tau_i + \pi/\widetilde{\omega}} \widetilde{F_m} \cdot \dot{\widetilde{x}}_i d\tau \quad \approx \quad +\frac{2\pi}{\widetilde{\omega}} \widetilde{\sigma} \, r^2(\tau_i), \tag{3.18b}$$

by integrating over a period around τ_i (a period being $2\pi/\widetilde{\omega}$). The approximations in eq. (3.18) are obtained by considering the expressions of the forces and using the linear solution.

The friction force $\widetilde{F_f}$ is opposite to the velocity and therefore acts as a damping force, producing a negative work $\widetilde{W_f}$. Over a cycle, the friction dissipates the energy $(2\pi/\widetilde{\omega})\,\zeta_f\, r^2$ from the resonator, which tends to stabilize the system. In the absence of phase change, the energy of the resonator $\widetilde{E}_r$ and the oscillation amplitude decrease over time, so the resonator settles to the equilibrium position after a while. With phase change however, the system can become unstable. A phase change proportional and opposite to the position (see eq. (3.12b) and fig. 3.5, evaporation (condensation) increases as the meniscus goes in the heat source (sink)) produces a force $\widetilde{F_m}$ on the liquid plug which is in phase with the velocity and acts as positive feedback (also called negative damping). It produces a positive work $\widetilde{W_m}$ which injects the energy $(2\pi/\widetilde{\omega})\,\widetilde{\sigma}\, r^2$ into the resonator over a cycle and tends to destabilize the system.

We found in the linear solution that the system is unstable for $\Pi > 1$. Here, we see from

$$\widetilde{W}_{m,\text{cycle}} + \widetilde{W}_{f,\text{cycle}} \approx \frac{2\pi}{\widetilde{\omega}} \left(\widetilde{\sigma} - \zeta_f\right) r^2(\tau_i) = \frac{2\pi}{\widetilde{\omega}} \zeta_f \left(\Pi - 1\right) r^2(\tau_i) \tag{3.19}$$

that the net energy injected into the resonator over a cycle ($\widetilde{W}_{m,\text{cycle}} + \widetilde{W}_{f,\text{cycle}}$) is proportional to $\Pi - 1$. When $\Pi > 1$ (corresponding to $\widetilde{\sigma} > \zeta_f$), the energy injected by phase change is greater than the energy dissipated by friction. So, at each cycle, the net injected energy in the resonator $\widetilde{W}_{m,\text{cycle}} + \widetilde{W}_{f,\text{cycle}}$ is positive. This is why the energy of the resonator, $\widetilde{E}_r$ as well as the oscillation amplitude, increase over time when $\Pi > 1$. In fact, we have the ratio $\widetilde{W}_{m,\text{cycle}}/\widetilde{W}_{f,\text{cycle}} \approx \widetilde{\sigma}/\zeta_f = \Pi$; one can understand the instability number as the ratio of the injected energy to the dissipated energy.

From our model and under the limits mentioned above, we see that having an evaporation rate $\widetilde{\Delta \dot{m}_g}$ proportional and opposite to the meniscus position leads to a force completely in phase with velocity, which solely injects energy in the system. It is the simplest expression possible to produce self-oscillations. One notices that since the pressure $\widetilde{\Delta P_g}$ is a function of the mass of vapor (the integral of the phase change rate), $\widetilde{F_m}$ and $\widetilde{\Delta \dot{m}_g}$ are not in phase. A delay is introduced by the integral (see the phasor representation in fig. 3.5c), so the evaporation rate in phase with position leads to a force in phase with velocity.

3.4.3 Resonator Energy

The works inject (dissipate) energy into (from) the resonator; the energy of the resonator $\widetilde{E}_r$ is related to the work applied on it. This can be formally shown by converting the momentum balance eq. (3.12a) into an energy equation(simply multiply by velocity and integrate)

$$\widetilde{E}_r \left|_{\tau_0}^{\tau_1} \right. = \widetilde{K} + \widetilde{U}_r \quad \left|_{\tau_0}^{\tau_1} \right. = \widetilde{W}_m + \widetilde{W}_f \quad \left|_{\tau_0}^{\tau_1} \right. \tag{3.20}$$

Equation (3.12a) shows that the energy gain of the resonator $\widetilde{E}_r \left|_{\tau_0}^{\tau_1} \right.$ between a time τ_0 and a time τ_1 is equal to the net work $\widetilde{W}_m + \widetilde{W}_f$ done during that time interval. If at τ_0, the system is at equilibrium (where $\widetilde{E}_r = 0$) and then the energy gain $\widetilde{E}_r \left|_{\tau_0}^{\tau_1} \right.$ simply corresponds to the total resonator energy $\widetilde{E}_r(\tau_1)$.

Under the limits considered at the beginning of section 3.4, the phase change and the friction are perfectly in phase with the velocity, they purely inject or dissipate energy, and eq. (3.20) is enough. In a more general case however, phase change and friction could be partially in phase with the position and thus store some potential energy. For example,

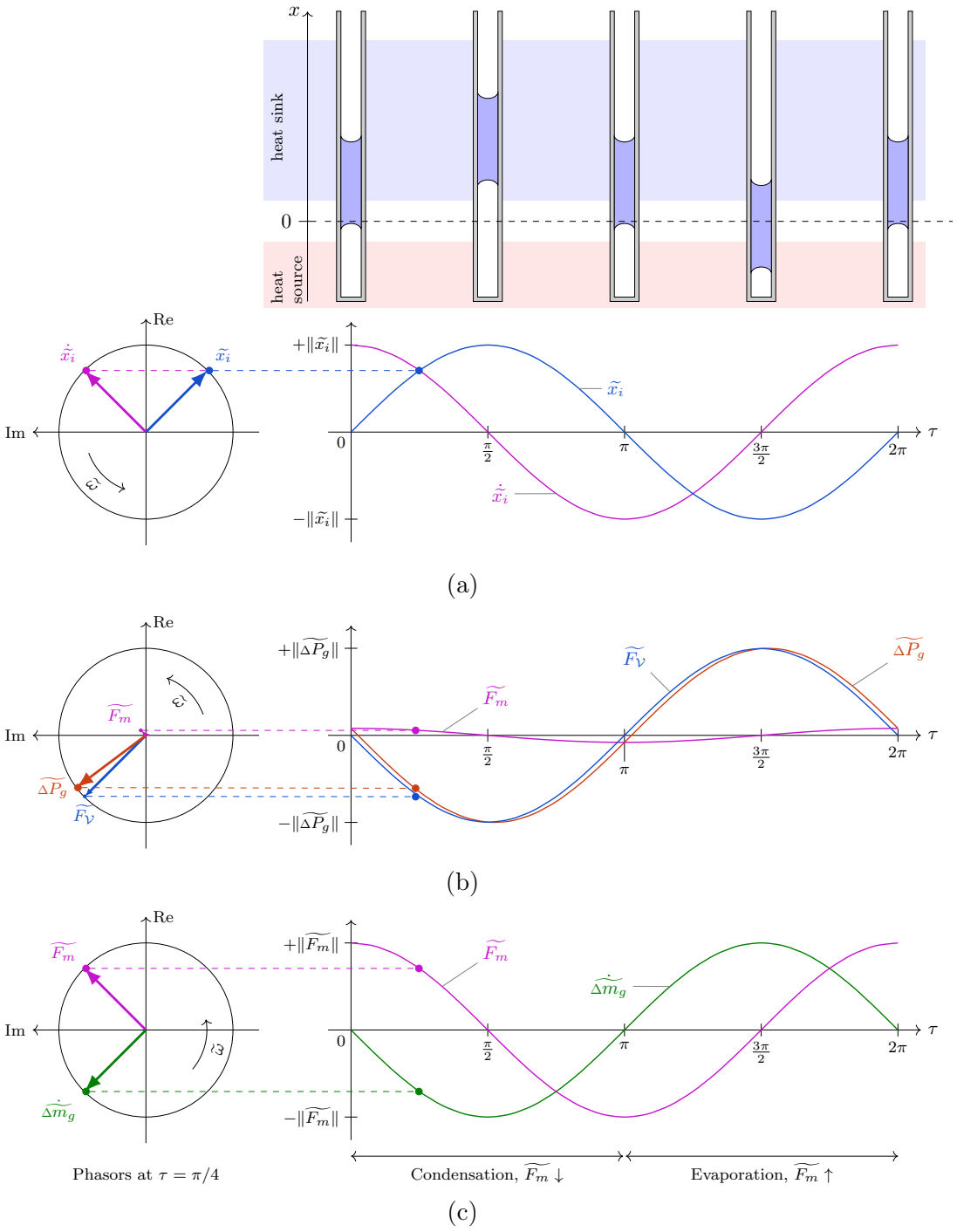

Figure 3.5 The variables evolving over one oscillation period are shown as well as phasor representations at $\tau = \pi/4$ for $\zeta_f = 0.04$ and $\Pi = 1.01$. The interest is in the phasing between variables, so only the sinusoidal part of the solution is shown. (a) Evolution of meniscus position and velocity. (b) Components $\widetilde{\Delta P_g}$, the spring force $\widetilde{F_\mathcal{V}}$, which is opposite to the meniscus position, and the feedback force $\widetilde{F_m}$, which is in phase with the velocity. (c) Evaporation rate, opposite to the meniscus location, which produces the force $\widetilde{F_m}$; it can be seen that $\widetilde{F_m}$ is delayed by a quarter of a period compared to the evaporation rate.

this happens for $\widetilde{F_m}$ when $\widetilde{\sigma}$ and ζ_f are not small and differ significantly from one another (top left and bottom right corners in fig. 3.4); $\widetilde{F_m}$ then contributes to the resonator and affects the frequency (fig. A.2d). Potential energy can also be stored by $\widetilde{F_m}$ when the oscillation amplitude is large enough such that nonlinearities become significant. This can also happen for $\widetilde{F_f}$ when non-Poiseuille friction is taken into account (see section 3.2.3). To take these effects into account, we can split the phase change force $\widetilde{F_m}$ into a component in phase with position $\widetilde{F}_{m,\alpha}$ and a component in phase with velocity $\widetilde{F}_{m,\beta}$ such that $\widetilde{F_m} = \widetilde{F}_{m,\alpha} + \widetilde{F}_{m,\beta}$. The friction force can be split in the same way. The works $\widetilde{W}_{m,\alpha}$ and $\widetilde{W}_{f,\alpha}$ produce no net work on the resonator over a cycle and they conserve energy, so they can be written as potentials $\widetilde{U}_m = -\widetilde{W}_{m,\alpha}$ and $\widetilde{U}_f = -\widetilde{W}_{f,\alpha}$. On the contrary, $\widetilde{W}_{m,\beta}$ and $\widetilde{W}_{f,\beta}$ are purely injecting or dissipating energy. It now makes sense to define a total system energy $\widetilde{E}_{sys}$ which includes the energy of the resonator $\widetilde{E}_r$ plus the potentials $\widetilde{U}_m$ and $\widetilde{U}_f$. A conservation equation

$$\widetilde{E}_{sys}\Big|_{\tau_0}^{\tau_1} = \widetilde{K} + \widetilde{U}_r + \widetilde{U}_m + \widetilde{U}_f \quad \Big|_{\tau_0}^{\tau_1} = \widetilde{W}_{m,\beta} + \widetilde{W}_{f,\beta} \quad \Big|_{\tau_0}^{\tau_1} \tag{3.21}$$

relates the system energy $\widetilde{E}_{sys}$ to the works $\widetilde{W}_{m,\beta}$ and $\widetilde{W}_{f,\beta}$.

3.5 Experimental Validation

In this section we validate experimentally the instability mechanism presented above. In section 3.5.1 we described the setup and the basic behavior we observe. In section 3.5.2 we present an experiment where the startup of the oscillations is triggered. Sections 3.5.3 and 3.5.4 provide results based on this experiment. In section 3.5.3 we consider the early stage of the startup where the motion is sinusoidal and we confirm that the mass of vapor and friction force lead to positive feedback and a damping force, respectively. We also compare the theoretical model to the experiment. In section 3.5.4 we confirm, well beyond the linear regime, that phase change does positive work while friction does negative work and we show that the net work leads to corresponding variations in oscillation amplitude. This confirms that the positive feedback and the damping force are correctly identified.

3.5.1 Experimental Setup and Basic Experiment

We use the experimental setup shown in fig. 3.6, which is inspired by the work of Rao et al. [92]. A glass tube is used as a single-branch PHP, with internal and external diameters of 2.2 and 4.1 mm respectively. The tube is closed at one end by an analog pressure sensor (Omega PX-26-005DV) with a custom preamplifier board providing vapor pressure measurements with a tolerance of ± 0.07 kPa, while the other end is connected to a vacuum

pump system with a PVC tube to control the external pressure, if needed. Motion of the liquid plug is measured by recording the rear meniscus position with a high-speed camera (PCO.1200hs) with a tolerance due to calibration of $\pm 0.016\%$. Acquisition of pressure measurements and synchronization with the meniscus position are made with a Keithley KPCI-3110 data acquisition board. To ensure reliability of the results, the tube is cleaned with an atmospheric corona discharge treatment before every experiment. The tube is heated at the closed end by a heat source, a reservoir filled with glycerin maintained at a temperature T_H. This reservoir consists of a larger tube capped with polydimethylsiloxane (PDMS) plugs at both ends, allowing the test tube to go through (the PDMS plug one on the heat sink side has a length of 5 mm). The temperature T_H is measured by a thermocouple (Omega 5TC-TT-K-30-36) and maintained by a heater (Omega Lux heater CSH-1011001/120 with a controller RKC Instrument REX-C100, limited by a voltage regulator). A pressure relief valve (not shown in the figure) prevents overpressurization of the glycerin. Also, to keep the evaporator temperature uniform, a mixer spins a stir bar in the glycerin. In the experiment, we assume $T_{g,0} = T_H$. The SBPHP tube is cooled on the other side at a temperature T_L (measured by a thermocouple Omega 5TC-TT-K-30-36 and an Agilent 34970A acquisition unit) by a reservoir filled with water circulating from a thermostatic bath (Polyscience refrigerating circulator, 9506A11C). In order to observe self-oscillations below the maximal evaporator temperature T_H allowed by the setup, we had to insert a capillary into the SBPHP tube (Polymicro, external diameter of 350 µm). A long thin film forms along the capillary, which effectively acts as a groove. This thin film can evaporate much faster than the meniscus. We think that it enhances the phase change and effectively reduces the thermal resistance R_{th} in Π, allowing oscillations to occur at a lower evaporator temperature T_H. The small liquid plug between the vapor bubble and the pressure sensor has a constant volume at all times and does not influence the oscillations, acting similarly to a dry closed end.

The first steps of the experiment are carried out as follows. The tube is filled with deionized water. The temperature of the heater is increased progressively while the external pressure is at atmospheric conditions ($\hat{P}_e = P_{atm}$). Close to $T_H = 100\,^{\circ}\mathrm{C}$, a single vapor bubble appears in the heat source section and increases in size until an equilibrium is reached, with the vapor-liquid interface located at the PDMS plug. During the experiments, we found that, from a stable state, increasing the thermal gradient (by increasing T_H) above a threshold leads to self-oscillations. From self-oscillations, decreasing the thermal gradient below the threshold returns the system to a stable state. Likewise, decreasing (increasing) the external pressure $\hat{P}_e$ (with the vacuum pump) leads to self-oscillations (stability). Finally, we were able to qualitatively control R_{th} by controlling the length of the capillary

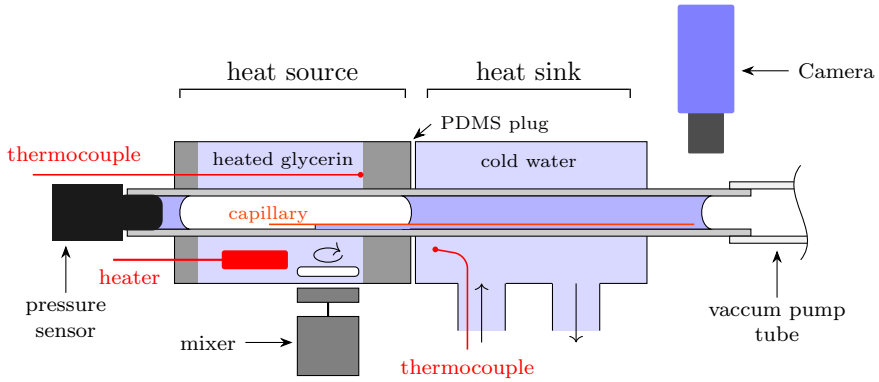

Figure 3.6 Schematic of the instrumented SBPHP experimental setup, not to scale.

exposed in the vapor. From a stable state, pushing the capillary towards the vapor leads to self-oscillations (length of the thin film is increased). On the contrary, pulling the capillary out returns the system to a stable state. These results are in line with the predicted effects of those parameters from the instability number Π.

3.5.2 Startup Experiment - Measurements

To validate the theoretical explanation further, we measured quantities during the startup of the oscillations. Initial conditions for the experiments were $T_H = 103\,°\text{C}$, $T_L = 20\,°\text{C}$, $\hat{P}_e = P_{atm}$, $L_\ell = 10\,\text{cm}$ and $L_{g,0} = 8\,\text{cm}$. The temperature T_H was then increased to $104\,°\text{C}$ which led to startup of the oscillations. Measurements are shown in fig. 3.7. Position and pressure are extracted as discussed above. The mass of vapor can be derived from position and pressure using the ideal gas law (3.3). Simple heat transfer estimations show that the vapor is very much isothermal in our experiment, so T_g is taken as constant. The friction force is derived from the momentum balance (3.1). More details on how quantities are extracted from measurements are provided in appendix A.2.1. At the beginning of the startup (see the close-up in graphs), the dynamics is linear and quantities vary in a sinusoidal fashion. As the oscillation amplitude increases, the dynamics become nonlinear, harmonics in the measurements start to appear, and the system eventually reaches a steady-state regime. We must highlight that the quantities derived from the measurements are independent of our theoretical model. Only the ideal gas law and momentum balance are assumed, which are very reasonable hypotheses. In this experiment, the natural frequency $f_n = \omega_n/(2\pi) = 17.9\,\text{Hz}$. The measured frequency slightly varies in time: It is $18.44\,\text{Hz}$ initially and $17.23\,\text{Hz}$ in the steady-state regime. During the startup, the kinetic Reynolds number averages $\text{Re}_\omega = 133$ (with a minimum of 130 and maximum of 140), so the condition $\text{Re}_\omega \ll 4$ required for Poiseuille flow is not met and we expect

more of an oscillating velocity profile as described in section 3.2.3 and appendix A.1.2 (we will compare friction force expressions in the next section). The friction coefficient (for oscillating friction) is $\zeta_{f\omega} = 0.06$. We can estimate the phase-change coefficient $\widetilde{\sigma}$ from the measurements (see appendix A.2.1 for details) and we get $\widetilde{\sigma} = 0.104 \pm 0.014$. The resulting instability number is $\Pi = \widetilde{\sigma}/\zeta_{f\omega} \approx 1.73$.

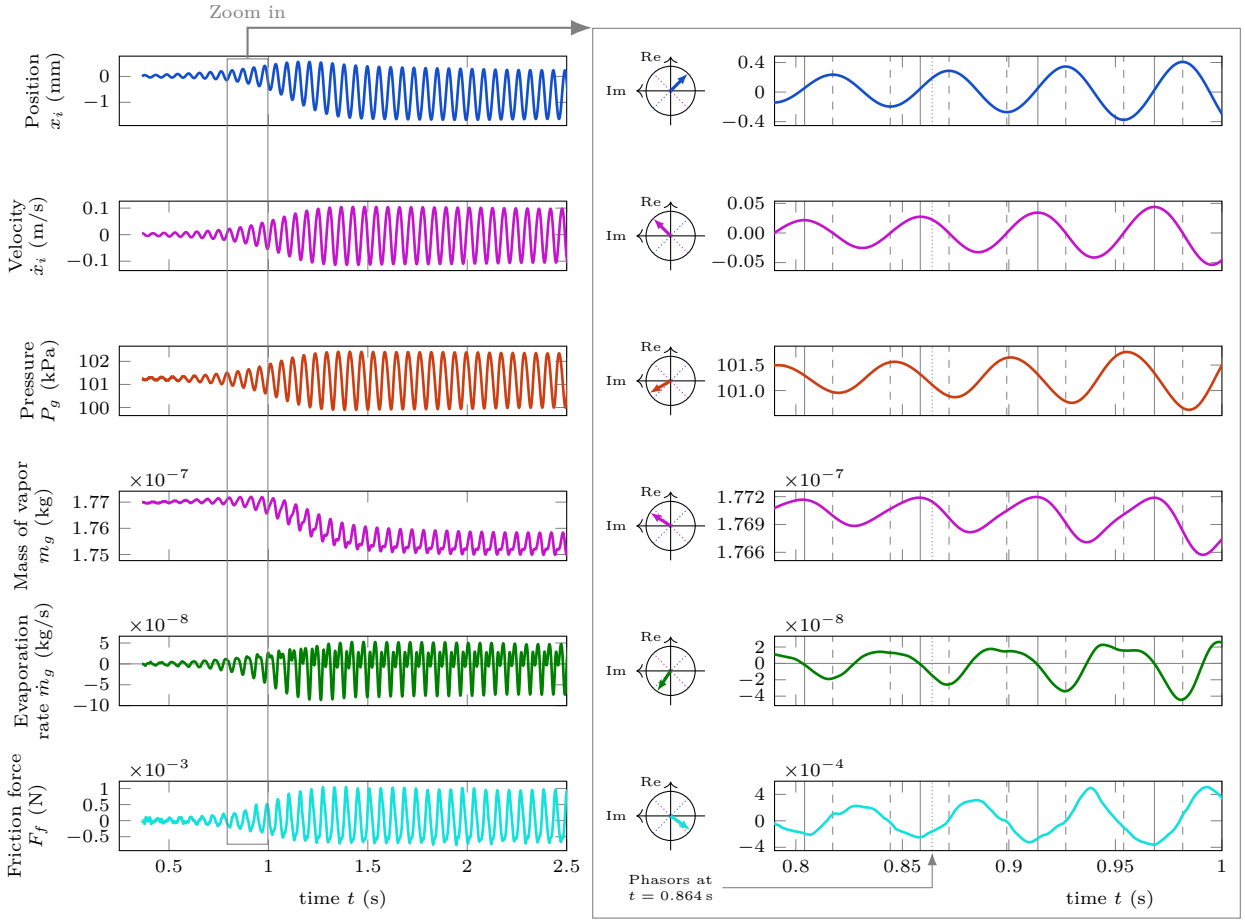

Figure 3.7 Various quantities measured during the startup. The mass of the vapor m_g is in phase with the velocity, so it acts as feedback; the friction force F_f is opposed to the velocity, so it acts as dissipation. The dotted lines in the phasor graphs represent the directions of x_i and $\dot{x}_i$.

3.5.3 Mass of Vapor as Positive Feedback and Friction as Damping Force

From our linearized theoretical model, we predicted (see section 3.4) that the mass of vapor would be mostly in phase with the velocity, leading to a positive feedback force, while the friction would be mostly in opposite phase with velocity, leading to a damping force. In this section we verify if that is indeed what we observe in the experiment. Here we only consider the early stage of the startup, where the motion is mostly sinusoidal, such that we

can use the phase to compare quantities to one another. Experimental measurements and theoretical curves corresponding to the experimental conditions are displayed in fig. 3.8. On the left-hand side , we display the phasors for each quantities in the referential $x_i - \dot{x}_i$ so that we can clearly see their phase (angle) relative to the position x_i and the velocity $\dot{x}_i$.

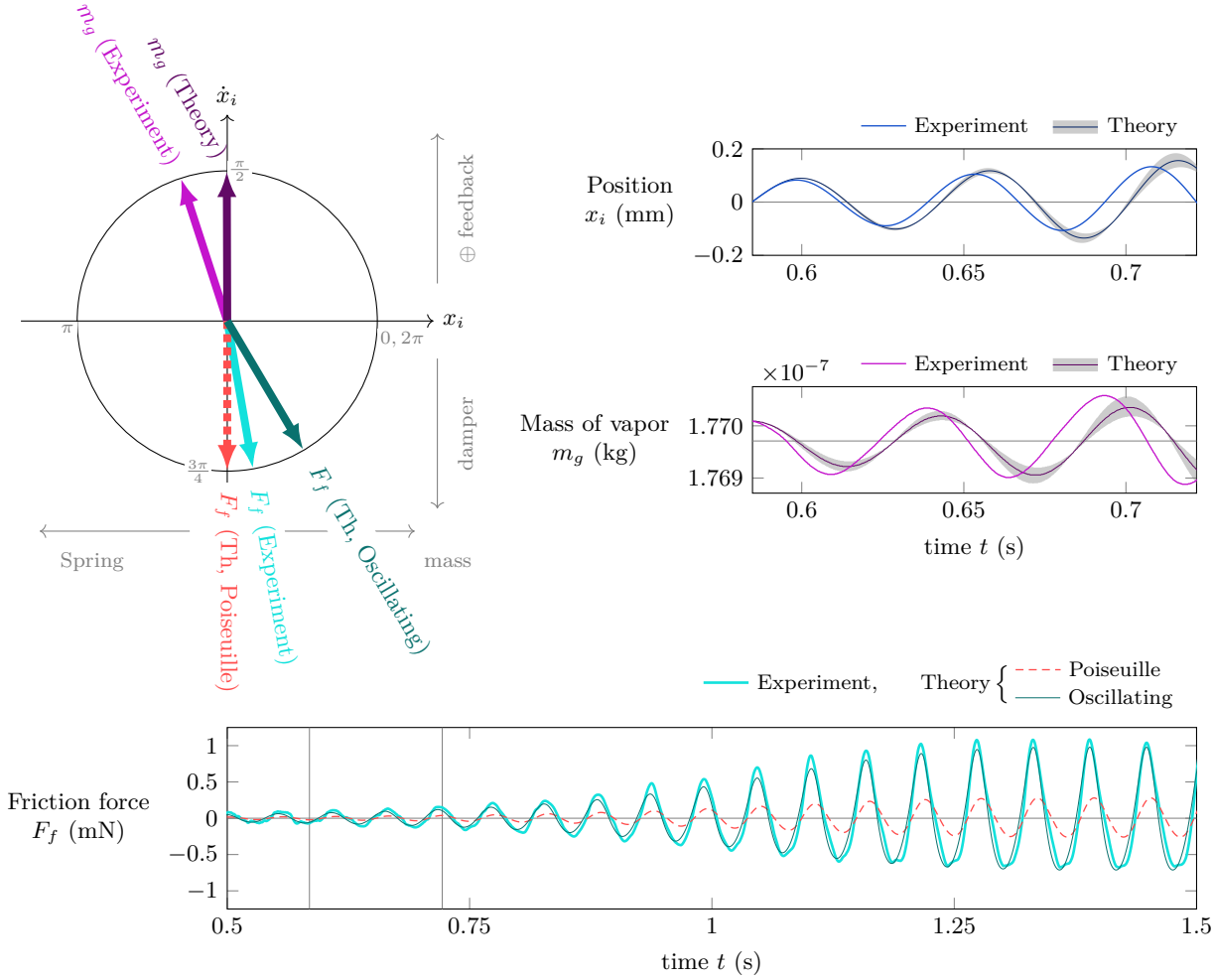

Figure 3.8 Measured and theoretical position x_i and mass of vapor m_g in the early stage of the startup, as well as friction force F_f, all showing close agreement. The theoretical curves displayed are based on $\zeta_{f\omega} = 0.06$ and $\widetilde{\sigma} = 0.104 \pm 0.014$ (the uncertainty on $\widetilde{\sigma}$ is shown by the gray, shaded area). On the left-hand side, each quantity is represented as a phasor in the referential $x_i - \dot{x}_i$ (only the angle is considered here, not the amplitude). The angles vary only slightly over the duration 0.58-0.72 s. The averages are considered in the phasor diagram.

Experimental Curves

In fig. 3.8 the measured mass of vapor follows a sinusoidal curve of growing amplitude and is mostly in phase with the velocity, leading to a positive feedback force. It also leads to a

small spring force. The measured friction also follows a sinusoidal curve growing in time [3]. The measured friction force is mostly in the opposite phase with velocity, so it mostly acts as a damping force, but also has a small inertial component.

From our experimental measurements, we confirmed that the mass of vapor leads to positive feedback and the friction to a damping force, as we expected from our theoretical analysis. Crucially, this conclusion is independent of our theoretical model; the only hypotheses considered are the ideal gas law and the momentum balance on the liquid plug.

Theory Versus Experiment

We now compare the theoretical solution to the experiment (see fig. 3.8). To produce the theoretical curves for position x_i and mass of vapor m_g, we used the general solution eq. (A.33) (but assuming an isothermal vapor) to take into account the effect of oscillating friction. In the friction force graph of fig. 3.8, we included the curves from theoretical friction force, both from Poiseuille and oscillating friction (3.9). In those expressions, we used experimental velocity and pressure in order to verify the friction models alone.

First of all, we see that both theoretical and experimental curves have a sinusoidal profile growing in amplitude at the early stage of the startup. Regarding the frequency, we observe that the theoretical one ($f = 17.18\,\mathrm{Hz}$) is close to but slightly lower than the experimental one (which varies from 18.44 Hz to 17.23 Hz). Concerning the growth rate, we observe that the experimental and theoretical ones are similar and inside the uncertainty bounds. In the phasor diagram, we observe that the theoretical m_g is perfectly in phase with velocity, while the experimental one is mostly in phase with velocity but also has a small component opposite to the position. Now considering friction, the Poiseuille and the oscillating friction amplitudes average, respectively, 27% and 82% respectively of the experimental value in the early stage of the startup (around $t = 0.65\,\mathrm{s}$) and 30% and 93% once the steady state is reached. In terms of phase, the Poiseuille friction is purely dissipative (the angle relative to $-x_i$ equals 0), while the oscillating friction (the relative angle averages 0.17π rad in the early stage and 0.15π rad in the steady state) captures the inertial component observed experimentally (the relative angle averages 0.05π rad in the early stage and 0.07π rad in the steady state).

There is good qualitative and quantitative agreement between theory and experiment with some errors in frequency prediction and in the angle shift for the mass of vapor and friction force. We found that the oscillating friction closely matches the experimental friction force

3. Note that the friction curve is noisy initially (around t=0.4 s) because of the inaccuracy in the motion detection which is significant at very small amplitude (friction force is highly sensitive to noise in the position since it is obtained by the momentum balance, which involves a second derivative $\ddot{x}_i$).

and is more accurate than the Poiseuille model (keeping in mind the case studied was at large Re_ω). Such slight differences are to be expected between theory and experiment: the theoretical phase change model does not include a long thin film as produced by the capillary in the experiment and the oscillating friction model does not include the effects of the menisci on the flow field.

3.5.4 Energy analysis - Phase Change Injects Energy, Friction Dissipates

So far, we only looked at the phase of the forces relative to position and velocity, but their amplitude is also of crucial importance. One may be interested in confirming that the amplitude of the positive feedback force from phase change is greater than the damping force from the liquid viscous friction and that the net resulting force corresponds to the amplitude growth observed experimentally. This would confirm that the phase change is the only feedback, while viscous friction is the only damping force. Such analysis is made complicated by the fact that the forces are not perfectly aligned with velocity and that, as the amplitude grows, harmonics start to appear in the signal due to nonlinearities. Energy analysis deals with those complications in a natural way: one simply has to compute the work over a cycle to obtain the net effect of the related force during an oscillation's cycle. Here we experimentally demonstrate that phase change does positive work while friction does negative work and that the energy E_{sys} (related to the oscillation's amplitude) varies accordingly. We apply energy and work formulations from section 3.4.3 to the startup measurements presented in the section 3.5.2.

We compute the non conservative work per cycle from phase change $W_{m,\beta,\mathrm{cycle}}$ (see fig. 3.9a) which turns out to be positive from the beginning to the end of the measurements. This confirms that phase change injects energy into the system. Likewise, the work done per cycle by friction $W_{f,\beta,\mathrm{cycle}}$ is found to be negative (see fig. 3.9a ; the value $-W_{f,\beta,\mathrm{cycle}}$ is displayed to make amplitude comparison to $W_{m,\beta,\mathrm{cycle}}$ easier). At each cycle, the net work done is $W_{m,\beta,\mathrm{cycle}}+W_{f,\beta,\mathrm{cycle}}$, shown in fig. 3.9b. This net work increases the system energy E_{sys}, as shown in fig. 3.9c, computed from $E_{sys} = K+U_r+U_m+U_f$, eq. (3.21). In fig. 3.9 we can see at the beginning that phase change does more work than friction and the net injected energy is positive, which is why the energy of the system E_{sys} and the oscillation amplitude increase. At 1.19 s, the net injected energy reaches a maximum corresponding to the inflection point in E_{sys}. Beyond 1.5 s, the net injected energy gets close to 0 and the energy of the system saturates.

In this experiment we confirmed that the energy injected into the system (due to positive feedback force) comes from phase change and that the dissipated energy (due to damping

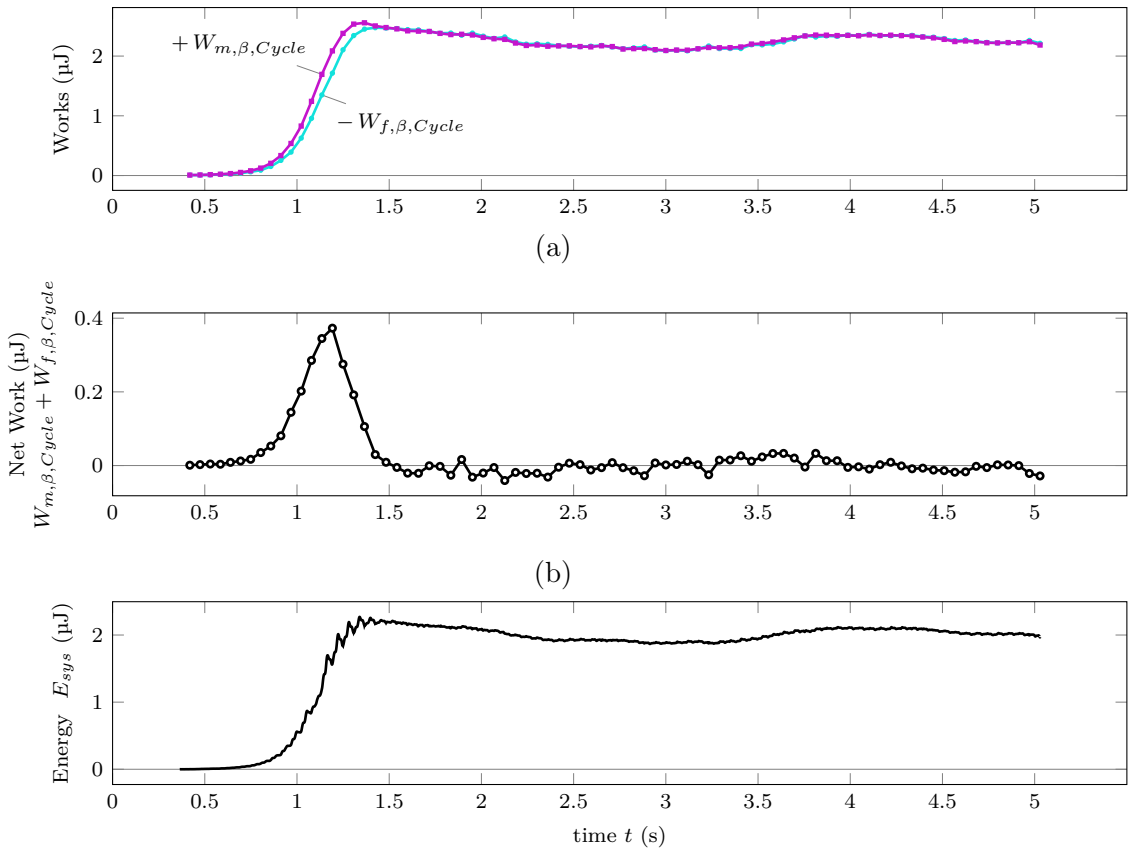

Figure 3.9 Energy analysis of the startup (same experiment as in fig. 3.7). (a) Works from phase change ($W_{m,\beta,\text{cycle}}$) and friction ($W_{f,\beta,\text{cycle}}$) (the value $-W_{f,\beta,\text{cycle}}$ is displayed to make the comparision of the magnitude to $W_{m,\beta,\text{cycle}}$ easier). The work $W_{m,\beta,\text{cycle}}$ is positive, so phase change is injecting energy into the system; the work $W_{f,\beta,\text{cycle}}$ is negative, so friction is dissipating energy from the system into the environment. (b) Net work on the system per cycle: $W_{m,\beta,\text{cycle}}$ is initially greater than $W_{f,\beta,\text{cycle}}$, so the net work on the system is positive; the net work eventually gets close to 0 around 1.5 s. (c) Total energy of the system. The energy of the system (as well as the oscillation amplitude) increases as long as the net work is positive and saturates around 1.5 s.

force) is due to viscous friction. The energy findings further support the argumentation that the self-oscillating behavior appears when the pressure force from phase change overcomes the friction force. It also allows us to understand that the oscillation amplitude varies according to the net injected energy into the system, beyond the linear regime. Once again, this experimental validation is independent of our theoretical model; it only assumes the ideal gas law and the momentum balance equation.

3.6 Perspectives on Related Work

In this section we discuss how our approach compares to the literature and extrapolate from our results to reach more general conclusions about the SBPHP dynamics. We first discuss the resonator representation and then the instability mechanism and finally expand on how a more realistic phase change representation than the one used in our model would influence the dynamics.

3.6.1 The Resonator

The existence of a spring-mass system in the SBPHP has been predicted by other authors [69, 105]. Here we deduced its existence from the model, by linearization. A side benefit of this approach is to clarify the fact that the pressure force can be separated into two components and that it is the change of vapor volume which is responsible for the spring effect. We clarified that this analysis is valid when $\widetilde{\sigma}$ and ζ_f are small. Otherwise, more precise expressions for the angular frequency and the growth rate are available (see A.1.3).

3.6.2 Instability Mechanism

Our analysis made it clear that the oscillations in the SBPHP come from a thermofluidic instability. The SBPHP dynamics however has often been incorrectly described as a forced harmonic oscillator [69, 70]. In a forced system, oscillations always occur (no threshold). Furthermore, the oscillation amplitude depends on the amplitude and frequency of the forcing. In sharp contrast, our results show that the oscillations in the SBPHP are self-driven, under the condition that the instability number is greater than unity (threshold). The frequency of the feedback force is not set externally but depends on the system itself. Furthermore, the final amplitude of such an instability depends on the nonlinearities of the system (the study of which is beyond the scope of this article).

In this paper we provide a conclusive explanation for the instability mechanism based on linear stability analysis, a classical approach for instabilities. We found that the phase change tends to make the system unstable, while the viscous friction (between the liquid and the wall) tends to stabilize it. After a perturbation of the equilibrium, the oscillations grow when the phase-change coefficient $\widetilde{\sigma}$ is greater than the friction coefficient ζ_f. The

instability in the SBPHP was studied before by other researchers, but it had remained not well understood. Das et al. [20] showed numerically that including the phase change in their model allowed self-oscillations to occur. In their model, phase change occurs at the meniscus and on a thin liquid film. Inconveniently, their representation of the liquid film, introduced to predict the phase-change more accurately, made it impossible to obtain continuous linearized equations around the equilibrium. As a consequence, they were unable to apply linear stability analysis. Without analytical results, they were unable to explain how the phase change led to instability. Based on a similar model, Nikolayev [85] studied the instability threshold further, using analytical techniques. He found the thermal gradient of the wall at equilibrium to be a key factor promoting the instability, as we did. However, the model retained the same liquid film representation as that of Das et al. [20], so Nikolayev was still unable to apply linear stability analysis. This complicated the analysis, such that a basic understanding of the instability mechanism remained out of reach. The friction was assumed negligible in the instability analysis. We have shown here that, on the contrary, the friction is essential to the description of the SBPHP instability mechanism, since it is where the dissipation comes from. Also, the analytical results obtained were only approximate and their range of validity was unknown. Besides, no expression for the motion close to the equilibrium (like our linearized solution) was provided.

Finally, we remark that no experimental validation of the instability mechanism has been carried on so far. Our experimental results (section 3.5) are therefore of prime importance. They confirm the understanding of the instability mechanism we reached from the theory and, crucially, do so with very few hypotheses. Only the momentum balance and the perfect gas law are assumed; the experimental analysis does not rely on our simplified model of the phase change. At the beginning of the startup, where the motion is mostly sinusoidal, the mass of vapor was shown to be in phase with the velocity, leading to positive feedback (negative damping) and the friction was shown to be opposite to velocity, leading to a damping force. Well beyond the beginning of the startup, the energy analysis confirmed that the injected energy came from the mass of vapor while the dissipated energy came from the friction. We were able to conclude (beyond the validity of the linearization) that the evolution of the amplitude depends on the net work injected (phase change and friction doing positive and negative work respectively). The steady-state regime was reached when the net injected energy was null. We think that our experimental results definitively settle the question of the instability mechanism and shed some light on the SBPHP physics beyond the startup.

3.6.3 More Realistic Phase Change

The importance of the thin liquid film on phase change in the SBPHP is well known [20, 92, 34] and, consequently, substantial effort has been devoted to modeling it [126, 20, 85]. Such approaches are required to quantitatively predicts the evaporation rate. Here we used a more simplistic approach with the aim of understanding the qualitative role of phase change. We can extrapolate our results to more general phase change, whether it occurs locally, from a liquid film on a plain surface, from a groove, or from other configurations.

In our model, phase change occurs locally at the meniscus and is a function of a thermal resistance R_{th}. This led to a phase change proportional and opposite to the meniscus position, in the linear approximation. We later found that such phase change produces a force in phase with velocity (m_g has a $\pi/2$ delay relative to $\dot{m}_g$ in fig. 3.5), which injects energy into the system. Importantly, this conclusion is more general than local phase change at the meniscus; any phase change in antiphase with position (with a proportionality constant $\widetilde{\sigma}$ as in eq. (3.12b)) will lead to positive feedback. The instability criterion remains $\Pi > 1$ with $\Pi = \widetilde{\sigma}/\zeta_f$. A more general phase change waveform could be partially in antiphase with the position and partially in phase with the velocity. In this case, the resulting mass of vapor m_g would produce a force having both a feedback component which enhances the instability and a spring or inertial component which affects the oscillation frequency. However, for the phase change to make the system unstable, we still have that the component in antiphase with position must be large enough so that it produce a sufficiently large positive feedback force. In addition to the phase, we of course expect the phase change from a liquid film to be significantly greater than the phase change from the meniscus alone, leading to a greater coefficient $\widetilde{\sigma}$ due to an overall lower thermal resistance R_{th} (thin film and spread over a large area). This is what we observed in the experiment: from a stable state, pushing the capillary towards the vapor increased the length of the liquid film and led to self-oscillations (most likely by increasing $\widetilde{\sigma}$).

Our understanding was confirmed by the experiment: although the phase change configuration tested here (capillary inserted in the tube) is relatively complex, the resulting mass of vapor produces the desired positive feedback force which injects energy into the system. The instability mechanism is the same as that predicted from the theory. Finally, it is worth noting that a broader range of configurations (groove, microstructures, etc.) could be imagined to control the phase change (in order to increase the amplitude, enhance the heat transfer, etc.), but it must provide the antiphase evaporation and condensation required for the instability mechanism.

3.7 Conclusion

In this paper we provided a framework to understand and think about the physics in the SBPHP. Careful modeling made it possible to study the SBPHP instability by linear stability analysis, a classical approach for instabilities. An exact solution of the linearized model was obtained, from which a clear understanding of the SBPHP dynamics was derived. Experimental validation confirmed our conclusions.

In accordance with the literature, we found that the pressure variations of the vapor due to a change of volume produce a spring force, which leads to a resonator when coupled with the inertia of the liquid mass, explaining the oscillatory behavior. In the analytical solution, the oscillation amplitude grows as $e^{\widetilde{\alpha}\tau}$, with $\widetilde{\alpha} \approx \widetilde{\sigma} - \zeta_f$, where the coefficient $\widetilde{\sigma}$ comes from phase change and the coefficient ζ_f comes from viscous friction. As expected, viscous friction acts as a damping force and tends to stabilize the oscillations by dissipating the energy of the system. On the other hand, phase change leads to variations of the mass of vapor, which changes the vapor pressure and ultimately produces a positive feedback force (also called negative damping) on the liquid plug, destabilizing the oscillations by injecting energy into the system. We provided an exact instability criterion, based on a dimensionless instability number $\Pi = \widetilde{\sigma}/\zeta_f$. The instability (oscillation's startup) occurs when the phase-change coefficient $\widetilde{\sigma}$ is greater than the friction coefficient ζ_f, when $\Pi > 1$.

This understanding of the instability mechanism was then confirmed experimentally. Crucially, our experimental validation is independent of the theoretical model. In the early stage of the startup, measurements show that the mass of vapor is in phase with velocity, leading to a positive feedback force, while the friction is opposite to velocity, leading to a damping force. By energy analysis, we then showed for the full startup that phase change injects energy into the system while friction dissipates it. We found that the net injected energy led to a corresponding growth (and saturation when reaching steady state) in the system's energy and oscillation amplitude. This confirms that the feedback and damping forces are correctly identified. Beyond the linear regime to which our analytical solution was restricted, the energy analysis of the experimental data suggests that the amplitude is controlled by the net injected energy into the system.

We conclude that this work has provided an experimentally validated explanation for the self-oscillating behavior observed in pulsating heat pipes. At the end of the startup, the oscillation amplitude saturates. This obviously limits the heat transfer capability of the system. Future theoretical work should go beyond the startup and address the final regime of the oscillations. This understanding could lead to a significant increase in the heat transfer performance of pulsating heat pipes and self-oscillating heat engines.

Acknowledgements

We are grateful to Alexandre Juneau-Fecteau and Thomas Skotnicki for discussions. We also acknowledge financial support from the NSERC through the Scholarship and Discovery Programs (Canada) and the ANRT CIFRE Program (France).

CHAPTER 4

WHAT LEADS TO THE STEADY-STATE REGIME

Avant-propos

Auteurs et affiliation:

Albert Tessier-Poirier: étudiant au doctorat à l'Université de Sherbrooke (1,2).

Richard H. Rand: professeur à Cornell University (3,4).

Luc G. Fréchette: professeur à l'Université de Sherbrooke (1,2).

1) Institut Interdisciplinaire d'Innovation Technologique (3IT), Université de Sherbrooke, Sherbrooke, QC, Canada, 2) Laboratoire Nanotechnologies Nanosystèmes (LN2), CNRS UMI-3463, Université de Sherbrooke, Canada, 3) Sibley School of Mechanical and Aerospace Engineering, Cornell University, Ithaca, New York 14853, USA, 4) Department of Mathematics, Cornell University, Ithaca, New York 14853, USA.

Date de soumission: 2020-11-04.

Date d'acceptation: 2021-12-28.

État d'acceptation: version finale publiée.

Revue: Nonlinear Dynamics.

Référence: [114].

Titre français: Ce qui limite l'amplitude des oscillations dans le caloduc pulsé mono-branche.

Titre anglais: What limits the oscillations amplitude in the single-branch pulsating heat pipe.

Contribution au document: J'ai mené et réalisé l'ensemble des travaux expérimentaux et théoriques présentés dans cet article. Les coauteurs ont contribués par des conseils et suggestions lors de la recherche et lors de la rédaction du document.

Résumé français: Dans cet article, nous montrons que l'amplitude des oscillations augmente puis sature durant le démarrage du caloduc pulsé mono-branche (SBPHP) dû à l'interaction entre un mécanisme d'instabilité et un mécanisme limitant, produit par des

nonlinéarités. Le SBPHP est un tube de faible diamètre fermé à une extrémité (qui est chauffée) et ouvert à l'autre extrémité, dans lequel une bulle de vapeur est suivie d'une colonne de liquide. Augmenter la température de la zone chaude au-delà d'un seuil critique mène à des oscillations de la colonne de liquide. L'amplitude des oscillations augmente initialement, puis sature, alors que le système atteint un régime permanent. Pour décrire cette dynamique, nous nous basons sur un modèle théorique connu du SBPHP. Ce modèle est basé sur la somme des forces sur la colonne de liquide et inclut la différence de pression entre la vapeur et l'environnement et la friction visqueuse entre le liquide et les parois. La pression dans la vapeur varie en fonction de la compression/dilatation de la bulle de vapeur, mais aussi en fonction de l'évaporation ou condensation, alors que la colonne de liquide oscille entre la zone chaude et la zone froide. La pression (décrite par la loi des gaz parfaits) et l'évaporation et la condensation (limitées dans les zones chaudes et froides) rendent les équations différentielles du modèle nonlinéaires. En appliquant la réduction par variété centrale, suivie de la réduction sous forme normale, nous trouvons une solution analytique approximative (décrivant la position et la vitesse de la colonne de liquide, en plus de la masse de vapeur, en fonction du temps). La solution analytique décrit bien le démarrage et le régime permanent. À l'aide de notre solution analytique, nous montrons que l'augmentation initiale en amplitude est due au mécanisme d'instabilité (produit par l'interaction entre le changement de phase et la friction visqueuse) alors que la saturation en amplitude est due aux nonlinéarités de pression et de changement de phase, le système approchant un régime permanent correspondant à un cycle limite. Le cycle limite est créé par une bifurcation de Poincaré-Andronov-Hopf. Nous montrons que l'amplitude dans le régime permanent peut être grandement augmentée en augmentant l'instabilité ou en réduisant les nonlinéarités. Cela peut être fait en augmentant le changement de phase ou en réduisant la friction. En conclusion, la dynamique du SBPHP devrait être vue comme la combinaison d'un mécanisme d'instabilité qui tend à faire croître l'amplitude et d'un mécanisme limitant produit par les nonlinéarités, qui limite l'amplitude.

Résumé anglais: In this paper, we show that the oscillations amplitude increases and then saturates during the startup in the Single-Branch Pulsating Heat Pipe (SBPHP) due to the interplay between an instability mechanism and a limiting mechanism produced by nonlinearities. The SBPHP is a small tube closed at one end (which is heated) and open at the other, in which sits a single vapor bubble followed by a liquid plug. Increasing the heater temperature above a critical value leads to oscillations of the liquid plug. The oscillations amplitude initially increases over time and eventually saturates (the system reaches a steady-state). To describe this dynamics, we start from a known theoretical SBPHP model. The model is derived from the momentum balance on the liquid plug

which includes both the pressure difference between the vapor and the environment and the viscous friction between the liquid and the wall. Pressure in the vapor varies due to compression and expansion of the vapor bubble, but also due to evaporation and condensation as the liquid plug oscillates between the heat source and the heat sink. Both the pressure (described by perfect gas law) and the evaporation and condensation (limited in both the heat source and the heat sink) make the differential equations in the model nonlinear. By applying the center manifold reduction technique followed by the normal form reduction technique, we obtain an approximate analytical solution (describing the position and velocity of the liquid plug, and the mass of vapor, as a function of time). The analytical solution describes well the startup and the subsequent steady-state. Using this solution, we show that the initial increase in oscillations amplitude is due to the instability mechanism (produced by the interplay of phase-change and viscous friction) while the following amplitude saturation is due to the pressure and phase-change nonlinearities, as the system reaches a steady-state corresponding to a limit cycle. The limit cycle is created through a Poincaré-Andronov-Hopf bifurcation. We find that one can greatly increase the oscillations amplitude in the steady-state by increasing the equilibrium instability and by decreasing these nonlinearities. This can be done by increasing the phase-change and by decreasing the friction. We conclude that the SBPHP dynamics should be viewed as a combination of an instability mechanism which tends to increase the oscillations amplitude and a limiting mechanism produced by nonlinearities, which limits the amplitude.

Note: pour satisfaire aux exigences de l'Université de Sherbrooke, la version de l'article présentée dans cette thèse diffère de la version officielle.

4.1 Introduction

In fluid dynamics, numerous interesting flows develop from instabilities such as viscous fingering (Saffman-Taylor instability [100, 45]), the transition to turbulence of the flow in a pipe [97, 28], the vortices arising from the flow within two rotating cylinders (Taylor-Couette flow [110]) and the convection cells developing in a fluid heated from beneath (Rayleigh-Bénard instability [11, 12, 96]). Some instabilities give rise to self-oscillations, where the periodicity is generated not externally but from the phenomenon itself and where the oscillations are sustained over time by a positive feedback mechanism [52]. This is the case for the self-oscillations of an aeroelastic structure known as flutter [115, 116, 2] and the thermoacoustic self-oscillations of the Rijke tube [98, 94, 95], for example. One such instability giving rise to self-oscillations occur in devices called Pulsating Heat Pipes (PHP). The heat pipe is a popular cooling solution (for electronic devices for example) that uses evaporation and condensation to transfer heat very effectively [30]. The pulsat-

ing heat pipe (PHP) is a special type of heat pipe, made of a meandering tube in which multiple vapor bubbles and liquid plugs move, effectively transferring heat from the heat source to the colder side [3, 30]. Yet, the dynamics inside the PHP is not well understood, which makes it difficult to improve performance and reliability. As a first step towards a better understanding, researchers have studied a simpler device, the Single-Branch Pulsating Heat Pipe (SBPHP). The SBPHP is a straight tube closed at one end and open at the other which is filled with a liquid (fig. 4.1). The closed-end is heated and a vapor bubble eventually forms. The system reaches an equilibrium, with a single vapor bubble, followed by a single liquid plug and then air, all standing still. From this equilibrium state, increasing the temperature of the heater above a threshold leads to oscillations of the liquid plug, which can be self-sustained indefinitely.

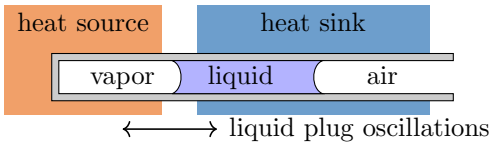

Figure 4.1 Schematic of a Single-Branch Pulsating Heat Pipe (SBPHP); the liquid plug may oscillate indefinitely under appropriate conditions.

In this paper, we focus on the SBPHP dynamics only, as opposed to the PHP with multiple branches, vapor bubbles and liquid plugs, which we will refer to as a multi-branch pulsating heat pipe (MBPHP). Although the research on SBPHP was initially justified as a first step toward a better understanding of MBPHP, SBPHP are now considered as interesting for applications in their own rights. First, they could be used as cooling devices themselves, with little modifications (e.g. in a closed U-shaped configuration [128], where a vapor bubble is followed by a liquid plug, followed by a second vapor bubble). They could also be used as micro-pumps [26]. Finally, they are studied as energy harvesting devices, to convert waste heat into electricity, in a device called a Self-Oscillating Fluidic Heat Engine (SOFHE) [78]. SOFHE devices could be used to power wireless sensors, which are expected to be more common in the future with the advancement of the Internet of Things paradigm [108, 109].

To this day, developing a basic understanding of the SBPHP dynamics is the subject of ongoing research. One may ask: why does the liquid plug exhibit an oscillatory behavior? Das et al. [20] answered that question by considering a simple model, assuming no phase-change. They found that the vapor in the SBPHP acts as a spring: compressing or expanding the vapor leads to a force (approximately) proportional and opposite to the displacement. This spring, coupled with the inertia of the liquid plug, leads to a spring-mass

system (also called resonator) which is why oscillations are possible in the SBPHP. Due to dissipation, from the viscous friction between the liquid and the wall, the oscillations should decay after a small perturbation of the equilibrium. However, experiments show that, by increasing the temperature of the heat source, it is possible to bring the equilibrium to an unstable state where oscillations spontaneously appear and grow over time (see fig. 4.2a). One may then ask: what explains this oscillation startup? An important step was made by Das et al. [20], who showed numerically that including the phase-change led to sustained oscillations. Based on the same model, Nikolayev [85] studied the oscillation startup analytically. He identified the temperature gradient at the equilibrium as a key parameter. Later on, Tessier-Poirier et al. [112] showed, both theoretically and experimentally, that the instability mechanism is due to the interplay between the phase-change and the friction. The evaporation-condensation leads to a change of pressure which acts as a positive feedback (also called negative damping, because it is opposed to the friction). When the positive feedback is greater than the friction, a perturbation of the equilibrium leads to oscillations growing exponentially, in the linear approximation. The instability criterion is expressed by an instability number Π (unstable when $\Pi > 1$) analogous to other instability numbers such as the Rayleigh or Taylor numbers for the Rayleigh-Bénard and Taylor-Couette instabilities, respectively. Although we focus on the SBPHP here, we note that Jun and Kim [55] found experimental evidence for such an instability mechanism in the MBPHP.

In contrast to the linearized model, where the oscillations amplitude increases exponentially forever, we observe experimentally that the oscillations amplitude eventually saturates (fig. 4.2a). At that point, the SBPHP reaches a steady-state which can be maintained indefinitely. One may then ask: what limits the oscillations amplitude? In other words, we would like to know what defines the steady-state oscillating regime and how we can control it. This question has received little attention so far [127]. Both theoretically and experimentally, the oscillations amplitude is usually noticed but not explained. This is partially due to the strong tendency to focus mainly on the heat transfer capabilities, since the PHP is usually considered for cooling applications. Of course, in PHP, the heat transfer capabilities very much depend on whether there are oscillations or not, and on their amplitude and frequency (see [56]). The performance of energy harvesting applications (SOFHE) also depends on the oscillations amplitude and the frequency (there is no power output in the absence of oscillations). Understanding why there is a steady-state and how the oscillations amplitude and frequency in the steady-state can be controlled is therefore of prime importance to increase the performance for cooling and for energy harvesting.

Some studies have evaluated the effect of parameters on the oscillations amplitude. Das et al. [20] found experimentally that increasing the temperature of the heat source led to an increase in amplitude. They also found by numerical simulations that decreasing the thermal resistance associated with the phase-change led to an increase in amplitude. Spinato et al. [105] studied a MBPHP where the power input of the heater was controlled. Increasing it led to an increase in the oscillations amplitude. However, although the effect of parameters is interesting, it does not constitute an explanation of the oscillating steady-state. We would benefit from a theoretical framework that explains the mechanisms leading to the steady-state, so that we can better control it. Such theoretical framework would be helpful to guide the design of cooling, pumping and energy harvesting devices based on the operating principle of PHP.

In this paper, we address the question of what limits the oscillations amplitude, using analytical and numerical nonlinear dynamics techniques. Some insight on the question can be gained by considering a phase-space representation: the state of the system is given by a point moving in space over time, with the position and velocity of the liquid-vapor meniscus as well as the mass of vapor as coordinates. We can see from experimental data (fig. 4.2b) that the system, starting from the initial state, spirals toward a single closed loop in phase-space. This corresponds to what is known in nonlinear dynamics as a stable (meaning attractive) limit cycle [1]. The dynamics on the limit cycle is periodic and corresponds to the oscillating steady-state regime. The geometry of the limit cycle dictates the oscillating amplitude. Here, we use a nonlinear theoretical model of the SBPHP to explain why such limit cycle exists and how one can control its size. We introduce the model in section 4.2. We simulate numerically the startup and show that the system approaches a steady-state corresponding to a limit cycle, just like in the experiment. We show that the saturation of the amplitude and the limit cycle are caused by the nonlinearities. We then obtain an approximate analytical solution of the model's nonlinear dynamics using center manifold reduction and normal form techniques (section 4.3.1). Using those analytical results, we show how the oscillations amplitude grows over time during the startup due to the instability mechanism (linear part) and then, how the instability mechanism is counterbalanced by the limiting mechanism (nonlinear part) such that the amplitude saturates and the system reaches an oscillating steady-state corresponding to a limit cycle (section 4.3.2-4.3.3). We prove that both the pressure and the phase-change nonlinearities included in the model are limiting mechanisms, meaning that they limit the

1. Experimental measurements over a longer time span show slight fluctuations of the limit cycle, but those occur on a longer time scale and are likely due to undesirable fluctuations of the external parameters such as the heat source temperature.

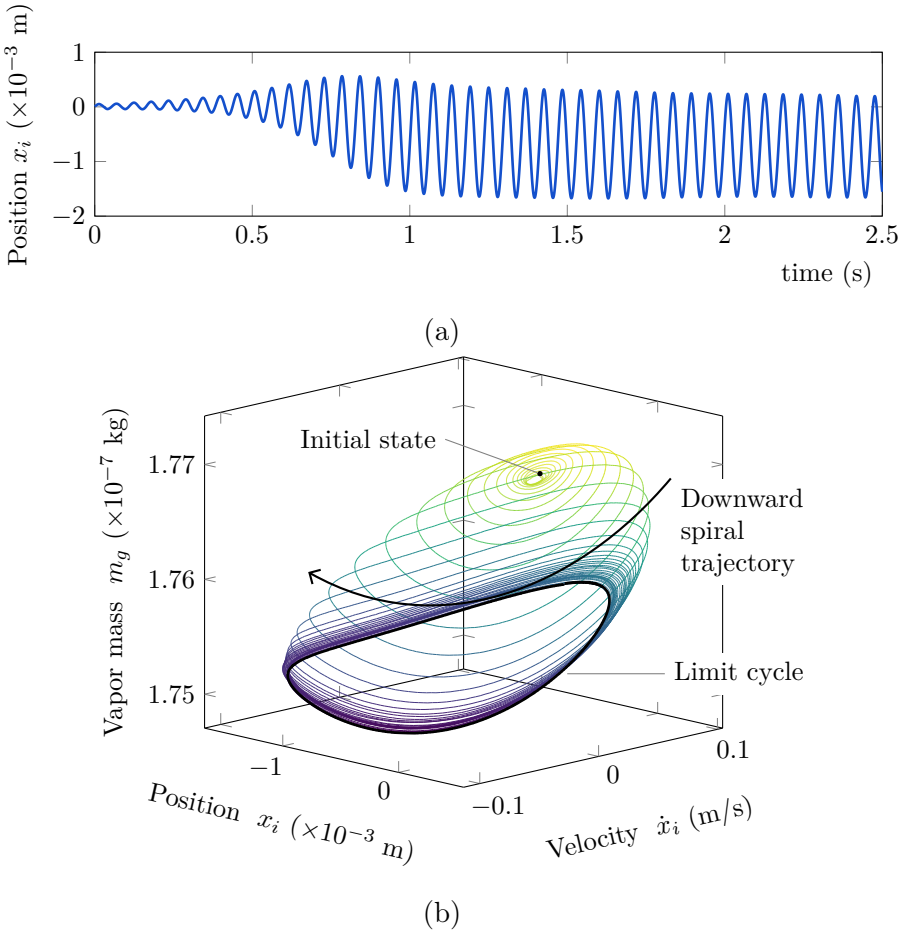

Figure 4.2 Experimental data recorded during the startup of an SBPHP (data available in supplementary materials, data from [112]); (a) position of the liquid-vapor meniscus relative to the equilibrium, as a function of time, (b) state of the system evolving over time in phase-space with the position of the meniscus, velocity of the meniscus and mass of vapor as coordinates, the system approaching a limit cycle.

oscillation amplitude and are responsible for the existence of the limit cycle / steady-state (section 4.3.3). The limit cycle is created through a Poincaré-Andronov-Hopf bifurcation. Finally, based on our analytical solution, we discuss how one can increase the oscillation amplitude in the steady-state by controlling the instability mechanism and the limiting mechanism (section 4.3.3). More specifically, we show how those mechanisms depend on the phase-change and friction. This article extends and complements previous works on the subject [113, 111] and provides a rigorous framework for devices based on the PHP principle.

4.2 Model and Numerical Results

In this section, we first describe the theoretical model (section 4.2.1). We then provide its linear solution, useful to predict the startup, and introduce two key parameters: the bifurcation parameter δ and the instability number Π (section 4.2.2). In section 4.2.3, we introduce two parameters, c_P and c_T, to include or exclude the pressure and the phase-change nonlinearities, respectively. Finally, we carry out numerical simulations of the nonlinear differential equations (section 4.2.4). Contrary to the linear case, we do observe saturation of the amplitude in the nonlinear case, as the system reaches an oscillating steady-state regime. The effects of nonlinearities on the steady-state regime are explored further.

4.2.1 Modeling

To describe the oscillations, we use a known model of the SBPHP [112] with some simplifications, resulting in the system of equations (4.7). Here we provide an overview of the derivation of this system of differential equations. The momentum balance is applied on the liquid plug as

$$m_\ell \ddot{x}_i = \left(P_g - \hat{P}_e\right) A + F_f, \tag{4.1}$$

with x_i the meniscus position (as defined in fig. 4.3a) and $\ddot{x}_i$ the liquid plug acceleration (with m_ℓ the mass of liquid). The forces are due to the gas pressure of the vapor P_g, the external pressure P_e, gravity if the tube is tilted and the friction force from the walls, F_f, with $F_f \propto \dot{x}_i$. In eq. (4.1), the external pressure and the gravity are combined in a single term, the augmented pressure $\hat{P}_e$, with $\hat{P}_e = P_e + \rho_\ell\, g\, L_\ell \sin\theta$, where ρ_ℓ is the density of liquid, g the gravitational acceleration, L_ℓ the length of liquid and θ is the angle of the tube relative to the horizontal. The vapor's pressure can be described by the perfect gas law: $P_g = (m_g R_g T_g) \,/\, (x_i + L_{g,0})\, A$, where m_g is the mass of vapor, R_g is the gas constant for vapor, T_g is the vapor temperature (which we will assume constant [112]), $L_{g,0}$ is the length of vapor at equilibrium (see fig. 4.3a) and A is the tube's inner cross-section area.

The mass of vapor m_g varies through phase-change (evaporation and condensation). The phase-change in the PHP is quite complex. In addition to the phase-change at the meniscus, significative phase-change may come from a thin liquid film laid on the walls by the meniscus ([92, 34]). The thickness of the liquid film may vary spatially. Both the thickness and the length of the liquid film also vary over time. Moreover, the geometry of the liquid film, the phase-change and the liquid plug dynamics are all dynamically coupled. To model the phase-change, approaches of varying complexities have been considered, ranging from local phase-change at the meniscus (assuming a short liquid film) [112], to liquid film with a fixed thickness fully covering the internal walls [103], to liquid film of fixed

thickness and varying length [20], to liquid film with varying thickness and varying length [93, 22, 83, 7, 99] to full on CFD approaches [67, 118, 38] (see [86] for a comprehensive litterature review). The choice of the modeling approach is a trade-off between simplicity (better suited for analytical approaches and to build intuitions about the physics, allow faster simulations) and accuracy (more detailed physics, higher quantitative prediction power). From an engineering point of view, one might be interested into controlling the phase-change to improve the performance. Beyond the plain surface usually considered in PHP, the tube can be engineered in order to enhance the phase-change. Various approaches have been used including sintered powder wick [129], hydrophilic and hydrophobic inner surfaces [43, 42], corrugations [119], microgrooves [90], reentrant cavities [62] and the addition of a small glass fiber as a wicking structure [112]. Thus, there is not only one phase-change physics to model but multiple ones, depending on the chosen design. The modeling approaches mentioned above for plain surfaces do not directly apply to the engineered tubes. In fact, no single model of the phase-change would be suited for all possible cases. Here, our goal is to reach a qualitative understanding of the steady-state regime. Thus, we choose a simple phase-change model, corresponding to local phase-change at the meniscus, proportional to the temperature difference between the wall and meniscus and with a continuous axial wall temperature profile (see [112] for a schematic of the thermal resistance model). Once linearized, this phase-change produces a force in phase with velocity [112] and thus constitutes the simplest phase-change possible to produce a positive feedback force and the oscillations startup. Keeping in mind that one can control the phase-change with engineered tubes, this phase-change profile could be used as a point of reference, to which various engineering strategies could be compared. In our model, the phase-change rate is given by:

$$\dot{m}_g = \frac{T_w(x_i) - T_{g,sat}}{H_v R_{th}}. \tag{4.2}$$

In this expression, $T_w(x_i)$ is the wall temperature at the meniscus position, $T_{g,sat}$ is the temperature of the meniscus (at saturation), H_v is the enthalpy of vaporization and R_{th} is the phase-change thermal resistance. We assume the wall temperature $T_w(x)$ to be set by the thermal boundary conditions of the heat source and heat sink, such that it follows an arctangent profile (fig. 4.3a).

In this system, there is only one equilibrium, corresponding to a static liquid plug and constant mass of vapor. In the momentum balance, having $\ddot{x}_i = 0$ leads to $P_g - \hat{P}_e = 0$ ($F_f = 0$ since $\dot{x}_i = 0$) so $P_g = P_{g,0} = \hat{P}_e$ (note that the 0 subscript refers to values at equilibrium). Having no net phase-change, $\dot{m}_g = 0$, so $T_w(x_i) = T_{g,sat}$. This last relation

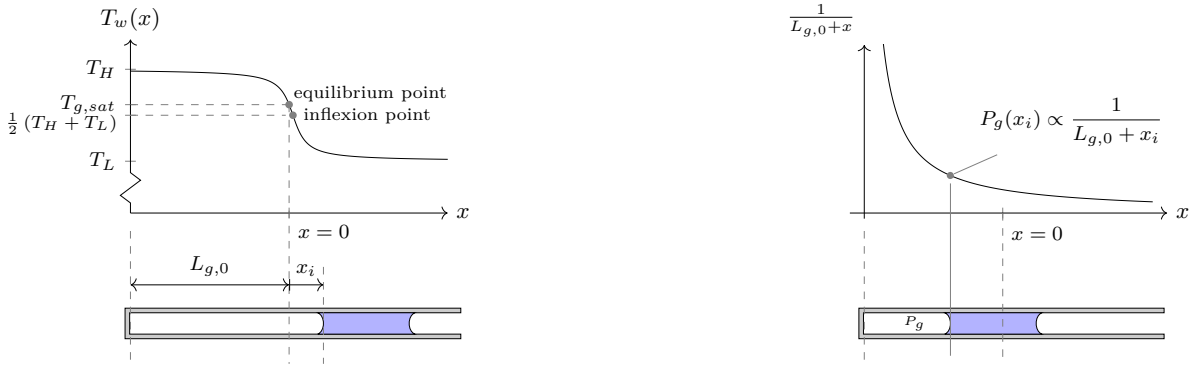

(a) (b)

Figure 4.3 Nonlinearities in the system. (a) Nonlinear wall temperature profile along the x axis, the x_i location is defined as the meniscus position relative to the equilibrium point, which corresponds to $T_w = T_{g,sat}$: This nonlinear temperature profile leads to a nonlinear phase-change ($\dot{m}_g$ being a function of T_w, eq. (4.2)); figure adapted from [112]. (b) Pressure of the gas (P_g) is nonlinear and proportional to $1/(L_{g,0} + x_i)$.

defines the physical location of the meniscus at equilibrium. The distance along the tube from the closed end to that location is defined as $L_{g,0}$. The meniscus position x_i is defined relative to that equilibrium location. At equilibrium, the mass of vapor is defined as $m_{g,0}$ and the meniscus position is $x_i = 0$.

Dimensionless Variables

We now replace variables by their perturbations relative to the equilibrium and make them dimensionless. We get

$$q_1 \equiv \frac{x_i}{L_{g,0}} \,, \qquad q_2 \equiv \frac{d\,q_1}{d\,\tau} = \left(\frac{1}{\omega_n\, L_{g,0}}\right) \frac{d\,x_i}{d\,t} \qquad \text{and} \qquad q_3 \equiv \frac{m_g - m_{g,0}}{m_{g,0}} \,, \tag{4.3}$$

with the new variables q_1, q_2 and q_3 being the dimensionless perturbations relative to the equilibrium for the position, velocity and mass of vapor respectively [2]. The introduction of the variable q_2 for the velocity might seems unnecessary, but it will be needed for the phase-space representation, as seen later on. We also introduce a dimensionless time $\tau = \omega_n\, t$, with $\omega_n = \sqrt{P_{g,0}/\left(\rho_\ell L_\ell L_{g,0}\right)}$ being the natural angular frequency. Time derivatives (e.g. $\dot{q}_1$) of dimensionless variables are made with respect to the dimensionless time τ.

2. We may omit to specify the dimensionless phase-space variables and parameters as *dimensionless* in the following, for conciseness.

Dimensionless Momentum Balance and Pressure Nonlinearity

We substitute the dimensionless variables in the momentum balance eq. (4.1) and obtain $\dot{q}_2 = \widetilde{\Delta P_g} + \widetilde{F_f}$, where $\dot{q}_2$ is the dimensionless acceleration, $\widetilde{\Delta P_g}$ the dimensionless pressure difference and $\widetilde{F_f}$ the dimensionless friction. We have $\widetilde{F_f} = F_f/(m_\ell L_{g,0}{\omega_n}^2)$ which simplifies to $\widetilde{F_f} = F_f/(P_{g,0}A)$ after substitution of ω_n. For Poiseuille flows, the friction force is proportional to the velocity and we have $\widetilde{F_f} = -2\zeta_f q_2$, where ζ_f is the dimensionless friction coefficient defined later on. Similarly, the dimensionless pressure difference given by $\widetilde{\Delta P_g} = (P_g - \hat{P}_e)A/(m_\ell L_{g,0}{\omega_n}^2)$ simplifies to $\widetilde{\Delta P_g} = (P_g - \hat{P}_e)/P_{g,0}$. Using $\hat{P}_e = P_{g,0}$, the ideal gas law and introducing the new variables, we obtain [3]

$$\widetilde{\Delta P_g} = \underbrace{-\left(\frac{1}{1+q_1}\right) q_1}_{\widetilde{F_\mathcal{V}}} + \underbrace{\left(\frac{1}{1+q_1}\right) q_3}_{\widetilde{F_m}}. \tag{4.4}$$

Substitution in the momentum balance gives

$$\dot{q}_2 = \widetilde{\Delta P_g} + \widetilde{F_f} = \underbrace{-\left(\frac{1}{1+q_1}\right) q_1}_{\widetilde{F_\mathcal{V}}} + \underbrace{\left(\frac{1}{1+q_1}\right) q_3}_{\widetilde{F_m}} \underbrace{-2\,\zeta_f\; q_2}_{\widetilde{F_f}}, \tag{4.5}$$

where $\widetilde{F_\mathcal{V}}$ is a dimensionless pressure force from compression and expansion of the vapor bubble (corresponding to a displacement q_1). $\widetilde{F_m}$ is a dimensionless pressure force due to a change of mass in the vapor bubble (q_3). As discussed in section 4.1, Tessier-Poirier et al. [112] found that $\widetilde{F_\mathcal{V}}$ is a nonlinear spring while $\widetilde{F_m}$ acts as a positive feedback, in opposition to the damping force, $\widetilde{F_f}$. Note that the pressure components $\widetilde{F_\mathcal{V}}$ and $\widetilde{F_m}$ are nonlinear (due to the coefficient $1/(1+q_1)$) because the ideal gas law is nonlinear. We call this the pressure nonlinearity. As displayed in fig. 4.3b, the pressure increases nonlinearly as the meniscus moves toward the closed end and ultimately prevents the meniscus from going beyond the closed end.

Dimensionless Phase-Change Rate and Corresponding Nonlinearity

We now substitute dimensionless variables in the phase-change equation eq. (4.2) with T_w given by an arctangent profile and obtain [4]

$$\dot{q}_3 = T_{HL}\, \arctan\left[-\left(\frac{2\sigma}{T_{HL}\cos^2[\psi/2]}\right) q_1 - \tan\left[\frac{\psi}{2}\right]\right] + \frac{\psi}{2}\, T_{HL}. \tag{4.6}$$

3. We assumed T_g constant, see [112] for the general case.

4. This equation was first obtained in Tessier-Poirier et al. [112]. Here, we made some change of variables to reach a more useful form (see App. B.2.1).

where $\dot{q}_3$ is the dimensionless evaporation rate described as a function of the position q_1 and where σ, T_{HL} and ψ are dimensionless parameters defined later on. The arctangent wall temperature profile leads to a nonlinear phase-change, saturating in both the heat source and the heat sink. We call this the phase-change nonlinearity. By controlling the parameters, the profile can look mostly linear (large T_{HL}) or more like constant evaporation in the heat source and constant condensation in the heat sink with a sharp transition in between (large σ and low T_{HL}).

System of Equations

We now combine the dimensionless momentum balance and evaporation rate in a set of first order differential equations , given by

$$\dot{q}_1 = q_2, \tag{4.7a}$$

$$\dot{q}_2 = \underbrace{-\left(\frac{1}{1+q_1}\right) q_1}_{\widetilde{F_{\mathcal{V}}}} + \underbrace{\left(\frac{1}{1+q_1}\right) q_3}_{\widetilde{F_m}} \underbrace{-2\,\zeta_f\; q_2}_{\widetilde{F_f}}, \tag{4.7b}$$

$$\dot{q}_3 = T_{HL}\, \arctan\left[-\left(\frac{2\sigma}{T_{HL}\cos^2[\psi/2]}\right) q_1 - \tan\left[\frac{\psi}{2}\right]\right] + \frac{\psi}{2}\, T_{HL}. \tag{4.7c}$$

This system has only one equilibrium ($\dot{q}_1 = \dot{q}_2 = \dot{q}_3 = 0$) at $q_1 = q_2 = q_3 = 0$. The dimensionless parameters are given by

$$\sigma = \frac{L_{g,0}}{2m_{g,0}\omega_n H_v R_{th}} \left(\frac{-dT_w}{dx}\right)_{x=0}, \tag{4.8a}$$

$$\zeta_f = \frac{8\pi\mu L_\ell}{2m_\ell \omega_n}, \tag{4.8b}$$

$$\psi = \pi\ \left(\frac{1+T_L/T_H}{1-T_L/T_H} - \frac{2\,T_{g,sat,0}/T_H}{1-T_L/T_H}\right), \tag{4.8c}$$

$$T_{HL} = \frac{T_H - T_L}{\pi m_{g,0}\omega_n H_v R_{th}}. \tag{4.8d}$$

The parameters σ and ζ_f are the phase-change coefficient and the friction coefficient, respectively. Note that dT_w/dx is the axial wall thermal gradient and μ is the dynamic viscosity. The parameter T_{HL} is simply the dimensionless temperature difference between the heat source (at temperature T_H) and the heat sink (at temperature T_L). The impact of T_{HL} on the dynamics is to limit the phase-change in both the heat source and the heat

sink, so we call it the phase-change limit. The fact that the equilibrium point does not necessarily coincide with the inflexion point of the wall temperature profile (see fig. 4.3a) is taken into account by the parameter ψ. The parameter ψ is an indirect measure of the distance between these two points [5]. The equilibrium is located where $T_w(x) = T_{g,sat,0}$ while the inflexion point is located where $T_w(x) = \frac{1}{2}(T_H + T_L)$ (see fig. 4.3a). When the equilibrium is exactly at the inflexion point, $T_{g,sat,0} = \frac{1}{2}(T_H + T_L)$, we have $\psi = 0$. The deviation ψ ranges between $-\pi$ (for $T_{g,sat,0} = T_H$, the equilibrium is far into the heat source) and $+\pi$ (for $T_{g,sat,0} = T_L$, the equilibrium is far into the heat sink). The ψ expression is shown graphically in fig. B.1. Finally, note that we dropped the tildes used by Tessier-Poirier et al. [112] to highlight dimensionless quantities.

4.2.2 Linear Solution

As we will show later on, it turns out that the saturation of the amplitude is due to nonlinearities. To highlight this, we show in this section that the oscillations amplitude from linear equations does not saturate and we will show later on that the oscillations amplitude from nonlinear equations does. The linear analysis provided here is based on Tessier-Poirier et al. [112]. Linearization of eq. (4.7) around the equilibrium $q_1 = q_2 = q_3 = 0$ gives

$$\dot{q}_1 = q_2, \tag{4.9a}$$

$$\dot{q}_2 = -q_1 + q_3 - 2\,\zeta_f\; q_2, \tag{4.9b}$$

$$\dot{q}_3 = -2\,\sigma\, q_1. \tag{4.9c}$$

In the following discussion, we will assume small σ and ζ_f (but exact expressions are also available [112]). Equations (4.9) have the following solution [112, Eq.(A30a)]

$$q_n = a_{n,1}\, e^{\lambda_1 \tau} + a_{n,2}\, e^{\delta\tau} \sin\left(\omega\tau + \varphi_n\right), \tag{4.10}$$

with $n = 1, 2, 3$ and $a_{n,1}$, $a_{n,2}$ and φ_n being constants fixed by initial conditions.

5. Tessier-Poirier et al. [112] used a parameter $\widetilde{C_{th}}$. Here, we use ψ instead, based on the relation $\psi = 2\widetilde{C_{th}}/T_{HL}$. We use ψ because $\widetilde{C_{th}}$ only appears in the ratio $2\widetilde{C_{th}}/T_{HL}$ in the normal form solution. Also ψ has some nice properties such as being bounded between $-\pi$ and $+\pi$ and being a function of only T_H, T_L and $T_{g,sat,0}$. See App. B.2 for details.

We have $\lambda_1 = -2\sigma$, so the first exponential in eq. (4.10) vanishes over time. The parameter ω is the dimensionless angular frequency, given by $\omega = 1$. The parameter δ is the dimensionless growth rate (also called bifurcation parameter later on) given by

$$\delta \equiv \sigma - \zeta_f. \tag{4.11}$$

After a small perturbation of the equilibrium, the oscillations grow (startup) when $\delta > 0$, when the phase-change coefficient σ is greater than the friction coefficient ζ_f. Instead of δ, we can also use the ratio σ/ζ_f as an instability criterion, which leads to a simpler expression. We define

$$\Pi \equiv \frac{\sigma}{\zeta_f} = \frac{\rho_\ell \, R_g \, T_{g,0} \, \left|T'_{w,0}\right|}{8\pi \, \mu \, H_v R_{th} \, \hat{P}_e}, \tag{4.12}$$

as the instability number. Note that δ and Π are related by the equation $\delta = \zeta_f(\Pi - 1)$. The equilibrium is stable (unstable) for $\Pi < 1$ ($\Pi > 1$). Also, note that either δ or Π as instability criteria are exact (they are valid beyond the approximations of small σ and ζ_f, which we mentioned above).

Importantly, in the unstable case, we see that the amplitude $a_{n,2}\, e^{\delta\tau}$ from the linear solution eq. (4.10) grows without bounds, contrary to experimental results. This is because the linear solution is only valid at small amplitude. As the amplitude grows, nonlinearities are not negligible anymore and must be taken into account to accurately predict the dynamics. In section 4.2.4, we will see from numerical resolution of the nonlinear differential equation that, indeed, including the nonlinearities does lead to a saturation of the oscillations amplitude.

4.2.3 Modified Equations - Introducing Nonlinearity Coefficients

In the following, we would like to study each nonlinearity separately. To do so, we introduce coefficients in the system of equations, such that we can include or exclude each nonlinearity. The technique works as follows: for some nonlinear function f, and its linearization f_L, we define a new function g as

$$g = f_L + c f_{NL} = (1 - c) f_L + c f, \qquad \text{with } f_{NL} \equiv f - f_L, \tag{4.13}$$

where the nonlinearity is controlled by the parameter c. Having $c = 0$ gives $g = f_L$ (g is then linear) and $c = 1$ gives $g = f$ (g is now nonlinear). We now use this approach for the

system eq. (4.7), considering its linearization eq. (4.9), leading to

$$\dot{q}_1 = q_2, \tag{4.14a}$$

$$\dot{q}_2 = \left[1 - c_P \left(\frac{q_1}{1+q_1}\right)\right](-q_1 + q_3) - 2\,\zeta_f\; q_2, \tag{4.14b}$$

$$\dot{q}_3 = -2\sigma\,(1-c_T)\; q_1 + c_T\,\widetilde{T_{HL}}\left(\arctan\left[-\left(\frac{2\sigma}{\widetilde{T_{HL}}\cos^2[\psi/2]}\right)q_1 - \tan\left[\frac{\psi}{2}\right]\right] + \frac{\psi}{2}\right), \tag{4.14c}$$

where c_P controls the pressure nonlinearity and c_T controls the phase-change nonlinearity. The system is completely linear for $c_P = c_T = 0$, includes only the pressure nonlinearity for $c_P = 1$ and $c_T = 0$, includes only the phase-change nonlinearity for $c_P = 0$ and $c_T = 1$ and includes both nonlinearities for $c_P = c_T = 1$.

4.2.4 Numerical Simulations and Limit Cycle

Here, we use numerical simulations [6] to better understand the dynamics of eq. (4.14), including the nonlinearities. We will show that including nonlinearities leads to the saturation of the amplitude (section 4.2.4). The system reaches a steady-state after a while, corresponding to a limit cycle. Finally, we will study how the nonlinearities influence the steady-state.

Evolution in Time, Phase-Space and Limit Cycle

In fig. 4.4a, the position q_1 is shown as a function of time from numerical simulation, after a small perturbation of the equilibrium and for an unstable equilibrium ($\Pi = 1.25$). We observe that the amplitude of the oscillations grows and then saturates. The system reaches an oscillating steady-state. Clearly, including the nonlinearities leads to the saturation of the amplitude since, in the linear case, the amplitude grows without bounds (envelope shown in fig. 4.4a).

In fig. 4.4b, we show the evolution of the system in phase-space for the same conditions as fig. 4.4a (see Strogatz [107] for an introduction to phase-space). The system starts from the initial coordinates, spirals downward and reaches a steady-state (thick black line). This behavior suggests the existence of a limit cycle, just like observed experimentally (fig. 4.2b). A limit cycle is an isolated closed trajectory in phase-space, where isolated means neighboring trajectories are not closed (they are either attracted to or repelled

6. We used the ODE45 numerical solver from Matlab unless specified otherwise.

by the limit cycle) [107, chapter 7]. Besides the fact that the limit cycle is an elegant representation of the steady-state, it is also a useful concept. A system starting from any initial conditions (a point in phase-space) in the basin of attraction of a stable limit cycle (stable here means attractive) will be attracted to the limit cycle. Thus, the system will reach the same limit cycle, with the same amplitude, whatever the initial conditions are. Predicting the geometry of the limit cycle is the equivalent of predicting the motion in the steady-state regime. The analytical approach presented in section 4.3 will prove the existence of the limit cycle and its stability.

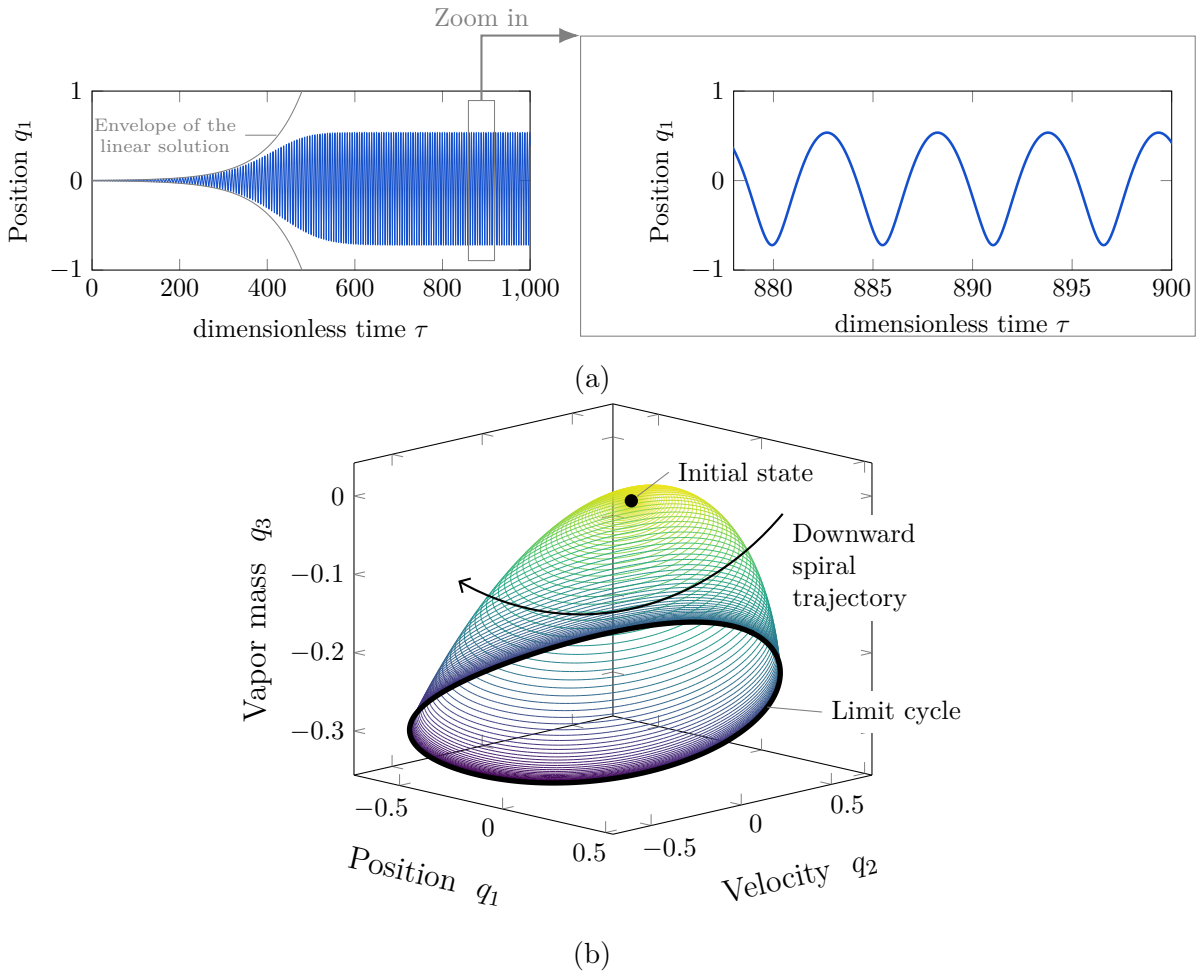

Figure 4.4 (Color online). Numerical simulation of eq. (4.14), for $c_P = c_T = 1$, $\zeta_f = 0.05$, $\sigma = 0.0625$ (so $\Pi = 1.25$), $T_{HL} = 0.1$ and $\psi = 0$ and from a small perturbation of the equilibrium (initial conditions: $q_1(0) = 0.0025$ and $q_2(0) = q_3(0) = 0$). (a) Dimensionless position q_1 as a function of dimensionless time τ, (b) evolution of the system in phase-space: we observe that the system approaches a closed trajectory, which we expect is a limit cycle.

Effect of Nonlinearities on the Steady-State

The identified nonlinearities affect the steady-state reached by the system. In this section, we will show the effects on the steady-state of each of the nonlinearities, which differ from one another. In fig. 4.5, we show steady-states from numerical simulations, for various instability number Π values, for the pressure nonlinearity only ($c_P = 1, c_T = 0$) on the left and for the phase-change nonlinearity only on the right ($c_P = 0, c_T = 1$).

Let's first consider the pressure nonlinearity. Figure 4.5a shows limit cycles in the plane $q_1 - q_2$. We see that increasing the instability number Π leads to an increase in the size of the limit cycle. The limit cycle looks very much circular at low Π but then deforms as Π is increased, due to the pressure nonlinearity. The dimensionless pressure difference $\widetilde{\Delta P_g}$, given by eq. (4.4), is shown in fig. 4.5c as a function of the position q_1. We see that the pressure increases drastically as the liquid plug approaches the closed end at $q_1 = -1$ (the meniscus is at the closed end when $x_i = -L_{g,0}$ corresponding to $q_1 = -1$, since $q_1 = x_i/L_{g,0}$). This drastic increase is due to the pressure nonlinearity: as $q_1 \to -1$, the factor $1/(1 + q_1)$ tends to $+\infty$ so $\widetilde{\Delta P_g}$ tends to $+\infty$ as well. The pressure nonlinearity is what prevents the liquid plug from going beyond the closed end. See the contrast with fig. 4.5d where the pressure is linearized, there is no sharp increase in pressure for q_1 negative. The pressure nonlinearity leads to a flattening of the limit cycle at high Π (see fig. 4.5a): the system (a point on the limit cycle moving in the clockwise direction) approaches the closed end at great negative velocity (lower left) but suddenly bounces back on the closed end due to the sharp rise in pressure, and moves back toward the open end at the same velocity but now positive (upper left). The pressure nonlinearity ultimately limits the oscillations amplitude as we will see later on.

Let's now look at the effects of the phase-change nonlinearity. Again, increasing Π leads to an increase of the limit cycle's size (see fig. 4.5b), but the limit cycles remain very much circular, in contrast to the pressure nonlinearity. The phase-change nonlinearity appears as a limiting mechanism (an arctangent) in the evaporation rate equation eq. (4.7c). By plotting $\dot{q}_3(q_1)$ in fig. 4.5f, we see that indeed, the evaporation rate saturates, following an arctangent. This effect is more apparent for larger Π (and larger amplitude). The nonlinearity leads to a smaller evaporation rate $\dot{q}_3$ than if it was linear (see dashed lines for references). This ultimately limits the oscillations amplitude as we will see later on. Note that in contrast, $\dot{q}_3$ is linear in fig. 4.5e.

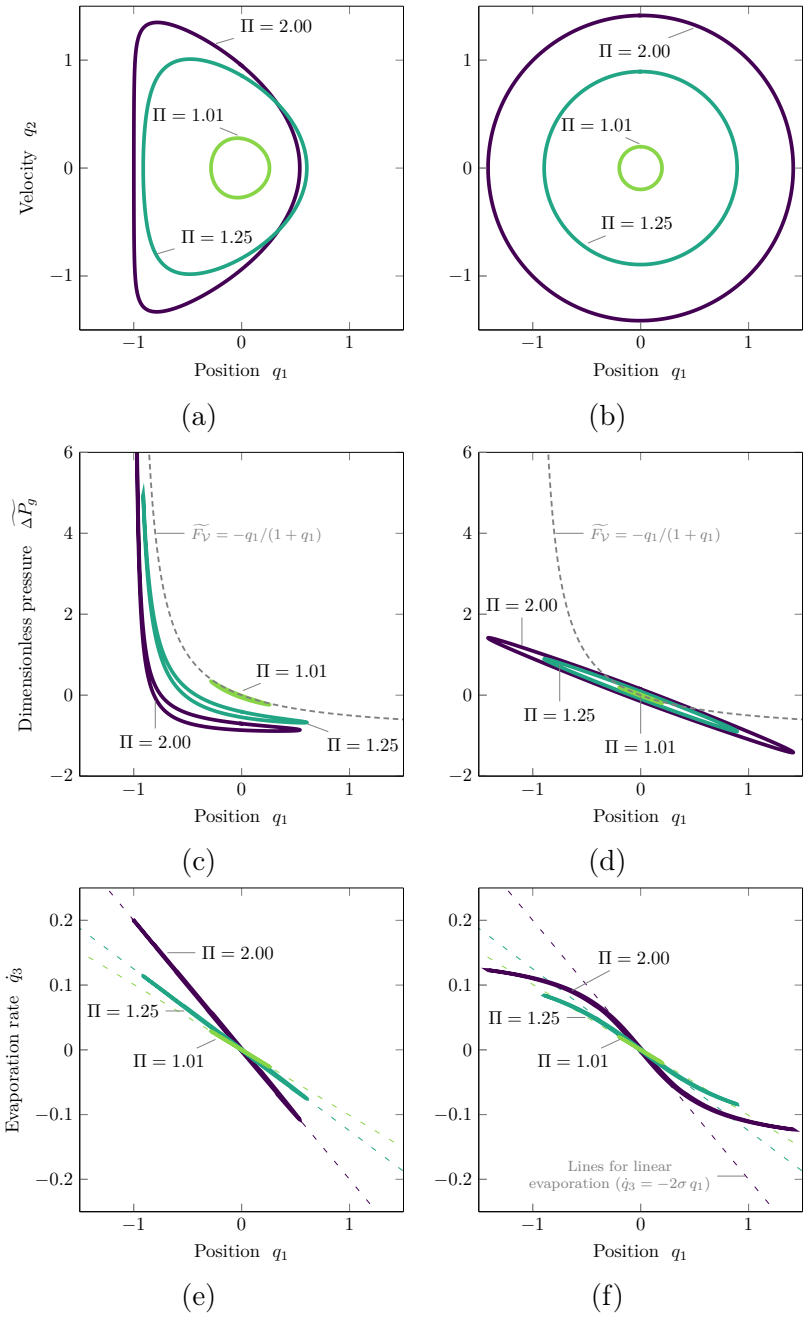

Figure 4.5 (Color online). Steady-state regimes for various instability number Π values and for the pressure nonlinearity (a,c,e) and or the phase-change nonlinearity (b,d,f). The effect of each of the nonlinearities on the dynamics can be observed. Parameters are $\zeta_f = 0.05$, $T_{HL} = 0.1$, $\psi = 0$ and σ is given by $\sigma = \zeta_f\, \Pi$.

4.3 Analytical Solution Based on Normal Form Approach

In this section, we obtain an approximate analytical solution of the system of differential equations (4.14). We use it to better understand the dynamics, how the oscillations

amplitude evolves over time and what controls the steady-state regime. Numerical results as presented in section 4.2.4 are useful, but limited, since they are only valid for the considered parameters and initial conditions. In contrast, the analytical approach followed in this section will lead to a simple and compact expression for the oscillations amplitude, valid for a range of parameters and initial conditions. Thus, from the analytical results, one can qualitatively predict the behavior of the system without having to perform new calculations, leading to a better understanding of the dynamics [7]. Another benefit of the analytical approach is that we identify key groups of parameters that control the dynamics of system. Lastly, the analytical approach allows us to obtain rigorous results such as proving the existence of the limit cycle.

In section 4.3.1, we apply the center manifold reduction and the normal form techniques to obtain the approximate analytical solution. We then show how the oscillation amplitude evolves after a perturbation of the equilibrium (section 4.3.2). We show that the saturation of the amplitude is due to nonlinearities. Finally, we analyze the steady-state regime reached by the system and prove the existence of the limit cycle (section 4.3.3).

4.3.1 Normal Form Expression and Approximate Analytical Solution

We now apply successive nonlinear techniques to simplify the equations. The detailed procedure, based on well established theory [124, 91, 82], is given in appendix B.1. First, we reduce the three dimensional system to only two, using the center manifold reduction technique. In the process, we have to introduce the quantity $\delta = \sigma - \zeta_f$, which is called the bifurcation parameter. We will describe its role in more details later on. We then make the equations simpler by transforming them into their normal form. The full procedure transforms eq. (4.14) into the two-dimensional normal form system of equations

$$\dot{z}_1 = \alpha z_1 - \omega z_2 + (a z_1 - b z_2)\left(z_1^2 + z_2^2\right) + \mathcal{O}(|z_1|^5, |z_2|^5), \tag{4.15a}$$

$$\dot{z}_2 = \omega z_1 + \alpha z_2 + (b z_1 + a z_2)\left(z_1^2 + z_2^2\right) + \mathcal{O}(|z_1|^5, |z_2|^5), \tag{4.15b}$$

where $z_1(\tau)$ and $z_2(\tau)$ are the new phase-space variables, related to q_1, q_2 and q_3. The new parameters α, ω, a and b are functions of δ and the other original parameters. This new system of equations is topologically equivalent to the original one (conserves the qualitative

7. See De Regt and Dieks [21, p.150,151] for a description of what *understanding* is. A key point is that understanding of a phenomenon is achieved when the scientist can "recognize qualitatively characteristic consequences of [the theory] without performing exact calculations".

features), near the point $q_1 = q_2 = q_3 = \delta = 0$. Equation (4.15) has the solutions

$$z_1 = r(\tau)\cos\left[\theta(\tau)\right], \tag{4.16a}$$

$$z_2 = r(\tau)\sin\left[\theta(\tau)\right], \tag{4.16b}$$

where the amplitude r and the phase θ are functions of time τ and are described by the uncoupled differential equations (App. B.1.2)

$$\dot{r} = d\delta r + a_0 r^3 + \mathcal{O}(\delta^2 r, \delta r^3, r^5), \tag{4.17a}$$

$$\dot{\theta} = \omega_0 + c\delta + b_0 r^2 + \mathcal{O}(\delta^2, \delta r^2, r^4), \tag{4.17b}$$

with the following expressions for d, ω_0 and c

$$d \equiv \frac{1}{1 + 4{\zeta_f}^2}, \tag{4.18a}$$

$$\omega_0 \equiv 1, \tag{4.18b}$$

$$c = \frac{2\zeta_f}{1 + 4{\zeta_f}^2}. \tag{4.18c}$$

The expression for b_0 will not be given here since it is not needed for the analysis (it does not affect the amplitude r and only slightly affects the angular frequency), but it can be obtained by the normal form procedure [40]. The parameter a_0 is much more important, it expresses the effect of the phase-change and pressure nonlinearities on the amplitude vector field $\dot{r}$. It is given by

$$a_0 = a_{0,T} + a_{0,PT} + a_{0,P}, \tag{4.19a}$$

where we split a_0 into three components, $a_{0,T}$, $a_{0,PT}$ and $a_{0,P}$ which are non-zero if $c_T = 1$, $c_T = c_P = 1$ and $c_P = 1$, respectively. The quantity $a_{0,T}$ is the contribution to a_0 of the phase-change nonlinearity solely and $a_{0,P}$, the contribution of the pressure nonlinearity solely, while $a_{0,PT}$ appears when both nonlinearities are active. These are defined as

$$a_{0,T} \equiv \left(\frac{-2{\zeta_f}^3 \left(1 + {\zeta_f}^2 \cos\left[\psi\right]\right)}{{T_{HL}}^2 (1 + \cos\left[\psi\right]) \left(1 + {\zeta_f}^2\right) \left(1 + 4{\zeta_f}^2\right)} \right) c_T, \tag{4.19b}$$

$$a_{0,PT} \equiv \left(\frac{{\zeta_f}^2 \sin\left[\psi\right] \left(3 + 4{\zeta_f}^2\right)}{4T_{HL} \left(1 + \cos\left[\psi\right]\right) \left(1 + {\zeta_f}^2\right) \left(1 + 4{\zeta_f}^2\right)} \right) c_P c_T, \tag{4.19c}$$

$$a_{0,P} \equiv \left(\frac{-\zeta_f}{8 \left(1 + {\zeta_f}^2\right)} \right) c_P. \tag{4.19d}$$

The expression for a_0 will be studied in more detail in section 4.3.3. We will also discuss what the amplitude $r(\tau)$ actually looks like in a moment. At this point however, the reader might rightfully wonder how r is related to the amplitude in the original variables q_i, the ones we really care about. Performing the inverse transformations (as detailed in appendix B.1.3), we obtain an approximate solution for the original phase-space variables q_i

$$q_i = \tfrac{1}{2} A_{i0} + A_{i1} \sin\left(\theta + \varphi_{i1}\right) + A_{i2} \sin\left(2\theta + \varphi_{i2}\right), \tag{4.20a}$$

where the coefficients for the dimensionless position q_1 can be approximated as

$$A_{10} \approx c_P \, r(\tau)^2, \tag{4.20b}$$

$$A_{11} \approx r(\tau), \tag{4.20c}$$

$$A_{12} \approx \tfrac{1}{2} c_P \sigma \, r(\tau)^2, \tag{4.20d}$$

assuming small δ, small ζ_f and $\psi = 0$. We see from those approximations that the fundamental $A_{11} \sin\left(\theta + \varphi_{11}\right)$ is the dominant oscillating term (at small amplitude r, the quantity r^2 is very small), and that $r(\tau)$ is a good approximation for the oscillations amplitude in q_1.

Now, to find the amplitude $r(\tau)$ from the normal form, one can solve the truncated (neglecting the higher order terms) eq. (4.17a), by separation of variables and partial fraction

decomposition. We get

$$r(t) = r_{LC} \cdot \sqrt{\frac{1}{1 + ({r_{LC}}^2/{r_0}^2 - 1)\ e^{-2d\delta\, t}}}, \tag{4.21}$$

where the quantity r_{LC} is the limit cycle amplitude (we will show that and define what it means later on) and is given by

$$r_{LC} \equiv \sqrt{\frac{-d\delta}{a_0}}. \tag{4.22}$$

4.3.2 How the Amplitude Evolves During Startup: Normal Form Vector Field

We will now discuss how the amplitude $r(\tau)$ evolves over time after a perturbation of the equilibrium, based on the vector field $\dot{r} = d\delta r + a_0 r^3$ (eq. (4.17a)). We will discuss the following four cases: 1a) stable equilibrium ($d\delta < 0$) and linear dynamics ($a_0 = 0$), 1b) unstable equilibrium ($d\delta > 0$) and linear dynamics ($a_0 = 0$), 2a) unstable equilibrium ($d\delta > 0$) and nonlinear dynamics ($a_0 < 0$) and 2b) unstable equilibrium ($d\delta > 0$) and nonlinear dynamics ($a_0 < 0$). The vector field $\dot{r}(r)$ for all four cases is shown in fig. 4.6a. How the amplitude $r(\tau)$ evolves over time is shown in fig. 4.6b. Finally, keeping in mind that $r(\tau)$ is the amplitude of the oscillations in $z_1(\tau)$ and $z_2(\tau)$, the corresponding motion in $z_1(\tau)$ is shown in fig. 4.6c and fig. 4.6d.

Linearized Vector Field

Let's consider the linearized system first [8], by taking $a_0 = 0$ in eq. (4.17a). We get $\dot{r}(\tau) = d\delta\, r$ which are straight lines in the graph $\dot{r}(r)$ (fig. 4.6a). Solving $\dot{r}(\tau) = 0$ for r, we find that there is only one equilibrium at $r = 0$ (fixed point in nonlinear dynamics terms). The stability of the fixed point is given by the derivative $d\dot{r}/dr$ at that point, we have $d\dot{r}/dr(r = 0) = d\delta$. The quantity $d\delta$ corresponds to the slope of the straight lines in fig. 4.6a. Given that $d > 0$ is always true (this is obvious from eq. (4.18a), given $\zeta_f > 0$), the stability of the equilibrium depends on the bifurcation parameter δ only.

For $\delta < 0$ (negative slope), the equilibrium is stable: a small perturbation in r leads to a negative $\dot{r}$, meaning that r decreases in time, so the amplitude r decreases back to $r = 0$. For $\delta > 0$ (positive slope), the equilibrium is unstable: a small perturbation in r leads to a

8. Note that we already obtained the linear solution in section 4.2.2. The normal form's results presented here are equivalent, within the approximation of small δ and from a perturbation of the equilibrium. Looking at the linear case again, but from the normal form's perspective, allows to better understand the normal form's differential equation (4.17a) and serve as a reference for the nonlinear case.

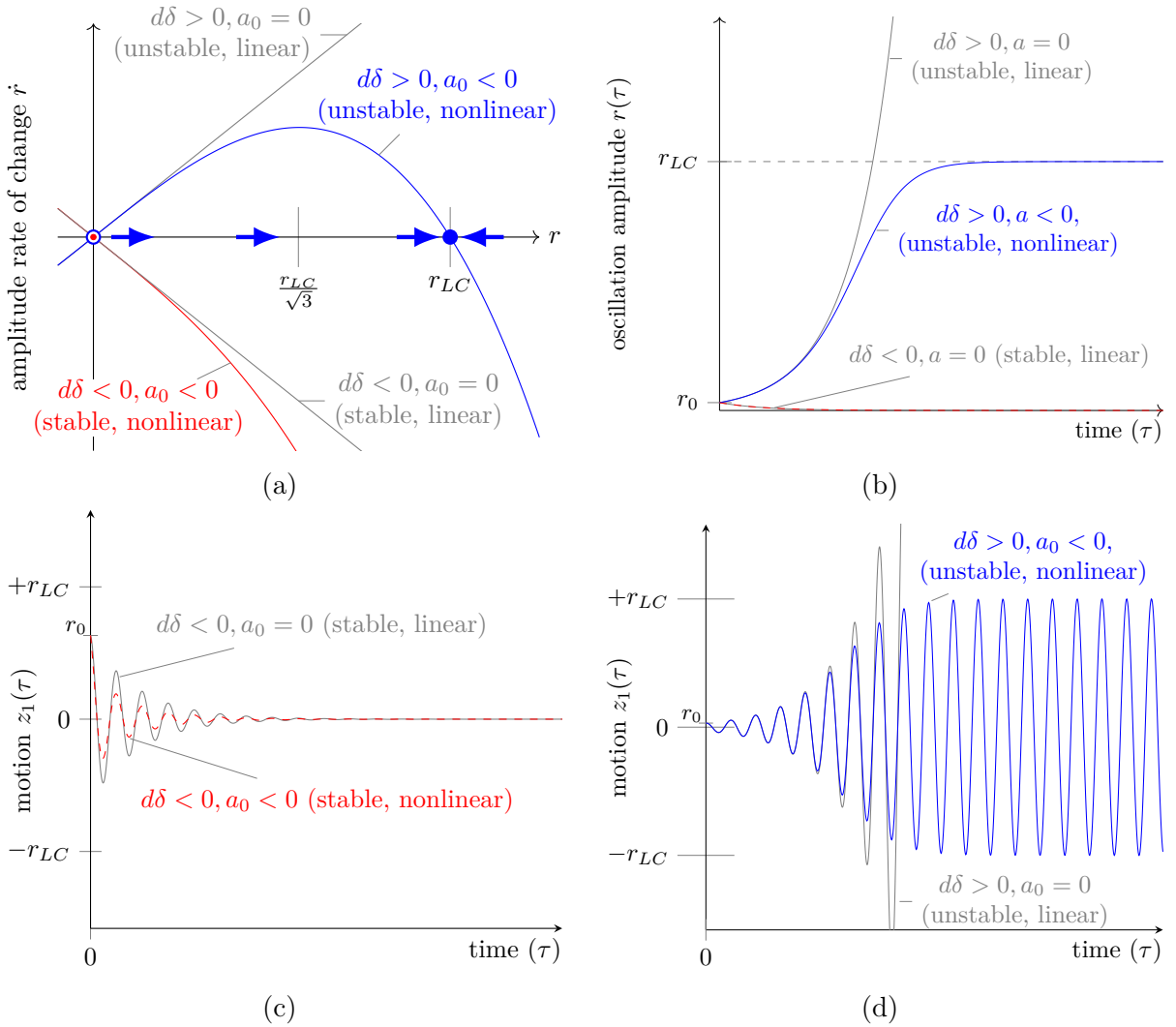

Figure 4.6 (Color online). Behavior of the normal form eq. (4.17). (a)Vector field $\dot{r}(r)$ from eq. (4.17a). The amplitude r increases (decreases) over time for $\dot{r} > 0$ ($\dot{r} < 0$). Here, the equilibrium $r = 0$ is stable (unstable) for $d\delta < 0$ ($d\delta > 0$) and a steady-state oscillating regime (stable limit cycle) exists at $r = r_{LC}$ for $d\delta > 0$ and $a_0 < 0$. (b) Evolution of the amplitude $r(\tau)$ after a small perturbation r_0 of the equilibrium $r = 0$; the unstable nonlinear solution saturates at the amplitude r_{LC}. (c) Typical linear and nonlinear solutions $z_1(\tau)$ for a stable equilibrium ($d\delta < 0$). (d) Typical linear and nonlinear solutions $z_1(\tau)$ for an unstable equilibrium ($d\delta < 0$).

positive $\dot{r}$, meaning that r increases in time, so the amplitude r increases without bounds. The analysis above is confirmed by solving $\dot{r}(\tau) = d\delta\, r$, leading to $r(\tau) = r_0\, e^{d\delta\, \tau}$. After a perturbation of the equilibrium, the amplitude r decreases exponentially for $d\delta < 0$ and increases exponentially for $d\delta > 0$ (see fig. 4.6b).

The stability criterion is the same as the one obtained from the linearized equations (section 4.2.2). The stability analysis of the equilibrium $r = 0$ remains valid when nonlinear terms are taken into account, according to the Hartman-Grobman theorem [107, 124] (except for the borderline case where $\delta = 0$ exactly, the stability then depends on a_0).

Nonlinear Vector Field

Let's now consider the full vector field $\dot{r} = d\delta r + a_0 r^3$ (eq. (4.17a)) with $a_0 \neq 0$. Note that for $c_P = c_T = 0$, we have $a_0 = 0$, confirming that the a_0 term expresses the effect of the pressure and wall phase-change nonlinearities. We will consider $a_0 \leqslant 0$ in the following (we show that this is the case when $\psi = 0$ in section 4.3.3, the more general case is analyzed in App. B.2). Because of the a_0 term, the function $\dot{r}(r)$ is no longer a straight line in fig. 4.6a, but curves downwards. The quantity $d\delta$ still controls the slope of the curve $\dot{r}(r)$ at $r = 0$, hence the stability of the equilibrium. When $\delta < 0$, the slope at $r = 0$ is negative so the equilibrium is stable and, because of nonlinearities, the decrease in amplitude occurs faster than the linear case (stable nonlinear case in fig. 4.6c and fig. 4.6a).

By increasing δ above 0, the slope at $r = 0$ is now positive so the equilibrium becomes unstable. The function $\dot{r}(r)$ now corresponds to the unstable nonlinear case in fig. 4.6a. Following this curve helps understand how the amplitude evolves over time. After a perturbation of the equilibrium $r = 0$ (a small increase in r), $\dot{r}$ is positive so r keeps increasing over time. As r grows (we move to the right on the graph), the nonlinear term $-a_0 r^3$ becomes significant relative to the term $d\delta\, r$, and the amplitude rate of change $\dot{r}$ eventually decreases until it reaches 0, whereupon r then reaches a constant value $r = r_{LC}$.The point $r = r_{LC}$ is stable (attractive): for $r < r_{LC}$, the amplitude r increases toward r_{LC} and for $r > r_{LC}$, r decreases toward r_{LC}.

Figure 4.6b shows the corresponding evolution of r as a function of time. Remember that r is the amplitude of the oscillating motion in z_1 and z_2 (eq. (4.16)). The corresponding oscillations in z_1 are shown in fig. 4.6d. We clearly see the saturation of the amplitude. The fixed point $r = r_{LC}$ in fig. 4.6a corresponds to oscillating motion of constant amplitude r (a steady-state). Because it is attractive, it is called a stable limit cycle in nonlinear dynamics: it corresponds to a closed, attractive curve in phase-space (as represented in fig. 4.7).

4.3.3 The Steady-State Regime: Limit Cycle

In the previous section, we established how the amplitude evolves over time, and explained how it can reach a steady-state, which corresponds to a limit cycle. Here, we focus on the steady-state, on the limit cycle. We show that, as the bifurcation parameter δ crosses 0, the limit cycle is created through a Poincaré-Andronov-Hopf bifurcation (section 4.3.3).

In section 4.3.3, we then discuss necessary conditions for the bifurcation. We find that nonlinearities are responsible for the limit cycle existence. Finally, we provide an expression for oscillation amplitude on the limit cycle (r_{LC}) and discuss how to increase it (section 4.3.3). To do so, we will find that one may increase the instability or reduce the nonlinearities.

Bifurcation: What happens When δ Is Progressively Increased Above 0

As shown in fig. 4.6a, the stable nonlinear case has only one stable fixed point at $r = 0$ while the unstable nonlinear case has one unstable fixed point at $r = 0$ and one stable fixed point at $r = r_{LC}$. Here, we discuss how we go from one case to the other by progressively increasing the bifurcation parameter δ while other parameters are held constant, using what is known as a bifurcation diagram (fig. 4.7, top). We also display motion in phase-space for various δ values (bottom).

For $\delta < 0$, there is only one stable fixed point at the equilibrium $r = 0$, shown by the solid line at $r = 0$. Trajectories in the $z_1 - z_2$ phase-space are stable spirals. As δ is increased above 0, the solid line at $r = 0$ bifurcates into a dashed line corresponding to the now unstable equilibrium at $r = 0$ and a solid line (upper branch) corresponding to a second (stable) fixed point at $r = r_{LC}$. This new fixed point corresponds to a limit cycle in the phase-space $z_1 - z_2$, with a radius of r_{LC}.

The creation of the limit cycle as the bifurcation parameter δ is increased above 0 is called [9]a supercritical Poincaré-Andronov-Hopf bifurcation (conditions and proof will be given in section 4.3.3). Because the limit cycle is stable, any initial conditions close enough to the limit cycle lead to motion in phase-space tending toward that steady-state (see how the spirals tend toward the limit cycle). Notice that, as δ is increased further, the limit cycle's radius r_{LC} keeps increasing (upper branch). For the z_1 and z_2 variables, the limit cycle corresponds to periodic oscillations of a constant amplitude r_{LC}, a steady-state (given by eq. (4.24)). The saturation of the amplitude in time shown in fig. 4.6d is explained by the existence of the limit cycle in phase-space.

Nonlinearities As the Limiting Mechanism and Limit Cycle Existence

In this section, we discuss why we must have $a_0 < 0$ for a stable limit cycle to be created and we show that this is the case, due to the nonlinearities. We show that both the pressure and the phase-change nonlinearities contribute to a negative a_0, meaning that both nonlinearities are limiting mechanisms.

9. This bifurcation is commonly called a Hopf bifurcation but we use the longer denomination, *Poincaré-Andronov-Hopf bifurcation*, to acknowledge the contributions of Poincaré and Andronov, as recommended by Wiggins [124, p.385].

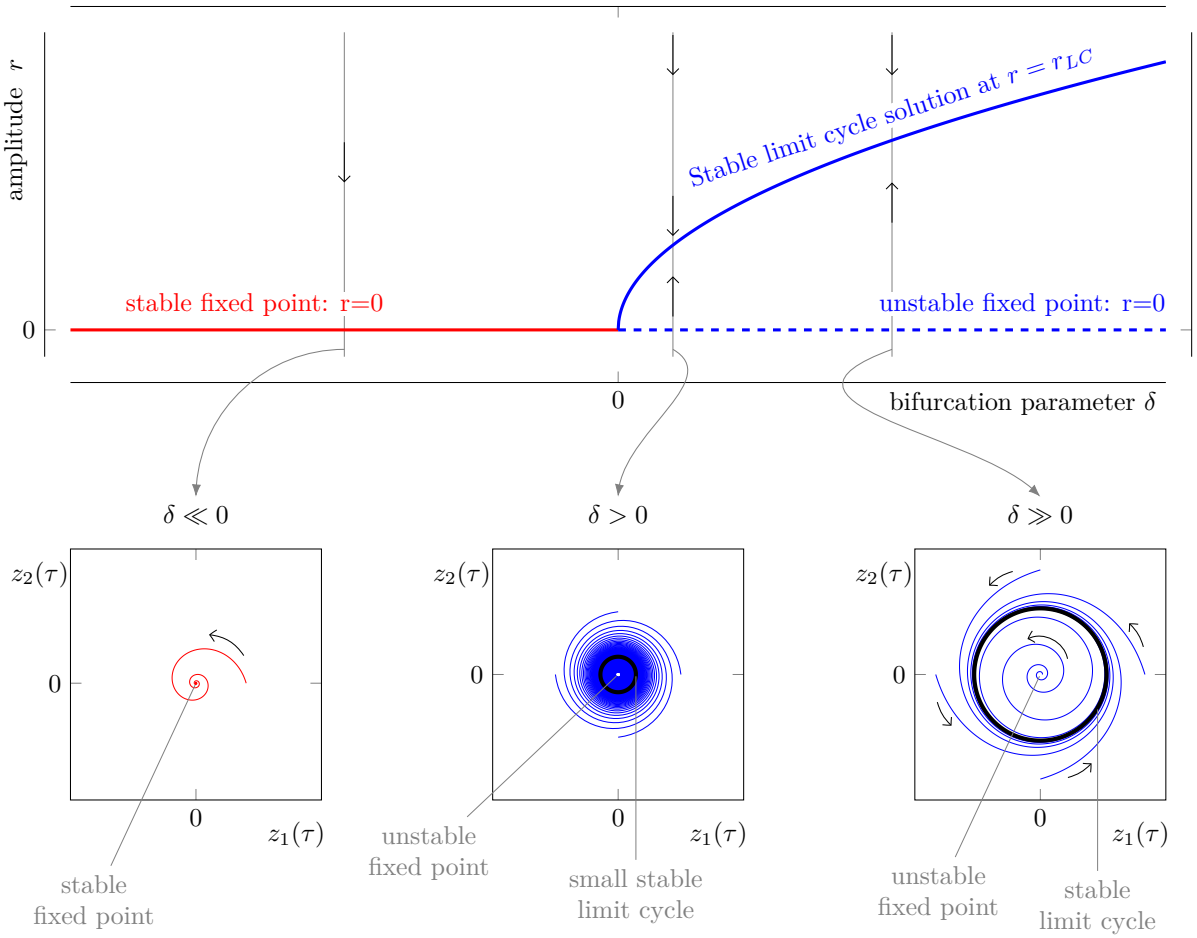

Figure 4.7 (Color online). Bifurcation diagram ($a_0 < 0$) on top and trajectories in the z phase-space at different δ values. The bifurcation diagram shows solutions of $\dot{r} = 0$ as a function of the bifurcation parameter δ (other parameters are held constant). For $\delta < 0$, there is only a stable fixed point at the equilibrium $r = 0$. At $\delta = 0$, the equilibrium becomes unstable and a second fixed point at $r = r_{LC}$ is created, corresponding to a stable limit cycle (Poincaré-Andronov-Hopf bifurcation). In the z phase-space, the limit cycle is the circular trajectory; other trajectories are attracted by the limit cycle.

In section 4.3.2 we discussed how the term a_0 is responsible for the curvature of $\dot{r}(r)$. For $a_0 < 0$, $\dot{r}(r)$ curves downward, so that the amplitude r eventually saturates at the limit cycle amplitude r_{LC}. For $a_0 > 0$, $\dot{r}(r)$ would curve upward, so that there would not be any saturation of the amplitude, the amplitude would keep growing forever (given the normal form approximation). Thus, we check to see if we indeed have $a_0 < 0$. Finally, recall that a_0 expresses the effect of phase-change and pressure nonlinearities on the vector field $\dot{r}$ (see section 4.3.1). When looking for $a_0 < 0$, we thus check to see if the nonlinearities are limiting mechanisms.

Examining eq. (4.19), we see that we have $a_{0,P} < 0$ always (keeping in mind $0 < \zeta_f < +\infty$). The pressure nonlinearity alone therefore tends to saturate the amplitude. The phase-change is more complicated because of the deviation ψ. Let's consider $\psi = 0$ first, meaning that the equilibrium is located exactly at the inflexion point ($T_{g,sat,0} = \frac{1}{2}(T_H + T_L)$). The quantities $a_{0,T}$ and $a_{0,PT}$ become:

$$a_{0,T} = \left(\frac{-{\zeta_f}^3}{{T_{HL}}^2 \left(1 + 4{\zeta_f}^2\right)} \right) c_T, \tag{4.23a}$$

$$a_{0,PT} = 0. \tag{4.23b}$$

In that case, we clearly have $a_{0,T} < 0$ (keeping in mind that $T_{HL} > 0$ and $0 < \zeta_f < +\infty$) and the phase-change nonlinearity thus also tends to saturate the amplitude. Both nonlinearities put together lead to $a_0 < 0$ (there is no combined effect since $a_{0,PT} = 0$). In the App. B.2, we verify that those conclusions also hold for small deviations ψ. For larger deviations we find that, under some conditions, the phase-change nonlinearity can be temporarily non-saturating such that $a_0 > 0$. A steady-state regime still exists but is not produced by a Poincaré-Andronov-Hopf bifurcation.

So far, our analysis only considered the truncated form of eq. (4.17). But what about the higher order terms we neglected, do they affect our conclusions? The short answer is no. The Poincaré-Andronov-Hopf bifurcation theorem [124, sec.20.2] ensures that for δ sufficiently small, the following two cases hold: 1) $a_0 < 0, d\delta < 0$: the origin is an asymptotically stable fixed point, 2) $a_0 < 0, d\delta > 0$: the origin is an unstable fixed point and there exists an asymptotically stable limit cycle. This theorem enables us to prove the existence of the limit cycle born from a supercritical Poincaré-Andronov-Hopf bifurcation and to prove that the pressure and phase-change (for ψ small enough) nonlinearities are both limiting mechanisms in our model.

Analyzing the Limit Cycle Amplitude

The steady-state amplitude is given by r_{LC} (in the z variables as well as in the $q's$ variables, see eq. (4.20)). We can obtain the solution for the limit cycle by solving eq. (4.17a) with $\dot{r} = 0$. The limit cycle solution is, for $-\infty < \frac{d\delta}{a_0} < 0$ and δ sufficiently small

$$z_1 = r_{LC} \cos(\theta), \tag{4.24a}$$

$$z_2 = r_{LC} \sin(\theta), \tag{4.24b}$$

where r_{LC} and $\theta(\tau)$ are respectively the limit cycle amplitude and the phase, and are given by

$$r_{LC} = \sqrt{\frac{-d\delta}{a_0}}, \qquad \text{(as given earlier in eq. (4.22))} \ , \tag{4.24c}$$

$$\theta(\tau) = \Omega\,\tau + \theta_0 \qquad \text{with} : \ \Omega \equiv \omega_0 + \left(c - \frac{b_0\,d}{a_0}\right)\delta. \tag{4.24d}$$

In order to find the limit cycle solution in the original variables q_i, we can simply substitute the expressions of the amplitude r_{LC} and of the angular frequency Ω in eq. (4.20).

In applications, one is usually interested in increasing the oscillations amplitude in the steady-state. We will first discuss how the amplitude is affected by the macro parameters $d\delta$ (instability) and a_0 (nonlinearities). We will then discuss how the physics, the phase-change and the friction, affect both $d\delta$ and a_0 and thus control the amplitude. Analyzing r_{LC} expression eq. (4.24c), we clearly see that one may increase the amplitude by increasing the instability $d\delta$ or by decreasing the nonlinearities through a_0. The r_{LC} expression is displayed in fig. 4.8a. To analyze the effect of parameters $d\delta$ and a_0 on r_{LC} further, it is useful to look at partial derivatives (see fig. 4.8b, based on expressions derived below). Partial derivatives provide a measure of sensitivity. Starting with $d\delta$ we have

$$\frac{\partial\, r_{LC}}{\partial\,(d\delta)} = \frac{1}{2\,\sqrt{d\delta\,(-a_0)}}\ . \tag{4.25}$$

Keeping in mind that $d\delta > 0$ and $a_0 < 0$ (for a stable limit cycle to exist in the normal form equations), we have $\partial\, r_{LC}/\partial\,(d\delta) > 0$: increasing $d\delta$ always increases the amplitude. Also, close to the bifurcation (for $d\delta \to 0^+$ from the right), we have $\partial\, r_{LC}/\partial\,(d\delta) \to +\infty$, so changing only slightly $d\delta$ has a huge impact on the amplitude. As $d\delta$ increases, the amplitude of the derivatives decreases toward 0: the impact of $d\delta$ on the amplitude decreases. The partial derivative for a_0 is

$$\frac{\partial\, r_{LC}}{\partial a_0} = \frac{\sqrt{d\delta}}{2\ (-a_0)^{3/2}}. \tag{4.26}$$

Keeping in mind that $d\delta > 0$ and $a_0 < 0$, we have $\partial\, r_{LC}/\partial a_0 > 0$, so increasing a_0 increases the amplitude. Because a_0 is negative, this means that bringing a_0 closer to 0, reducing the nonlinearities, increases the amplitude. We note that close to the bifurcation (for $d\delta \to 0^+$ from the right), the derivative tends toward 0: the oscillation amplitude is

barely affected by the nonlinear term a_0 (as long as $a_0 < 0$). However, as $d\delta$ increases, the derivative increases and a_0 becomes more and more important. We find that, in order to increase the oscillation amplitude, one has to first increase the linear (instability) term $d\delta$. As the amplitude increases, the effect of the linear term decreases and it becomes more and more useful to reduce the nonlinearity by bringing a_0 closer to 0. The threshold at which both derivatives are equal is given by: $d\delta = -a_0$.

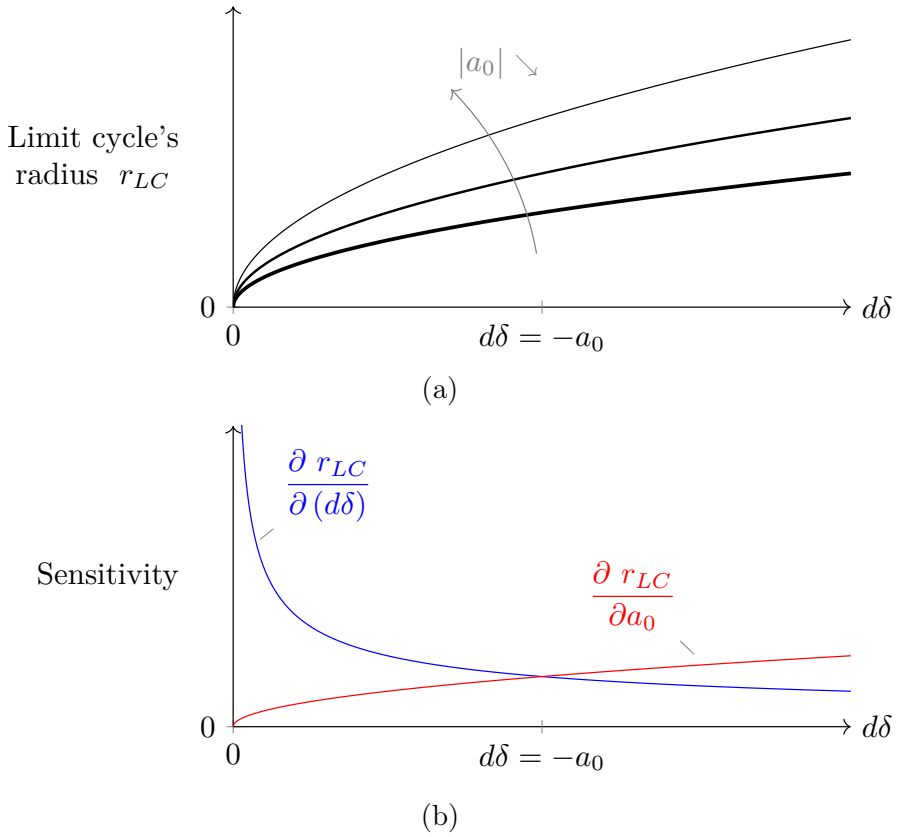

Figure 4.8 (Color online). (a) Limit cycle's radius r_{LC} (and oscillations amplitude) as function of the instability measure $d\delta$. One can increase the amplitude by increasing the instability ($d\delta$) or by decreasing the nonlinear parameter a_0. (b) Sensitivity measures given by the derivatives eq. (4.25) and eq. (4.26). We see that the amplitude r_{LC} mostly depends on the linear quantity $d\delta$ at small $d\delta$, which corresponds to small amplitude r_{LC}. As $d\delta$ (and the amplitude r_{LC}) increases, the importance of $d\delta$ decreases and the importance of the nonlinear parameter a_0 increases.

Now that we know the amplitude can be increased by increasing $d\delta$ and bringing a_0 closer to zero, let's discuss how the physics impacts both $d\delta$ and a_0. The instability $d\delta = (\sigma - \zeta_f)/(1 + 4{\zeta_f}^2)$ can be increased by increasing either the phase-change (σ) or by decreasing the friction (ζ_f). The nonlinear parameter a_0 is affected by both the phase-change nonlinearity and by the pressure nonlinearity. For the phase-change nonlinearity

only, we have $a_0 = a_{0,T} = -{\zeta_f}^3/\left({T_{HL}}^2(1+4{\zeta_f}^2)\right)$ (eq. (4.23a)). We can bring a_0 closer to 0 and increase the amplitude by increasing the phase-change limit T_{HL} (this makes the phase-change profile more linear) or by decreasing ζ_f. For the pressure nonlinearity only, $a_0 = a_{0,P} = -\zeta_f/\left(8(1+{\zeta_f}^2)\right)$ (eq. (4.19d)). We can bring a_0 closer to 0 and increase the amplitude by decreasing ζ_f.

To better understand how the physics impact the amplitude, let's look at explicit expressions of r_{LC} for each nonlinearities individually while assuming $\psi = 0$ for simplicity. The amplitude for the phase-change nonlinearity only is given by:

$$r_{LC}(c_P = 0, c_T = 1) = \sqrt{\frac{-d\delta}{a_{0,T}}} = \frac{T_{HL}}{\zeta_f}\sqrt{\Pi - 1}, \tag{4.27a}$$

while for the pressure nonlinearity only, we have:

$$r_{LC}(c_P = 1, c_T = 0) = \sqrt{\frac{-d\delta}{a_{0,P}}} = (2 - 3{\zeta_f}^2)\sqrt{2\,(\Pi - 1)} \; + \; \mathcal{O}({\zeta_f}^4), \tag{4.27b}$$

where we considered a series in terms of ζ_f to get a simpler expression (given that ζ_f is typically small in experiments). In the expressions above, we used the instability number $\Pi = \sigma/\zeta_f$ (with $\delta = \zeta_f(\Pi - 1)$). Using Π leads to simpler r_{LC} expressions and is nicely expressed in terms of the physical parameters (eq. (4.12)). The amplitude for the phase-change nonlinearity only can be increased by increasing the phase-change (either by increasing σ which increases Π or by increasing the phase-change limit T_{HL}) and by decreasing the friction (ζ_f decreases and $\Pi = \sigma/\zeta_f$ increases). For the pressure nonlinearity only, the amplitude can be increased by increasing the phase-change (increasing σ increases Π) and by decreasing the friction (ζ_f decreases and $\Pi = \sigma/\zeta_f$ increases). One could expect the length $L_{g,0}$ to appear in the pressure nonlinearity (by reducing $L_{g,0}$, the liquid plug should get closer to the closed end and the pressure should be more nonlinear), but Π is independent of $L_{g,0}$ (eq. (4.12)) so $r_{LC}(c_P = 1, c_T = 0)$ is not a function of $L_{g,0}$. This is because we used $L_{g,0}$ to make the equations dimensionless. The *dimensional* amplitude is $L_{g,0} \cdot r_{LC}$ and is now proportional to $L_{g,0}$. Consequently, for the pressure nonlinearity case, increasing $L_{g,0}$ reduces the nonlinearity and increases the amplitude. For the phase-change nonlinearity, we have that $T_{HL}/\zeta_f \propto 1/L_{g,0}$ (because $T_{HL} \propto 1/m_{g,0}$, eq. (4.8)) so the dimensional amplitude does not depend on $L_{g,0}$.

The normal form solution is only valid close to the instability threshold. So, to study the effect of the parameters further, we study the amplitude numerically. To that end, we use

the continuation Matlab package MatCont 7.2 [23]. The Hopf bifurcation is first detected, from which a limit cycle is continued. The limit cycle is detected by orthogonal collocation, which is considered the most reliable numerical approach for limit cycle detection [66]. We first study the effect of the phase-change in fig. 4.9a. Here, we keep ζ_f constant so the instability number Π shows the effect of σ only. We see that increasing the phase-change coefficient σ (by increasing Π) leads to a strong increase in the amplitude close to the instability threshold (Π close to 1). The amplitude is less sensitive to σ for large Π. Increasing the phase-change limit T_{HL} also increases the amplitude. The amplitude is less sensitive to T_{HL} for Π close to 1 and more sensitive for large Π. These confirm our normal form results. We conclude that we can increase the oscillations amplitude significantly by controlling the phase-change (in fig. 4.9a, the dimensional amplitude ranges from 0 to close to $0.8L_{g,0}$). Here however, there is a limit at which point increasing the phase-change further has no more impact on the amplitude: for both large Π and large T_{HL}, the amplitude reaches a plateau (this was not captured by the normal form). We then study the effect of the friction in fig. 4.9b. Here, we keep σ constant so the instability number Π shows the effect of ζ_f only. We see that increasing Π by decreasing the friction leads to an increase in amplitude.

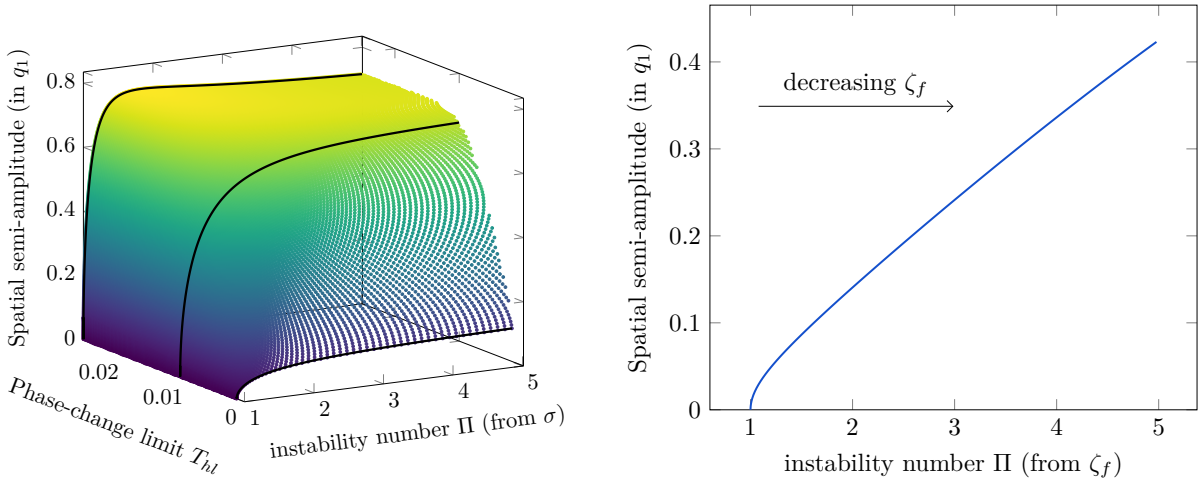

Figure 4.9 Semi-amplitude in q_1 (half the peak-to-peak amplitude) obtained by numerical continuation of eq. (4.14) using MatCont 7.2 [23]. (a) Effect of phase-change, through Π (shows the effect of σ since ζ_f is fixed) and phase-change limit T_{HL}, with: $c_P = c_T = 1$ and $\zeta_f = 0.01$. (b) Effect of friction through Π (shows the effect of σ since σ is fixed), with: $c_P = c_T = 1$, $\sigma = 0.01$ and $T_{HL} = 0.001$.

4.4 Discussion

In this section, we first describe a general approach to increase the amplitude and the performance in real devices. Then, we discuss simplifications considered in our model and how the neglected physics could quantitatively affect the dynamics in the SBPHP.

4.4.1 General Approach to Increase Amplitude and Performance

From our approach, we can provide general guidelines to maximize the (steady-state) amplitude and, to some extent, the performance (heat transfer capabilities for PHP, power output for SOFHE, etc.).

One should first make sure the oscillations start by promoting the instability mechanism either by increasing the phase-change (σ) or by decreasing the friction (ζ_f), to ensure $\Pi > 1$. Once this is done, what matters to increase the amplitude is still to increase the instability, as discussed in section 4.3.3. From our thermal resistance model for phase-change, we found that a phase-change in anti-phase with the position led to a force purely in phase with velocity, purely injecting energy into the system (see [112, Sec. VI.C] for more details). For more general phase-change mechanisms than the one we consider, we thus still have to increase the phase-change component in anti-phase with the position in order to increase the amplitude. As one increases the steady-state amplitude by increasing the instability, one should consider reducing the limiting mechanism (nonlinearities) to increase the amplitude further. In our model, the effect of the phase-change nonlinearity could be reduced by increasing the phase-change limit (T_{HL}) and by reducing the friction (ζ_f) while the effect of the pressure nonlinearity could be reduced by reducing the friction (ζ_f) and increasing the length of vapor at equilibrium ($L_{g,0}$).

From our model, we find that the amplitude can be greatly increased by increasing the phase-change (either by increasing σ or T_{HL}). This supports the idea that engineered tubes (using sintered powder wick, surface treatments, cavities, glass fiber, groove, microstructures, etc.) to control the phase-change can have a massive impact on the amplitude and the performance. It is important to point out that it is not only the magnitude of the phase-change but also the timing of it, relative to the position, that matter. It would be interesting to further study, both theoretically and experimentally, how controlling the magnitude and the timing of the phase change could impact the amplitude. This could help the design of engineered tubes and allow to increase the performance beyond what is currently achieved.

4.4.2 Simplifications and Perspective on More Accurate Models

Our work here is based on several simplifications. The goal of this paper was not to consider a quantitatively accurate model valid in all circumstances. Rather, we wanted to analyze a simplified model which captures the most relevant characteristics observed in the experiment, while still being amenable to relatively simple mathematical techniques. By doing so, we were able to highlight interesting properties, such as the limit cycle and how it is controlled by an instability mechanism (linear) and a limiting mechanism (nonlinearities).

One major hypothesis in our model concerns the phase-change. It is known in the literature that significant phase-change may come from a thin liquid film left on the wall (on the vapor side) by the movement on the liquid plug [92, 34]. In our model, we chose not to include the liquid film explicitly (all the phase-change is represented as a thermal resistance, proportional to wall temperature at the meniscus). We did so for a few reasons. First, a simple thermal resistance makes it much easier to apply our mathematical techniques. Second, a simple thermal resistance captures the basic linear role of the phase-change (including from a thin-film) which is to produce a positive feedback force. Third, the thin-film modeling is not necessarily more accurate nor more general than our model since, in applications, the phase-change could be controlled to increase the performance by various means, such that it differs significantly from a thin liquid film. For all these reasons, our basic model provides a good basis for an initial study and for further investigations. With that said, we note that a different phase-change (from a thin-liquid film, a groove, microstructures, etc.) could affect the instability mechanism and also introduce new nonlinearities.

Let's now mention a few additional physics which could be added to our model (last two were included in [112]). Those physics will be negligible or not depending on the parameters of the system. First, we could allow the wall temperature T_w to vary over time (e.g. imposed heat flux instead). We could also consider the variations of saturation temperature $T_{g,sat}$ when variations of pressure are large enough (Clausius-Clapeyron relation, see [112, Sec. IIB]). Finally, we could assume the temperature of vapor T_g to vary over time (see [112, Sec. II]).

4.5 Conclusion

In this paper, we answered the question of what limits the oscillations amplitude by uncovering a limiting mechanism, produced by nonlinearities. To do so, we first found an approximate analytical solution of the nonlinear differential equations describing the

SBPHP dynamics, based on center manifold reduction and normal form techniques. We described how, during startup, the oscillations amplitude first increases but then saturates at a given value, reaching a steady-state regime corresponding to a stable (attractive) limit cycle. We also showed that the limiting mechanism is due to nonlinearities. Our model includes two nonlinearities, the pressure and the phase-change nonlinearities. We showed that the pressure nonlinearity always contributes to the saturation of the amplitude while the phase-change nonlinearity contributes to the saturation of the amplitude under some conditions. We then analyzed how to control the oscillations amplitude. We found that one can increase the amplitude by increasing the instability mechanism and reducing the limiting mechanism (nonlinearities). The SBPHP dynamics is best understood as the interplay of an instability mechanism which pushes for an increase of the oscillations amplitude and a limiting mechanism produced by nonlinearities, which limits it. We found that increasing the instability is more effective close to the instability threshold while reducing the nonlinearities is more effective far from it (at large amplitude). By either increasing the phase-change or decreasing the friction, the instability mechanism is increased and the limiting mechanism is reduced, such that the oscillations amplitude can be greatly increased. Our approach also highlights some new and promising research paths. One would be to investigate methods to better control the phase-change, to increase the oscillations amplitude. Future research could also be undertaken on specific devices to explore if other nonlinearities are present, beyond the phase-change and pressure nonlinearities studied herein.

Acknowledgements

We are grateful to our colleagues Nooshin Karami, Étienne Léveillé and Ali Hossein Nikkhah for discussions on the subject. A special thanks to Nooshin Karami who also provided helpful comments on the manuscript. We also acknowledge financial support from the NSERC through the Scholarship and Discovery Programs (Canada).

Data Availability Statement

The dataset analyzed during the current study is made available in the supplementary materials.

Conflict of Interest

The authors declare that they have no conflict of interest.

CHAPTER 5

ACCURATE SOLUTION FOR THE STEADY-STATE

5.1 Introduction

In this chapter, I investigate the dynamics of the system in the steady-state (limit cycle), from low to large oscillation amplitudes using numerical continuation and I obtain accurate expressions for the dynamics, using analytical and semi-analytical approaches, for each nonlinearities individually and valid for a large range of the parameters. So far, we have the normal form approximation as an analytical solution describing the dynamics (chapter 4). However, this approximation is only valid close to the instability threshold (for small enough instability number Π). We would like to know what happens has we go further beyond the instability threshold, how the dynamics looks like as we increase Π and how it can be controlled. We answer these questions here, by a combination of numerical, analytical and semi-analytical techniques. Understanding how to control the dynamics is interesting in itself. The analytical approximations we obtain will also be useful to evaluate the performance for energy harvesting applications (chapter 6).

So, we may first ask: why is the normal form not valid anymore for a large enough instability number Π? One important approximation in the normal form approach is to consider not the full vector field, but its Taylor expansion (Order 3). One can see in fig. 5.1 how the Taylor expansion of the two main functions in the vector field is quite a poor approximation for a large enough amplitude. Thus, one cannot expect the normal form to perform well far from the instability threshold. In this chapter, we will use the averaging technique instead of the normal form. Averaging is typically applied to the Taylor expanded vector field, but doing so would not lead to more accurate results than the normal form. Here, we apply averaging to the full vector field. By doing so, we will obtain a very accurate, as well as compact, solution for the phase-change nonlinearity. For the pressure nonlinearity, averaging does not work as well. In order to still obtain a useful expression of the dynamics, I build a Fourier series expression inspired by the averaging approximation, with parameters fitted from the numerical results. The expression obtained is very accurate for a large range of Π values and within an acceptable range of ζ_f values.

This chapter is structured as follows. I will first briefly present the model and the general form of the solution on the limit cycle (section 5.2) and then study the phase-change nonlinearity alone (section 5.3) and the pressure nonlinearity alone (section 5.4). For each nonlinearity, we will first study the dynamics numerically, using numerical continuation. We will look at the waveforms, perform a spectral analysis over the numerical continuation and look at the overall oscillations amplitude. We will then apply averaging. We will compare to the numerical continuation the normal form, the averaging and the fit (for the pressure nonlinearity). Finally, we will discuss our understanding of the dynamics in the light of our results. In section 5.5, we will discuss why the averaging performed as well for the phase-change nonlinearity and not as well for the pressure nonlinearity. The work here preceded the numerical study of the amplitude in chapter 4. It was actually informative into the choice of how to study and present the amplitude there.

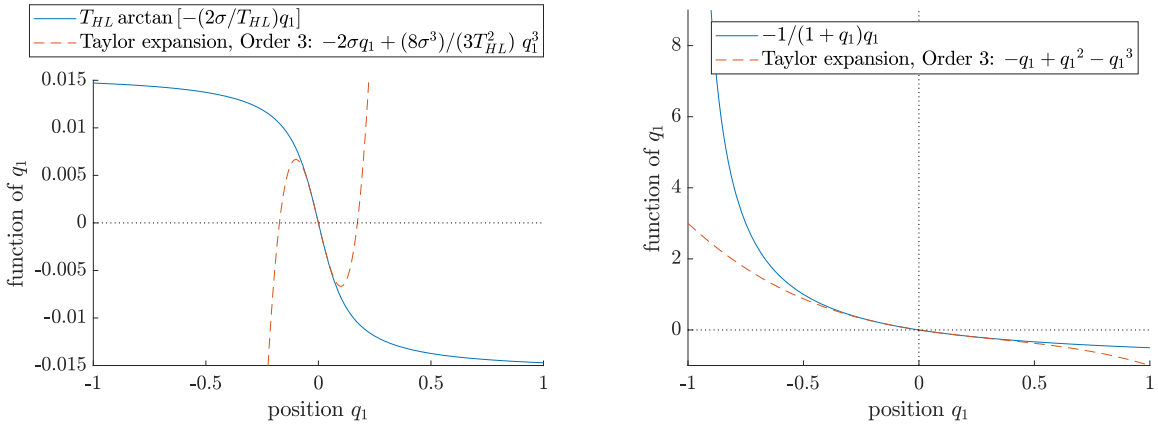

(a) (b)

Figure 5.1 Functions appearing in the vector field and their order three Taylor expansion: a) $T_{HL}\arctan\left[-2(\sigma/T_{HL})q_1\right]$ (phase-change nonlinearity) and b) $-1/(1+q_1)$.

5.2 The Model

The system of differential equations is given by eq. (4.14), repeated here for convenience:

$$\dot{q}_1 = q_2, \tag{5.1a}$$

$$\dot{q}_2 = \left[1 - c_P \left(\frac{q_1}{1+q_1}\right)\right](-q_1 + q_3) - 2\,\zeta_f\; q_2, \tag{5.1b}$$

$$\dot{q}_3 = -2\sigma\,(1-c_T)\; q_1 + c_T\, T_{HL} \left(\arctan\left[-\left(\frac{2\sigma}{T_{HL}\cos^2[\psi/2]}\right) q_1 - \tan\left[\frac{\psi}{2}\right]\right] + \frac{\psi}{2}\right), \tag{5.1c}$$

with q_1, q_2 and q_3 the dimensionless perturbations relative to the equilibrium for the meniscus position, the liquid plug velocity and the mass of vapor, respectively. Also, σ is the phase-change coefficient, ζ_f is the friction coefficient and T_{HL} is a parameter related to the temperature difference between the heat source and the heat sink (see eq. (4.8)). One can study only the phase-change nonlinearity by considering $c_T = 1$ and $c_P = 0$ or only the pressure nonlinearity, by considering $c_T = 0$ and $c_P = 1$. This system has one equilibrium at $q_1 = q_2 = q_3 = 0$. For $\Pi = \sigma/\zeta_f > 1$, the equilibrium is unstable and the system eventually settles on a limit cycle. On the limit cycle, the dynamics is periodic. It can therefore be represented by a Fourier series. The position q_1 is given by:

$$q_1 = \tfrac{1}{2}A_0 + \sum_{k=1}^{k=\infty} A_k \,\sin\left(k\theta + \varphi_k\right) \quad \text{with: } \theta(\tau) = \Omega\tau\ . \tag{5.2}$$

The amplitudes A_k and the angular frequency Ω vary in terms of the parameters σ, ζ_f and T_{HL}.

5.3 Phase-change Nonlinearity

5.3.1 Numerical

To study the limit cycle, we use numerical continuation (using the Matlab package MatCont [23]). We make a first continuation along Π and detect the Hopf bifurcation from which the limit cycle is detected. We then make a continuation of the limit cycle, meaning that, as we increase Π, we follow the limit cycle. Within the continuation, the limit cycle is detected by orthogonal collocation. Figure 5.2 shows the limit cycles detected during the continuation.

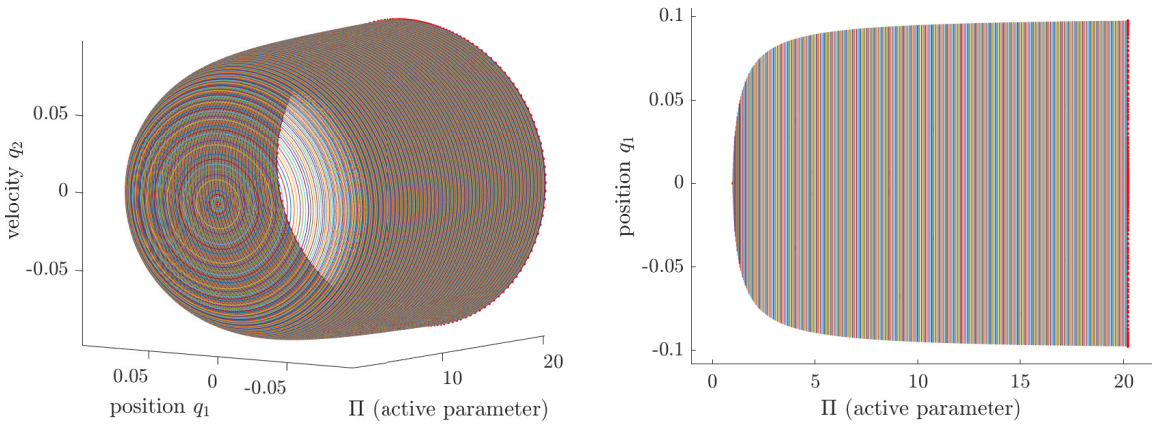

(a) 3D view

(b) 2D view

Figure 5.2 continuation of the limit cycle (two views are displayed) . In this run, 400 limit cycles were generated (each closed line is a limit cycle).

We now look at the waveforms. In fig. 5.3, the evolution of the phase-space variables q_1, q_2 and q_3 on the limit cycle, over time (for one period) and for various Π values is displayed. We can make a few observations. First, we clearly see that the amplitude increases as a function of Π. Second, both the position q_1 and the velocity q_2 seem close to sinusoidal even for large Π values. However, the mass of vapor q_3 approaches a triangular profile.

The phase-change nonlinearity leads to a saturation of the phase-change rate $\dot{q}_3$, which is a function of the position q_1, exclusively. We can see that clearly by comparing the nonlinear phase-change rate $\dot{q}_3$ to the linearized one, as a function of time (fig. 5.4a) and as a function of q_1 (fig. 5.4b, which reproduce the atan function eq. (5.1c)).

In order to characterize the limit cycle solution, it is useful to look at the amplitudes A_k in the Fourier series (eq. (5.2)). The first few A_k are shown in fig. 5.5, as a function of Π. First, we see that A_1 is much larger than the other components, even for large Π. Thus, the solution q_1 remains almost perfectly sinusoidal. Looking at the amplitude A_1 (the fundamental), we see that it increases sharply as a function of Π close to $\Pi = 1$ and then saturates for Π going to infinity. We will study how the amplitude varies as function of the other parameters (ζ_f and T_{HL}) in the analytical solution section.

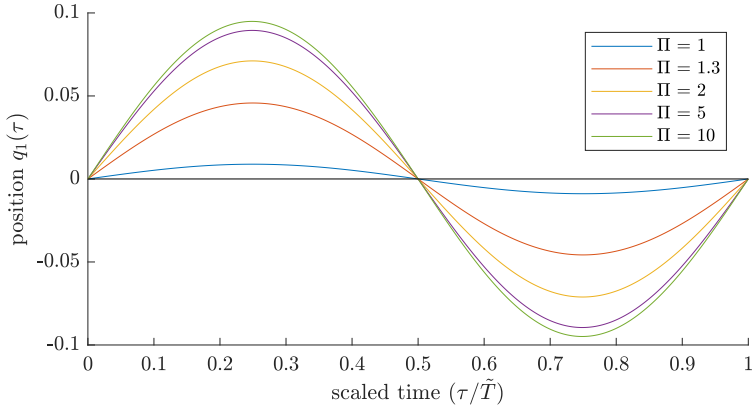

(a)

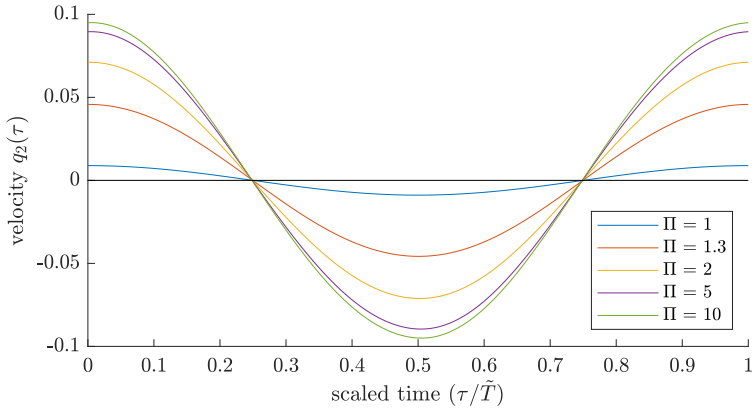

(b)

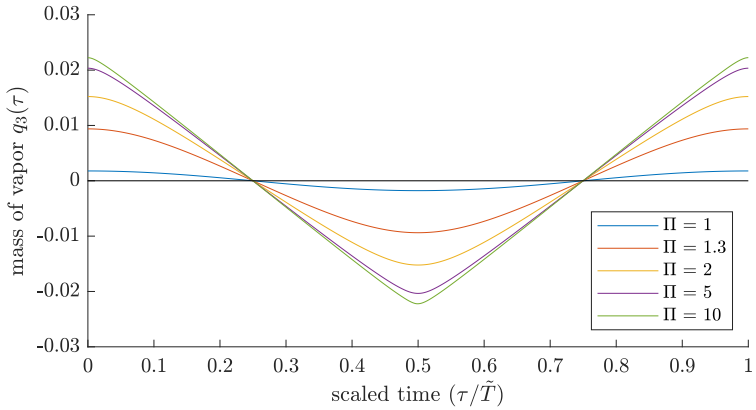

(c)

Figure 5.3 Phase-space variables q_1, q_2 and q_3, as a function of time, over one limit cycle, for various Π values, with $\zeta_f = 0.10$ and $T_{HL} = 0.01$.

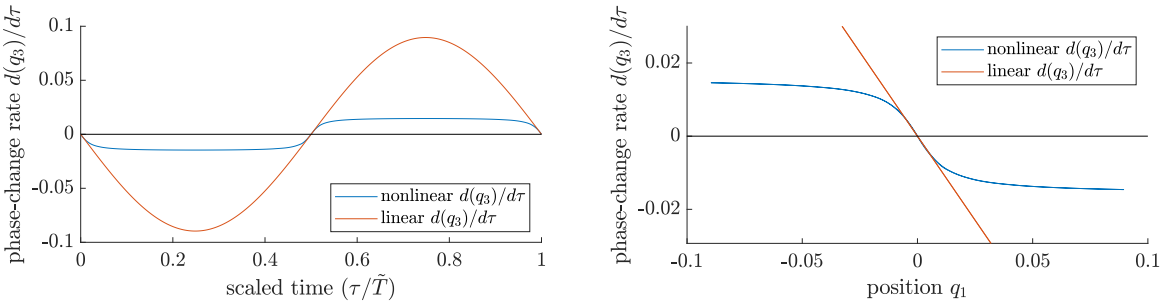

(a) (b)

Figure 5.4 linear and nonlinear phase-change rate as function of time (a) or position q_1 (b).

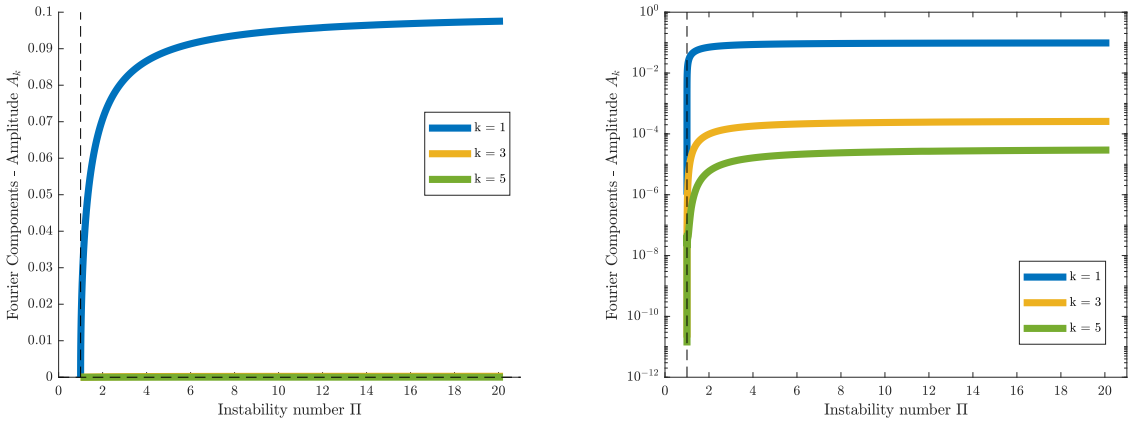

(a) (b)

Figure 5.5 Amplitude A_k of the Fourier series for q_1, as a function of Π, obtained by numerical continuation,, in linear scale (a) and logarithmic scale (b), to highlight the amplitudes of the harmonics; A_2 and A_4 are too small to be accurately represented here.

5.3.2 Analytical Solution

We now proceed to apply the averaging technique to the system of equations (see appendix C for details). The approach initially follows the same procedure as the normal form: we consider δ as a variable and add the vector field equation $\dot{\delta} = 0$, we align the system along its eigenbasis (standard form) and apply the center manifold reduction. We then proceed with the averaging steps. The system is transformed into polar coordinates, a small parameter ε is introduced and the variables are scaled. We then average the polar vector field. We first consider the asymptotic expansion, compare with normal forms and verify that the topological equivalence is preserved within the flat center manifold approximation. We then average the full vector field and solve for the amplitude and angular frequency of the limit cycle. We finally obtain the following approximation on the limit cycle:

$$\begin{bmatrix} q_1 \\ q_2 \\ q_3 \end{bmatrix} = \begin{bmatrix} -r_{LC}\,\cos(\theta) \\ +r_{LC}\,\sin(\theta) \\ +2\zeta_f\, r_{LC}\,\sin(\theta) \end{bmatrix} , \tag{5.3}$$

where r_{LC} is the amplitude and where $\theta = \Omega\tau + \varphi$, with Ω the angular frequency. We have that r_{LC} and Ω are given by the following:

$$r_{LC} = \frac{T_{HL}}{\zeta_f}\sqrt{\frac{\Pi - 1}{\Pi}} , \tag{5.4a}$$

$$\Omega = 1 , \tag{5.4b}$$

which differs from normal form (eq. (4.27a)).

Let's now compare with numerical results, starting by the amplitude as a function of the instability number Π and for various T_{HL}/ζ_f values. For the amplitude, we consider the radius of the limit cycle (r_{LC}), given directly by the analytical formula and which can be easily computed from the numerical data. Numerical values for the amplitude, along Π are shown by the thick solid lines in fig. 5.6. The amplitudes from normal form are shown by the dotted lines. Although the normal form predictions are valid for Π close to 1, they quickly diverge from the numerical results as Π increases. Averaging results are shown by the solid black lines. They match the numerical results almost perfectly, and are valid for all Π values. For the angular frequency Ω, we find that it is indeed always equal to 1, as predicted by averaging (fig. 5.7).

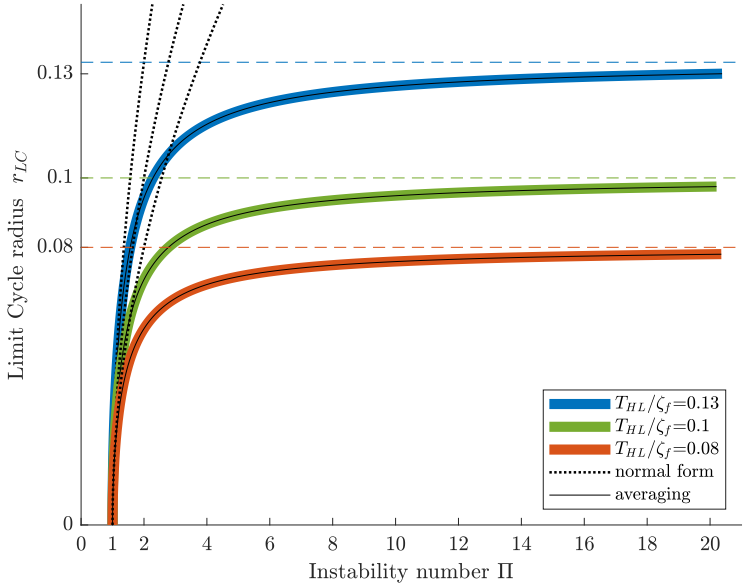

Figure 5.6 Oscillations amplitude (given by the limit cycle radius r_{LC}) as a function of Π and for various ζ_f given by numerical continuation, normal form and averaging.

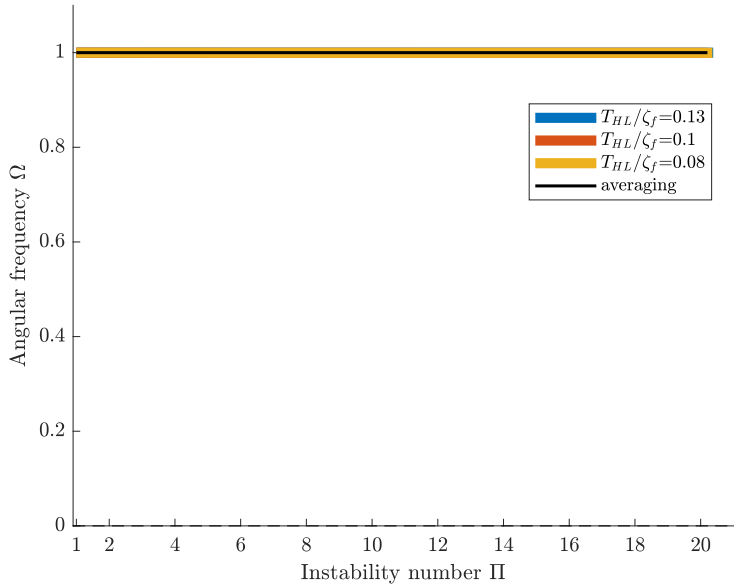

Figure 5.7 Angular frequency Ω as a function of Π and for various ζ_f given by numerical continuation, and averaging.

Let's now compare the waveform for a large instability number Π (fig. 5.8). We see that averaging reproduces almost perfectly the position q_1 and velocity q_2. The harmonics are more significant in the numerical solution for the mass of vapor q_3, and there is thus a small

discrepancy with the averaging result (which is purely sinusoidal). The harmonics are even more important in the evaporation rate $\dot{q}_3$ and merely deriving in time the averaging solution for q_3 leads to a poor approximation of the waveform (fig. 5.8d). However, substitution of the averaging solution for q_1 into the differential equation for $\dot{q}_3$ (eq. (5.1c))leads to an almost perfect representation of the phase-change rate. The differential equation produces the required harmonics with the nonlinearity (arctan function). Thus, we conclude that we obtained expressions able to reproduce very accurately the waveforms, using averaging.

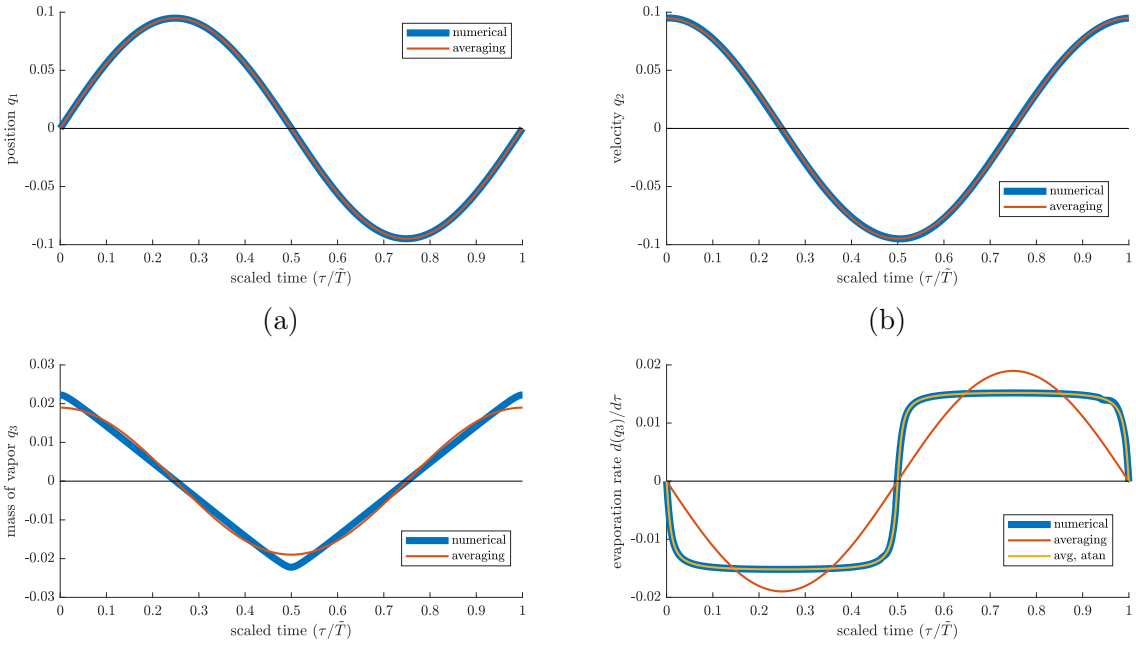

Figure 5.8 Comparison of the waveforms obtained numerically and from averaging, for the position (q_1), the velocity (q_2), the mass of vapor (q_3) and the phase-change rate ($\dot{q}_3$).

5.3.3 Analysis of the Solution

We now analyze the amplitude, based on the averaging result. First note that r_{LC} can be written as: $r_{LC} = T_{HL}/\zeta_f \sqrt{1 - 1/\Pi}$. Clearly, r_{LC} is purely imaginary for $\Pi < 1$ (real part equal zero). At $\Pi = 1$, r_{LC} is 0. Then, r_{LC} increases sharply and finally tends to an asymptote at T_{HL}/ζ_f for $\Pi \to \infty$. We can see that in fig. 5.6. We see that r_{LC} is very sensitive to Π for Π close to 1. There, increasing $\Pi = \sigma/\zeta_f$ by either increasing σ or decreasing ζ_f leads to a sharp increase in amplitude but r_{LC} is barely affected by a change in T_{HL}. By contrast, for large Π, r_{LC} is barely sensitive to Π and increasing the phase-change slope σ has almost no impact on the amplitude. One can however increase r_{LC} by either increasing the phase-change limits T_{HL} or by decreasing the friction coefficient ζ_f. We conclude that close to the instability threshold (Π close to one), the system is dominated by the linear terms while, far from the instability threshold, the system is dominated by the nonlinearity (the factor T_{HL}/ζ_f).

5.4 Pressure Nonlinearity

For the pressure nonlinearity, we proceed similarly than for the phase-change nonlinearity.

5.4.1 Numerical

Numerical continuation of the limit cycle is shown in fig. 5.9. Let's now look at the waveforms. In fig. 5.10, the evolution of the phase-space variables q_1, q_2 and q_3 on the limit cycle, over time (for one period) and for various Π values is displayed. We can see a general trend: the amplitude for the position q_1 and for the velocity q_2 increases with Π. For q_1, for large Π (from 1.5 to 2), q_1 does not go as far in the positive direction but goes further in the negative direction. Importantly, contrary to the phase-change nonlinearity, the dynamics evolves from purely sinusoidal to not purely sinusoidal as Π is increased.

We can see that more clearly by a spectral analysis (fig. 5.11). We see that although A_1 is the large component, the other components becomes significative for a large enough Π. This is why the solution is not purely sinusoidal. As for the phase-change nonlinearity, we see that the fundamental (A_1) increases sharply as function of Π close to $\Pi = 1$ and then saturates for Π going to infinity. Interestingly, we see that the maximum value of A_1 is reached at a finite Π. This is not the full amplitude of q_1 however, which also depends on the other A_k.

For the pressure nonlinearity, there are only two parameters in the system, Π and ζ_f. In fig. 5.12, we display the fundamental A_1 for various ζ_f. For $\zeta_f < 0.25$, A_1 is barely affected by ζ_f (for a fixed Π). We see some effect for very large ζ_f, but only for $1 < \Pi < 1.8$.

At large enough Π, all the curves converge and the effect of ζ_f alone is not noticeable anymore.

Finally, it is interesting to not only look at the components of the Fourier series but at the overall size of the limit cycle. We look at the semi-amplitude (peak-to-peak amplitude divided by two) for q_1, q_2 and q_3 in fig. 5.13. We find that the semi-amplitude in q_1 saturates while the semi-amplitude in the velocity q_2 does not (at least within the range studied). The averaged radius of the limit cycle r_{LC} falls between the semi-amplitude in q_1 and q_2.

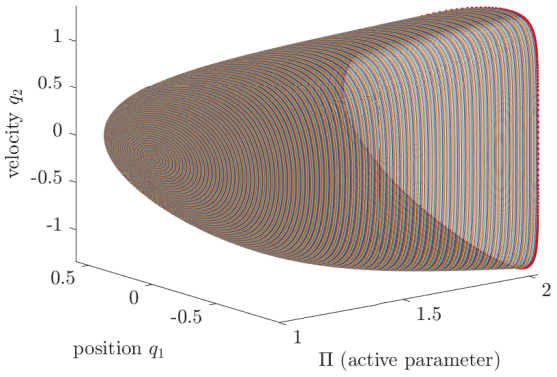

(a) 3D view

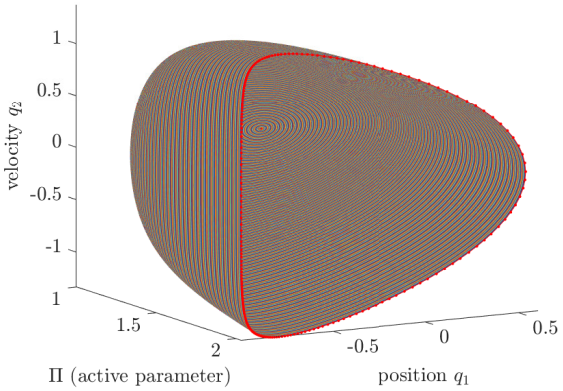

(b) 3D view

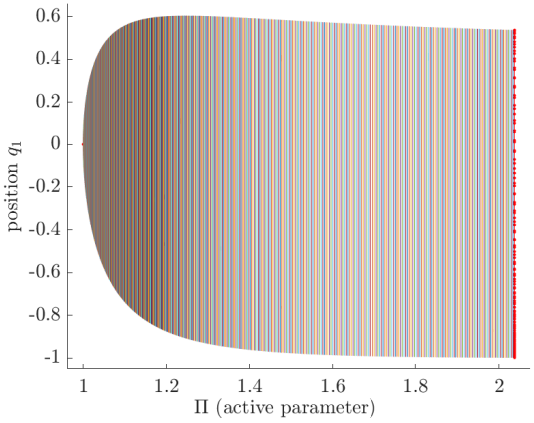

(c) 2D view

Figure 5.9 Continuation of the limit cycle (with different views displayed). In this run, 540 limit cycles were generated (each closed line is a limit cycle).

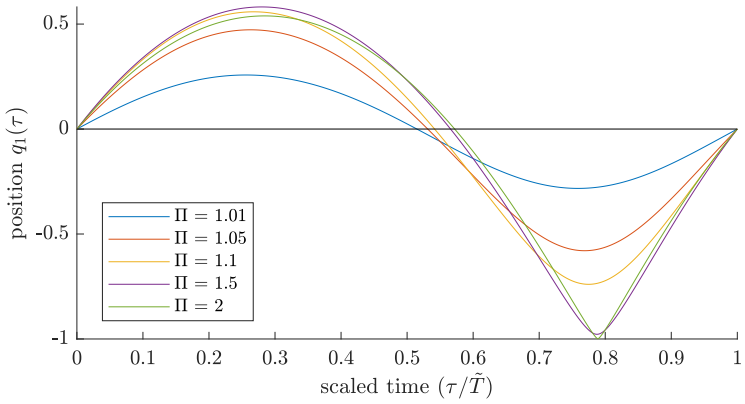

(a)

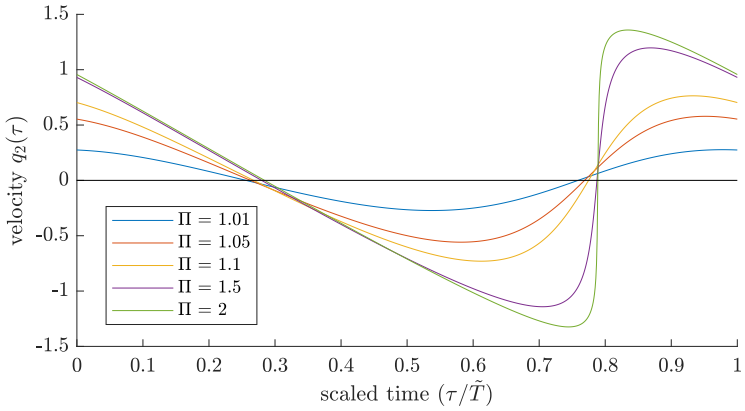

(b)

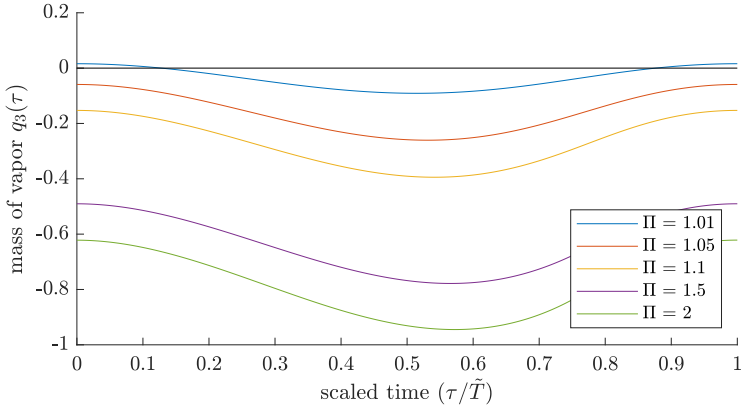

(c)

Figure 5.10 Phase-space variables q_1, q_2 and q_3, as a function of time, over one limit cycle, for various Π values, with $\zeta_f = 0.10$.

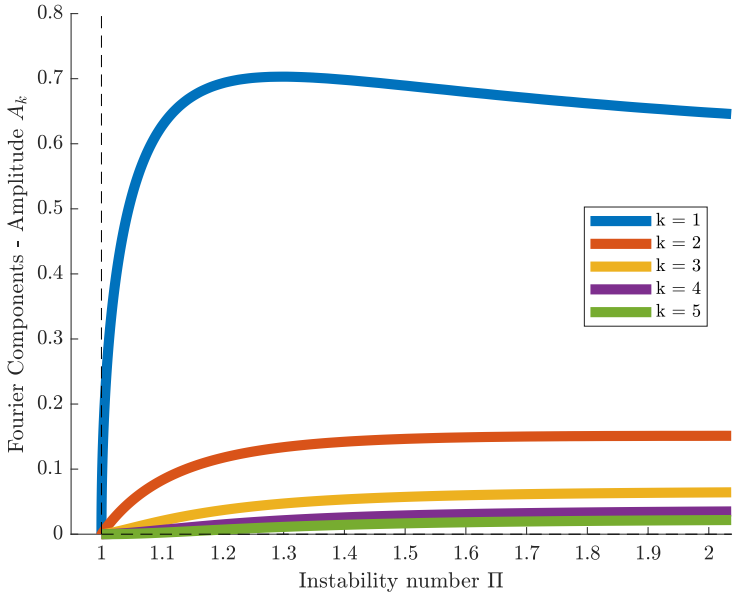

Figure 5.11 Amplitude A_k of the Fourier series for q_1, as a function of Π, obtained by numerical continuation.

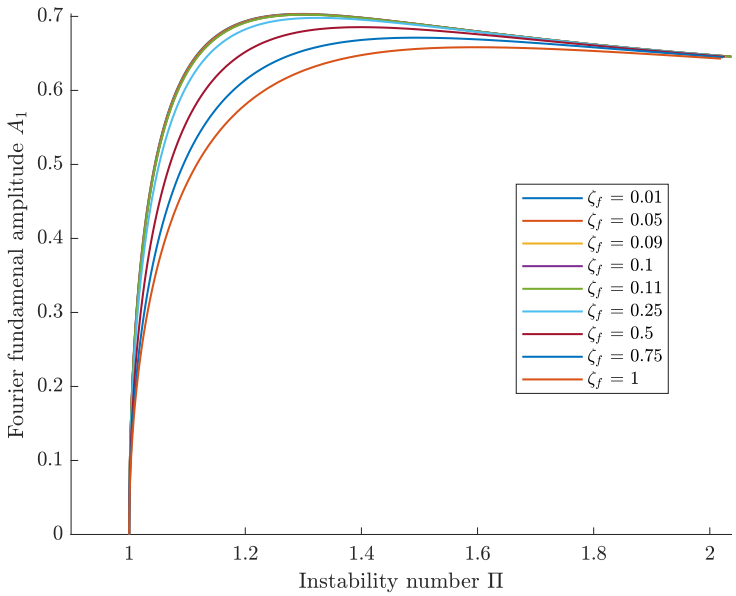

Figure 5.12 Amplitude A_1 of the Fourier series for q_1, as a function of Π for various ζ_f, obtained by numerical continuation.

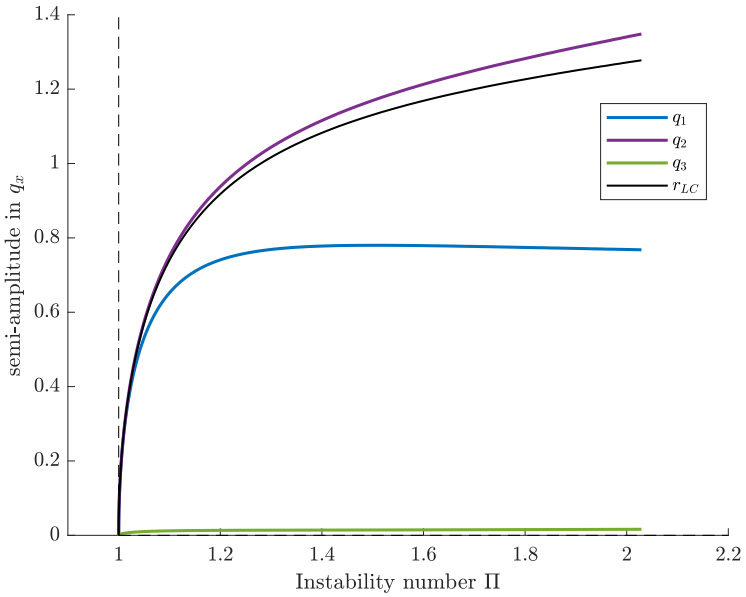

Figure 5.13 Semi-amplitude for q_1, q_2 and q_3, as a function of Π, for $\zeta_f = 0.01$, obtained by numerical continuation.

5.4.2 Analytical Solution

We perform averaging for the pressure nonlinearity as we did with the phase-change nonlinearity [1]. However, the test to validate the flat center manifold assumption turns out negative, which is the first sign of trouble. Proceeding nonetheless, we find:

$$\begin{bmatrix} q_1 \\ q_2 \\ q_3 \end{bmatrix} = \begin{bmatrix} -r_{LC}\,\cos(\theta) \\ +r_{LC}\,\sin(\theta) \\ +2\sigma\, r_{LC}\,\sin(\theta) \end{bmatrix} , \tag{5.5}$$

where again, r_{LC} is the amplitude, $\theta = \Omega\tau + \varphi$, with Ω the angular frequency and where we have that r_{LC} and Ω are given by the following:

$$r_{LC} = \sqrt{\frac{\Pi^2 - 1}{\Pi^2}} , \tag{5.6a}$$

$$\Omega = \frac{\Pi^2 + {}^1\!/_2\,\Pi + {}^1\!/_2}{\Pi + 1} , \tag{5.6b}$$

which differs from normal form (eq. (4.27b)). In fig. 5.14, we can compare the amplitude r_{LC} from numerical continuation, normal form, and averaging, as a function of Π and for various ζ_f. We see that r_{LC} from numerical continuation increases sharply from the instability threshold $\Pi = 0$ and keeps increasing afterwards. We see that changing ζ_f does change r_{LC}, for sufficiently large Π. Here, however we consider a very large range for ζ_f (which is typically below 0.10). The normal form solution works well for small Π, but quickly diverges as Π increases. It however captures the effect of various ζ_f. The averaging solution works fine for large ζ_f (and does not increase excessively as the normal form) but does not perform as well for small ζ_f. In contrast with the normal form solution, the averaging solution does not capture the explicit dependency over ζ_f (there is only one line for averaging in fig. 5.14). It turns out that this is because we made the approximation of a flat center manifold to get the averaging solution [2].

I tried various approaches to get a more accurate analytical solution than normal form and the averaging (when compared to numerical continuation) . These included averaging coupled with linear and nonlinear transformations, perturbation of the nonlinear conservative oscillator, harmonic balance and matched asymptotics (for a distinct solution at

1. With a few exceptions: for the pressure nonlinearity, one can get better averaging results by a preliminary transformation (introducing $q_3^\star = q_3/(-2\sigma)$) and with an appropriate scaling of the eigenvectors.

2. If we perform averaging with a Taylor expansion of the vector field without this assumption, we get a solution which depends on ζ_f explicitly, just like the normal form.

large Π). I was not successful with these approaches however and had to eventually give up. I still wonder if there is a way one could get a accurate solution for the limit cycle analytically. In general, finding accurate analytical solutions for limit cycle is an uncharted territory in applied mathematics, which makes progress difficult for any specific applications. Mathematical approaches to obtain accurate analytical solutions for limit cycles would be extremely useful in engineering, since limit cycles appears in many applications.

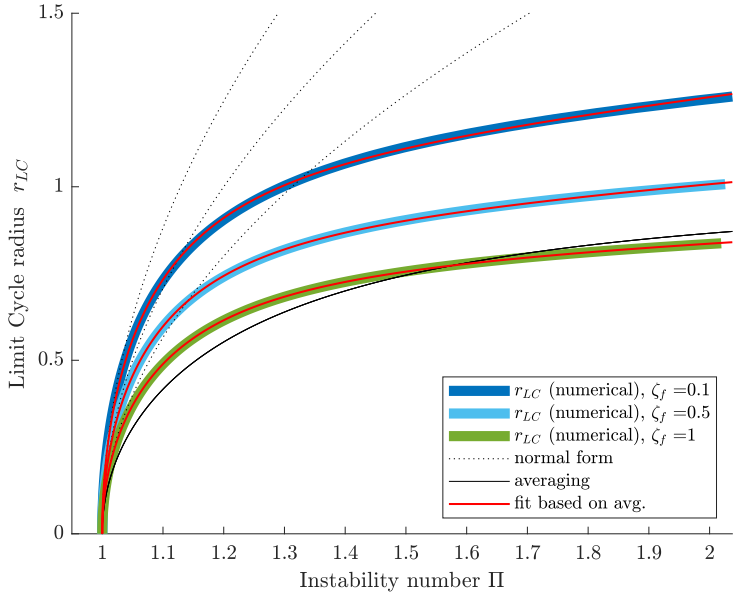

Figure 5.14 Oscillations amplitude (given by the limit cycle radius r_{LC}) as a function of Π and for various ζ_f given by numerical continuation, by normal form, by averaging and by a modified expression (see text).

Given the relative unsuccess of the analytical approaches, I looked for semi-analytical solutions, meaning solutions based on the analytical solution but improved by the introduction of some parameters, which are fitted using numerical results. For example, would it be possible to improve the expression of r_{LC} given by averaging? We can add a few parameters in the r_{LC} approximation to make it work better. I ended up with $r_{LC} = L\sqrt{(\Pi^{k_a+k_b}-1)/\Pi^{k_a}}$. Fitting the parameters L, k_a and k_b to the numerical curves gives the fit lines in fig. 5.14. We see that they match r_{LC} almost perfectly. Thus, if we could obtain expressions for those parameters in terms of ζ_f, we could get a accurate expression for r_{LC}. In this approach however, the solution remains purely sinusoidal and will necessarily fail to reproduce the harmonics seen in the waveforms. To get a accurate expression for the dynamics including the harmonics, I decided to develop an expression

for each components of the Fourier series solution eq. (5.2). I ended up with:

$$A_0 = 0 \ , \tag{5.7a}$$

$$A_k = a_k \left(1 + b_k e^{-\tau_k \Pi}\right) \left(\frac{\Pi^{n_k} - 1}{\Pi^{n_k}}\right)^{\frac{k}{2}} \quad \text{for } k \neq 0 \ , \tag{5.7b}$$

$$\Omega = \frac{p_1 \Pi^2 + p_2 \Pi + p_3}{\Pi + p_1 + p_2 + p_3 - 1} \ , \tag{5.7c}$$

$$\varphi_k = \begin{cases} \frac{\pi(1-k)}{2} + k\varphi_s & \text{for k odd,} \\ \frac{\pi(1-k)}{2} - \pi + k\varphi_s & \text{for k even.} \end{cases} \tag{5.7d}$$

In A_k, the parameters a_k, τ_k and n_k are fitted for each harmonics. To take into account the dependency in ζ_f, we express b_k as a function of ζ_f, also fitted. The expression for A_k is a generalization of eq. (5.6a). To construct the A_k expression, I started from the form $\sqrt{(\Pi^2 - 1)/\Pi^2}$ and generalized it by allowing the exponent to vary, added a prefactor, etc. In Ω, the parameters p_i are themselves expressed as functions of ζ_f, obtained by fitting. The expression for Ω is a generalization of eq. (5.6b). In φ_k, the parameter φ_s is the shift of the fundamental and can be chosen as desired (because the time reference is arbitrary). Thus, this solution is not purely sinusoidal, but includes harmonics.

In fig. 5.15, I compare the semi-analytical solution to the results obtained by numerical continuation. We see that they match perfectly, for all the harmonics. Our solution is able to produce the quasi-sinusoidal oscillations at low Π (where A_1 dominates) all the way to the dynamics with additional harmonics at higher Π. Our solution also predicts the angular frequency quite well (fig. 5.16). We can see how the solution matches the dynamics in fig. 5.17 where we compare the waveforms for $\Pi = 2$. The prediction for the position q_1 is very accurate, the prediction for the velocity q_2 is quite good (although we see the oscillations from the Fourier series) and the prediction for the mass of vapor q_3 is quite good as well [3]. The prediction for the phase-change rate $\dot{q}_3$ is very accurate (just like the position, given that $\dot{q}_3 = -2\sigma q_1$). Even more accurate results could be obtained by considering more harmonics. Relative to the fit, the averaging performs poorly.

3. Note that, for q_3 I used in the fit the mean value obtained from the numerical continuation (I did not fit that value, since it is rarely useful, we usually care about the phase-change rate).

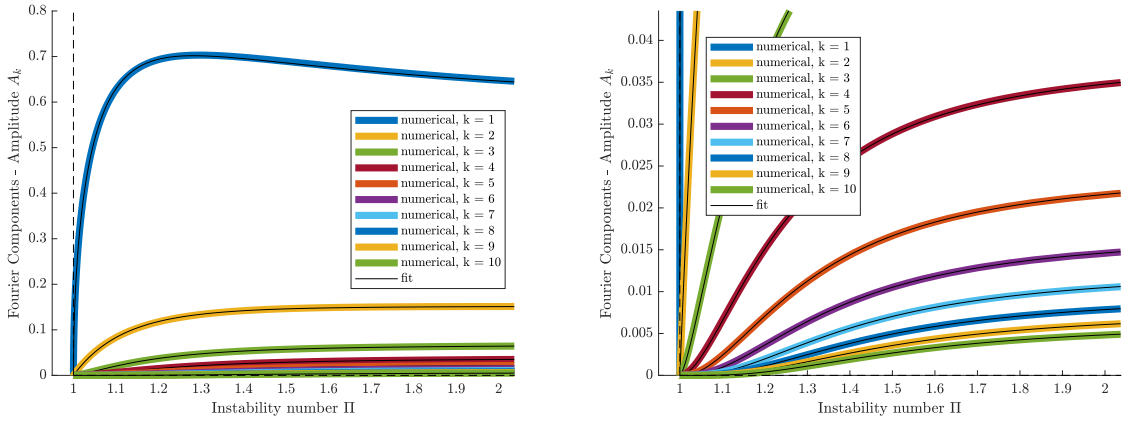

(a) (b)

Figure 5.15 Amplitude A_k of the Fourier series for q_1 for $\zeta_f = 0.10$ as a function of Π (b is a zoom in to show the higher order harmonics), obtained by numerical continuation (thick colored lines) and by the semi-analytical approach (thin black line).

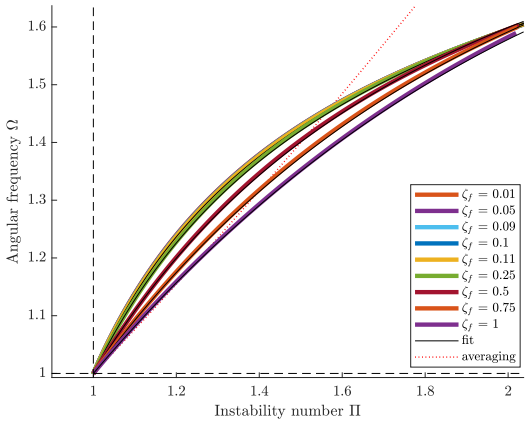

Figure 5.16 Angular frequency Ω, as a function of Π for various ζ_f,from numerical continuation (thick colored lines), averaging (red dotted line) and the semi-analytical approach (thin black line).

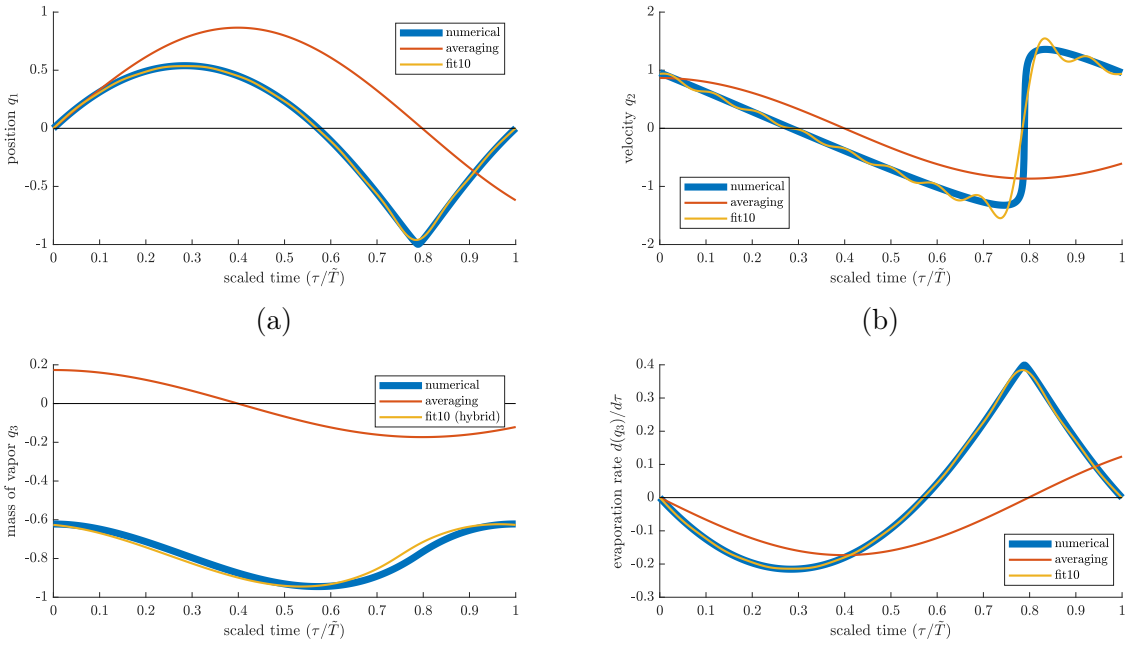

Figure 5.17 Comparison of the waveforms obtained numerically and from averaging, for the position (q_1), the velocity (q_2), the mass of vapor (q_3) and the phase-change rate ($\dot{q}_3$), with $\Pi = 2$ and $\zeta_f = 0.01$.

5.4.3 Analysis of the Solution

We now analyze the amplitude based on the averaging, the fit and the numerical results obtained above. For the pressure nonlinearity, there are only two parameters in the differential equations, the instability number Π (defined as $\Pi = \sigma/\zeta_f$) and the friction coefficient ζ_f. First, we note that, at $\Pi = 0$, the limit cycle radius r_{LC} is 0 but increases sharply as Π is increased further (the derivative $dr_{LC}/d\Pi$ is actually infinite for $\Pi \to 0^+$). The instability number Π can be increased by either increasing the phase-change coefficient σ or by decreasing the friction coefficient ζ_f. The amplitude is very sensitive to Π for Π close to 1. The effect of ζ_f alone (for a fixed Π) is not significative on the amplitude (see A_1 fig. 5.12). Large ζ_f are required to see an effect, and the change in amplitude only occurs within a range of Π ($1 < \Pi < 1.8$), the value at large Π is unaffected. This is to say that the effect of σ and ζ_f mostly comes from Π.

The amplitude in q_1 saturates as Π is increased at large values (see fig. 5.13). The amplitude in q_1 is constrained by the closed end in the negative direction (q_1 cannot go beyond -1) and it seems this also constrain the motion in the positive direction (possibly because the evaporation can only occur between $-1 < q_1 < 0$ and the evaporation and condensation must balance out on the limit cycle). Interestingly, the amplitude in the velocity q_2 keeps increasing.

For the pressure nonlinearity, there is no nonlinear parameter such as the phase-change limits T_{HL} for the phase-change nonlinearity. The pressure nonlinearity comes from the fact that the pressure rises nonlinearly as the liquid plug approaches the closed end. We could thus expect that the length of the liquid plug at the equilibrium $L_{g,0}$ would come into play: for very large $L_{g,0}$, the pressure nonlinearity effect should be felt only at large amplitudes. However, we found that the amplitude depends mostly on Π and Π is independent of $L_{g,0}$. So, why does not $L_{g,0}$ affect the amplitude? It turns out this is because we considered the *dimensionless* amplitude so far. We made the position dimensionless in terms of $L_{g,0}$. To get the *dimensional* amplitude, we must multiply the dimensionless one by $L_{g,0}$. One can expect that the *dimensional* amplitude for the pressure nonlinearity alone is roughly proportional to $L_{g,0}$.

5.5 Discussion

One might be surprised by how good the solution for averaging is for the phase-change nonlinearity, even far from the instability threshold. One may also wonder why the averaging does not work as well for the pressure nonlinearity. I would like to briefly provide my thoughts on the subject, even though I have not reached a definitive answer. I will

show below that the conservative system remains linear even for large amplitude, for the phase-change nonlinearity alone, while it becomes strongly nonlinear if the pressure nonlinearity is included. The averaging approach I considered is based on the solution of the linear conservative system and is thus unable to correctly predict the dynamics when the pressure nonlinearity is included.

Starting from the system of differential equations eq. (5.1), we have $\dot{q}_1 = q_2$ and the momentum balance given by:

$$\underbrace{\dot{q}_2 = -\left(\frac{1+(1-c_P)\,q_1}{1+q_1}\right) q_1}_{\text{Conservative system}} \underbrace{+\left(\frac{1+(1-c_P)\,q_1}{1+q_1}\right) q_3 - 2\,\zeta_f\; q_2}_{\text{injects/dissipates energy}} \;. \tag{5.8}$$

If we include the pressure nonlinearity, we have $c_P = 1$, so:

$$\underbrace{\dot{q}_2 = -\left(\frac{1}{1+q_1}\right) q_1}_{\text{Conservative system}} \underbrace{+\left(\frac{1}{1+q_1}\right) q_3 - 2\,\zeta_f\; q_2}_{\text{injects/dissipates energy}} \tag{5.9}$$

and if we exclude the pressure nonlinearity (e.g. we wish to study the phase-change nonlinearity alone), we have $c_P = 0$, so:

$$\underbrace{\dot{q}_2 = -q_1}_{\text{Conservative system}} \quad \underbrace{+q_3 - 2\,\zeta_f\; q_2}_{\text{injects/dissipates energy}} \;. \tag{5.10}$$

We will now apply a technique for conservative system which relates to an energy point of view, often described as *vector field possessing an integral* (see [124, chap.5, p.77]). This will enable us to find the closed trajectories in phase-space for the conservative system. We look at the conservative system alone in eq. (5.8), we assume there is no phase-change and no friction:

$$\underbrace{\underbrace{\dot{q}_2}_{\text{inertial term}} = \underbrace{-\left(\frac{1+(1-c_P)\,q_1}{1+q_1}\right) q_1}_{\text{nonlinear restoring force}}}_{\text{Conservative system}} \;. \tag{5.11}$$

The conservative system is composed of the inertial term $\dot{q}_2$ and the nonlinear restoring force. We can multiply both sides of this equation by $q_2 d\tau$ and integrate over time between τ_0 and τ_1, which leads to:

$$\Delta\widetilde{K} = -\Delta\widetilde{U}_r \tag{5.12}$$

with $\Delta\widetilde{K} = \widetilde{K}(\tau_1) - \widetilde{K}(\tau_0)$ and $\Delta\widetilde{U}_r = \widetilde{U}_r(\tau_i) - \widetilde{U}_r(\tau_0)$ and where $\widetilde{K}$ and $\widetilde{U}_r$ are the kinetic and potential energy respectively, defined as:

$$\widetilde{K}(\tau_i) = \tfrac{1}{2}\dot{q}_2^2 \ , \tag{5.13}$$

$$\widetilde{U}_r(\tau_i) = \tfrac{1}{2}{q_1}^2 + c_P\left(q_1 - \ln\left[1+q_1\right] - \tfrac{1}{2}{q_1}^2\right) \ . \tag{5.14}$$

We may define $\widetilde{E}_r = \widetilde{K} + \widetilde{U}_r$ as the energy of the resonator, leading to:

$$\widetilde{E}_r = \widetilde{K} + \widetilde{U}_r = \tfrac{1}{2}{q_2}^2 \ + \ \tfrac{1}{2}{q_1}^2 + c_P\left(q_1 - \ln\left[1+q_1\right] - \tfrac{1}{2}{q_1}^2\right) \ . \tag{5.15}$$

so that the equation $\Delta\widetilde{K} = -\Delta\widetilde{U}_r$ above becomes $\Delta\widetilde{E}_r = 0$; the energy of the resonator does not change over time, because the system is conservative. Assuming we fix the energy level $\widetilde{E}_r$ (initial conditions), we may solve eq. (5.15) for q_2:

$$q_2 = \pm\sqrt{2\widetilde{E}_r - {q_1}^2 - c_P\left(2q_1 - 2\ln\left[1+q_1\right] - {q_1}^2\right)} \ . \tag{5.16}$$

For the phase-change nonlinearity only, we have $c_P = 0$ and:

$$q_2 = \pm\sqrt{2\widetilde{E}_r - {q_1}^2} \ . \tag{5.17}$$

while, if we include the pressure nonlinearity, we have $c_P = 1$ and:

$$q_2 = \pm\sqrt{2\widetilde{E}_r - 2q_1 - 2\ln\left[1+q_1\right]} \ . \tag{5.18}$$

Equations (5.16) to (5.18) describe the orbits the system follows in the phase-space (q_1, q_2). This is shown in fig. 5.18, where the solid lines and dashed lines include and exclude the pressure nonlinearity, respectively. Various orbits, corresponding to various energy level $\widetilde{E}_r$ are shown. If the pressure nonlinearity is excluded, the orbits are circles (eq. (5.17) is the equation of a circle, with a radius $r = \sqrt{2\widetilde{E}_r}$). If the pressure nonlinearity is included, the orbits given by eq. (5.18) look like circles for small $\widetilde{E}_r$, but look much different as $\widetilde{E}_r$ is increased. We remark that these orbits look remarkably similar to the limit cycles with or without the pressure nonlinearity (see figs. 4.5a and 4.5b).

Now, we may see the complete system described by eq. (5.8) as a conservative system plus a perturbation which consists in injection/dissipation of energy. We may view the injection/dissipation of energy as making the system slowly move from one energy level $\widetilde{E}_r$ to another, with the dynamics on one energy level $\widetilde{E}_r$ being well described by the

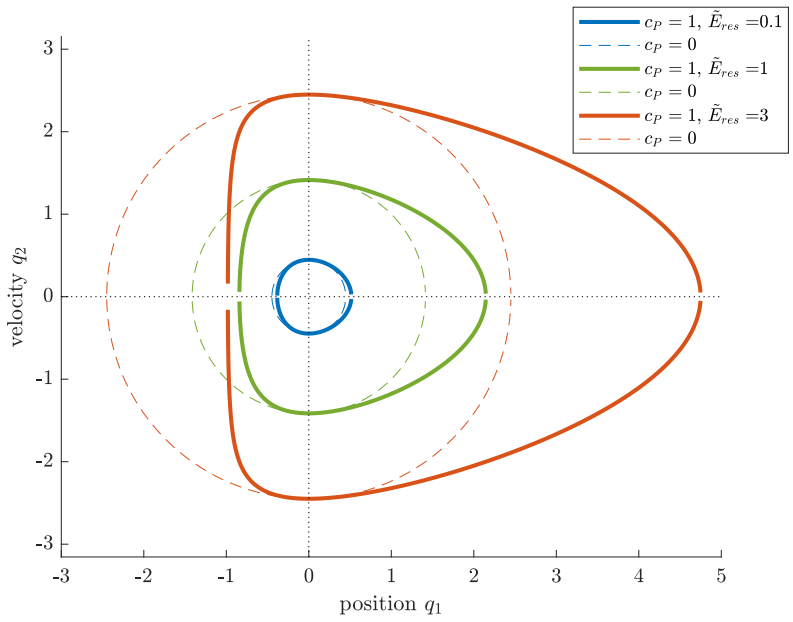

Figure 5.18 Orbits in phase-space for the conservative system with pressure nonlinearity (dashed lines) or phase-change nonlinearity (solid lines).

conservative system. For large instability numbers $\Pi = \sigma/\zeta_f$, this might not be true during the startup, but might still be true on the limit cycle itself, if we simply assume that the injection and the dissipation of energy cancel out on the limit cycle (and, additionally, do not produce a significant change of energy within one cycle). If this is correct, the dynamics on the limit cycle is well described by the conservative system (by eq. (5.15)). This is reminiscent of the approach taken by averaging where one considers the linear solution of the conservative system, but then allows the amplitude to vary slowly, based on the perturbation. Importantly, in averaging, a further assumption is usually [4] taken: one considers the solution of the *linearized* conservative system, with $q_1 = r\cos(\theta)$ and $q_2 = -r\sin(\theta)$ for example. This solution corresponds to circles in the phase-space.

Now, if we look at the system without the pressure nonlinearity ($c_P = 0$), the momentum balance is given by eq. (5.10). If the injection/dissipation of energy can be neglected on the limit cycle, than the momentum balance is linear. The solution is thus sinusoidal and corresponds to circles in phase-plane (q_1, q_2). We found numerically that, indeed, the limit cycles look like circles even for large Π (fig. 4.5b). This is why I believe the averaging solution works so well. By contrast, the momentum balance with the pressure nonlinearity ($c_P = 1$), given by eq. (5.9), is nonlinear even if the injection/dissipation

4. Coppola and Rand [18] were able to study the nonlinear system $\ddot{x} + \alpha x + \beta x^3 + \varepsilon g(x, \dot{x}) = 0$ without assuming β small. They did so by applying the variations of parameters to the solution of the nonlinear system with $\varepsilon = 0$, which is given by elliptic functions.

of energy can be neglected. The solution is therefore not sinusoidal if the amplitude is large enough. The orbits are not circular, but given by eq. (5.18). This is why I believe the averaging solution does not work as well. In a weakly nonlinear regime (small Π) the averaging will perform correctly, but as Π is increased, the sinusoidal solution leading to circular orbits does not match the conservative system dynamics anymore. So, to summarize, the averaging solution is the correct solution of the conservative system without the pressure nonlinearity, even at large amplitude, while the averaging solution is not the correct solution of the conservative system when the pressure nonlinearity is included, if the amplitude is large. In this explanation, I assume that the injection and dissipation of energy can be neglected on the limit cycle. This would have to be verified to validate the explanation.

5.6 Conclusion

In this chapter, I investigated the dynamics of the system on the steady-state using numerical continuation over a large range of the parameters involved, studying small to large oscillations amplitudes. I also obtained accurate analytical and semi-analytical formulas describing the dynamics. I studied each nonlinearities individually.

Phase-change nonlinearity alone. The position and the velocity remained quite sinusoidal but harmonics were more important in the mass of vapor q_3 and in the evaporation rate $\dot{q}_3$. I used averaging to obtain a accurate analytical formula describing the dynamics. I found that one can increase the oscillations amplitude by increasing the instability number, either by increasing the phase-change coefficient σ or decreasing the friction coefficient ζ_f. For large Π, the amplitude can be increased furthermore by decreasing ζ_f or by increasing the phase-change limit T_{HL}. The dimensionless angular frequency Ω is a constant (meaning the dimensional angular frequency is unaffected by the nonlinearity).

Pressure nonlinearity alone. The dynamics transitions from sinusoidal to not sinusoidal (bouncing regime, significative harmonics) as Π is increased. I generalized the averaging solution into a Fourier series approximation where the parameters were fitted using the numerical continuation, leading to a accurate approximation fo the dynamics including the harmonics. I found that one can increase the oscillations amplitude by increasing the Π, either by increasing the phase-change coefficient σ or decreasing the friction coefficient ζ_f. When considering the *dimensional* amplitude, one finds that it can also be increased by increasing the length of vapor $L_{g,0}$. The dimensionless angular frequency Ω grows with Π (meaning the dimensional angular frequency would be higher at higher amplitude).

The solution obtained here will be used to study the power output in SOFHE in chapter 6.

CHAPTER 6

HOW AN ENERGY HARVESTING DEVICE BEHAVES

Avant-propos

Auteurs et affiliation:

Albert Tessier-Poirier: étudiant au doctorat à l'Université de Sherbrooke (1,2).

Nooshin Karami: étudiante au doctorat à l'Université de Sherbrooke (1,2).

Richard H. Rand: professeur à Cornell University (3,4).

Luc G. Fréchette: professeur à l'Université de Sherbrooke (1,2).

1) Institut Interdisciplinaire d'Innovation Technologique (3IT), Université de Sherbrooke, Sherbrooke, QC, Canada, 2) Laboratoire Nanotechnologies Nanosystèmes (LN2), CNRS UMI-3463, Université de Sherbrooke, Canada, 3) Sibley School of Mechanical and Aerospace Engineering, Cornell University, Ithaca, New York 14853, USA, 4) Department of Mathematics, Cornell University, Ithaca, New York 14853, USA.

Date de soumission: 2021-01-20.

État d'acceptation: corrections majeures demandées. J'ai retiré le manuscript, mais le présente tout de même ici, parce que je juge les résultats intéressants. Une nouvelle version du manuscript, qui diffère significativement de celle présentée ici, est présentée au chapitre 7.

Revue: Applied Thermal Engineering.

Titre français: Récupération d'énergie avec le moteur thermofluidique auto-oscillant (*Self-Oscillating Fluidic Heat Engine*, SOFHE) - Principes de bases.

Titre anglais: Energy Harvesting with the Self-Oscillating Fluidic Heat Engine (SOFHE) - Basic Principles.

Contribution au document: J'ai mené et réalisé l'ensemble des travaux présentés dans cet article. Les coauteurs ont contribués par des conseils et suggestions lors de la recherche et lors de la rédaction du document.

Résumé français: Nous démontrons comment augmenter la puissance produite par le moteur fluidique auto-oscillant (SOFHE), un dispositif conçu pour la production d'énergie électrique à partir de chaleur perdue et basé sur le fonctionnement du caloduc pulsé mono-branche (SBPHP). Comme pour le SBPHP, on retrouve dans le SOFHE un tube fermé à une extrémité, qui comprend une bulle de vapeur suivie d'une colonne de liquide, qui oscille lorsque l'extrémité fermée est chauffée. On retrouve aussi dans le SOFHE un transducteur électromécanique qui transforme une partie de l'énergie cinétique de la colonne de liquide en énergie électrique. Pour permettre la conception de dispositifs SOFHE, il est utile de comprendre ce qui influence la puissance et comment l'augmenter. Pour établir cette compréhension, nous proposons un modèle théorique du SOFHE qui inclut un transducteur purement dissipatif et nous obtenons une solution analytique précise décrivant la dynamique des oscillations ainsi que la puissance produite. Nous montrons que l'amplitude des oscillations décroît lorsque la charge (du transducteur) est augmentée. La charge doit être maintenue en dessous d'une certaine valeur maximale pour maintenir les auto-oscillations. La puissance atteint un maximum pour une valeur optimale de la charge. Nous montrons également comment la puissance peut être augmentée en augmentant l'instabilité, ce qui peut être fait en augmentant le changement de phase ou en réduisant la friction. L'efficacité atteint également un maximum pour une valeur optimale de la charge. Finalement nous montrons comment la récupération d'énergie basée sur des auto-oscillateurs (tel que SOFHE) diffère significativement de la récupération d'énergie basée sur des oscillateurs forcés.

Résumé anglais: We theoretically show how to increase the power output of the Self-Oscillating Fluidic Heat Engine (SOFHE), a device intended to generate electric power from waste heat and based on the Single-Branch Pulsating Heat Pipe (SBPHP) working principle. As a SBPHP, SOFHE includes a tube closed at one end containing a vapor bubble followed by a liquid plug, which oscillates as the closed end is heated. In addition, SOFHE includes an electromechanical transducer to transform some of the liquid plug's kinetic energy into electrical energy. To allow the design of SOFHE devices, an understanding of what influences its power output and how one can increase it is required. To establish this understanding, we formulate a theoretical model of SOFHE with a damping-based transducer and obtain a precise analytical solution describing the oscillation's dynamics as well as the power output. We show that the oscillation's amplitude decreases as the transducer's damping coefficient increases. We find that the coefficient must be kept below a maximum value to maintain the self-oscillations. We then show that the power reaches a maximum for an optimal value of the transducer's damping coefficient. We also find that one can increase the power by increasing the instability, by increasing

the phase-change or reducing the friction. The efficiency also has a maximum at an optimal value of the transducer's damping coefficient. Finally, we use the SOFHE description to show how energy harvesting based on self-oscillators differs significantly from energy harvesting based on forced-oscillators.

Note: pour satisfaire aux exigences de l'Université de Sherbrooke, la version de l'article présentée dans cette thèse diffère de la version soumise.

6.1 Introduction

A Pulsating heat pipe (PHP) is a cooling device, made of a meandering tube in which vapor bubbles and liquid plugs coexist. Self-oscillations of the vapor bubbles and liquid plugs allow for heat transfer from the heat source to a colder region, called the heat sink, through both latent heat (evaporation and condensation) and sensible heat. These self-oscillations can also be observed in a simpler device, called the Single-Branch Pulsating Heat Pipe, which is a small tube closed at one end and open at the other, in which a single vapor bubble coexists with a single liquid plug (see tube in fig. 6.1).

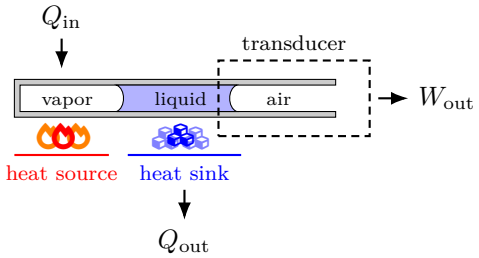

Figure 6.1 Schematic of the Self-Oscillating Fluidic Heat Engine (SOFHE) based on the self-oscillating phenomenon of the Single-Branch Pulsating Heat Pipe (SBPHP).

Although the PHP was initially designed for cooling purposes, there is now an increased interest in energy harvesting applications [79, 78, 111, 125, 80, 75, 104]. Indeed, in a PHP, part of the heat absorbed is converted into mechanical energy (the oscillations of the liquid plug). By adding an electromechanical transducer to the PHP, part of this mechanical energy can be converted into electrical energy. One ends up with a device capable of harvesting waste heat from the environment and converting it into electricity. A major application for such devices is to power wireless sensors. In the context of the "Internet of Things" (IoT) paradigm, one envisions a network of wireless sensors embedded into the environment (home, car, airplanes, etc.) for enhanced functionalities. This includes temperature sensors, pressure sensors, accelerometers, etc. However, the development of the IoT depends on technical innovations in a number of important fields, particularly

wireless sensors reliability and lifetime [4, 109]. A wireless sensor networks powered solely by batteries requires battery changes, which is impractical, especially for a large number of nodes or when the nodes are located in remote areas. A solution to this problem is to couple the sensor to an energy harvester, which will harness nearby energy sources (vibration, thermal gradient, light, etc.) to power the sensor and make it truly autonomous [108]. In this context, energy harvesting based on PHPs could come into play as an interesting solution.

Many energy harvesters are based on oscillating phenomena. It is useful to distinguish between harvesting from forced oscillators, where the periodicity comes from an external source and self-oscillators, where the periodicity is generated by the oscillator itself [52]. Forced-oscillating harvesters include the popular approach of coupling a mechanical spring-mass system to a piezoelectric, to harvest energy from vibrating structures [9]. Also falling in that category is the P^3 heat engine and relatives [122, 16, 8], where an external mechanism drives periodic injection of heat into a two-phase working fluid, coupled to a buckling piezoelectric membrane. Self-oscillating harvesters includes harvesting from flutter and other aeroelastic instabilities [29, 5, 24, 10, 6]. Some heat engines also fall into that latter category such as the heat engine from IMTEK [46, 47] which is similar to the P^3 engine, but where the periodic heat injection is self-driven by the oscillations. Let's also mention the demonstration of energy harvesting from periodic, self-sustained, explosive evaporation in a chamber coupled to a piezoelectric membrane [68].

Energy harvesting based on PHPs is also part of the self-oscillating harvester category. Energy harvesting from multi-branch PHP coupled to various types of transducers has been demonstrated, including electromagnetic [79], piezoelectric [80], interfacial electrical double layer [104] and pyroelectric [125]. Energy harvesting based on a single-branch PHP as shown in fig. 6.1 has also been demonstrated, a concept coined Self-Oscillating Fluidic Heat Engine (SOFHE) [78, 111, 75]. However, beside these experimental results, there is no theoretical framework yet to describe energy harvesting based on PHPs. A qualitative understanding of how the PHP energy harvesters behave is needed. There is a number of questions that should be addressed regarding energy harvesting based on the PHP principle. By adding the transducer to the SBPHP as in fig. 6.1, an additional force, called a *load*, is applied to the liquid plug. Since the goal of the device is to harvest energy, this force should be dissipative and will likely affects the SBPHP dynamics. It is of prime importance for the design of SBPHP harvesting devices to understand the impact of the load on the oscillation dynamics. Will the self-oscillations stop when the load is applied? If not, how the oscillation amplitude will varies as function of the load? How

much load can one apply before the self-oscillations die out? Moreover, we would like to understand how to increase the power output of the device. We would like to know how the power output vary as a function of the load. Does it reach a maximum and if so, at which load value? Finally, we would like to understand how the characteristics of the internal dynamics in the SBPHP (rate of evaporation and condensation, viscous friction, etc.) impact the power output. What should one aim for when controlling the internal dynamics in the SBPHP, in order to maximize the power output?

Here, we tackle those questions for SOFHE, aiming at a qualitative understanding of energy harvesting based on SBPHPs. We start from an existing SBPHP model [112, 114] and add an electromechanical transducer, represented by an additional damping force (section 6.2.1). We then derive some general results (section 6.2.2), first showing how the transducer impacts the SBPHP thermofluidic instability, required to maintain the self-oscillations. This gives bounds to the transducer force. We then derive general expressions for the power output and the efficiency. Finally, we study the power and the efficiency in two distinct cases, when the dynamics is dominated by 1) the temperature nonlinearity (section 6.3) and 2) the pressure nonlinearity (section 6.4). In the discussion (section 6.5), we highlight some general results for self-oscillating harvesters and show how they qualitatively differ from forced-oscillating harvesters. To that end, an appendix describing the energy harvesting from a linear forced oscillator is included (D.1).

6.2 Model and Basic Results

6.2.1 Model

In order to build a model for SOFHE's dynamics, we proceed as for the SBPHP [112, 114], with some simplifications described in the discussion. First, the momentum balance is applied to the liquid plug, as:

$$m_\ell \ddot{x}_i = \left(P_g - \hat{P}_e\right) A + F_f + F_L, \tag{6.1}$$

with x_i the position of the vapor-liquid interface (refered to as the meniscus from now on), relative to an equilibrium to be found later on. Thus, $\dot{x}_i$ and $\ddot{x}_i$ are the velocity and the acceleration of the liquid plug, respectively. $P_g A$ is the force applied by the vapor's pressure on the liquid plug. The force $\hat{P}_e A$ combines the force $P_e A$, due to the pressure of the air, and the gravitational force if the tube is tilted, with $\hat{P}_e = P_e + \rho_\ell g L_\ell \sin\theta$, where P_e is the external pressure, ρ_ℓ the liquid density, g the gravitational acceleration, L_ℓ the length of the liquid plug and θ the angle of the tube relative to the horizontal.

The term F_f is the friction force between the liquid plug and the wall. Assuming Poiseuille flow, with $c_f = 8\pi\mu L_\ell$, we can write:

$$F_f = -c_f \, \dot{x}_i \ . \tag{6.2}$$

The term F_L is the load, the force exerted by the transducer on the liquid plug, to harvest energy from the oscillations (the L subscript standing for *Load*). We consider a basic type of transducer called velocity-damped, which produce a force F_L proportional and opposite to velocity, meaning it is a purely dissipative force (just like F_f). So, the impact of the velocity-damped transducer on the dynamics can be simply understood has increased friction. With c_L a proportionality constant (to be defined by the transducer's characteristics), we have:

$$F_L = -c_L \, \dot{x}_i \ . \tag{6.3}$$

The pressure in the vapor, P_g, can be described by the perfect gas law:

$$P_g = \frac{m_g R_g T_g}{(x_i + L_{g,0})\, A} \ . \tag{6.4}$$

where $(x_i + L_{g,0})A$ is the volume of vapor. We will assume T_g constant here. The mass of vapor varies due to evaporation and condensation, as the liquid plug oscillates between the heat source and the heat sink. We consider a simple thermal resistance model for the heat transfer between the walls and the vapor, through the liquid and close to the meniscus, leading to:

$$\dot{m}_g = \frac{\dot{Q}}{H_v} = \frac{T_w(x_i) - T_{g,sat}}{H_v R_{th}} \ , \tag{6.5}$$

with m_g the mass of vapor and $\dot{m}_g$ the phase-change rate ($\dot{m}_g$ positive or negative for evaporation or condensation, respectively), $\dot{Q}$ the heat transfer responsible for the phase-change, H_v the enthalpy of vaporization, $T_w(x_i)$ the temperature of the wall close to the meniscus, $T_{g,sat}$ the temperature of the meniscus (at saturation conditions) and R_{th} the thermal resistance. The temperature of the wall varies between the heat source and the heat sink. We assume $T_w = T_H$ in the heat source, $T_w = T_L$ in the heat sink and assume

a smooth transition between the two. Such profile is well described by an arctangent, as:

$$T_w(x) = \frac{T_H - T_L}{\pi} \arctan\left[-\left(\frac{\pi \left| T'_{w,0} \right|}{T_H - T_L} \right) x \right] + \frac{T_H + T_L}{2} , \tag{6.6}$$

where $\left| T'_{w,0} \right|$ is the thermal gradient in the axial direction, at $x = 0$.

Equations (6.1) to (6.6) constitute a complete set of nonlinear differential equations, which can be solved for the position x_i. This system has one equilibrium, where the liquid plug does not move and the mass of vapor is constant, which can be obtained by solving for $\dot{x}_i = \ddot{x}_i = \dot{m}_g = 0$. We will denote quantities at equilibrium by the 0 subscript (e.g. $P_g = P_{g,0}$, $m_g = m_{g,0}$ and so on). At equilibrium, we find that $P_g = P_{g,0} = \hat{P}_e$ (eq. (6.1)). Also, no net phase-change at the equilibrium implies $T_w(x_i) = T_{g,sat}$, corresponding to the position $x_i = 0$ (from eqs. (6.5) and (6.6)). The equilibrium is located at a distance $L_{g,0}$ of the wall at the closed end.

To study the dynamics, it is useful to use variables relative to this equilibrium. We also make the variables dimensionless, using $m_{g,0}$, $L_{g,0}$, $1/\omega_n$, $T_{g,0}$ as the characteristics mass, length, time and temperature, where $\omega_n = \sqrt{P_{g,0}/(\rho_\ell L_{g,0} L_\ell)}$ is the natural frequency. We thus have:

$$q_1 = \frac{x_i}{L_{g,0}} , \tag{6.7a}$$

$$q_2 = \frac{dq_1}{d\tau} = \frac{1}{\omega_n L_{g,0}} \frac{dx_i}{dt} , \tag{6.7b}$$

$$q_3 = \frac{m_g - m_{g,0}}{m_{g,0}} , \tag{6.7c}$$

as the dimensionless position, velocity and mass of vapor. The dynamics is now described in terms of the dimensionless time $\tau = \omega_n t$. We note that substitution of q_1 and q_2 in the momentum balance shows that forces can be made dimensionless by a characteristic force $m_\ell L_{g,0} {\omega_n}^2 = P_{g,0} A$. Substitution of eq. (6.7) into eqs. (6.1) to (6.6), yields the following system of dimensionless differential equations (in a phase-space representation):

$$\dot{q}_1 = q_2 , \tag{6.8a}$$

$$\dot{q}_2 = -\left(\frac{1}{1 + q_1} \right) q_1 + \left(\frac{1}{1 + q_1} \right) q_3 - 2\,\zeta\, q_2 , \tag{6.8b}$$

$$\dot{q}_3 = T_{HL} \arctan\left[-\left(\frac{2\sigma}{T_{HL}} \right) q_1 \right] . \tag{6.8c}$$

The dimensionless parameters σ, ζ and T_{HL} are defined as:

$$\sigma = \frac{L_{g,0}}{2m_{g,0}\omega_n H_v R_{th}} \left|T'_{w,0}\right| , \tag{6.9a}$$

$$\zeta = \zeta_f + \zeta_L , \tag{6.9b}$$

$$\zeta_f = \frac{8\pi\mu L_\ell}{2m_\ell\omega_n} , \tag{6.9c}$$

$$\zeta_L = \frac{c_L}{2m_\ell\omega_n} , \tag{6.9d}$$

$$T_{HL} = \frac{T_H - T_L}{\pi m_{g,0}\omega_n H_v R_{th}} . \tag{6.9e}$$

The quantity σ is called the phase-change coefficient. The quantity ζ, called the combined dissipative coefficient, includes the friction coefficient ζ_f and the harvester coefficient ζ_L. T_{HL} is the difference of temperature $T_H - T_L$, made dimensionless.

Equation (6.8b) is simply the momentum balance, with the acceleration $\dot{q}_2$ on one side and the forces on the other. The first two terms on the right-hand side come from the pressure difference applied on the liquid plug. The term $-(1/(1+q_1))q_1$ comes from variations of pressure due to a change of volume and acts as a nonlinear restoring force. This term coupled with the dimensionless inertial term ($\dot{q}_2$) leads to a spring-mass system. The term $-(1/(1+q_1))q_3$ comes from variations of pressure due to variations of the mass of vapor. It can be shown that the resulting force is in phase with velocity, thus acting as a positive feedback, which tends to increase the oscillation's amplitude [112]. The prefactor $1/(1+q_1)$ makes the momentum balance nonlinear and comes from the pressure nonlinearity. As shown in fig. 6.2, the nonlinearity makes the restoring force rise to infinity when the vapor bubble is compressed significantly (for q_1 approaching -1), preventing the liquid plug from going through the closed end. The last term, $-2\,\zeta\ q_2$ is a dissipative force, which includes both the friction and the transducer.

Finally, eq. (6.8c) is the phase-change rate. It is also nonlinear, it saturates in both the heat source and the heat sink as shown in fig. 6.3, due to the nonlinear wall temperature profile. Although our model was constructed by assuming phase-change close to the meniscus with a simple thermal resistance model, the resulting phase-change expression, eq. (6.8c), is more general than this. It simply represents a linear phase-change rate close to the equilibrium (optimal, because it leads to a force perfectly in phase with velocity [112]),

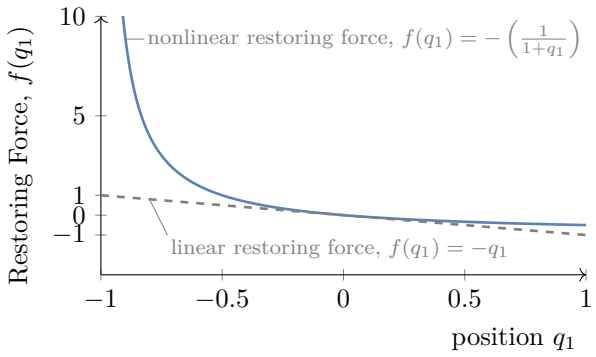

Figure 6.2 Effect of the pressure nonlinearity on the restoring force.

which saturates in both the heat source and the heat sink. Thus the nonlinearity studied here is really a limitation of the phase-change rate. We will also draw more general conclusions valid for other phase-change profiles in section 6.5.

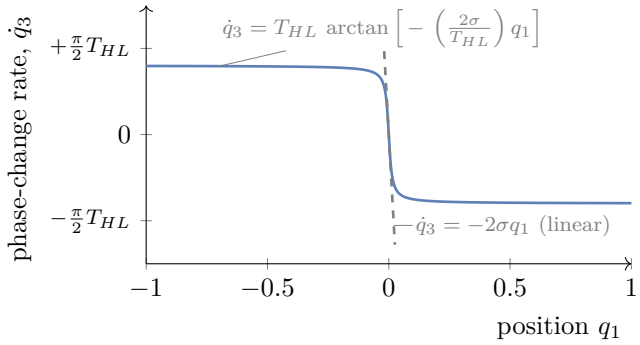

Figure 6.3 Nonlinear phase-change profile, due to the wall temperature nonlinearity.

Which nonlinearity dominates depends on which effect, the nonlinear pressure or the saturation of the phase-change, is seen first during the startup. This is controlled in eq. (6.8) by T_{HL}. The pressure nonlinearity dominates for T_{HL} large, while the temperature nonlinearity dominates for small T_{HL} (see Tessier-Poirier et al. [114] for details).

6.2.2 Basic Results and Understanding, Oscillations' Dynamics

The dynamics of eq. (6.8) has been studied before for the SBPHP, so without harvesting, with $\zeta_L = 0$ and $\zeta = \zeta_f$ (see [112, 114] and chapter 5). Those results can still be used here, by simply adding ζ_L to ζ_f (the model is the same, we simply change a parameter). Equation (6.8) has one equilibrium at $q_1 = q_2 = q_3 = 0$. Numerical simulations show that this system may exhibit self-oscillations.

Linear Stability Analysis with Harvesting

Tessier-Poirier et al. [112] performed a linear stability analysis of eq. (6.8). They showed that, after a small perturbation of the equilibrium, the position q_1 oscillates with an am-

plitude increasing over time if the phase-change coefficient (σ) which produce the positive feedback is greater than the dissipation (ζ). This occurs when the instability number Π is greater than one, with:

$$\Pi = \frac{\sigma}{\zeta} = \frac{\Pi_0}{1 + (\zeta_L/\zeta_f)} , \quad \Pi_0 = \frac{\sigma}{\zeta_f} = \frac{\rho_\ell \, R_g \, T_{g,0} \, \left|T'_{w,0}\right|}{8\pi \, \mu \, H_v R_{th} \, \hat{P}_e} . \tag{6.10}$$

When there is no harvesting, $\zeta_L = 0$, we simply have $\Pi = \Pi_0$, Π_0 is the instability number without harvesting. Let's assume now that SOFHE is first started without harvesting from equilibrium, by increasing Π_0 above one [1]. The oscillations first increase in amplitude and eventually settle down in a steady-state (limit cycle) due to the nonlinearities [113, 114]. We then progressively increase ζ_L to harvest some energy. As a consequence, Π will progressively decrease. Ultimately, ζ_L will reach a maximum value $\zeta_{\mathrm{L,max}}$ where Π will reach 1, the total damping being large enough to kill the self-oscillations. At this point, for $\zeta_L \geqslant \zeta_{\mathrm{L,max}}$, there is no more limit cycle, the equilibrium is stable, and we cannot extract energy. Solving eq. (6.10) for $\zeta_L = \zeta_{\mathrm{L,max}}$ with $\Pi = 1$, we get:

$$\zeta_{\mathrm{L,max}} = \zeta_f \, (\Pi_0 - 1) \ . \tag{6.11}$$

In order to extract energy, we must keep $0 < \zeta_L < \zeta_{\mathrm{L,max}}$, so it makes sense to consider the ratio:

$$Z_{\mathrm{L}} \equiv \frac{\zeta_L}{\zeta_{\mathrm{L,max}}} = \frac{\zeta_L}{\zeta_f \, (\Pi_0 - 1)} . \tag{6.12}$$

The harvesting ratio Z_{L} must be kept between 0 and 1 to harvest energy while maintaining the oscillations. We can redefine the parameters of the system in terms of Z_{L} instead of ζ_L, leading to:

$$\zeta_L = \zeta_f \, (\Pi_0 - 1) \, Z_{\mathrm{L}} , \tag{6.13a}$$

$$\zeta = \zeta_f + \zeta_L = \zeta_f \, (1 + (\Pi_0 - 1) \, Z_{\mathrm{L}}) \ , \tag{6.13b}$$

$$\Pi = \frac{\sigma}{\zeta} = \frac{\Pi_0}{1 + (\Pi_0 - 1) \, Z_{\mathrm{L}}} . \tag{6.13c}$$

1. Typically, by increasing the temperature of the heat source, which increases the thermal gradient at the equilibrium $\left|T'_{w,0}\right|$, which in turns increases the phase-change coefficient σ, finally leading to an increase in Π_0.

We clearly see from eq. (6.13c) that we have $\Pi = \Pi_0$ for $Z_\mathrm{L} = 0$ (unstable equilibrium if $\Pi_0 > 1$) and $\Pi = 1$ (stable equilibrium and no limit cycle) for $Z_\mathrm{L} = 1$.

Dynamics on the Limit Cycle (in the Steady-State)

Now, on the limit cycle (steady-state), the solution is periodic and can thus be represented by Fourier series. The position is given by the following Fourier series in amplitude-phase form :

$$q_1 = \tfrac{1}{2}A_0 + \sum_{k=1}^{k=\infty} A_k \sin\left(k\theta + \varphi_k\right) \quad , \text{ with: } \theta(\tau) = \Omega\tau \ . \tag{6.14a}$$

The velocity $q_2 = \dot{q}_1$ is then simply obtained by applying the derivative in time:

$$q_2 = 0 + \sum_{k=1}^{k=\infty} k\Omega\, A_k \cos\left(k\theta + \varphi_k\right) \ . \tag{6.14b}$$

Of course, the amplitudes A_k and the angular frequency Ω are functions of the parameters of the system. Because the amplitudes and the frequency are affected differently by each nonlinearities, we study each of them individually in sections 6.3 and 6.4.

6.2.3 General Power Output Expression

We now wish to compute the averaged power generated by the velocity-damped harvester. To do so, we will first consider the work done by the load. The (dimensionless) infinitesimal work done by the load $\widetilde{F_L}$ over the displacement of the liquid plug dq_1 is given by $d\widetilde{W_L} = \widetilde{F_L}\, dq_1$. We make the substitution $dq_1 = \dot{q}_1 d\tau = q_2 d\tau$, so that $d\widetilde{W_L} = \widetilde{F_L}\, q_2 d\tau$. Because $\widetilde{W_L}$ is the work done by the load $\widetilde{F_L}$ on the liquid plug, we have $\widetilde{W_L} < 0$ when the load is dissipative (the load is extracting energy from the liquid plug). In that case, the energy harvested is positive and given by $-\widetilde{W_L}$. We may define $\widetilde{W_\mathrm{h}} = -\widetilde{W_L}$ as the harvested energy, with $\widetilde{W_\mathrm{h}} > 0$ when the load is extracting energy. Integrating $d\widetilde{W_\mathrm{h}} = -\widetilde{F_L}\, q_2 d\tau$ over a cycle leads to the energy harvested over a cycle:

$$\widetilde{W}_{h,\mathrm{Cycle}} = \int_\mathrm{Cycle} d\widetilde{W_\mathrm{h}} = -\int_\mathrm{Cycle} \widetilde{F_L}\, q_2 d\tau \ . \tag{6.15}$$

Given a velocity-damped harvester force $\widetilde{F_L} = -2\zeta_L q_2$ and with the substitution $\zeta_L = \zeta_f\left(\Pi_0 - 1\right) Z_\mathrm{L}$ (eq. (6.13a)):

$$\widetilde{W}_{h,\mathrm{Cycle}} = 2\zeta_f\left(\Pi_0 - 1\right) Z_\mathrm{L} \int_\mathrm{Cycle} {q_2}^2 d\tau \ . \tag{6.16}$$

Substitution of the solution for q_2, eq. (6.14b), and performing the integration leads to:

$$\widetilde{W}_{h,\text{Cycle}} = 2\pi\Omega\,\zeta_f\,(\Pi_0 - 1)\,Z_\text{L}\,\sum_{k=1}^{+\infty} k^2 {A_k}^2\ . \tag{6.17}$$

The dimensionless power averaged over a cycle, defined as $\overline{\dot{W}}_h$, is obtained by simply dividing $\widetilde{W}_{h,\text{Cycle}}$ by the period $\widetilde{T} = 2\pi/\Omega$, leading to:

$$\overline{\dot{W}}_h = \frac{\Omega}{2\pi}\,\widetilde{W}_{h,\text{Cycle}} = \zeta_f\,(\Pi_0 - 1)\,Z_\text{L}\,\Omega^2\,\sum_{k=1}^{+\infty} k^2 {A_k}^2 \tag{6.18}$$

If there is only the fundamental (as it is the case for averaging), then we simply have $\overline{\dot{W}}_h = \zeta_f\,(\Pi_0 - 1)\,Z_\text{L}\,\Omega^2\,{A_1}^2$. The power output will be studied in more details for each nonlinearities in sections 6.3 and 6.4.

Carrying the analysis above in terms of dimensional quantities (dimensional force, displacement and so on), and then making the conversion to dimensionless quantities, we find that the dimensional work can be obtained by multiplying $\widetilde{W}_{h,\text{Cycle}}$ by $L_{g,0}P_{g,0}A$ while the dimensional power can be obtained by multiplying $\overline{\dot{W}}_h$ by $\omega_n L_{g,0}P_{g,0}A$.

6.2.4 General Efficiency Expression

SOFHE's efficiency is given by the ratio of the harvested work to the energy injected in the system, over a cycle. To estimate the energy injected into the system, we consider the heat transfer leading to phase-change. We obtain the dimensionless energy injected into the system over a cycle $\widetilde{Q}_{\text{in,cycle}}$ given by:

$$\widetilde{Q}_{\text{in,cycle}} = \int_{\text{Cycle},\ \dot{q}_3 > 0} \dot{q}_3\,d\tau\ , \tag{6.19}$$

which can be made dimensional simply by multiplying by $m_{g,0}H_v$. The efficiency, given by the ratio of the dimensional work over the cycle $(L_{g,0}P_{g,0}A)\widetilde{W}_{h,\text{Cycle}}$, to the dimensional energy injected into the system over a cycle, $(m_{g,0}H_v)\widetilde{Q}_{\text{in,cycle}}$, leading to the following after simplifications:

$$\eta = \left(\frac{R_g T_{g,0}}{H_v}\right)\frac{\widetilde{W}_{h,\text{Cycle}}}{\widetilde{Q}_{\text{in,cycle}}}\ , \tag{6.20}$$

where $\widetilde{W}_{h,\mathrm{Cycle}}$ and $\widetilde{Q}_{\mathrm{in,cycle}}$ can be obtained from eqs. (6.17) and (6.19), respectively. We will pursue the analysis for each nonlinearities individually. To estimate the energy injected into the system, we considered two hypotheses: 1) sensible heat is negligible compared to latent heat [2], 2) enthalpy of vaporization is constant. Based on typical experimental results and using the Rankine Cycle as a benchmark, those two hypotheses yield negligible error [58]. For very large pressure variations though, beyond what is currently observed experimentally, those hypotheses may not hold. We will take this limitation into consideration in our estimations below. In any case, the efficiency must be below the Carnot efficiency $\eta = 1 - T_L/T_H$.

6.3 Wall Temperature Nonlinearity

As mentioned before, the steady-state (limit cycle) is due to the nonlinearities. The behavior of the system differs, whether the pressure nonlinearity or the wall temperature nonlinearity dominates, so we choose to study the harvesting for each nonlinearity individually. We will first consider the temperature nonlinearity only, so that we linearize the momentum balance and eq. (6.8) becomes:

$$\dot{q}_1 = q_2 \ , \tag{6.21a}$$

$$\dot{q}_2 = -q_1 + q_3 - 2\,\zeta\ q_2 \ , \tag{6.21b}$$

$$\dot{q}_3 = T_{HL}\ \arctan\left[-\left(\frac{2\,\zeta\,\Pi}{T_{HL}}\right) q_1 \right] \ , \tag{6.21c}$$

where we made the substitution $\sigma = \zeta\,\Pi$ and where ζ and Π given by eq. (6.13). For such a system, a very precise analytical solution can be found using averaging (see chapter 5), given by eq. (6.14) with:

$$A_1 = \frac{T_{HL}}{\zeta}\sqrt{\frac{\Pi - 1}{\Pi}} = \frac{\sqrt{1 - Z_{\mathrm{L}}}}{1 + (\Pi_0 - 1)\,Z_{\mathrm{L}}}\ \frac{T_{HL}}{\zeta_f}\sqrt{\frac{\Pi_0 - 1}{\Pi_0}} \ , \tag{6.22a}$$

$$\Omega = 1 \ , \tag{6.22b}$$

2. We do not take into account the heat transfer not leading to phase-change (heat conduction through the walls in the axial direction and heat convection between the walls and the liquid plug) in the engine's efficiency considered here. Including these would lead to an overall efficiency lower than the engine's efficiency.

where the second part in eq. (6.22a) was obtained by substitution of ζ and Π with eqs. (6.13b) and (6.13c). All the other A_k equal to 0. Thus, the solution is purely sinusoidal.

The amplitude A, given by eq. (6.22a), is displayed in fig. 6.4a as a function of the harvesting coefficient ratio Z_L. At $Z_\mathrm{L} = 0$, there is no harvesting, the amplitude is maximal. As Z_L increases, the amplitude progressively decreases, because there is more and more damping (harvesting is just damping for the system). At $Z_\mathrm{L} = 1$, ζ_L is large enough such that $\Pi = 1$, the amplitude reaches 0, the limit cycle collapses on the equilibrium which becomes stable.

6.3.1 Power

The power output for the temperature nonlinearity only is given by substitution of eq. (6.22) into eq. (6.18), leading to:

$$\dot{\overline{W}}_h = \frac{Z_\mathrm{L}\left(1 - Z_\mathrm{L}\right)}{\left(1 + \left(\Pi_0 - 1\right) Z_\mathrm{L}\right)^2} \frac{{T_{HL}}^2}{\zeta_f} \frac{\left(\Pi_0 - 1\right)^2}{\Pi_0} \ . \tag{6.23}$$

The power $\dot{\overline{W}}_h$ as a function of Z_L is shown in fig. 6.4b. At $Z_\mathrm{L} = 0$, there is no power, since there is no harvesting force applied on the system ($\zeta_L = 0$). As Z_L increases, the power $\dot{\overline{W}}_h$ increases, reaches a maximum and then decreases, to finally reach 0 again. This is because, at that point, the dissipative force is so great that there are no more oscillations ($A = 0$).

One can easily find the two zeroes by inspection of eq. (6.23):

$$\dot{\overline{W}}_h = 0 \Rightarrow Z_\mathrm{L} = 0 \text{ or } Z_\mathrm{L} = 1 \ . \tag{6.24}$$

The power $\dot{\overline{W}}_h$ reaches a maximum at an optimum value of $Z_\mathrm{L} = Z_{L,\mathrm{opt}}$. It can be easily obtained by setting the derivative $d(\dot{\overline{W}}_h)/dZ_\mathrm{L} = 0$. We obtain:

$$Z_{L,\mathrm{opt}} = \frac{1}{1 + \Pi_0} \ . \tag{6.25}$$

The maximum power is obtained by taking $Z_\mathrm{L} = Z_{L,\mathrm{opt}}$ in eq. (6.23), leading to:

$$\dot{\overline{W}}_{h,max} = \frac{1}{4} \frac{{T_{HL}}^2}{\zeta_f} \left(\frac{\Pi_0 - 1}{\Pi_0}\right)^2 \ . \tag{6.26a}$$

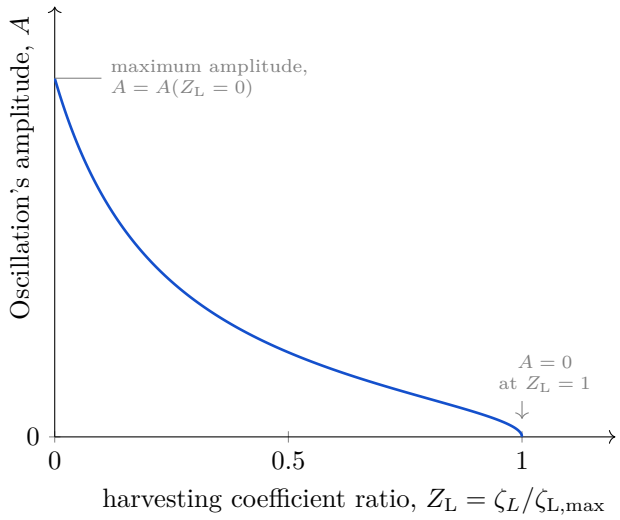

(a)

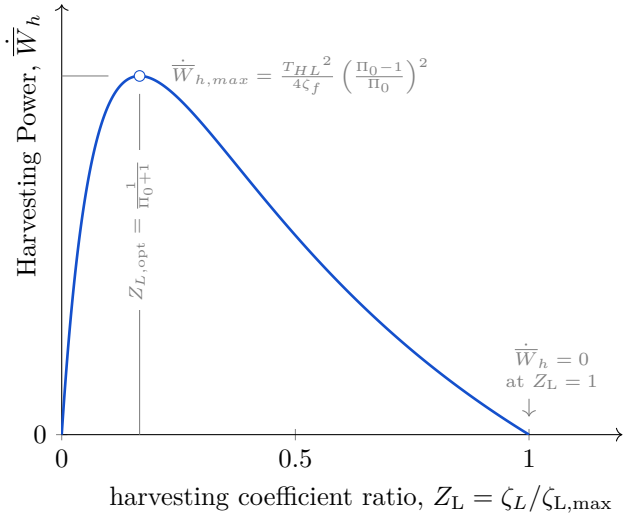

(b)

Figure 6.4 Curves evaluated for $\Pi_0 = 5$, $\zeta_f = 0.10$ and $T_{HL} = 0.01$. (a) Amplitude A as a function of the harvesting coefficient ratio $Z_{\mathrm{L}} = \zeta_L/\zeta_{\mathrm{L,max}}$, the amplitude progressively decrease towards 0 as Z_{L} goes from 0 to 1. (b) Power curve; As the harvesting coefficient ratio Z_{L} is progressively increased, the power $\dot{\overline{W}}_h$ first increase, then reaches a maximum and then decreases, eventually reaching 0 at $Z_{\mathrm{L}} = 1$.

Effect of Π_0

A key parameter in eqs. (6.23) and (6.26a) is Π_0. In fig. 6.5, several curves for various Π_0 are displayed. Π_0 is the parameter that defines the instability threshold in the absence of harvesting force. By increasing Π_0, we increase the instability (Π increases as well, eq. (6.13c)) and the oscillation's amplitude as well as the power output. One can increase

$\Pi_0 = \sigma/\zeta_f$ by increasing the phase-change coefficient σ, through an increase of the heat source temperature T_H for example. Also note that, as we increase Π_0 and the power increases, the maximum point shifts to the left (Z_{opt} decreases) and the curves become more asymmetric.

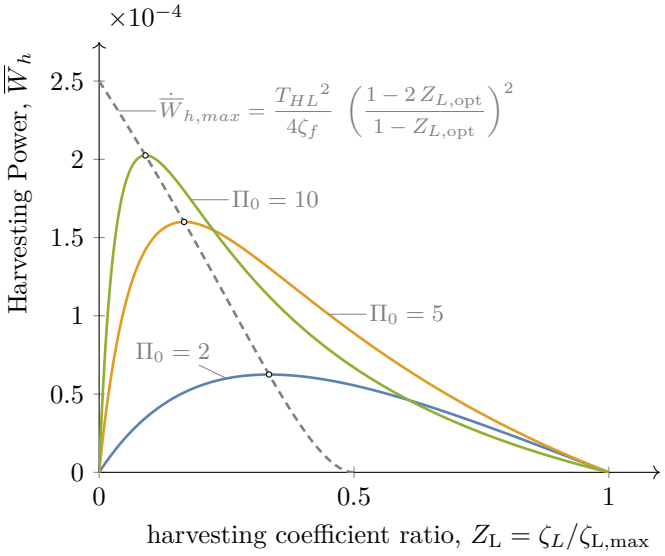

Figure 6.5 Effect of Π_0 on the power curves ; curves for $\zeta_f = 0.10$ and $T_{HL} = 0.01$.

How the maximum power evolves as a function of Π_0 is shown in fig. 6.5 by the dashed curve. To obtain such a curve, we first solved eq. (6.25) for Π_0 and substitute the result in eq. (6.26a), leading to:

$$\dot{\overline{W}}_{h,max} = \frac{T_{HL}{}^2}{4\zeta_f}\left(\frac{1-2\,Z_{L,\text{opt}}}{1-Z_{L,\text{opt}}}\right)^2 . \tag{6.26b}$$

Equation (6.26a) and eq. (6.26b) are equivalent formulas, they both show how $\dot{\overline{W}}_{h,max}$ evolves, but the former in terms of Π_0 and the latter in terms of $Z_{L,\text{opt}}$.

Studying $Z_{L,\text{opt}}$ and $\dot{\overline{W}}_{h,max}$ in detail

In fig. 6.6, we show $Z_{L,\text{opt}}$ evolves in terms of Π_0. For $\Pi_0 \to 1$ (the system is close to the instability threshold), we have $Z_{L,\text{opt}} \to 1/2$, meaning the optimal ζ_L is equal to $\frac{1}{2}\zeta_{\text{L,max}}$, the ζ_L that kills the oscillations (also, the optimal ζ_L must be very small given that $\zeta_{\text{L,max}}$ approaches 0, eq. (6.11)). As Π_0 increases, $Z_{L,\text{opt}}$ decreases. For $\Pi_0 \to +\infty$, $Z_{L,\text{opt}} \to 0$. In that limit, we have that the optimal ζ_L approaches ζ_f (this can be shown by equating eq. (6.12) to eq. (6.25) and solving for ζ_L).

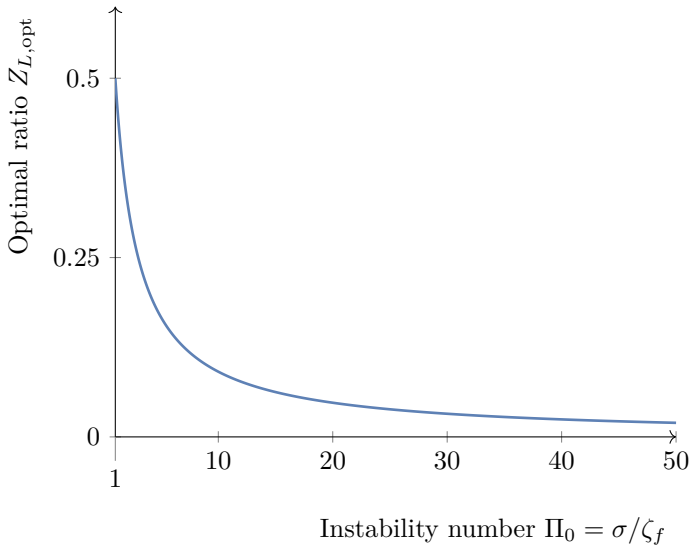

Figure 6.6 Optimal harvesting coefficient ratio $Z_{L,\text{opt}}$ (Z_L where $\dot{\overline{W}}_h = \dot{\overline{W}}_{h,max}$) as a function of Π_0 ; for $\zeta_f = 0.10$ and $T_{HL} = 0.01$.

The maximum power $\dot{\overline{W}}_{h,max}$ (obtained at $Z_\text{L} = Z_{L,\text{opt}}$) evolves in terms of Π_0 following eq. (6.26a) and as displayed in fig. 6.7. Initially 0 at the instability threshold $\Pi_0 = 1$, it gradually increases and eventually saturates at ${T_{HL}}^2/4\zeta_f$. This can be shown by taking the limit of eq. (6.26a):

$$\lim_{\Pi_0 \to +\infty} \dot{\overline{W}}_{h,max}(\Pi_0) = \frac{{T_{HL}}^2}{4\zeta_f} \ . \tag{6.27}$$

Looking at fig. 6.7 one finds that increasing the instability number Π_0 above 1 leads to a slowly increasing power first (the curve is flat at $\Pi_0 = 1$). During this stage, increasing the instability serves mostly to increase the oscillation's amplitude. As Π_0 is increased furthermore, the power starts to increase rapidly. At this stage, the power is dominated by Π_0, a linear property, and depends only slightly on the other parameters. We conclude that the instability number Π_0 is a key parameter to increase the power output, especially close to the instability threshold. One must increase it to increase the amplitude first and then to increase the power. As Π_0 is increased even more, the power eventually saturates. In this latter stage, the power depends less on the instability number Π_0 and more on ${T_{HL}}^2/4\zeta_f$, which can be seen as a nonlinear characteristic.

6.3.2 Efficiency

To compute the efficiency based on eq. (6.20) for the temperature nonlinearity alone, we need $\widetilde{W}_{h,\text{Cycle}}$ and $\widetilde{Q}_{\text{in,cycle}}$. The work $\widetilde{W}_{h,\text{Cycle}}$, after substitution of eq. (6.22) into eq. (6.17),

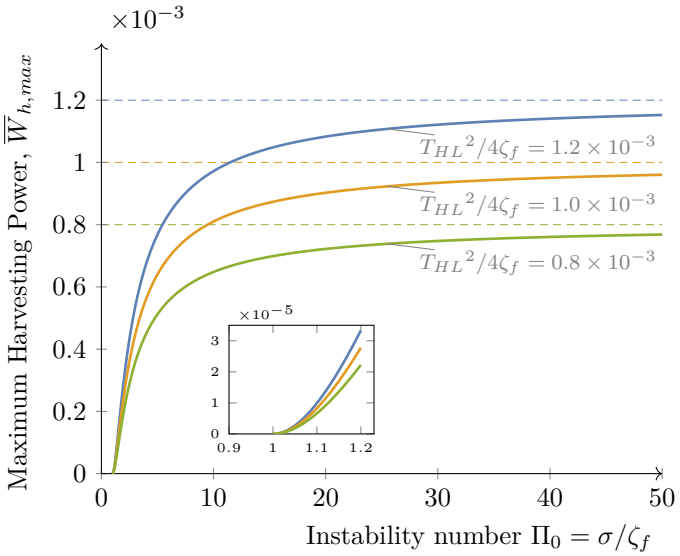

Figure 6.7 Effect of Π_0 on the power curves; curves for $\zeta_f = 0.10$ and $T_{HL} = 0.01$.

is given by:

$$\widetilde{W}_{h,\text{Cycle}} = 2\pi \ \frac{Z_\text{L}\left(1 - Z_\text{L}\right)}{\left(1 + \left(\Pi_0 - 1\right) Z_\text{L}\right)^2} \ \frac{{T_{HL}}^2}{\zeta_f} \frac{\left(\Pi_0 - 1\right)^2}{\Pi_0} \ . \tag{6.28}$$

The work in terms of Z_L follows an asymmetrical bell shaped curve just like the power output (the power is just the work divided by 2π, since $\Omega = 1$ eq. (6.18)).

The energy injected in the system over a cycle, $\widetilde{Q}_{\text{in,cycle}}$, can be obtained by substitution of eq. (6.22) into eq. (6.19). Given the analytical solution for the temperature nonlinearity alone, we get:

$$\widetilde{Q}_{\text{in,cycle}} = -T_{HL} \int_{\frac{\pi}{2}}^{\frac{3\pi}{2}} \arctan\left[\left(2\sqrt{\Pi\left(\Pi - 1\right)}\right) \ \cos(\theta)\right] d\theta \ , \tag{6.29}$$

with Π given by eq. (6.13c). This integral is difficult to perform analytically, so we do it numerically. As a function of Z_L, $\widetilde{Q}_{\text{in,cycle}}$ is maximal at $Z_\text{L} = 0$ (where the amplitude is maximal) and decreases monotonically to 0 at $Z_\text{L} = 1$ (where the amplitude is 0).

Given $\widetilde{W}_{h,\text{Cycle}}$ and $\widetilde{Q}_{\text{in,cycle}}$, the efficiency can then be evaluated using eq. (6.20). In fig. 6.8, various curves are displayed for various Π_0 numbers. The efficiency is 0 at $Z_\text{L} = 0$ and $Z_\text{L} = 1$ and reaches a maximum value in between. Increasing Π_0 leads to an increase in the efficiency (the maximum value in particular). Close to the instability threshold (close to $\Pi_0 = 1$), the optimal Z_L value is 2/3, which is different than the one for maximum

power output (at 1/2). As Π_0 increases, the optimal Z_L decreases and gets closer and closer to the one corresponding to the maximum power.

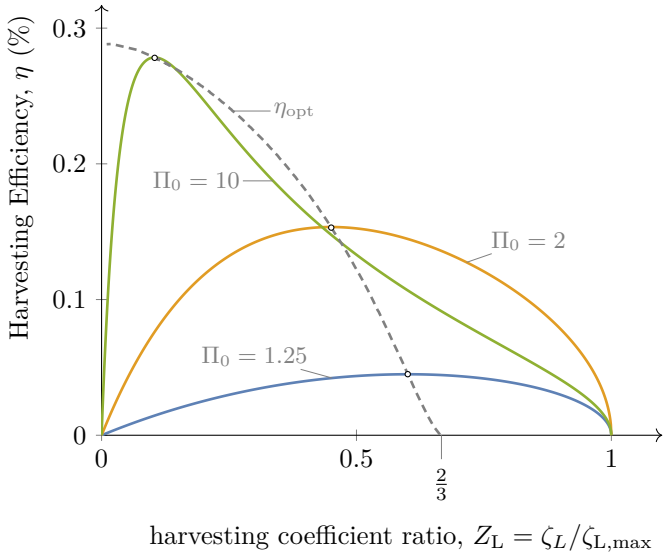

Figure 6.8 Harvesting efficiency along Z_L and for various Π_0 ; curves for $\zeta_f = 0.10$ and $T_{HL} = 0.01$ and $R_g T_{g,0}/H_v = 0.09$ (for water vapor at 170 °C).

6.4 Pressure Nonlinearity

We now consider only the pressure nonlinearity, so that we linearize the phase-change rate and eq. (6.8) becomes:

$$\dot{q}_1 = q_2 \ , \tag{6.30a}$$

$$\dot{q}_2 = -\left(\frac{1}{1+q_1}\right) q_1 + \left(\frac{1}{1+q_1}\right) q_3 - 2\,\zeta\; q_2 \ , \tag{6.30b}$$

$$\dot{q}_3 = -2\,\zeta\,\Pi\,q_1 \ , \tag{6.30c}$$

where we made the substitution $\sigma = \zeta\,\Pi$ and where ζ and Π given by eq. (6.13). For this system, a good expression for the dynamics can be found by fitting the Fourier components obtained by numerical resolution with expressions based on averaging results (chapter 5).

The dynamics is thus well described [3]by eq. (6.14) with:

$$A_0 = 0 \ , \tag{6.31a}$$

$$A_k = a_k \left(1 + b_k e^{-\tau_k \Pi}\right) \left(\frac{\Pi^{n_k} - 1}{\Pi^{n_k}}\right)^{\frac{k}{2}} \ , \tag{6.31b}$$

$$\Omega = \frac{p_1 \Pi^2 + p_2 \Pi + p_3}{\Pi + p_1 + p_2 + p_3 - 1} \ , \tag{6.31c}$$

$$\varphi_k = \begin{cases} \frac{\pi(1-k)}{2} + k\varphi_s & \text{for k odd,} \\ \frac{\pi(1-k)}{2} - \pi + k\varphi_s & \text{for k even.} \end{cases} \tag{6.31d}$$

The parameters are obtained by fitting each harmonics except for φ_s which can be chosen as desired (allows for time shift, time reference is arbitrary), see chapter 5 for details.

Thus, with the pressure nonlinearity, the solution is not purely sinusoidal, but exhibits harmonics. Close to the instability threshold (Π_0 close to 1), the motion is very much sinusoidal with the A_k for $k > 1$ negligible compared to A_1. For larger Π_0 however, the harmonics become more and more important (although A_1 remains the dominant term). We note that the solution only depends on the dimensionless parameters Π_0, ζ_f and Z_L.

In fig. 6.9, we display the amplitude in q_1 as a function of Z_L [4]. We see that the amplitude progressively decreases to 0 at $Z_\mathrm{L} = 1$.

6.4.1 Power

The power output $\overline{\dot{W}_h}$ for the pressure nonlinearity only is given by substitution of eq. (6.31) into eq. (6.18). It is displayed as a function of Z_L in fig. 6.10. Just like for the temperature nonlinearity, there is no power at $Z_\mathrm{L} = 0$, because there is no harvesting force and no power at $Z_\mathrm{L} = 1$, where the dissipative force is too large and kills the oscillations. The power reaches a maximum value in between. A key parameter to increase the power output is the instability number Π_0. Increasing Π_0 increases the power output significantly.

The power output is maximal at $Z_\mathrm{L} = Z_{L,\mathrm{opt}}$. For Π_0 close to 1, $Z_{L,\mathrm{opt}} = 0.5$, meaning that the optimal ζ_L is given by $\zeta_L = \frac{1}{2}\zeta_{\mathrm{L,max}}$. As Π_0 is increased, $Z_{L,\mathrm{opt}}$ increases, as displayed

3. The expression is more precise for Π close to 1 and low ζ. It is optimized for $1 < \Pi < 1.18$ and $\zeta_f < 0.05$ but still provide a good approximation in the range $1 < \Pi < 2$ and $0 < \zeta < 0.15$.

4. To represent the amplitude by a single term in fig. 6.9, instead of the A_k, we consider the semi-amplitude in q_1 (max of q_1 minus min of q_1, divided by two). However, for low Π_0 such as in fig. 6.9, simply taking A_1 would be very precise also, the other A_k being negligible there.

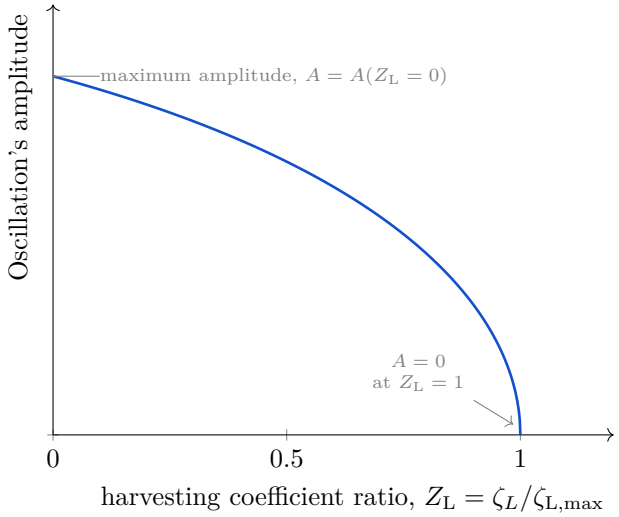

Figure 6.9 Amplitude as a function of the harvesting coefficient ratio $Z_L = \zeta_L/\zeta_{L,max}$, the amplitude progressively decrease towards 0 as Z_L goes from 0 to 1; curves obtained for $\Pi_0 = 1.05$ and $\zeta_f = 0.10$.

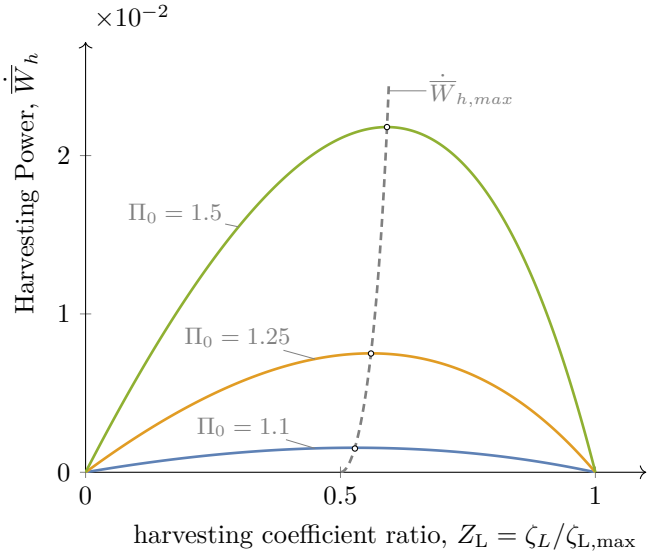

Figure 6.10 Effect of Π_0 on the power curves ; curves obtained for $\zeta_f = 0.10$.

in fig. 6.11. This behavior is different than the temperature nonlinearity, where $Z_{L,\text{opt}}$ was decreasing with Π_0.

The maximum power output $\dot{\overline{W}}_{h,max}$ ($\dot{\overline{W}}_h$ at $Z_L = Z_{L,\text{opt}}$) only depends on the dimensionless parameters Π_0 and ζ_f. We display $\dot{\overline{W}}_{h,max}$ as a function of Π_0 in fig. 6.12. We again see that increasing Π_0 increases $\dot{\overline{W}}_{h,max}$ significantly. For Π_0 close to one, $\dot{\overline{W}}_{h,max}$ only depends on the linear quantity Π_0. As Π_0 increases, $\dot{\overline{W}}_{h,max}$ also depends on ζ_f (at fixed Π_0). We do not observe a saturation of the power as for the temperature nonlinearity fig. 6.7. However, we did not push Π_0 as far. We limited the Π_0 value because the dynamics there

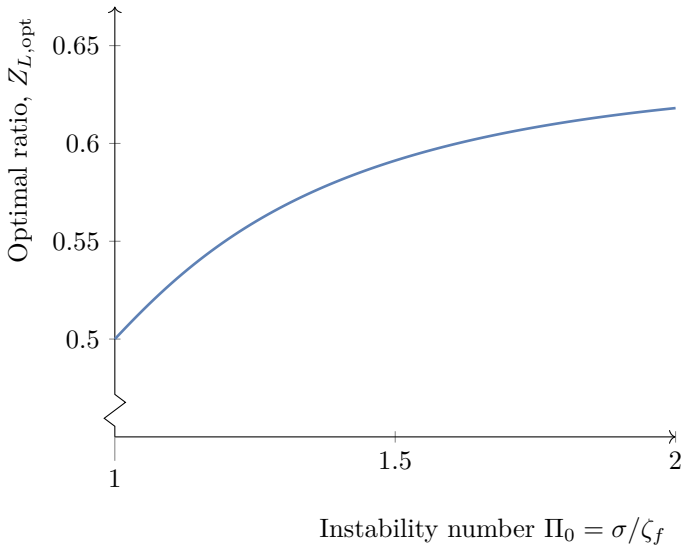

Figure 6.11 Optimal harvesting coefficient ratio $Z_{L,\mathrm{opt}}$ (Z_L where $\overline{\dot{W}}_h = \overline{\dot{W}}_{h,max}$) as a function of Π_0 ; for $\zeta_f = 0.10$.

is already quite extreme (large amplitude in q_1 and possibly large variations of pressure) which is probably not reachable experimentally and where some of our hypotheses would no longer be valid anyway.

6.4.2 Efficiency

To compute the efficiency based on eq. (6.20) for the pressure nonlinearity alone, we need $\widetilde{W}_{h,\mathrm{Cycle}}$ and $\widetilde{Q}_{\mathrm{in,cycle}}$. The work $\widetilde{W}_{h,\mathrm{Cycle}}$, is obtained by substitution of eq. (6.31) into eq. (6.17). It follows an asymmetrical bell shaped curve just like the power output. The energy injected in the system over a cycle, $\widetilde{Q}_{\mathrm{in,cycle}}$, is obtained by substitution of eq. (6.22) into eq. (6.19). The resulting efficiency is displayed in fig. 6.13 for various Π_0 numbers. Just like for the temperature nonlinearity, the efficiency is 0 at $Z_\mathrm{L} = 0$ and $Z_\mathrm{L} = 1$ and reaches a maximum in between. Increasing Π_0 significantly increases the efficiency. For Π_0 close to 1, the optimal value Z_L is 2/3, while the one for $\overline{\dot{W}}_{h,max}$ is 1/2. As Π_0 increases, the optimal value Z_L for maximum efficiency approaches the one for maximum power.

6.5 Discussion

6.5.1 Energy harvesting from Self-Oscillators Compared to Forced-Oscillators

Self-oscillators and forced oscillators have some important differences (see [52, sec.3.2] and [112, sec.VIB]). Because of that, energy harvesting principles differ. Here, we clarify

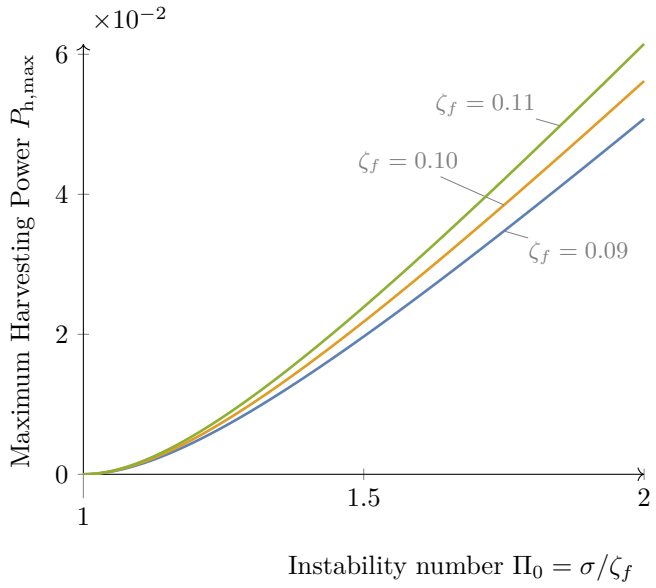

Figure 6.12 Maximum harvesting power $\overline{\dot{W}}_{h,max}$ as a function of Π_0, for various ζ_f.

these differences, considering the SOFHE model above as a prototypical self-oscillating harvester [5] and a spring-mass system (D.1) as a prototypical forced-oscillating harvester.

First, in a forced-oscillator, the forcing frequency ω can be controlled. The maximum power is obtained when $\omega = \omega_n$. By contrast, in a self-oscillator, the positive feedback is at the same frequency as the oscillations automatically (being expressed in terms of the phase-space variables q_i).

Then, in a forced-oscillator, the oscillation's amplitude progressively decreases as the harvesting coefficient ζ_L is increased, but small oscillations are always maintained. The power is maximized when the harvesting coefficient ζ_L is made equal to the friction coefficient ζ_f. This is known as *impedance matching*. The power curve tails off as ζ_L is increased beyond that, but never reaches 0 completely because the oscillation's amplitude is never 0.

The impedance matching principle does not apply to self-oscillating harvesters in general. In a self-oscillator, the instability has to be maintained to maintain the self-oscillations (one as to maintain Π above 1, section 6.2.2). As ζ_L is increased, the oscillation's amplitude progressively decreases and reaches 0 at $\zeta_L = \zeta_{\mathrm{L,max}} = \zeta_f\,(\Pi_0 - 1)$ (eq. (6.11)), where the damping is large enough to kill the instability. Also, as ζ_L is increased, the power increases, reaches a maximum and then reaches 0 at $\zeta_L = \zeta_{\mathrm{L,max}}$ as well. This threshold behavior

5. Note that some of the results we present here may not apply to all types of self-oscillators (e.g. in a subcritical Hopf bifurcation, a limit cycle may exist despite a stable equilibrium).

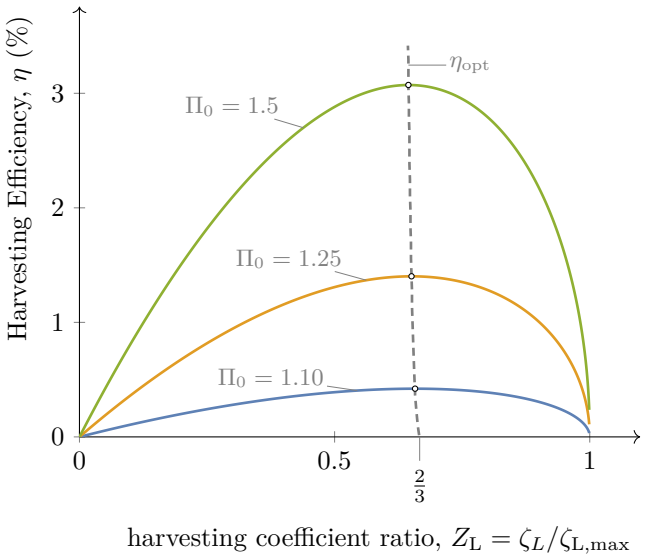

Figure 6.13 Harvesting efficiency along Z_{L} and for various Π_0 ; curves for $\zeta_f = 0.10$ and $R_g T_{g,0}/H_v = 0.09$ (for water vapor at 170 °C).

does not exist in the forced-oscillator. Close to the instability threshold, $\zeta_{\text{L,max}}$ is close to 0, because adding just a little more damping kills the oscillations. The optimal ζ_L, where the power is maximized, is equal to $Z_{\text{L}}\zeta_{\text{L,max}}$ with $Z_{\text{L}} = 1/2$ for Π_0 close to 1, and is thus also close to 0. This is far from impedance matching, which would impose $\zeta_L = \zeta_f$, where ζ_f could be large. Also, in the self-oscillating harvester, the optimal ζ_L given by $Z_{L,\text{opt}}\zeta_{\text{L,max}} = Z_{L,\text{opt}}\zeta_f\,(\Pi_0 - 1)$ is not just a function of the friction coefficient, but also the instability number Π_0. As Π_0 is increased, the optimal ζ_L drifts due to nonlinearities.

Finally, the efficiency in the forced-oscillations harvester increases monotonically as ζ_L is increased. Thus, one has to make a trade-off between maximum power and maximum efficiency. By contrast, in a self-oscillating harvester, the efficiency is 0 at both $\zeta_L = 0$ and $\zeta_L = \zeta_{\text{L,max}}$, reaching a maximum between those two values, at $\zeta_L = \frac{2}{3}\zeta_{\text{L,max}}$ for Π_0 close to 1. For the two nonlinearities studied, the ζ_L for maximum power and the ζ_L for maximum efficiency get closer and closer as we increased the instability number Π_0. Thus, there is less of a trade-off for maximum power and maximum efficiency in a self-oscillating harvester.

6.5.2 Design Considerations

We would like here to identify design considerations derived from our analysis.

6.5.3 Limitations

We made a few hypotheses when building the model, in order to simplified the analysis. The friction expression assumes Poiseuille flow, which is quite precise for a long enough

liquid plug relative to the diameter and for low value of dynamic Reynolds numbers, (see [112, 1] for details and more sophisticated expressions). We also assumed the vapor isothermal, the saturation temperature constant and physical parameters to be constant (liquid density, viscosity, enthalpy of vaporization, etc.). Finally, we assumed $T_{g,sat} = (T_H + T_L)/2$ so that the equilibrium is located perfectly at the inflexion point of the phase-change profile. More complete models are available ([112, 114]).

One major hypothesis in our model is the phase-change representation. Our expression is valid for phase-change local to the meniscus. It can also represent a “good" phase-change profile to aim for experimentally because it produces a force perfectly in phase with velocity close to the equilibrium. More importantly though, our results close to the instability threshold barely depends on the nonlinearities and so they should be applicable to various phase-change profile different than the one considered. In particular, we expect the results discussed in section 6.5.1 to hold independently of the phase-change expressions.

6.6 Conclusion

In this paper, we studied energy harvesting for a Single-Branch Pulsating Heat Pipe coupled to an electromechanical transducer, a device coined Self-Oscillating Fluidic Heat Engine (SOFHE). We showed that the harvesting coefficient must be kept between 0 and a maximum value to maintain the thermofluidic instability driving the self-oscillations. We studied SOFHE's dynamics further when the temperature nonlinearity dominates first, and then when the pressure nonlinearity dominates. Some characteristics are shared by both cases. The power as a function of the harvesting coefficient follows an asymmetrical bell shaped curve. Close to the instability threshold, the maximum power output is obtained by tuning the harvesting coefficient to half its maximum value (the one killing the oscillations). Given the harvesting coefficient at its optimal value, we obtained curves for the maximum power as a function of the instability number Π_0 and other parameters. For both nonlinearities, increasing the instability number leads to an increase in oscillations amplitude first, followed by a rapid increased in the power output. The efficiency also follows an asymmetrical bell shaped curve but, close to the instability threshold, the maximum is obtained by tuning the harvesting coefficient to two thirds of its maximum value.

For the power output, we found that, close to the instability threshold, the most relevant parameter is the instability number. One straightforward way to increase the instability is to increase the phase-change rate . Given our results, it seems promising to study ways to

improve evaporation and condensation. For example, adding microstructures in SOFHE might be a great way to improve the power output and the efficiency.

Finally, we note that studying the power output for SOFHE allowed for an interesting comparison between energy harvesting from self-oscillators and energy harvesting from forced oscillators. We draw some general distinctions in the discussion which allows for a better understanding of energy harvesting from oscillators.

Acknowledgements

We acknowledge financial support from the NSERC through the Scholarship and Discovery Programs (Canada).

CHAPTER 7

ENERGY PERSPECTIVE

7.1 Introduction

In chapter 6, we studied energy harvesting based on our mathematical model. One may argue that we considered a very specific phase-change profile and wonder if the analysis remains valid for a different profile. To address this, we adopt here an energy point of view, to describe SBPHP and SOFHE devices. The content presented here is a preliminary version of a new manuscript .

We will see that this energy perspective is very general: it can be used to analyze the dynamics for more or less any phase-change profiles, either theoretical or experimental. Also, it offers a simple explanation for the evolution of the oscillations amplitude over time: 1) the resonator stores energy, 2) the various forces produce work that injects energy into the resonator or dissipates energy from it and 3) the energy of the resonator as well as the oscillations amplitude increase when the net energy injected into the resonator is positive. The energy perspective enables an intuitive understanding of the dynamics. By computing the work done over each cycles, all the complicated details of the phase-change is reduced to a single number per cycle(and similarly for friction). We get the overall effect of the phase-change and the friction over each cycles, which is what matter when we are interested in controlling the oscillations amplitude or the power output of SOFHE. One can then study how to control the phase-change and the friction to change the work per cycle they produce. Below, we will first present the model, derive the expressions for the energy quantities and derive some basic general results (section 7.2). We will then consider a simple theoretical model (section 7.3), revisiting the questions of what leads to the startup and what leads to a steady-state regime (section 7.3.3). We will also show how the oscillations amplitude can be increased by increasing the phase-change work rate and reducing the friction work rate. The effect of the linear and nonlinear components will be made obvious. We will then investigate the effect of the load on the dynamics and the power output (sections 7.3.4 and 7.3.5). Finally, we will show how the same strategy used to increase the oscillations amplitude also leads to more power output (section 7.3.6). In section 7.4, we will show how our energy perspective can also be applied to experimental measurements, for the startup as well as the energy harvesting. The energy perspective provides guidelines to the design of better SOFHE devices.

7.2 General model and Basic Results

We now build a theoretical framework describing the SBPHP dynamics. We include a load, so that the framework also applies to the SOFHE device, for energy harvesting. Our goal is to reach a description of the SBPHP dynamics in terms of energy and work, with as few hypotheses as possible. The approach here will be very general. It applies to our more precise theoretical model (section 7.3) as well as the experimental data presented in section 7.4.

7.2.1 Basic Equations

We consider the geometry presented in fig. 7.1. Before the self-oscillations starts, the vapor bubble has a fixed length $L_{g,0}$. Once the self-oscillations starts, the vapor bubble length is L_g and varies over time. We define x_i as the position of the meniscus relative to the equilibrium ($x_i = L_g(t) - L_{g,0}$). The vapor has a pressure P_g, a mass m_g and a temperature T_g [1]. The liquid plug has a mass m_ℓ. The tube being open, the pressure on the external side is P_e.

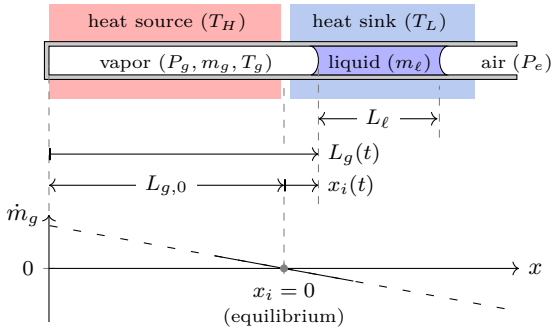

Figure 7.1 SBPHP model.

First, the momentum balance is applied to the liquid plug, as:

$$m_\ell \ddot{x}_i = \left(P_g - \hat{P}_e\right) A + F_f + F_L \ , \tag{7.1}$$

with $\ddot{x}_i$ the acceleration of the liquid plug. $P_g A$ is the force applied by the vapor pressure on the liquid plug. The force $\hat{P}_e A$ combines the force $P_e A$, due to the pressure of the air, and the gravitational force if the tube is tilted, with $\hat{P}_e = P_e + \rho_\ell g L_\ell \sin\theta$, where ρ_ℓ is the liquid density, g the gravitational acceleration, L_ℓ the length of the liquid plug and θ the angle of the tube relative to the horizontal. The force F_f is the friction force due to the interaction between the liquid and the walls and the force F_L is the load, the force that

1. The temperature of the vapor is equal to saturation at the liquid vapor interface but may differ significantly from saturation condition in the heat source (usually overheated, given T_H above the saturation temperature). Thus, we consider T_g as the spatial average of the vapor temperature here.

the transducer applies to the liquid plug. We expect both F_f and F_L to be dissipative force (we will consider specific expressions later on). The pressure in the vapor, P_g, can be described by the ideal gas law:

$$P_g = \frac{m_g R_g T_g}{(x_i + L_{g,0})\, A} \ , \tag{7.2}$$

where $(x_i + L_{g,0})A$ is the volume of vapor. The eqs. (7.1) and (7.2) (except for the load F_L) to describe the SBPHP dynamics are well-established [86]. In eq. (7.2), both the mass of vapor m_g and the temperature of vapor T_g may vary, and must therefore be described by additional equations.

The mass of vapor m_g varies due to evaporation and condensation, as the liquid plug oscillates between the heat source and the heat sink. Phase-change can occur on the meniscus but also on a liquid film left on wall by the liquid plug, during the oscillations. The latter is usually consider to be dominant, since the thermal resistance across the (thin) liquid film is much lower. A great deal of research has been carried on modeling the formation of this liquid film on the plain internal surface of the tube [20, 93, 22, 83, 7, 99, 67, 118, 38]. However, in an effort to enhance the phase-change, engineered tubes are also studied experimentally, where the surface of the tube is modified to create wicking structures [129, 43, 42, 119, 90, 62, 112]. It is not possible to express all possible configurations in a single phase-change expression. We will therefore not fix the phase-change expression right away to remain as general as possible. For the moment, we simply consider that the mass of vapor varies according to an overall phase-change expression, function of the position and possibly other variables:

$$\dot{m}_g = f(x_i, \dots) \ , \tag{7.3}$$

with m_g the mass of vapor and $\dot{m}_g$ the phase-change rate ($\dot{m}_g$ positive or negative for evaporation or condensation, respectively). The temperature of vapor T_g can be described by applying the energy conservation on the vapor bubble [112]:

$$\dot{T}_g = \frac{1}{c_v\, m_g} \left[\dot{m}_g \left(c_p T_{g,sat} - c_v\ T_g \right) - P_g A\, \dot{x}_i + \dot{Q}_g \right] \ , \tag{7.4}$$

where T_g is considered as the spatially averaged temperature of the vapor. Two interesting cases are worth considering: the isothermal case where the heat transfer between the walls and the vapor, $\dot{Q}_g$, is such that $\dot{T}_g = 0$ and the temperature of the vapor is constant and the adiabatic case, where $\dot{Q}_g = 0$.

Equations (7.1) to (7.4), plus the expressions for F_f and F_L, constitute a set of nonlinear differential equations, which can be solved for the position x_i, the mass of vapor m_g and the temperature of vapor T_g.

7.2.2 Equilibrium and Dimensionless Equations

Experiments show that the SBPHP has one equilibrium (the liquid plug does not move) that becomes unstable when the heat source temperature is increased. We will denote quantities at equilibrium by the 0 subscript (e.g. $P_g = P_{g,0}$, $m_g = m_{g,0}$ and so on). The equilibrium in the system of equations eqs. (7.1) and (7.3) can be obtained by solving for $\dot{x}_i = \ddot{x}_i = \dot{m}_g = \dot{T}_g = 0$ (liquid plug does not move, the mass and the temperature of vapor are constant). Doing so, we find from the momentum balance (eq. (7.1)) that $P_g = P_{g,0} = \hat{P}_e$. Now looking at the phase-change, we should have one length of the vapor bubble L_g where the net phase-change is 0, where $\dot{m}_g = 0$. This vapor bubble length is defined as $L_{g,0}$ and corresponds to $x_i = 0$ (given $x_i = L_g(t) - L_{g,0}$). From eq. (7.4), one expects that the temperature of the vapor at equilibrium $T_{g,0}$ approaches the temperature of the heat source, given the heat transfer between the walls and the vapor $\dot{Q}_g$. We now make the variables relative to their equilibrium values and dimensionless, using $1/\omega_n$, $L_{g,0}$, $m_{g,0}$, $T_{g,0}$ as the characteristics time, length, mass, and temperature, where $\omega_n = \sqrt{P_{g,0}/(\rho_\ell L_{g,0} L_\ell)}$ is the natural frequency. We get:

$$\tau = \omega_n t \quad \text{with: } \omega_n = \sqrt{P_{g,0} \,/\, (\rho_\ell L_{g,0} L_\ell)} \,, \tag{7.5a}$$

$$q_1 = \frac{x_i}{L_{g,0}} \,, \tag{7.5b}$$

$$q_2 = \frac{dq_1}{d\tau} = \frac{1}{\omega_n L_{g,0}} \frac{dx_i}{dt} \,, \tag{7.5c}$$

$$q_3 = \frac{m_g - m_{g,0}}{m_{g,0}} \,, \tag{7.5d}$$

$$q_4 = \frac{T_g - T_{g,0}}{T_{g,0}} \,, \tag{7.5e}$$

as the dimensionless time, position, velocity, mass of vapor and spatially averaged temperature of the vapor. Let's now rewrite the momentum balance eq. (7.1) in terms of dimensionless quantities eq. (7.5). The left-hand-side of the momentum balance becomes $m_\ell \ddot{x}_i = (m_\ell \omega_n^2 L_{g,0})\, \dot{q}_2$. Given the expression for ω_n, we have that $m_\ell \omega_n^2 L_{g,0} = P_{g,0} A$. The quantity $P_{g,0} A$ is the characteristic force in the system. Dividing both the left-hand-side

and the right-hand-side of the momentum balance by $P_{g,0}A$, we get:

$$\dot{q}_2 = \underbrace{\frac{(P_g - P_{g,0})\,A}{P_{g,0}A}}_{\widetilde{\Delta P_g}} + \underbrace{\frac{F_f}{P_{g,0}A}}_{\widetilde{F_f}} + \underbrace{\frac{F_L}{P_{g,0}A}}_{\widetilde{F_L}} , \tag{7.6}$$

as a dimensionless momentum balance equation. We used here the fact that $\hat{P}_e = P_{g,0}$ from the equilibrium conditions described above. The quantities $\widetilde{\Delta P_g}$, $\widetilde{F_f}$ and $\widetilde{F_L}$ are dimensionless forces from the pressure difference on the liquid plug, the friction due to the liquid-wall interaction and the load, respectively.

Substitution of the ideal gas law eq. (7.2) into $\widetilde{\Delta P_g}$, and substitution of the dimensionless quantities eq. (7.5), leads to the following expression for $\widetilde{\Delta P_g}$:

$$\widetilde{\Delta P_g} = \underbrace{-\frac{q_1}{1+q_1}}_{\widetilde{F_\mathcal{V}}} + \underbrace{\frac{q_3}{1+q_1}}_{\widetilde{F_m}} + \underbrace{\frac{q_4}{1+q_1}}_{\widetilde{F_T}} + \underbrace{\frac{q_3\,q_4}{1+q_1}}_{\widetilde{F_{mT}}} . \tag{7.7}$$

The pressure in the vapor can vary due to changes of volume (compression/expansion of the vapor bubble), changes of mass (dues to phase-change) and changes of temperature. In eq. (7.7), these effects are neatly expressed as individual dimensionless forces applying to the liquid plug (substitution in the momentum balance leads to $\dot{q}_2 = \widetilde{F_\mathcal{V}} + \widetilde{F_m} + \widetilde{F_T} + \widetilde{F_{mT}} + \widetilde{F_f} + \widetilde{F_L}$). The term $\widetilde{F_\mathcal{V}}$ expresses the force due to changes of volume (given a dimensionless displacement q_1). It acts as a nonlinear restoring force (as $-kq_1$, where $k = 1/(1+q_1)$) and is equal to zero for $q_1 = 0$. This term coupled with the dimensionless inertial term ($\dot{q}_2$) leads to a resonator (spring-mass system). As shown in fig. 7.2, the nonlinearity makes the restoring force rise to infinity when the vapor bubble is compressed significantly (for q_1 approaching -1), preventing the liquid plug from going through the closed end. The term $\widetilde{F_m}$ expresses the primary force due to changes of mass of vapor q_3. It is zero in the absence of phase-change since we then have $q_3 = 0$. Experimentally, $\widetilde{F_m}$ was found to be in phase with velocity, thus acting as a positive feedback, which tends to increase the oscillation's amplitude [112]. The term $\widetilde{F_T}$ expresses the primary force dues to changes of temperature of vapor q_4. It is zero for an isothermal vapor since we then have $q_4 = 0$. The term $\widetilde{F_{mT}}$ is a combined nonlinear force due to variations of mass of vapor and of temperature of vapor. It is zero if there is no phase-change or if the vapor is isothermal. The variations of temperature of the vapor are typically small in which case both $\widetilde{F_T}$ and $\widetilde{F_{mT}}$ are can be neglected. All forces are nonlinear because of the $1/(1+q_1)$ prefactor.

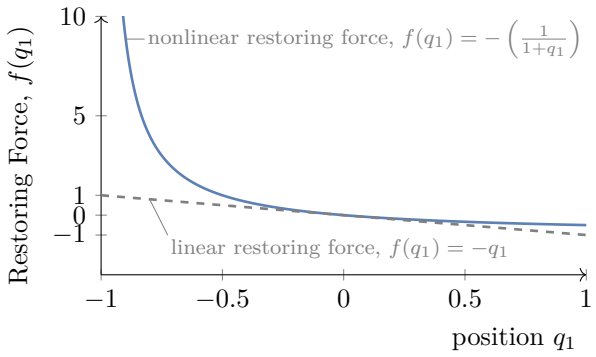

Figure 7.2 Effect of the pressure nonlinearity on the restoring force.

In addition to the momentum balance, both the phase-change equation (7.3) and the vapor energy equation (7.4) can be turned in dimensionless form, leading to differential equations for $\dot{q}_3$ and $\dot{q}_4$ (we will be more specific in section 7.3).

7.2.3 Energy Perspective

The momentum balance eq. (7.6) can be turned into an energy equation. We will find this energy perspective insightful. We start by providing definitions. We then obtain the energy balance equation in rate form (**Momentum Balance as an Energy Balance**). Finally, we use the energy balance to show that, for an isothermal vapor, the startup is explained by the interplay between the energy injected into the system by the phase-change and the energy dissipated by the friction (**Energy Perspective on the Startup**).

Definitions

The kinetic energy of the liquid plug is $K = \frac{1}{2} m_\ell \dot{x}^2$. We can express it in terms of dimensionless quantities, given $m_\ell = \rho_\ell L_\ell A$ and $\dot{x}_i = \omega_n L_{g,0}\, q_2$ (eq. (7.5c)), leading to $K = \frac{1}{2}\left(L_{g,0} P_{g,0} A\right) q_2^2$. The quantity $L_{g,0} P_{g,0} A$ is the characteristic energy (or characteristic work). We may define a dimensionless kinetic energy as:

$$\widetilde{K} = \frac{K}{L_{g,0} P_{g,0} A} = \tfrac{1}{2}\, q_2^2 \ . \tag{7.8}$$

The dimensionless force $\widetilde{F_{\mathcal{V}}}$, which acts as a restoring force, is conservative. It has a corresponding dimensionless potential energy $\widetilde{U}_r$ defined as $\widetilde{U}_r = -\int \widetilde{F_{\mathcal{V}}}\, dq_1$. Given $\widetilde{F_{\mathcal{V}}} = -q_1/(1+q_1)$, we get:

$$\widetilde{U}_r = \frac{U_r}{L_{g,0} P_{g,0} A} = q_1 - \ln\left[1 + q_1\right] \ . \tag{7.9}$$

We note that a Taylor expansion gives $\widetilde{U}_r = \frac{1}{2}q_1^2 + \mathcal{O}(q_1^3)$, so the potential energy is close to the one of a linear spring for q_1 small enough. In the momentum balance equation, the coupling of the dimensionless inertial term $\dot{q}_2$ and restoring force $\widetilde{F_\mathcal{V}}$ led to a resonator, a spring-mass system. The dimensionless energy of the resonator is given by $\widetilde{E}_r = \widetilde{U}_r + \widetilde{K}$:

$$\widetilde{E}_r = \frac{E_r}{L_{g,0}P_{g,0}A} = \underbrace{q_1 - \ln\left[1+q_1\right]}_{\widetilde{U}_r} + \underbrace{\tfrac{1}{2}\, q_2^2}_{\widetilde{K}} \ . \tag{7.10}$$

The energy of the resonator is related to the oscillations amplitude. We will find it useful to consider the energy averaged over one oscillation cycle. the averaged energy of the resonator is:

$$\overline{E_r}(\tau_i) = \frac{1}{\tilde{T}} \int_{\tau_i - \tilde{T}/2}^{\tau_i + \tilde{T}/2} \widetilde{E}_r(\tau) d\tau \ , \tag{7.11}$$

with $\tilde{T}$ the dimensionless oscillation period. Averaged kinetic energy $\overline{K}$ and potential energy $\overline{U_r}$ can be defined similarly. Later on, we will consider derivatives over time of energy quantities. The derivatives over time of $\widetilde{K}$, $\widetilde{U}_r$ and $\widetilde{E}_r$:

$$\dot{\widetilde{K}} = \dot{q}_2\, q_2 \ , \tag{7.12}$$

$$\dot{\widetilde{U}}_r = \frac{\partial \widetilde{U}_r}{\partial q_1}\, \frac{d\, q_1}{d\, \tau} = -\widetilde{F_\mathcal{V}}\, q_2 \ , \tag{7.13}$$

$$\dot{\widetilde{E}}_r = \dot{\widetilde{K}} + \dot{\widetilde{U}}_r \ . \tag{7.14}$$

We may also consider the derivative of the averaged resonator energy as (note that averaging and differentiation are interchangeable, Leibniz integral rule):

$$\overline{\dot{E}_r}(\tau_i) = \frac{1}{\tilde{T}} \int_{\tau_i - \tilde{T}/2}^{\tau_i + \tilde{T}/2} \dot{\widetilde{E}}_r(\tau)\ d\tau \ . \tag{7.15}$$

The averaged rates of change for the kinetic energy and for potential energy, $\overline{\dot{K}}$ and $\overline{\dot{U}_r}$, can be defined similarly. We will also consider work quantities done by the forces. The dimensionless [2] infinitesimal work done by a force $\widetilde{F_x}$ over a displacement of the liquid plug dq_1 is $d\widetilde{W}_x = \widetilde{F_x}\, dq_1$. With q_2 the velocity, we can also write $d\widetilde{W}_x = \widetilde{F_x}\, dq_1 = \widetilde{F_x}\, q_2\, d\tau$. Thus, the dimensionless work rate is:

$$\dot{\widetilde{W}}_x(\tau_i) = \widetilde{F_x}(\tau_i)\ q_2(\tau_i) \ . \tag{7.16}$$

This is in fact instantaneous dimensionless power. We will also use averaged quantities in the following. Averaging the work rate gives:

$$\overline{\dot{W}}_x(\tau_i) = \frac{1}{\tilde{T}} \int_{\tau_i - \tilde{T}/2}^{\tau_i + \tilde{T}/2} \widetilde{\dot{W}}_x \, d\tau = \frac{1}{\tilde{T}} \int_{\tau_i - \tilde{T}/2}^{\tau_i + \tilde{T}/2} \left(\widetilde{F_x} \, q_2 \right) \, d\tau \ , \tag{7.17}$$

with the dimensional form given by $(\omega_n \, L_{g,0} P_{g,0} A) \, \overline{\dot{W}}_x$.

Momentum Balance as an Energy Balance

Let's now consider the momentum balance, $\dot{q}_2 = \widetilde{F_{\mathcal{V}}} + \widetilde{F_m} + \widetilde{F_T} + \widetilde{F_{mT}} + \widetilde{F_f} + \widetilde{F_L}$. We may turn it into an energy balance equation in rate form by multiplying by the velocity q_2:

$$\dot{q}_2 q_2 = \left(\widetilde{F_{\mathcal{V}}} + \widetilde{F_m} + \widetilde{F_T} + \widetilde{F_{mT}} + \widetilde{F_f} + \widetilde{F_L} \right) \, q_2 \ .$$

The left-hand side is in fact the kinetic energy rate $\dot{\tilde{K}}$, the term $\widetilde{F_{\mathcal{V}}} \, q_2$ is $-\dot{\tilde{U}}_r$ and the other terms are dimensionless work rate. Rearranging, we thus get:

$$\dot{\tilde{E}}_r = \dot{\tilde{K}} + \dot{\tilde{U}}_r = \widetilde{\dot{W}}_m + \widetilde{\dot{W}}_T + \widetilde{\dot{W}}_{mT} + \widetilde{\dot{W}}_f + \widetilde{\dot{W}}_L \ .$$

Instead of studying the fast fluctuations of the energy within one cycle, we wish to study the slow variations from one cycle to the other, so we need an equation for the averaged rate of change of the energy, $\overline{\dot{E}_r}$. We average both sides (by multiplying by $(1/\tilde{T})d\tau$ and integrating over a period) and obtain and energy balance in rate form, averaged over a cycle:

$$\overline{\dot{E}_r}(\tau_i) = \overline{\dot{W}}_m(\tau_i) + \overline{\dot{W}}_T(\tau_i) + \overline{\dot{W}}_{mT}(\tau_i) + \overline{\dot{W}}_f(\tau_i) + \overline{\dot{W}}_L(\tau_i) \ . \tag{7.18}$$

This equation tells us that the energy of the resonator increases from one cycle to the other when the total averaged work rate done by the forces is positive. In the isothermal case, we simply have:

$$\overline{\dot{E}_r}(\tau_i) = \overline{\dot{W}}_m(\tau_i) + \overline{\dot{W}}_f(\tau_i) + \overline{\dot{W}}_L(\tau_i) \ . \tag{7.19}$$

2. We may define dimensional and dimensionless works produced by a given force as follow. The dimensional work W done by a dimensional force F between time t_0 and t_i is $W = \int_{t_0}^{t_i} F \, \dot{x} \, dt$. Substitution of dimensionless velocity, time and force using eq. (7.5) and the characteristic force $P_{g,0}A$, we get $W = L_{g,0} P_{g,0} A \int_{\tau_0}^{\tau_i} \widetilde{F} \, q_2 \, d\tau$. The quantity $L_{g,0} P_{g,0} A$ is the characteristic work (or characteristic energy). We define a dimensionless work as $\widetilde{W} = W/(L_{g,0} P_{g,0} A) = \int_{\tau_0}^{\tau_i} \widetilde{F} \, q_2 \, d\tau$.

Energy Perspective on the Startup

Let's consider the SBPHP dynamics during the startup, with no load and in the isothermal case. The energy balance eq. (7.18) simplifies to:

$$\dot{\overline{E_r}}(\tau_i) = \dot{\overline{W}}_m(\tau_i) + \dot{\overline{W}}_f(\tau_i) \ . \tag{7.20}$$

For the startup to occur, we should have $\dot{\overline{E_r}} > 0$ at first, so that the energy grows over time. The steady-state regime is reached when $\dot{\overline{E_r}} = 0$. Because the friction dissipates energy, $\dot{\overline{W}}_f$, is negative. Thus, for the energy as well as the oscillation amplitude to grow, the work rate done by phase-change $\dot{\overline{W}}_m$ must be greater than the work done by friction, we must have $\dot{\overline{W}}_m > -\dot{\overline{W}}_f$. Let's consider the equilibrium position (at $x_i = 0$, described in section 7.2.1). If, after a small perturbation $\dot{\overline{W}}_m < -\dot{\overline{W}}_f$, then the equilibrium is stable and the oscillations will die out. However, if $\dot{\overline{W}}_m > -\dot{\overline{W}}_f$, the oscillations will grow, until $\dot{\overline{W}}_m = -\dot{\overline{W}}_f$, where the system will settle in a steady-state. We will show that both numerically and experimentally in the following. Our description here was based on very few hypotheses and our conclusions are therefore general.

Energy Harvesting, Power Output

Let's now consider the energy harvested by the load. The dimensionless averaged work rate (or power) done over a cycle by the load is $\dot{\overline{W}}_L$ given by eq. (7.17) with the force F_L, leading to:

$$\dot{\overline{W}}_L = \frac{1}{\tilde{T}} \int_{\text{cycle}} \left(\widetilde{F_L}\, q_2 \right) \, d\tau \ . \tag{7.21}$$

For a dissipative load, $\dot{\overline{W}}_L < 0$, meaning the energy quantity $-\dot{\overline{W}}_L$ is extracted by the transducer from the resonator. We define:

$$\dot{\overline{W}}_h \equiv -\dot{\overline{W}}_L = -\frac{1}{\tilde{T}} \int_{\text{cycle}} \left(\widetilde{F_L}\, q_2 \right) \, d\tau \tag{7.22}$$

as the power output extracted by the transducer. When $\dot{\overline{W}}_h > 0$, the transducer is extracting energy for the resonator and the SOFHE device is harvesting energy from the heat source. The dimensional power output harvested is simply $(\omega_n\, L_{g,0} P_{g,0} A)\, \dot{\overline{W}}_h$. The power output $\dot{\overline{W}}_h$ can be computed given the load eq. (7.22) if we know ζ_L. It can also be computed given the energy balance. Assuming the system is in steady-state (on the limit

cycle), we have $\overline{\dot{E}_r} = 0$. Solving eq. (7.18) for $\overline{\dot{W}}_L$ and considering $\overline{\dot{W}}_h = -\overline{\dot{W}}_L$ leads to:

$$\overline{\dot{W}}_h = \overline{\dot{W}}_m + \overline{\dot{W}}_T + \overline{\dot{W}}_{mT} + \overline{\dot{W}}_f \tag{7.23a}$$

as the dimensionless average power output. In the isothermal case, this equation simplifies to:

$$\overline{\dot{W}}_h = \overline{\dot{W}}_m + \overline{\dot{W}}_f \ , \tag{7.23b}$$

with $\overline{\dot{W}}_m > 0$ and $\overline{\dot{W}}_f < 0$. We can use this expression to deduce the power output from $\overline{\dot{W}}_m$ and $\overline{\dot{W}}_f$.

7.3 Simple Theoretical Model

The equations presented in section 7.2 are general, but not sufficient to perform numerical simulations. One still needs expressions for the friction force F_f, for the load F_L, as well as the differential equation for the phase-change rate $\dot{m}_g$. Here, we will choose specific expressions for those, in order to obtain an simplified but complete model that we can study. We use the model to build our energy analysis approach, which we will then apply to experimental data in section 7.4. We will find from the experimental measurements that the behavior of the system is qualitatively similar than our simplified theoretical model.

7.3.1 Model

For the friction force F_f, we assume a Poiseuille flow. With $c_f = 8\pi\mu L_\ell$, we can write: $F_f = -c_f\,\dot{x}_i$. We defined dimensionless friction as $\widetilde{F_f} = F_f/(m_\ell\omega_n^2 L_{g,0}) = F_f/(P_{g,0}A)$ in eq. (7.6) so:

$$\widetilde{F_f} = -2\,\zeta_f\,q_2 \ , \qquad \text{with: } \zeta_f = \frac{c_f}{2m_\ell\omega_n} = \frac{8\pi\mu L_\ell}{2m_\ell\omega_n} \ , \tag{7.24}$$

with q_2 the dimensionless velocity and ζ_f the dimensionless friction coefficient. For the load F_L, we consider a basic type of transducer called velocity-damped. It produces a force F_L proportional and opposite to velocity, meaning it is a purely dissipative force (just like F_f). So, the impact of the velocity-damped transducer on the dynamics can be simply understood has increased friction. With c_L a proportionality constant (to be defined by the transducer's characteristics), we have: $F_L = -c_L\,\dot{x}_i$. The dimensionless load force is given by:

$$\widetilde{F_L} = -2\,\zeta_L\,q_2 \ , \qquad \text{with: } \zeta_L = \frac{c_L}{2m_\ell\omega_n} \ . \tag{7.25}$$

For the temperature of vapor, we will consider the isothermal case: the heat transfer $\dot{Q}$ maintains $\dot{T}_g = 0$, leading to $\dot{q}_4 = 0$. We now need to find the dimensionless phase-change rate $\dot{q}_3$. We first consider a linear profile given by $\dot{q}_3 = -2\sigma q_1$. This means that there is evaporation when the meniscus is in the heat source and condensation when the meniscus is in the condenser. Moreover, the phase-change rate is higher (linearly) as the meniscus goes deeper in the heat source or heat sink. Tessier-Poirier et al. [112] found that this profile matched well the experimental phase-change rate in the early stage of the startup (when the dynamics is linear). This profile is also the one that produces a force perfectly in phase with velocity (linearly), so it is the simpler one to consider to produce a feedback force. We will also consider a limiting mechanism to limit the phase-change rate (neither evaporation nor condensation can go to infinity), making it nonlinear. The final profile is shown in fig. 7.3. Tuning σ and T_{HL} allows to obtain a profile between a linear profile (large T_{HL}) or a step profile with constant evaporation and constant condensation (large σ and finite T_{HL}). We finally get the following system of differential equations:

$$\dot{q}_1 = q_2 \ , \tag{7.26a}$$

$$\dot{q}_2 = -\left(\frac{1}{1+q_1}\right) q_1 + \left(\frac{1}{1+q_1}\right) q_3 - 2\,\zeta\ q_2 \ , \tag{7.26b}$$

$$\dot{q}_3 = T_{HL}\ \arctan\left[-\left(\frac{2\sigma}{T_{HL}}\right) q_1\right] \ , \tag{7.26c}$$

with $\zeta = \zeta_f + \zeta_L$. Equation (7.26) has one equilibrium at $q_1 = q_2 = q_3 = 0$.

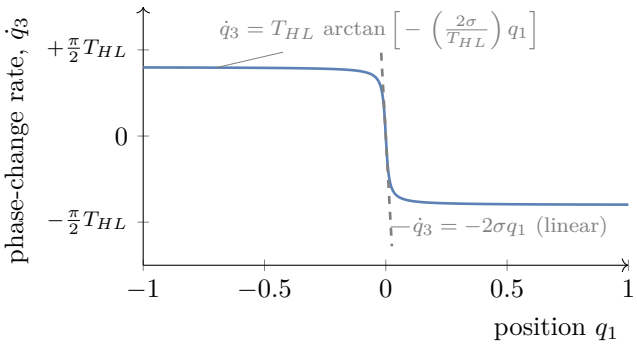

Figure 7.3 Phase-change profile limited by a nonlinearity.

7.3.2 Basic Results

The dynamics of eq. (7.26) has been studied before for the SBPHP, so without harvesting, with $\zeta_\mathrm{h} = 0$ and $\zeta = \zeta_f$ [112, 114]. Those results can still be used here, by simply adding ζ_h to ζ_f (the model is the same, we simply change a parameter).

Instability Threshold and Maximum Load

Tessier-Poirier et al. [112] performed a linear stability analysis of eq. (7.26). They showed that, after a small perturbation of the equilibrium, the position q_1 oscillates with an amplitude increasing over time if the phase-change coefficient (σ) which produced the positive feedback is greater than the dissipation (ζ). This occurs when the instability number Π is greater than one, with:

$$\Pi = \frac{\sigma}{\zeta} = \frac{\Pi_0}{1 + (\zeta_L/\zeta_f)}, \quad \Pi_0 = \frac{\sigma}{\zeta_f} = \frac{\rho_\ell \, R_g \, T_{g,0} \, \left|T'_{w,0}\right|}{8\pi \, \mu \, H_v R_{th} \, \hat{P}_e} \, . \tag{7.27}$$

When there is no harvesting, $\zeta_L = 0$, we simply have $\Pi = \Pi_0$, Π_0 being the instability number without harvesting. Let's assume now that SOFHE is first started without harvesting from equilibrium, by increasing Π_0 above one[3]. The oscillations first increase in amplitude and eventually settle down in a steady-state (limit cycle) due to the nonlinearities [113, 114]. We then progressively increase ζ_L to harvest some energy. As a consequence, Π will progressively decrease. Ultimately, ζ_L will reach a maximum value $\zeta_{\mathrm{L,max}}$ where Π will reach 1, the total damping being large enough to kill the self-oscillations. At this point, for $\zeta_L \geqslant \zeta_{\mathrm{L,max}}$, there is no more limit cycle, the equilibrium is stable, and we cannot extract energy. Solving eq. (7.27) for $\zeta_L = \zeta_{\mathrm{L,max}}$ with $\Pi = 1$, we get:

$$\zeta_{\mathrm{L,max}} = \zeta_f \, (\Pi_0 - 1) \, . \tag{7.28}$$

In order to extract energy, we must keep $0 < \zeta_L < \zeta_{\mathrm{L,max}}$, so it makes sense to consider the ratio:

$$Z_{\mathrm{L}} \equiv \frac{\zeta_L}{\zeta_{\mathrm{L,max}}} = \frac{\zeta_L}{\zeta_f \, (\Pi_0 - 1)} \, . \tag{7.29}$$

The harvesting ratio Z_{L} must be kept between 0 and 1 to harvest energy while maintaining the oscillations. We can redefine the parameters of the system in terms of Z_{L} instead of

3. Typically, by increasing the temperature of the heat source, which increases the thermal gradient at the equilibrium $\left|T'_{w,0}\right|$, which in turns increases the phase-change coefficient σ, finally leading to an increase in Π_0.

ζ_L, leading to:

$$\zeta_L = \zeta_f \left(\Pi_0 - 1\right) Z_{\mathrm{L}} \ , \tag{7.30a}$$

$$\zeta = \zeta_f + \zeta_L = \zeta_f \left(1 + \left(\Pi_0 - 1\right) Z_{\mathrm{L}}\right) \ , \tag{7.30b}$$

$$\Pi = \frac{\sigma}{\zeta} = \frac{\Pi_0}{1 + \left(\Pi_0 - 1\right) Z_{\mathrm{L}}} \ . \tag{7.30c}$$

We clearly see from eq. (7.30c) that we have $\Pi = \Pi_0$ for $Z_{\mathrm{L}} = 0$ (unstable equilibrium if $\Pi_0 > 1$) and $\Pi = 1$ (stable equilibrium and no limit cycle) for $Z_{\mathrm{L}} = 1$.

Energy Perspective in the Linear Approximation

We would like to look at the work and energy based on the solution for q_1, q_2 and q_3 in the linear approximation. Here, we further assume that $\delta = \zeta(\Pi - 1)$ is small. Doing so, and based on the definitions given in section 7.2.3, we find that the energy of the resonator is:

$$\widetilde{E}_r = \widetilde{K} + \widetilde{U}_r \quad \approx \frac{1}{2}\, \overline{r}^2(\tau_i) \quad , \tag{7.31a}$$

where $\overline{r}$ is the oscillations amplitude in q_1, averaged over a cycle (because the amplitude slowly grows during the startup). Thus, the energy and the amplitude are related. The average work rates are:

$$\dot{\overline{W}}_m(\tau_i) \approx +\sigma\ \overline{r}^2(\tau_i) \quad = +2\sigma\ \widetilde{E}_r(\tau_i) \ , \tag{7.31b}$$

$$\dot{\overline{W}}_f(\tau_i) \approx -\zeta_f\ \overline{r}^2(\tau_i) \quad = -2\zeta_f\ \widetilde{E}_r(\tau_i) \ , \tag{7.31c}$$

$$\dot{\overline{W}}_L(\tau_i) \approx -\zeta_L\ \overline{r}^2(\tau_i) \quad = -2\zeta_L\ \widetilde{E}_r(\tau_i) \ . \tag{7.31d}$$

On the right-hand side, we used the fact that $\overline{r}^2 = 2\widetilde{E}_r$ from eq. (7.31a). With these expressions, we see that $\dot{\overline{W}}_m$, $\dot{\overline{W}}_f$ and $\dot{\overline{W}}_L$ produce straight lines when displayed as function of $\widetilde{E}_r$. We will use that in the following, to compare to the work done in the nonlinear case. We also note that eq. (7.18) becomes:

$$\dot{\overline{E_r}}(\tau_i) = \dot{\overline{W}}_m(\tau_i) + \dot{\overline{W}}_f(\tau_i) + \dot{\overline{W}}_L(\tau_i) = 2\left(\sigma - \zeta\right) \widetilde{E}_r \ , \tag{7.32}$$

which is to say that the energy grows when $\sigma > \zeta$, when $\Pi = \sigma/\zeta > 1$. In fact, we have that $\dot{\overline{W}}_m/(\dot{\overline{W}}_f + \dot{\overline{W}}_L) = \sigma/\zeta = \Pi$, the instability number can be thought of as the ratio of the work done by phase change (energy injected into the resonator) to the work done by viscous friction and by the load (energy dissipated).

Power Output for the Simple Theoretical Model

Finally, let's evaluate the average work rate of the load $\overline{\dot{W}}_L$ and the harvesting power output $\overline{\dot{W}}_h$ for our simplified model. Here, we do not consider the linear approximation anymore. We substitute eq. (7.25) into eqs. (7.21) and (7.22) leading to:

$$\overline{\dot{W}}_L = \frac{1}{\widetilde{T}} \int_{\text{cycle}} \left(\widetilde{F_L}\, q_2 \right) \, d\tau \; = \frac{1}{\widetilde{T}} \int_{\text{cycle}} \left(-2\, \zeta_L\, {q_2}^2 \right) \, d\tau \; , \tag{7.33}$$

$$\overline{\dot{W}}_h = -\overline{\dot{W}}_L \qquad\qquad = \frac{1}{\widetilde{T}} \int_{\text{cycle}} \left(+2\, \zeta_L\, {q_2}^2 \right) \, d\tau \; . \tag{7.34}$$

The expression of $\overline{\dot{W}}_h$ above means that, in order to produce power, we need both a non-zero load ($\zeta_L > 0$) and non-zero oscillations amplitude such that ${q_2}^2 > 0$ on some part of the cycle. As ζ_L is increased, the amplitude in q_2 decreases, so ζ_L must not neither too small nor to large, there is an optimum value for ζ_L as we will show later on. Alternatively, $\overline{\dot{W}}_h$ can be deduced from eq. (7.23b).

7.3.3 System Without Load (Startup of the Oscillations)

We start by analyzing the system without the load, from an energy perspective. We will see what leads to the system growing in energy and then reaching a limit cycle, during the startup. We will also see how we can control the energy level $\widetilde{E}_r$ on the limit cycle using various strategies. This will be insightful later on when looking to increase the power output of the harvester. We first perform a numerical simulation of the startup. Starting from a small perturbation of the equilibrium, the oscillations grow in amplitude and eventually settle in a steady-state (fig. 7.4). Similarly, the energy of the resonator grows and reaches a constant value on the steady-state. During the startup, the phase-change does positive work while the friction does negative work. The net work is positive, grows and then decreases towards 0. This is why the resonator's energy grows and then saturates.

It is useful to plot works as function of $\widetilde{E}_r$, as in fig. 7.5. In the linear case, works follow straight lines. In the unstable case ($\sigma > \zeta_f$), the work done by phase-change is greater than the work done by friction, so that the energy keeps growing forever. In the nonlinear case, the works follows the straight lines at low $\widetilde{E}_r$, but then deviates due to nonlinearities. At some point, $\overline{\dot{W}}_m$ and $\overline{\dot{W}}_f$ meet: the work done by phase-change is equal to the work done by friction so that the net injected energy (black line) reaches 0 and the energy of the resonator reaches a constant value. The system has reached a limit cycle (indicated by the red point).

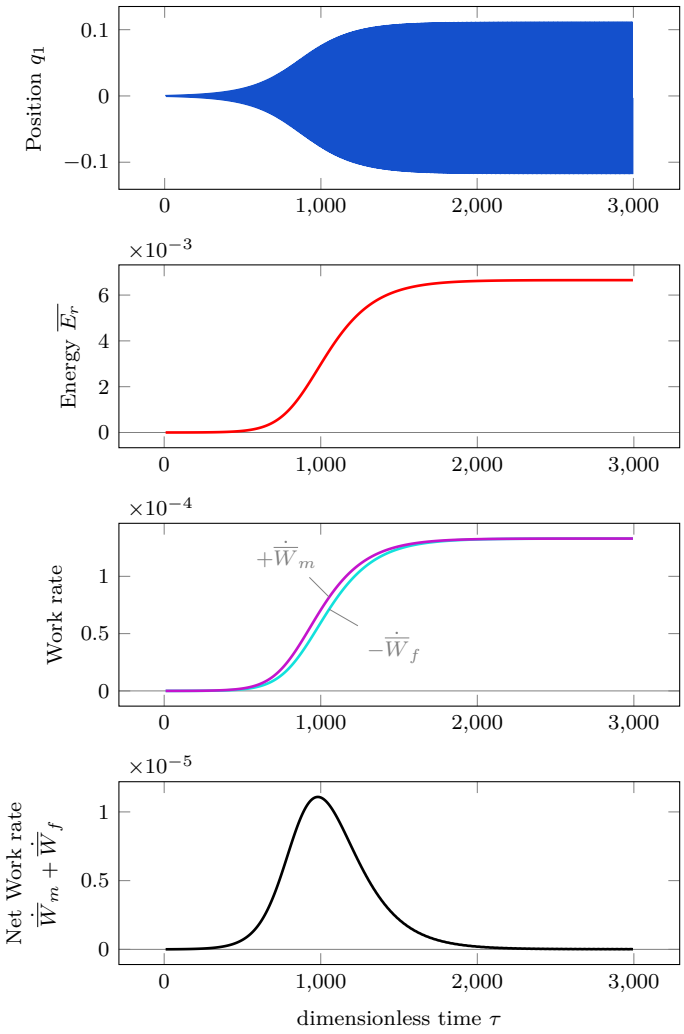

Figure 7.4 Dimensionless position, averaged energy and averaged work rate over time, during the startup; parameters are: $\sigma = 0.015$, $\zeta_f = 0.01$ and $T_{HL} = 0.002$.

Now, let's assume we wish to increase oscillations amplitude in the steady-state, meaning increasing the energy $\widetilde{E}_r$ on the limit cycle. To do so, we want $\dot{\overline{W}}_m$ and $\dot{\overline{W}}_f$ to meet at a larger $\widetilde{E}_r$. A few strategies come to mind. One could increase the slope of the phase-change or decrease the slope of the friction (those would be linear strategies). One could also try to control nonlinearities such that the phase-change drops from the linear line at a larger $\widetilde{E}_r$ (nonlinear strategies). Let's see how the graph is modified when using these strategies. In fig. 7.6, we increase the phase-change coefficient σ, leading to an increase in the slope of the phase-change $\dot{\overline{W}}_m$. The nonlinear work done by phase-change follows the greater slope and remains larger than the work for the smaller σ. The work done by friction $\dot{\overline{W}}_f$ remains on the same line. The net work is greater. We have that $\dot{\overline{W}}_m$ and $\dot{\overline{W}}_f$ meet at a greater $\widetilde{E}_r$, corresponding to larger oscillations amplitude. In fig. 7.7, we

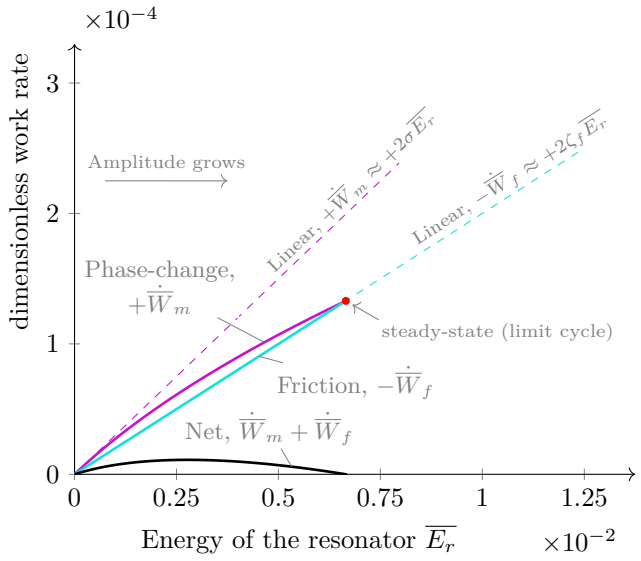

Figure 7.5 Work rate as function of the resonator's energy; same parameters as fig. 7.4.

increase the phase-change limit T_{HL} (nonlinear strategy). We see that both the slopes of $\overline{\dot{W}}_m$ and $\overline{\dot{W}}_f$ remain the same. However, as we increase T_{HL} the phase-change work $\overline{\dot{W}}_m$ remains linear a bit longer, and the drop from the linear line is delayed. This results in a greater $\widetilde{E}_r$. In fig. 7.8, we decrease the friction coefficient ζ_f. This leads to a decrease in the slope of $\overline{\dot{W}}_f$ while the slope of $\overline{\dot{W}}_m$ remains the same. The net work is greater and the system reaches a greater $\widetilde{E}_r$.

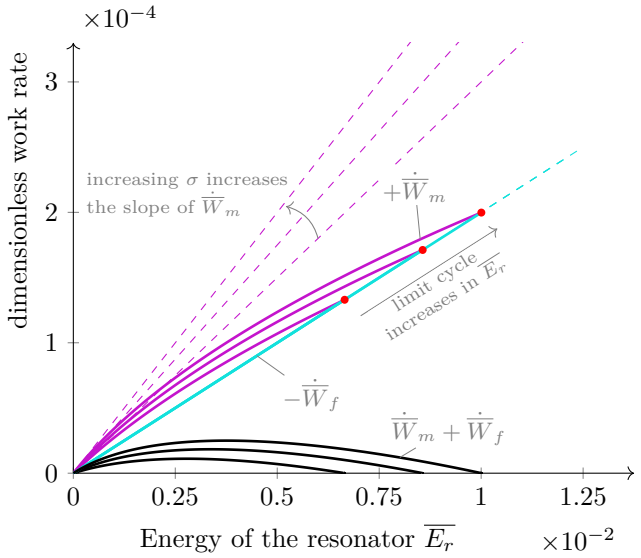

Figure 7.6 Effect of increasing the phase-change; parameters are: $\sigma = 0.015, 0.0175, 0.020$, $\zeta_f = 0.01$ and $T_{HL} = 0.002$, so $\Pi_0 = 1.5, 1.75, 2$.

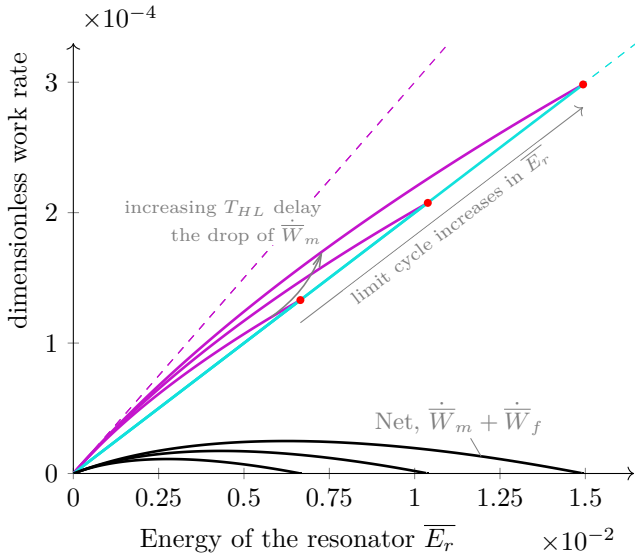

Figure 7.7 Effect of decreasing the limitation of the phase-change; parameters are: $\sigma = 0.015$, $\zeta_f = 0.01$ and $T_{HL} = 0.002, 0.0025, 0.0030$, with $\Pi_0 = 1.5$.

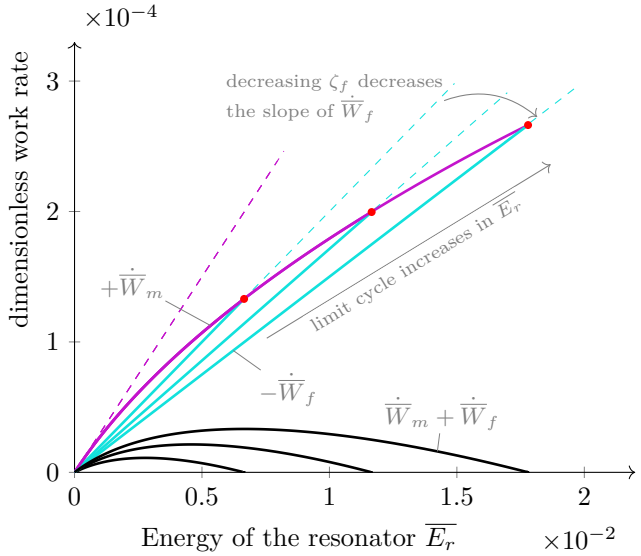

Figure 7.8 Effect of decreasing the friction; parameters are: $\sigma = 0.015$, $\zeta_f = 0.0075, 0.0086, 0.01$ and $T_{HL} = 0.002$, so $\Pi_0 = 1.5, 1.75, 2$.

7.3.4 Effect of the Load on the Dynamics

We now add a load to the system and see how this impacts the work rate as function of the energy. We have $\dot{\overline{E_r}} = \dot{\overline{W}}_m + \dot{\overline{W}}_f + \dot{\overline{W}}_L$ (eq. (7.19)). Because both the friction term $\dot{\overline{W}}_f$ and the load term $\dot{\overline{W}}_L$ are negative (they dissipate energy), we combined them in a single dissipative term: $\dot{\overline{W}}_d \equiv \dot{\overline{W}}_f + \dot{\overline{W}}_L$. In fig. 7.9, we show the startup for the system without load ($\zeta_L = 0$) and the system with a specific value of the load ($\zeta_L = 0.0013$). The system reaches a limit cycle when the curve $\dot{\overline{W}}_m$ meets $-\dot{\overline{W}}_d$, at which point $\dot{\overline{E_r}} = 0$. When we increase ζ_L from 0 to 0.0013, the slope of $-\dot{\overline{W}}_d$ increases such that the limit cycle is reached at a lower energy $\widetilde{E}_r$ corresponding to a lower oscillations amplitude.

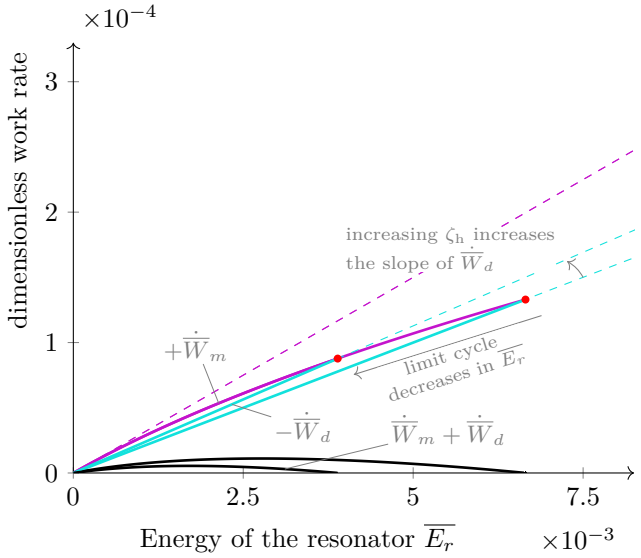

Figure 7.9 Effect of adding a load (increased dissipation); parameters are $\sigma = 0.015$, $\zeta_f = 0.01$ and $T_{HL} = 0.002$, so $\Pi_0 = 1.5$, $\zeta_L = 0$ and $\zeta_L = 0.0013$.

Now, we would like to show how the limit cycle progressively varies as we increase the load. We start from the steady-state without load ($\zeta_L = 0$) and then, we progressively increase the load until we reach $\zeta_L = \zeta_{\mathrm{L,max}}$ (see fig. 7.10). On each red dots of the curve, the system is on a limit cycle, so $\dot{\overline{E_r}} = 0$ and the work done by phase-change is equal to the total dissipative work ($\dot{\overline{W}}_m = -\dot{\overline{W}}_d = -\dot{\overline{W}}_f - \dot{\overline{W}}_L$). We also plot the corresponding work done by basic friction (blue dots). Here, we see that the limit cycle decreases in energy $\widetilde{E}_r$ as we increase the load. If we increase ζ_L too much, the energy $\widetilde{E}_r$ reaches 0, we killed the self-oscillations (section 7.3.2).

7.3.5 Effect of the Load on the Power and Efficiency

In fig. 7.10, the harvesting power $\dot{\overline{W}}_h$ is displayed (black dots). It corresponds to the difference [4]between the energy injected into the system per cycle (red dots) and the energy per cycle lost due to the viscous friction (blue dots). We see that $\dot{\overline{W}}_h$ is 0 at no load, 0 at

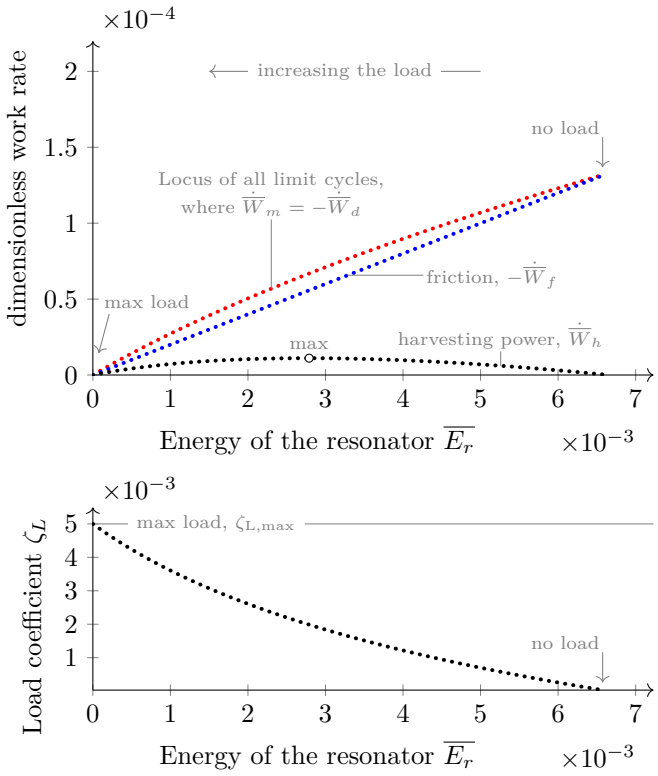

Figure 7.10 Steady-state as the load is progressively increased; parameters are $\sigma = 0.015$, $\zeta_f = 0.01$ and $T_{HL} = 0.002$, so $\Pi_0 = 1.5$, ζ_L varied between 0 and $\zeta_{\mathrm{L,max}}$.

the maximum load and that it reaches a maximum value in between. There is an optimal value for the load ζ_L in order to extract maximum power. This behavior can be explained as follows. The power $\overline{\dot{W}}_h$ is given by eq. (7.34) and is proportional to the integral of $\zeta_L {q_2}^2$ over a cycle. In the right corner of fig. 7.10, there is no load, $\zeta_L = 0$, so there is no power. In the left corner, $\zeta_L = \zeta_{\mathrm{L,max}}$, so there is no more self-oscillations and $q_2 = 0$, so there is no power. In between, we get both $\zeta_L > 0$ and ${q_2}^2 > 0$, so power is generated. There is a point where the balance is just right, such that there is significant load and amplitude and the power is maximized.

Let's focus exclusively on the harvesting power $\overline{\dot{W}}_h$ and the efficiency η for a moment. In fig. 7.11, both the harvesting power $\overline{\dot{W}}_h$ and the efficiency η are displayed as function of the harvesting coefficient ratio $Z_{\mathrm{L}} = \zeta_L/\zeta_{\mathrm{L,max}}$, for various Π_0 values. There is no power for no load on the left corner ($Z_{\mathrm{L}} = 0$) and for maximum load at the right corner ($Z_{\mathrm{L}} = 1$), with maximum power in between. We see that the power increases as we increase the instability number Π_0. Close to the instability threshold (Π_0 close to 1), the

4. we can write $\overline{\dot{W}}_h = \overline{\dot{W}}_m + \overline{\dot{W}}_f = \overline{\dot{W}}_m - (-\overline{\dot{W}}_f)$, from eq. (7.23b).

maximum power is reached for Z_{L} approaching 0.5, meaning that ζ_L must be half the $\zeta_{\mathrm{L,max}}$ to get maximum power. However, for Π_0 close to 1, $\zeta_{\mathrm{L,max}}$ actually approaches 0 because the system cannot handle more dissipation, increasing ζ_L just a little would kill the self-oscillations (eq. (7.28)). So, for Π_0 close to 1, the optimal ζ_L approaches 0. As Π_0 is increased, there is more room for larger ζ_L. We also see that the optimal $Z_{L,\mathrm{opt}}$ slightly shifts from 0.5 to the left. For the efficiency η, we also see that it is 0 for either no load ($Z_{\mathrm{L}} = 0$) or maximum load ($Z_{\mathrm{L}} = 1$). The efficiency increases as we increase Π_0. Close to the instability threshold (Π_0 close to 1), The maximum efficiency is reached at $Z_{\mathrm{L}} = 2/3$. This point shifts as we increase Π_0. Close to the instability threshold, the Z_{L} values for maximum power and maximum efficiency do not coincide. They get closer as Π_0 is increased.

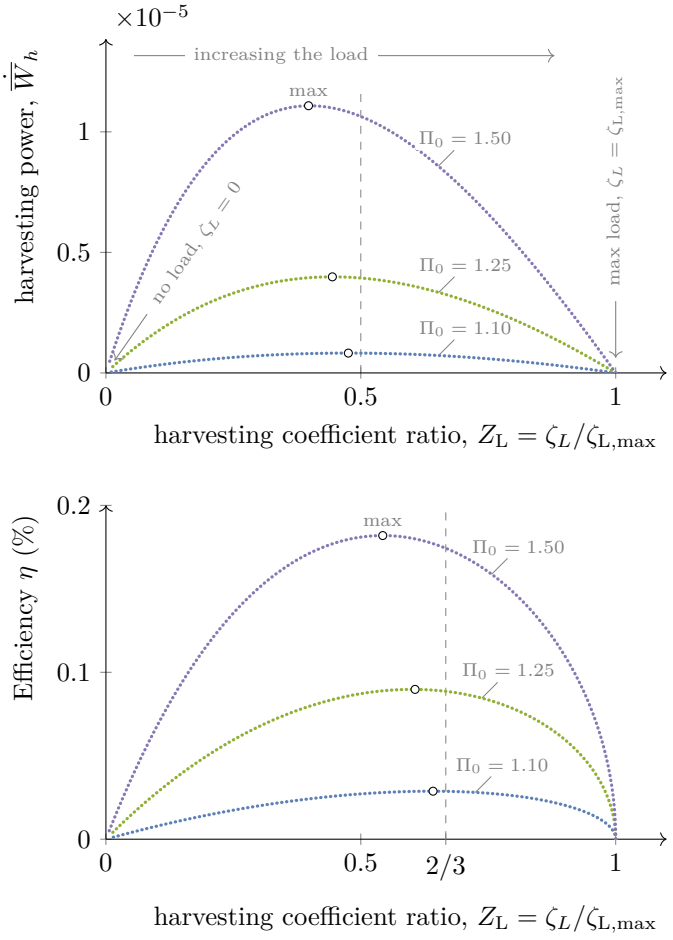

Figure 7.11 Power and efficiency as function of Z_{L}; parameters are $\zeta_f = 0.01$, $T_{HL} = 0.002$ and σ is adjusted to produce the given Π_0.

7.3.6 Increasing the Power Output

In section 7.3.5, we showed that the power could be increased by increasing Π_0. Here, we will be more thorough, and look for strategies to increase the power output. We will consider the same strategies we considered when looking at the startup with no load, where the goal was to increase the limit cycle energy level (section 7.3.3).

In fig. 7.12, we increase the phase-change coefficient σ. We expect that greater energy injected into the system would allow for more power output, and this is what we find indeed. Increasing σ increases the slope of $\overline{\dot{W}}_m$. The limit cycle with no load is located at a higher $\widetilde{E}_r$ value. As the load is increased, the curve $\overline{\dot{W}}_m = -\overline{\dot{W}}_d$ is higher, while the friction curve $-\overline{\dot{W}}_f$ remains unchanged. The harvesting work $\overline{\dot{W}}_h$ being obtained by the red dots minus the blue dots, the curves with larger σ leads to greater harvesting work.

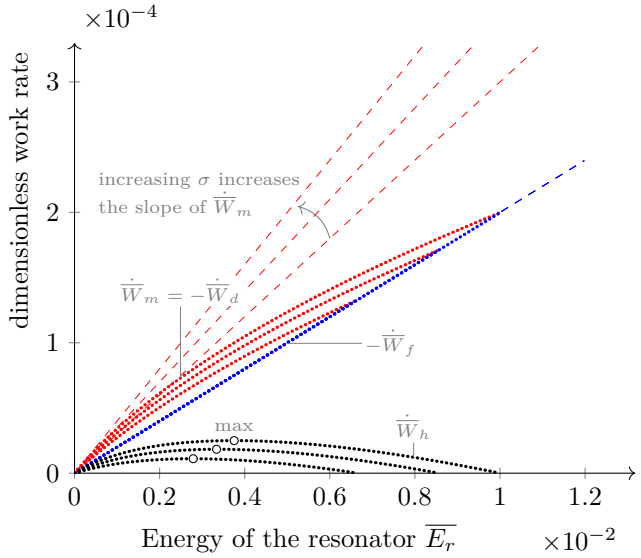

Figure 7.12 Effect of increasing the phase-change on the limit cycles for various loads; parameters are: $\sigma = 0.015, 0.0175, 0.020$, $\zeta_f = 0.01$ and $T_{HL} = 0.002$, so $\Pi_0 = 1.5, 1.75, 2$.

In fig. 7.13, we increase the phase-change limit T_{HL}. Again, we expect that this will lead to more energy injected into the system and larger power outputs, and we find just that. Increasing T_{HL} leads to a limit cycle with no load located at a higher $\widetilde{E}_r$ value. The slopes of both curves remain unchanged (because we used a nonlinear strategy). Increasing T_{HL} however keeps $\overline{\dot{W}}_m = -\overline{\dot{W}}_d$ closer to the linear line, such that the difference between the red dots and the blue dots is larger, giving larger power output $\overline{\dot{W}}_h$.

In fig. 7.14, we decrease the friction coefficient ζ_f. We would expect that this allows for a greater load and greater power output, and this is confirmed. Decreasing ζ_f decreases the slope of $-\overline{\dot{W}}_f$, such that the difference between the red dots and the blue dots is larger,

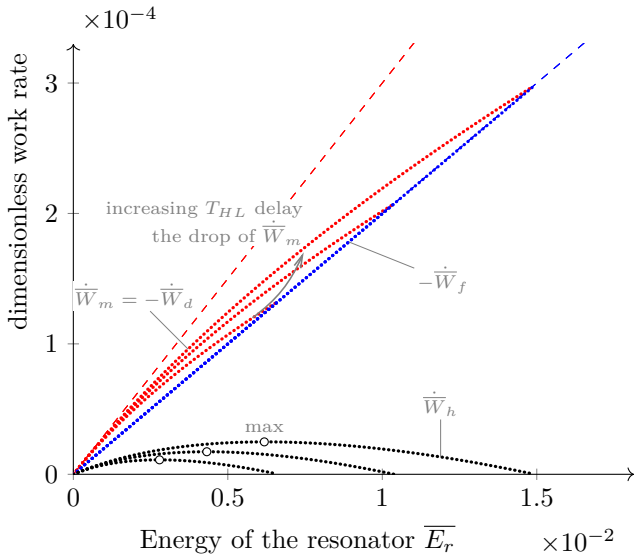

Figure 7.13 Effect of decreasing the limitation of the phase-change on the limit cycles for various loads; parameters are: $\sigma = 0.015$, $\zeta_f = 0.01$ and $T_{HL} = 0.002, 0.0025, 0.0030$, with $\Pi_0 = 1.5$.

leading to greater $\overline{\dot{W}}_h$. To conclude, we found here that increasing the work done by phase-change (either by σ or T_{HL}) or decreasing the work done by friction both allowed to increase the harvesting power.

Let's now explore the power output over a larger range of the parameters. We first study the phase-change parameters, σ and T_{HL}. We vary both parameters and, for each (σ, T_{HL}), we perform a numerical continuation along ζ_L and find the maximum power output $\overline{\dot{W}}_{h,max}$. In fig. 7.15, $\overline{\dot{W}}_{h,max}$ is displayed along Π_0 (increased by increasing σ) and T_{HL}. Looking at the black line on the left (for low T_{HL}), we see that increasing Π_0 allows to increase the power output. The power eventually saturates there. For some positive Π_0, increasing the phase-change limit also allows to increase the power output. The power also saturates for large enough T_{HL}. Overall, we find here that increasing the phase-change by increasing either σ or T_{HL} leads to an increase in the power output. We now look at the effect of friction coefficient ζ_f. We again find the maximum power output by numerical continuation (fig. 7.16). We see that the power increases as we increase Π_0 (by decreasing ζ_f). The power flattens out at large Π_0. We find here that decreasing the friction increases the power output. One cannot however increase the power to infinity simply by decreasing the friction. If the energy injected into the system by the phase-change is not large enough (controlled by σ or T_{HL}), the power output will remain small.

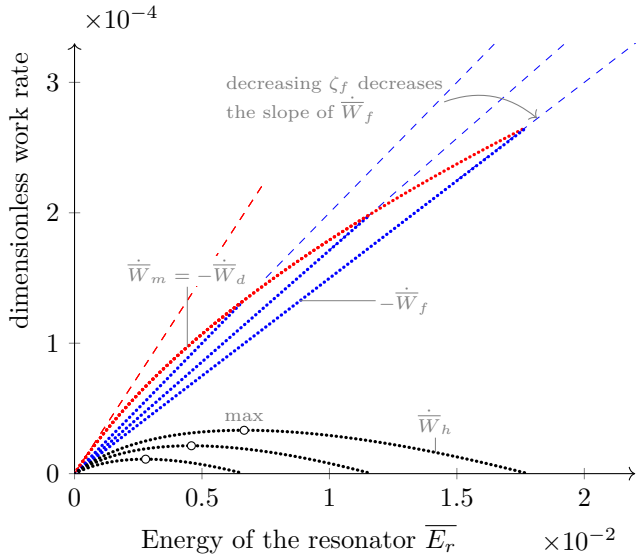

Figure 7.14 Effect of decreasing the friction on the limit cycles for various loads; parameters are: $\sigma = 0.015$, $\zeta_f = 0.0075$, 0.0086, 0.01 and $T_{HL} = 0.002$, so $\Pi_0 = 1.5, 1.75, 2$.

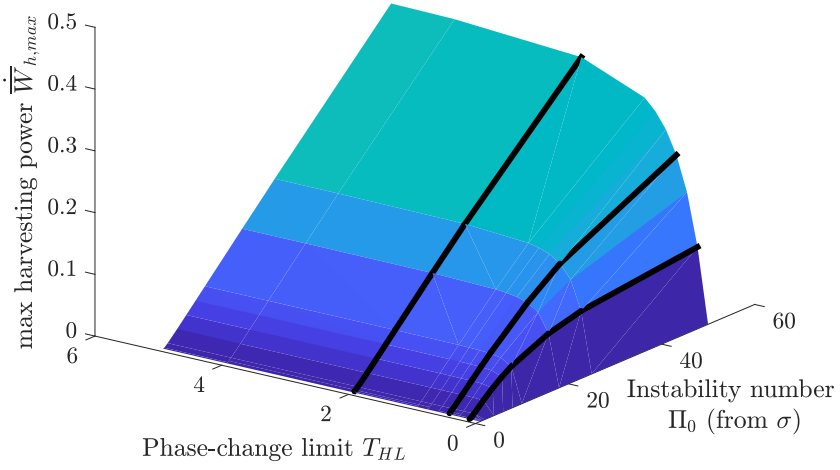

Figure 7.15 Maximum power $\overline{\dot{W}}_{h,max}$ as a function of Π_0 (by increasing σ) and T_{HL}, with $\zeta_f = 0.01$.

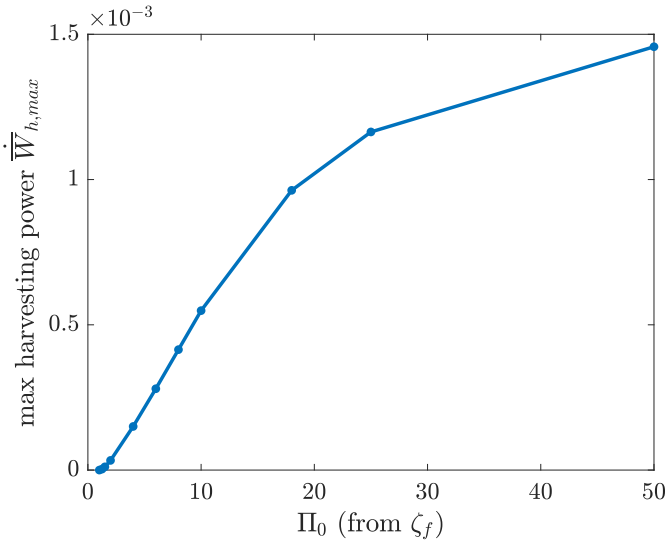

Figure 7.16 Maximum power $\overline{\dot{W}}_{h,max}$ as a function of Π_0 (by decreasing ζ_f), with $\sigma = 0.015$ and $T_{HL} = 0.002$.

7.4 Experimental

In this section, we use experimental data from other publications [112, 58] to show that experimental devices behave similarly than our simplified model. The experimental setup is shown in fig. 7.17. There is a single tube in which sits a single vapor bubble and a single liquid plug with the left-hand-side heated by the heat source (heated glycerin with circulation) and the other side cooled by the heat sink (circulating cold water). A pressure sensor measures the pressure in the vapor (the small liquid plug between the sensor and the vapor is incompressible) and a camera records the position of the meniscus on the right (both meniscus moves together, the liquid plug being incompressible). Both the pressure and the position are synchronized, which allows to measure indirectly the friction (momentum balance) and the mass of vapor (ideal gas law, assuming isothermal vapor). The behavior of the experimental device differs from our model in at least two ways: 1) the friction is in an oscillating regime (see [112] for details) and the phase-change, promoted by a thin liquid film along the capillary, is more complicated than the one we modeled. We will see however that our model allows to understand the behavior quite well.

Tessier-Poirier et al. [112] used the experimental setup shown in fig. 7.17 without the plastic junction to study the oscillations startup whereas Karami et al. [58] used the setup to study the potential of the device as a SOFHE. In a SOFHE, the self-oscillations convert thermal energy into mechanical energy which is then converted into electrical energy by an electromechanical transducer, to power a wireless sensor. Looking at the self-oscillations, the transducer is seen as a load. Karami et al. [58] added to the setup the plastic tube junction which could be pinched by a micrometer, as a proxy for the transducer's load effect. Pinching the tube produces additional friction and extracts mechanical energy from the self-oscillations, acting as a load. Doing so, Karami et al. [58] were able to study the impact of the load on the self-oscillations and to evaluate the mechanical work the device could produce. It is useful to study the mechanical work first, so that the performance of the self-oscillations and the efficiency of the electromechanical transducer can be studied independently.

7.4.1 System Without Load (Startup of the Oscillations)

Here, we look at the oscillations startup from an energy point of view, based on the experimental data from [112]. The position q_1 and energy variables are shown in fig. 7.18. The behavior is similar to the one described in section 7.3.3. As the oscillations amplitude grows, the energy level $\overline{E_r}$ grows as well. Here, the vapor is isothermal and there is no load, so the equation (7.19), $\dot{\overline{E_r}}(\tau_i) = \dot{\overline{W}}_m(\tau_i) + \dot{\overline{W}}_f(\tau_i)$, applies. The phase-change produces a positive average work rate $\dot{\overline{W}}_m$, while the friction produces a negative average work

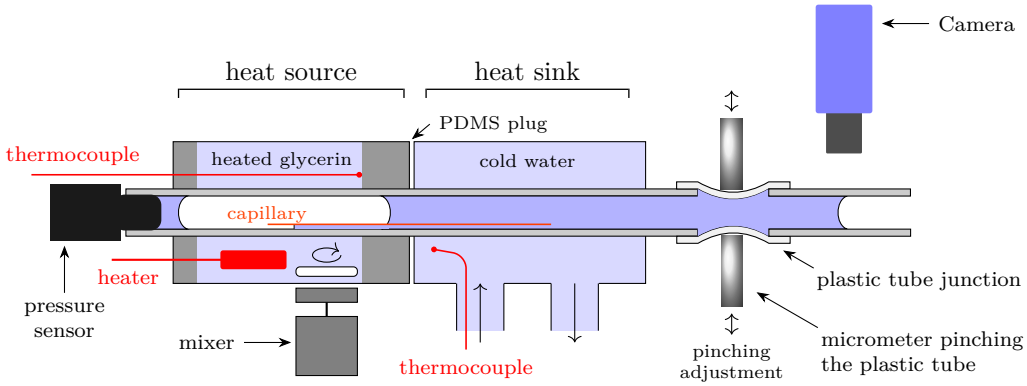

Figure 7.17 Experimental setup used in [112, 58]; figure adapted from [112].

rate $\overline{\dot{W}}_f$. The net work rate $\overline{\dot{W}}_m + \overline{\dot{W}}_f$ is positive and explains the growth in energy $\overline{E_r}$ during the startup, as well as the subsequent saturation, as $\overline{\dot{W}}_m + \overline{\dot{W}}_f$ reaches 0 and the system settles on the limit cycle. In fig. 7.19, we display the work rate as a function of $\overline{E_r}$. The phase-change $\overline{\dot{W}}_m$ is greater then the friction $-\overline{\dot{W}}_f$ initially, leading to a growth in $\overline{E_r}$, but the two curves eventually meet at a point corresponding to the limit cycle. We see that $\overline{\dot{W}}_m$ follows a straight line from the linear approximation initially, but then deviate from it due to the nonlinearity. The nonlinearity reduces the phase-change work $\overline{\dot{W}}_m$. Interestingly, we observe that the friction $-\overline{\dot{W}}_f$ also deviates due to the nonlinearity. The nonlinearity reduces $-\overline{\dot{W}}_f$, which is beneficial (the limit cycle would be located at $\overline{E_r} \approx 0.6$ otherwise). The net effect of the nonlinearity is however detrimental, as $\overline{\dot{W}}_m$ eventually meet $\overline{\dot{W}}_f$.

7.4.2 System With Load

Here, we look at the system with a load, based on the experimental data from [58]. In the experiment, there is no direct measure of the load coefficient ζ_L. Based on our theoretical approach, we propose a measure of ζ_L based on energetic quantities. For a velocity-damped load, we have (from eq. (7.33)):

$$\overline{\dot{W}}_L = \frac{1}{\tilde{T}} \int_{\text{cycle}} \left(\widetilde{F_L}\, q_2 \right) d\tau = \frac{1}{\tilde{T}} \int_{\text{cycle}} \left(-2\, \zeta_L\, {q_2}^2 \right) d\tau \ .$$

Given the kinetic energy $\widetilde{K} = \frac{1}{2}\, q_2^2$ (eq. (7.8)), we can write $q_2^2 = 2\widetilde{K}$, leading to:

$$\overline{\dot{W}}_L(\tau_i) = -2\zeta_L\, \frac{1}{\tilde{T}} \int_{\tau_i - \tilde{T}/2}^{\tau_i + \tilde{T}/2} \left(2\widetilde{K}(\tau) \right) d\tau$$

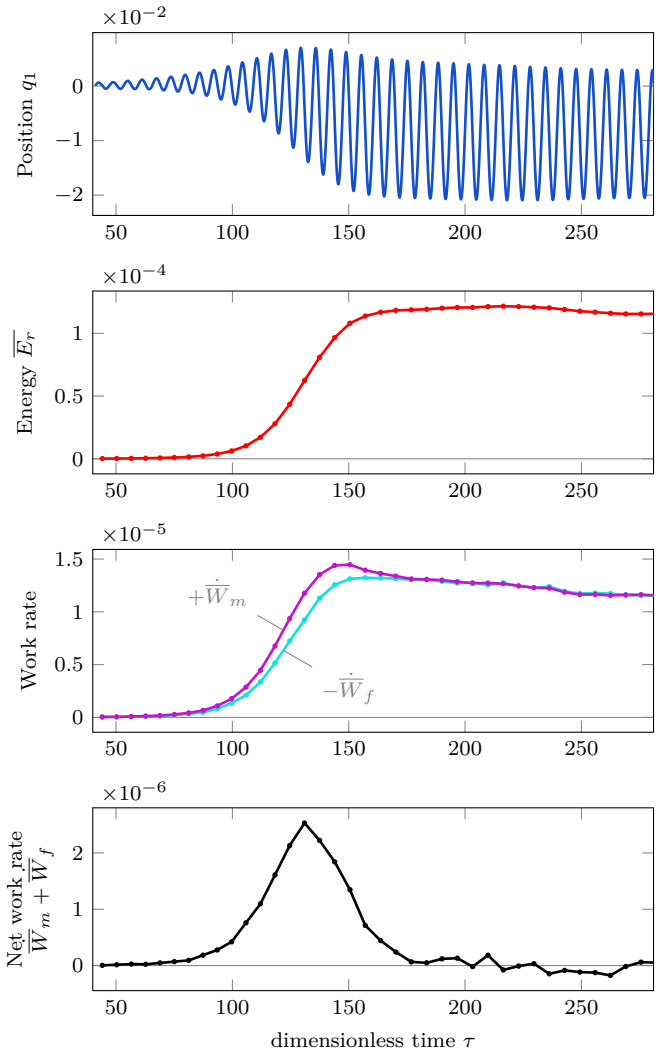

Figure 7.18 Position, averaged energy and averaged work rate over time; the main parameters are $T_H = 104\,°\text{C}$,$T_L = 20\,°\text{C}$, $D = 2.2\,\text{mm}$, $P_{g,0} = 101.3\,\text{kPa}$, $L_{g,0} = 8\,\text{cm}$, $L_\ell = 10\,\text{cm}$, $\omega_n = 112\,\text{rad/s}$ (data from [112]).

and considering $\overline{K}$ as the averaged kinetic energy,

$$\dot{\overline{W}}_L(\tau_i) = -4\zeta_L\,\overline{K} \qquad \text{with: } \overline{K} = \frac{1}{\tilde{T}}\int_{\tau_i-\tilde{T}/2}^{\tau_i+\tilde{T}/2} \widetilde{K}(\tau)\,d\tau\ .$$

We can use this expression as a definition for ζ_L, leading to:

$$\zeta_L \equiv\ -\,\frac{\dot{\overline{W}}_L}{4\overline{K}}\ . \tag{7.35}$$

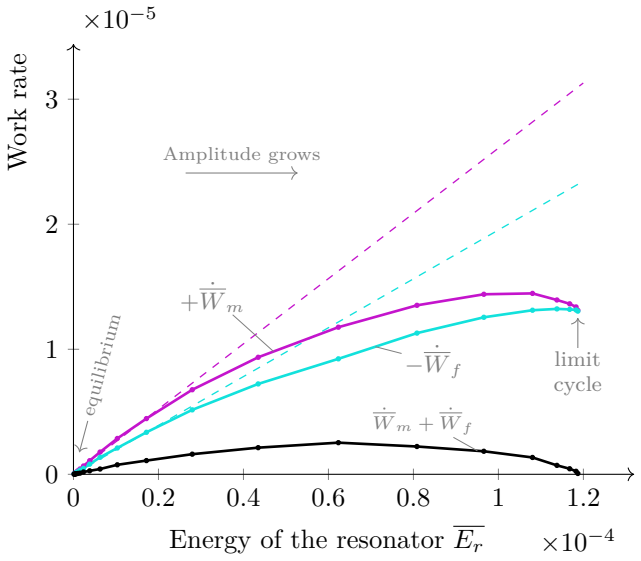

Figure 7.19 Work rate as a function of $\overline{E_r}$ during the startup (data from [112].

In the experiment, we can calculate $\dot{\overline{W}}_L$ and $\overline{K}$, so we can use eq. (7.35) to calculate ζ_L. This measure was used in [58].

In fig. 7.20, we show the work rate $\dot{\overline{W}}_m = -\dot{\overline{W}}_d$, the friction $\dot{\overline{W}}_f$, the power output $\dot{\overline{W}}_h$ and the load coefficient ζ_L. In this experiment, we start from the *no load* state at the highest $\widetilde{E}_r$ value. The tube is then progressively pinched and we see that ζ_L increases. We see that the system decreases in energy $\widetilde{E}_r$ as we increase the load. The phase-change work $\dot{\overline{W}}_m$ is greater than the friction $\dot{\overline{W}}_f$ which allows for positive power output $\dot{\overline{W}}_h$ produced by the load. We see that the power reaches a maximum at some value of ζ_L.

Let's now look at the power output $\dot{\overline{W}}_h$ and the efficiency in terms of Z_L (see fig. 7.21). There is some uncertainty here, because it is not so easy to estimate $\zeta_{\mathrm{L,max}}$ (we use the slope of $\dot{\overline{W}}_m$ and $\dot{\overline{W}}_f$ to estimate σ and ζ_L and then estimate $\zeta_{\mathrm{L,max}}$). We see that the power is 0 at no load, reaches a maximum and then decreases. The optimal value here is $Z_{L,\mathrm{opt}} \approx 0.25$. The efficiency follows the same trend. Those asymmetrical bell shape curves, similar to our theoretical curves, are explained by the fact that we harvest energy from a self-oscillating system rather that a forced oscillator. Most probably, the maximum power and the maximum efficiency do not occur at $Z_\mathrm{L} = 0.5$ and $Z_\mathrm{L} = 2/3$ respectively, because the system is too far away from $\Pi_0 = 1$. We estimate that $\Pi_0 \approx 3$ here. As seen in the theoretical model, the Z_L for maximum power or maximum efficiency can shift as Π_0 is increased, due to the nonlinearity.

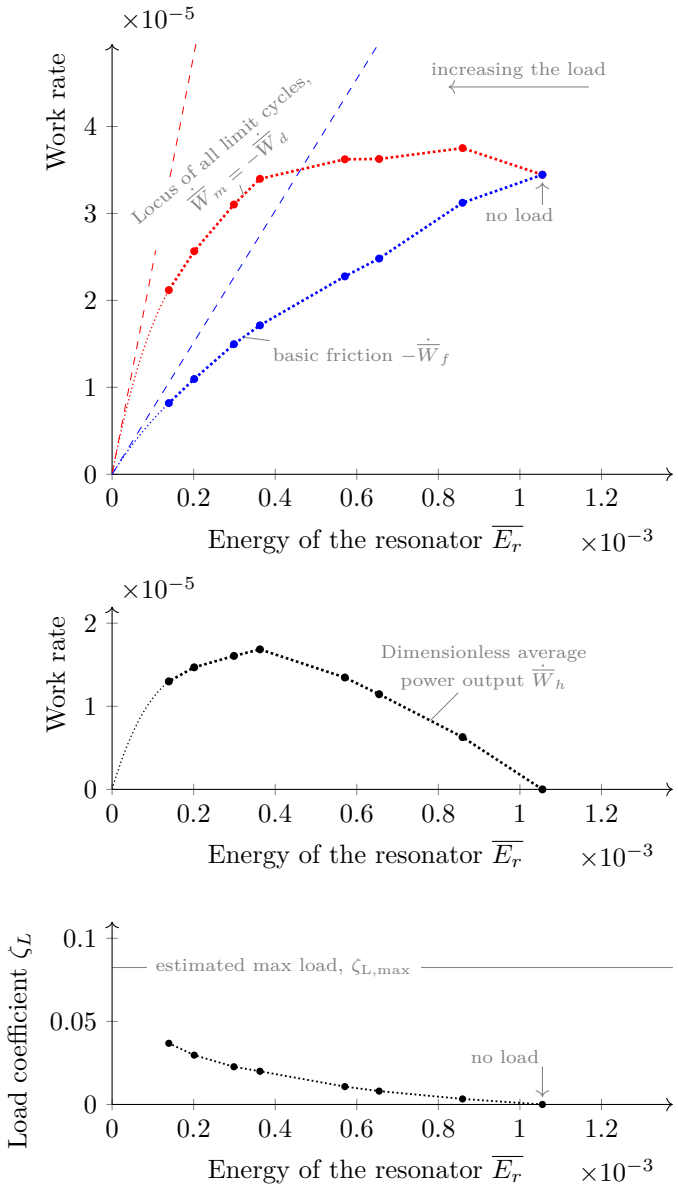

Figure 7.20 Steady-state as the load is progressively increased by pinching the tube; the main parameters are $T_H = 110\,°\text{C}$, $T_L = 20\,°\text{C}$, $D = 2.2\,\text{mm}$, $P_{g,0} = 101.3\,\text{kPa}$, $L_{g,0} = 8.5\,\text{cm}$, $L_\ell = 16\,\text{cm}$, $\omega_n = 86\,\text{rad/s}$ (data from [58]).

7.5 Discussion - How To Increase the Power Output

The obvious question now is how can we increase the power output $\overline{\dot{W}}_h$ in the device? The power output can be obtained from eq. (7.23b): $\overline{\dot{W}}_h = \overline{\dot{W}}_m - (-\overline{\dot{W}}_f)$, with $\overline{\dot{W}}_f < 0$. One must optimize the load ζ_L, such that the difference between $\overline{\dot{W}}_m$ and $-\overline{\dot{W}}_f$ is the largest possible. One must also decrease the losses from the viscous friction, $\overline{\dot{W}}_f$, and increase the energy injected by the phase-change, $\overline{\dot{W}}_m$ (at the value $Z_{L,\text{opt}}$). This latter point deserves more explanations. For a system without load on the limit cycle (with

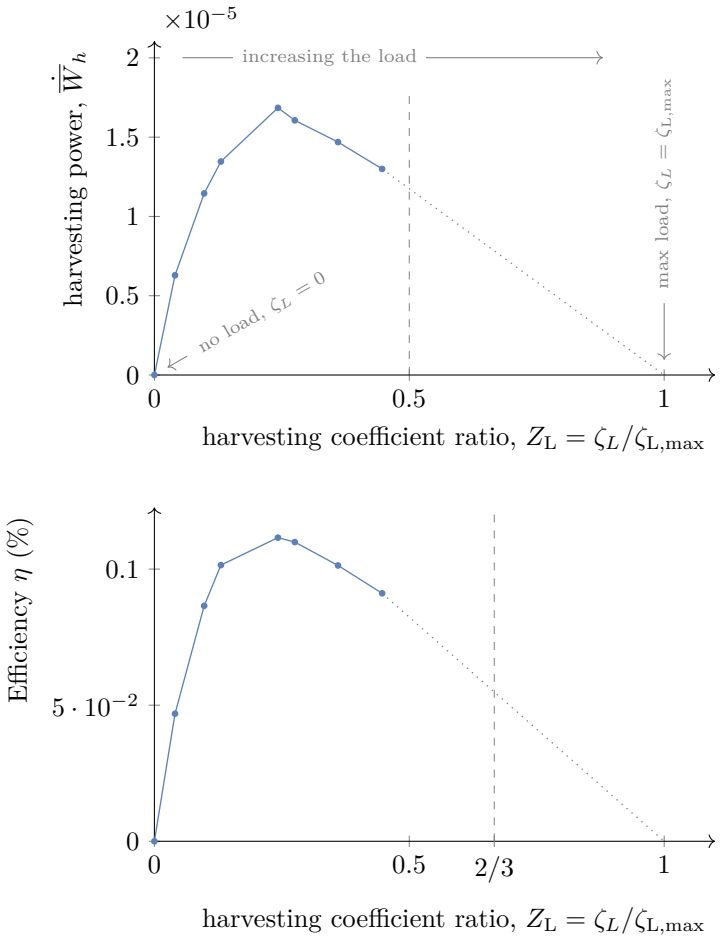

Figure 7.21 Power and efficiency as function of Z_L, for the same experiment as fig. 7.20.

$\overline{\dot{E}_r} = \overline{\dot{W}}_m + \overline{\dot{W}}_f = 0$), if we increase $\overline{\dot{W}}_m$ or decrease $\overline{\dot{W}}_f$ by tuning some parameters, we get that $\overline{\dot{E}_r} > 0$ again, the system grows in energy $\overline{E_r}$ until it reaches a new limit cycle where we again have $\overline{\dot{E}_r} = \overline{\dot{W}}_m + \overline{\dot{W}}_f = 0$, but with a bigger energy $\overline{E_r}$ level (corresponding to larger oscillations amplitude). Increasing $\overline{\dot{W}}_m$ or decreasing $\overline{\dot{W}}_f$ leads to a larger $\overline{E_r}$, corresponding to larger amplitude. Now, for a system with load, with a positive ζ_L, if we increase $\overline{\dot{W}}_m$ or decrease $\overline{\dot{W}}_f$ and keep ζ_L constant, the system would also move to a larger $\overline{E_r}$. On the other hand, we can also adjust ζ_L such that $\overline{E_r}$ is constant, in which case the extra energy will be consumed by the harvester, we will get a larger $\overline{\dot{W}}_h$. Increasing $\overline{\dot{W}}_m$ or decreasing $\overline{\dot{W}}_f$, while re-optimizing ζ_L, allows for greater power output. Looking back at the system without load, increasing the energy level $\overline{E_r}$ on the limit cycle without the load should allow for larger power output once the load is applied.

For the friction, we have a pretty good description of the force F_f either based on the Poiseuille flow as described in the model above, or by considering oscillating friction for

high Re_ω ([112]). Restricting our analysis to the Poiseuille flow, we could look at the dimensional parameters appearing in ζ_f (eq. (7.24)). However, we must be careful as many of these dimensional parameters can also impact other dimensionless parameters such as σ. If the oscillations amplitude depends mostly on $\Pi_0 = \sigma/\zeta_f$ (expected close to the instability threshold, Π_0 given by eq. (7.27)), then the only parameters from the friction coefficient that survive are ρ_ℓ and μ. Those can be changed by changing the fluid, but this will also affect Π_0 by changing R_g, H_v and R_{th} and the angular frequency by changing ρ_ℓ. The overall effect of changing the fluid is not obvious. One might expect the length of liquid L_ℓ to be important, but it does not appear in Π_0. We found experimentally that changing L_ℓ had no impact on the amplitude (for reasonable values of L_ℓ of course). There does not seem to be obvious ways to independently decrease the friction drastically. Also, we note that we found that decreasing the friction had little impact on the power output once large enough Π_0 are reached (section 7.3.6). From an energy point of view, $\dot{\overline{W}}_h = \dot{\overline{W}}_m + \dot{\overline{W}}_f$ on the limit cycle at some value of the load ζ_L. For small enough $\dot{\overline{W}}_f$, the limit cycle will be mostly fixed by the interplay of the phase-change (energy injected into the system) and the load (as the main dissipative term). Decreasing the friction even more should have little impact on the power output. This is what we found from the theoretical model. It was not possible to increase the power output to infinity just by decreasing the friction.

For the phase-change, we do not have a precise description of the phase-change rate $\dot{m}_g$, eq. (7.3), and of the resulting force $\widetilde{F_m}$. Our model should describe local phase-change at the meniscus quite well, but, in the experiment presented here, the phase-change is promoted by a liquid film along a capillary. Even without a capillary, it is found that, under some conditions, a thin liquid film is laid on the surface and contributes significantly to the overall phase-change. Nonetheless, given $\dot{\overline{W}}_m = (1/\tilde{T}) \int_{\text{cycle}} (\widetilde{F_m} q_2) d\tau$, we can conclude that we want $\widetilde{F_m}$ to be as large as possible and in phase with the velocity q_2. One should try to tune the phase-change to do so, in order to increase $\dot{\overline{W}}_m$. In our model, we found that a phase-change in phase and opposite to velocity, with $\dot{q}_3 = -2\sigma q_1$, led to a force in phase with velocity, in the linear regime [112]. This would be true for the experiment as well. We also found that a phase-change where we evaporate a lot in the heat source and condense a lot in the heat sink (eq. (7.26c) with large σ and large T_{HL}) performed very well. Such a phase-change profile can serve as a reference for the experiment. For local phase-change at the meniscus, a specific expression for the phase-change coefficient σ exists which makes Π_0 a function of R_g, $T_{g,0}$, $\hat{P}_e$, $\left|T'_{w,0}\right|$, H_v and R_{th}. It has been found experimentally that increasing the temperature of the heat source (which increases $T_{g,0}\left|T'_{w,0}\right|$), decreasing the external pressure $\hat{P}_e$ and introducing a capillary (which decreases R_{th} most probably)

allowed to make the oscillations unstable (startup). Further increasing (or decreasing) those parameters allowed to increase the oscillations amplitude. We therefore expect that those parameters would also increase the power output. Indeed, Karami et al. [58] found that the power could be increased by increasing the temperature of the heat source and by pushing the capillary further into the device. Increasing $\overline{\dot{W}}_m$ seems a promising approach to increase the power output. Experimentally, one can increase the phase-change drastically. This was done with a capillary tube in [112, 58]. More generally, the tube can be engineered to control the liquid film on the surface and thus control the phase-change. One might be able to tune the magnitude and the timing of the phase-change in order to maximize $\overline{\dot{W}}_m$.

Until now, we discussed how to increase the *dimensionless* average power output $\overline{\dot{W}}_h$. Of course, what we are really after is the dimensional one, given by $(\omega_n L_{g,0} P_{g,0} A)\,\overline{\dot{W}}_h$. The dimensional parameter $L_{g,0}$, $P_{g,0}$ and A, as well as the angular frequency ω_n also come into play. The power is not necessarily proportional to those parameters however, as they can also affect $\overline{\dot{W}}_h$ through the dimensionless numbers σ, ζ_f and T_{HL}. We can expect though that parameters which lead to an increase in ω_n without leading to a decrease in the oscillations amplitude should allow to increase the power output. Indeed Karami et al. [58] found that decreasing the length of the liquid plug allowed to increase ω_n and the power output.

7.6 Conclusion

In this chapter, we adopted an energy perspective, to study the dynamics of the self-oscillations and the energy harvesting capabilities of SOFHE. Based on very few hypotheses, we derived an energy balance equation which describes the evolution of the resonator energy $\overline{E_r}$ in terms of the work done by phase-change $\overline{\dot{W}}_m$ and by friction, $\overline{\dot{W}}_f$ (a more general case with variations of vapor temperature was also discussed). We first considered a simple theoretical model. We showed that the oscillations startup occurs when the work done by phase-change is greater than the work done by friction. A net positive energy is then injected at each cycles, leading to an increase of the energy of the resonator as well as the amplitude. The steady-state regime occurs because of the nonlinearities. In our model, the nonlinearities limit the work done by phase-change (it is less than if it was linear) whereas the friction remains linear. This means that the work done by friction eventually catches up with the phase-change, at which point no more energy is injected into the resonator: the resonator energy as well as the oscillations amplitude reaches a constant value. By increasing the slope of the phase-change work, reducing the slope of friction

work (linear strategies) or by delaying the drop of the phase-change (nonlinear strategy), we can increase the energy as well as the oscillations amplitude of the steady-state.

We then studied the effect of the load and showed that it has the same effect as increased friction. Too much load makes the equilibrium stable and kills the self-oscillations. A maximum power output is reached at an optimum value of the load. The same strategies used to increase the oscillations amplitude also lead to an increased power output.

Finally, we looked at experimental data, for both the startup and energy harvesting (where a load was applied) and showed that our energy perspective still applies. We used our energy quantities to show how the load coefficient can be deduced from known quantities.

We then discussed how to increase the power output more generally. One must increase the work done by phase-change and reduce the work done by friction. The former seems more promising, especially considering how the tubes can be engineered to control the magnitude and the timing of the phase-change. In those approaches, one should tune the phase-change to maximize the average work rate it produces.

CHAPTER 8

CONCLUSION FRANÇAISE

8.1 Sommaire et contributions

Je vais ici résumer la thèse, décrire le processus en termes d'étapes d'ingénierie (fig. 9.1) et identifier les publications scientifiques en cours de route.

Dans notre approche, nous avons construit un modèle mathématique principalement pour atteindre une compréhension scientifique des auto-oscillations dans le SBPHP. La plupart des éléments du modèle décrivent bien les expériences: l'équilibre des forces sur la colonne de liquide, la conservation de l'énergie sur la bulle de vapeur (condition isotherme s'applique, typiquement), la loi des gaz parfaits et l'expression pour la friction visqueuse (Poiseuille ou régime oscillant). En ce qui a trait au changement de phase toutefois, le modèle ne correspond pas tout à fait à l'expérience. Pour obtenir le démarrage des oscillations dans le SBPHP, nous avons dû introduire un tube capillaire. Cela signifie que l'hypothèse d'un changement de phase local n'était pas valide pour l'expérience. En conséquence, le modèle duquel nous avons dérivé nos résultats diffère du dispositif expérimental. Malgré cela, notre modèle capture l'essentiel de la physique du phénomène, incluant des aspects importants du changement de phase, nous permettant de comprendre le phénomène d'un point de vue qualitatif. Certaines prédictions quantitatives sont toutefois hors de portée. Dans l'espace des configurations possibles, le changement de phase peut être varié significativement en modifiant les parois internes du tube. Dans notre approche, l'objectif n'était pas de produire des prédictions quantitatives pour une configuration spécifique, mais bien d'atteindre une compréhension suffisamment générale pour nous guider dans l'exploration de l'espace des configurations, de manière à trouver une configuration performante. Nous avons fait ressortir l'importance du mécanisme d'instabilité et des nonlinéarités pour le démarrage, l'amplitude des oscillations et la puissance produite par SOFHE. Nous avons aussi proposé des lignes directrices pour contrôler ces éléments, en contrôlant le changement de phase et la friction. Nos conclusions sont suffisamment générales pour s'appliquer à la plupart des configurations possibles.

Chapitre 3. Ce qui explique les oscillations et le démarrage.
En partant de l'*observation* des oscillations de la colonne de liquide, nous nous sommes demandé d'où les oscillations proviennent. Un modèle mathématique est construit, puis

linéarisé et une solution analytique est obtenue. On trouve que la force produite par la différence de pression sur la colonne de liquide inclut une force de rappel $\widetilde{F_{\mathcal{V}}}$, produite par la dilatation et la compression de la bulle de vapeur (changement de volume). Nous avons montré que les oscillations sont *expliquées* par l'interaction entre la compression-dilatation de la bulle de vapeur qui agit comme un ressort et la masse de la colonne de liquide, menant à un système masse-ressort (ou résonateur). Nous avons prédit la fréquence des oscillations pour le démarrage. Notre approche complémente des travaux existants sur le sujet: nous avons montré que l'analyse est valide en présence du changement de phase, sous certaines conditions (changement de phase en anti-phase avec la position et faible $\sigma - \zeta_f$). Par la suite, nous avons testé expérimentalement la prédiction de la fréquence sur une plage des paramètres (expériences menées par Thomas Monin) et trouvé un bon accord entre la théorie et l'expérience, ce qui *valide* le système masse-ressort. On peut prédire la fréquence à la fois qualitativement et quantitativement et l'on peut contrôler la fréquence aisément.

En partant de l'*observation* selon laquelle les oscillations augmentent en amplitude durant le démarrage, nous nous sommes demandé ce qui explique le démarrage. Le modèle construit inclut également le changement de phase. Nous avons trouvé que la force produite par la différence de pression sur la colonne de liquide inclut aussi une force de rétroaction positive $\widetilde{F_m}$, due aux variations de masse de vapeur. Ces variations de masse proviennent de l'évaporation et de la condensation alors que la colonne de liquide oscille entre la zone chaude et la zone froide. Le démarrage s'explique par l'interaction entre le changement de phase menant à une force de rétroaction positive et la friction visqueuse entre le liquide et les parois, qui agit comme une force dissipative. L'équilibre devient instable et le démarrage se produit lorsque le coefficient du changement de phase (σ) est augmenté au-delà du coefficient de friction (ζ_f). Cela peut être élégamment représenté par un nombre nondimensionne, $\Pi = \sigma/\zeta_f$, avec le démarrage se produisant lorsque Π est augmenté au-delà de 1. Le nombre Π est analogue à d'autres nombres liés à des instabilités, tels que le nombre de Rayleigh (Ra) pour l'instabilité de Rayleigh-Bénard. Basé sur Π, on peut *prédire* que le démarrage peut être provoqué par l'augmentation du gradient thermique axial, par la réduction de la pression externe ou par la réduction de la résistance thermique (parmi d'autres paramètres). Nous avons *validé* le mécanisme d'instabilité en confirmant que le changement de phase produit un travail positive alors que la friction produit un travail négatif et en confirmant l'effet sur le démarrage des paramètres mentionnés précédemment. Nous avons atteint un bon *contrôle* pour le démarrage des oscillations. Bien que nous ne comprenons pas totalement comment contrôler le changement de phase dans l'expérience, nous savons maintenant que l'instabilité peut être contrôlée par l'intensité de la com-

posante du changement de phase en anti-phase avec la position, qui produit une force de rétroaction positive.

D'autres contributions originales sont incluses dans ce travail, dont 1) la première utilisation d'un tube capillaire comme structure mouillante que l'on peut contrôler (*découverte*), qui permet d'augmenter l'amplitude des oscillations de manière importante, 2) des mesures expérimentales lors du démarrage (position, pression, masse de vapeur, friction, etc.), 3) une expression théorique pour la force de friction dans un régime oscillant, validée expérimentalement et 4) une approche énergétique qui peut être utilisée pour étudier l'effet du changement de phase et la friction de manière très générale, à la fois théoriquement et expérimentalement.

Ce travail a fait l'objet d'une publication dans Physical Review Fluids [112].

Chapitre 4. Ce qui mène à un régime oscillant permanent.
Nous avons commencé par des *observations* expérimentales en réutilisant les mesures du démarrage et en montrant comment l'amplitude augmente initialement puis sature, alors que le système approche un régime permanent oscillant. Nous avons montré que, dans l'espace des phases, le système approche une boucle fermée (un cycle limite, correspondant au régime permanent oscillant). L'objectif ici était de considérer un *modèle* mathématique simple décrivant le phénomène et de l'utiliser pour mieux *comprendre* ce qui mène à la saturation de l'amplitude, ce qui explique l'existence du cycle limite et comment le contrôler. Nous avons considéré le modèle présenté au chapitre 3. Nous avons montré, en comparant la solution des équations linéarisées à la solution numérique des équations différentielles nonlinéaires, que la saturation et le cycle limite sont dus aux nonlinéarités. Nous avons ensuite obtenu une solution analytique approximative des équations nonlinéaires en utilisant la réduction par variété centrale suivie de la réduction par forme normale. Cette solution montre que, durant le démarrage, l'augmentation puis la saturation de l'amplitude est *expliquée* par l'interaction entre le mécanisme d'instabilité et un mécanisme limitant, produit par les nonlinéarités. Nous avons par la suite prouvé mathématiquement l'existence du cycle limite, créé par une bifurcation de Poincaré-Andronov-Hopf. Finalement, nous avons *prédit* l'amplitude des oscillations. Nous avons étudié comment *contrôler* l'amplitude des oscillations sur le cycle limite. L'amplitude peut être augmentée en augmentant l'instabilité ou en réduisant les nonlinéarités. Plus spécifiquement, cela implique que l'amplitude peut être augmentée en augmentant le changement de phase et en réduisant la friction. Nous avons étudié l'impact du changement de phase et de la friction sur l'amplitude quantitativement, par continuation numérique. Les conséquences sur la conception de PHP et de SOFHE sont discutées.

Ce travail complémente un article antérieur de conférence sur le rôle des nonlinéarités [111]. Une version préliminaire de ce travail a été publiée comme article de conférence [113], ce qui a ensuite mené à un manuscrit (accepté, en production) dans Nonlinear Dynamics Journal [114].

Chapitre 5. Solution analytique précise pour le régime permanent.
La solution analytique obtenue dans le chapitre 4 est seulement valide pour de faibles amplitudes d'oscillations. Ce chapitre porte sur une approche théorique pour mieux décrire et comprendre l'amplitude des oscillations dans le modèle. J'ai obtenu des solutions analytiques et semi-analytiques précises, valides pour toute la plage des paramètres. Premièrement, j'ai suivi le cycle limite par continuation numérique et examiné le diagramme spectral de la solution sur une grande plage des paramètres. J'ai ensuite appliqué la technique de moyennisation pour chaque nonlinéarités individuellement, sans approximer le champ vectoriel par sa série de Taylor. Cela m'a permis d'obtenir une solution extrêmement précise pour la dynamique, pour la nonlinéarité de changement de phase. Pour la pression nonlinéaire, la solution obtenue par moyennisation est incapable de reproduire les harmoniques dans la solution. J'ai donc proposé une solution modifiée, basée sur la forme obtenue par moyennisation, mais écrite comme une série infinie, qui s'avère également très précise. Les paramètres de cette solution modifiée sont obtenus à l'aide des résultats numériques. Pour les deux nonlinéarités, j'ai observé que, quand l'amplitude augmente, des harmoniques se développent dans la solution à cause des nonlinéarités. J'ai aussi trouvé que, pour augmenter l'amplitude, il faut d'abord augmenter l'instabilité puis réduire les nonlinéarités. Je m'attends à ce que principe soit valide pour n'importe quelles nonlinéarités. Les deux solutions analytiques obtenues ici ont été utilisées pour étudier la récupération énergétique dans le chapitre 6.

Chapitre 6. Comment se comporte un dispositif de récupération énergétique.
Dans ce chapitre, nous avons répondu à la question de comment se comporte un dispositif de récupération énergétique (SOFHE). Nous avons ajouté une charge (force dissipative proportionnelle à la vitesse représentant le transducteur électromécanique) au modèle décrit au chapitre 3. Nous avons adapté la solution obtenue au chapitre chapter 5, et obtenu une solution analytique très précise décrivant la dynamique (amplitude et fréquence) ainsi que la puissance produite et l'efficacité. Nous avons montré comment la puissance évolue en fonction de la charge: la puissance suit une courbe en cloche asymétrique, avec une puissance nulle pour une charge nulle, une puissance maximale pour une charge optimale et une puissance nulle pour une charge maximale. Pour cette charge maximale, la charge crée suffisamment de dissipation pour étouffer complètement les auto-oscillations. Ces

prédictions qualitatives ont été validés expérimentalement [58]. Notre modèle nous permet d'expliquer le comportement observé. Par la suite, nous avons montré comment la puissance peut être augmentée en augmentant le changement de phase et en réduisant la friction visqueuse (*contrôle*). Nous avons également étudié l'efficacité et montré qu'elle suit une courbe en cloche asymétrique. Nous avons ensuite discuté des conséquences de notre analyse pour la conception de SOFHE. Finalement, nous avons montré comment le comportement dans un récupérateur d'énergie auto-oscillant diffère de récupérateur d'énergie forcé. Des travaux sur le sujet ont fait l'objet d'un article de conférence [111]. Ce travail a par la suite été soumis au journal Applied Thermal Engineering.

Chapitre 7. Perspective énergétique.
Dans ce chapitre, nous avons revisité le démarrage, la saturation de l'amplitude et la puissance produite, d'un point de vue énergétique. Nous nous sommes d'abord attardés sur le modèle théorique. Nous avons montré que, durant le démarrage, le travail fait par le changement de phase est supérieur au travail (négatif) fait par la friction, de telle sorte qu'une énergie nette positive est injectée dans le système à chaque oscillation, menant à l'augmentation en énergie du résonateur et en amplitude d'oscillations. On peut observer visuellement que l'effet des nonlinéarités est de réduire le travail fait par le changement de phase, par rapport à sa valeur linéaire. Cela à pour conséquence que le travail fait par la friction rattrape éventuellement le changement de phase et que le système atteint donc un régime permanent. Nous avons ensuite montré comment contrôler l'instabilité (liée aux pentes à l'origine du travail fait par le changement de phase et la friction) et les nonlinéarités (la déviation par rapport au travail linéaire) pouvait permettre d'augmenter l'amplitude des oscillations. Quant à la puissance produite, les mêmes stratégies permettaient également de l'augmenter. Finalement, nous nous sommes attardés sur les données expérimentales pour le démarrage et pour la puissance produite. Le comportement est qualitativement le même que pour le modèle théorique. En se basant sur notre approche théorique, nous avons obtenu une équation permettant une mesure indirecte du coefficient de la charge, utile pour l'analyse des données expérimentales. De manière générale, on obtient que pour augmenter l'amplitude des oscillations ou la puissance produite, il faut augmenter le travail fait par le changement de phase et réduire le travail fait par la friction.

Notre approche permet de simplifier grandement le problème. On peut discuter du phénomène simplement en termes d'énergie du résonateur moyennée $\overline{E_r}$, du taux de travail moyenné fait par le changement de phase ($\dot{\overline{W}}_m$) et par la friction ($\dot{\overline{W}}_f$). Cette manière de penser est très générale: peut importe à quel point le changement de phase est compliqué,

ce qui compte est $\overline{\dot{W}}_m$, le taux du travail moyenné. Nos conclusions sur le rôle de $\overline{\dot{W}}_m$ et $\overline{\dot{W}}_f$ sont générales.

Ce chapitre est basé sur un manuscrit, pour une nouvelle soumission au journal Applied Thermal Engineering.

Quelques éléments de réflexions sur la compréhension scientifique

Dans notre approche, la compréhension scientifique a été atteinte de plusieurs façons. Autant que possible, des formules analytiques simples ont été obtenues à partir desquelles l'effet des paramètres pouvait être déduit. Nous avons réduit le nombre important de paramètres à seulement quelques macro-paramètres (ω_n, σ, T_{HL}, ζ_f), ayant une signification importante en termes de dynamique. En effet, ces macro-paramètres sont liés à des concepts abstraits introduits pour décrire la dynamique (résonateur, mécanisme d'instabilité, mécanisme limitant). Ces concepts capturent des aspects distincts de la dynamique (oscillations, démarrage, régime permanent). On peut penser à l'impact de la configuration en fonction de ces concepts et des macro-paramètres, pour prédire le comportement du phénomène qualitativement. Dans la section 1.3.1, j'ai décrit la compréhension scientifique d'un point de vue géométrique (figure 1.6). Nous avons été en mesure d'obtenir une telle représentation en fonction des macro-paramètres pour le comportement (figure 3.4), l'amplitude des oscillations (figure 4.9) et la puissance produite (figures 7.15 and 7.16). Finalement, en adoptant un point de vue énergétique, nous avons été en mesure de décrire la dynamique avec concision et de manière générale, en termes d'énergie du résonateur moyennée $\overline{E_r}$, du taux de travail moyenné produit par le changement de phase ($\overline{\dot{W}}_m$) et par la friction ($\overline{\dot{W}}_f$).

8.2 Recherches futures

À partir du modèle, nous avons trouvé que le changement de phase a un impact important sur l'amplitude des oscillations et sur la puissance produite. Cela est aussi appuyé par l'expérimental, par l'utilisation d'un capillaire pour favoriser la formation d'un film liquide, pour favoriser le changement de phase. Je soupçonne qu'il est possible d'aller beaucoup plus loin en contrôlant mieux le changement de phase. Il faut contrôler à la fois l'intensité du changement de phase et sa synchronisation avec la dynamique. Plus précisément, il faut contrôler le profil du changement de phase en fonction du temps en tout point, n'étant pas limités à une fonction sinusoïdale. Ce qui importe est de contrôler le changement de phase de manière à maximiser le taux de travail moyenné fait par le changement de phase sur un cycle, $\overline{\dot{W}}_m$. D'un point de vue théorique, une question intéressante est: quel serait un changement de phase optimal? D'un point de vue expérimental, le niveau de

contrôle requis sur le changement de phase pourrait être obtenu par microfabrication. Il est possible d'utiliser une gaufre de silicium pour l'une des parois, sur laquelle seraient gravés des micro-pilliers autour desquels se formeraient des films liquides, favorisant ainsi un changement de phase beaucoup plus important. En ajustant la géométrie de ces piliers (position, taille, densité, etc.), on pourrait contrôler le changement de phase en fonction du temps, et l'ajuster de manière à maximiser le travail fait sur un cycle par le changement de phase. Pour guider la conception, il serait utile de considérer le travail instantané fait par le changement de phase à chaque point du cycle. Ma collègue Nooshin Karami étudie en ce moment des approches de microfabrication pour contrôler le changement de phase.

Pour SOFHE, mon travail a surtout porté sur la partie moteur, mais une autre composante importante est le transducteur électromécanique. Il y a beaucoup à faire pour la conception du transducteur et son implémentation. Lorsque la partie moteur et le transducteur seront jugés suffisamment bons, il sera temps de concevoir et fabriquer un SOFHE pour une application spécifique.

CHAPTER 9

ENGLISH CONCLUSION

9.1 Summary and Contributions

Here, I will summarize the thesis, describing the progress in terms of the engineering steps (fig. 9.1) and identifying the scientific publications along the way.

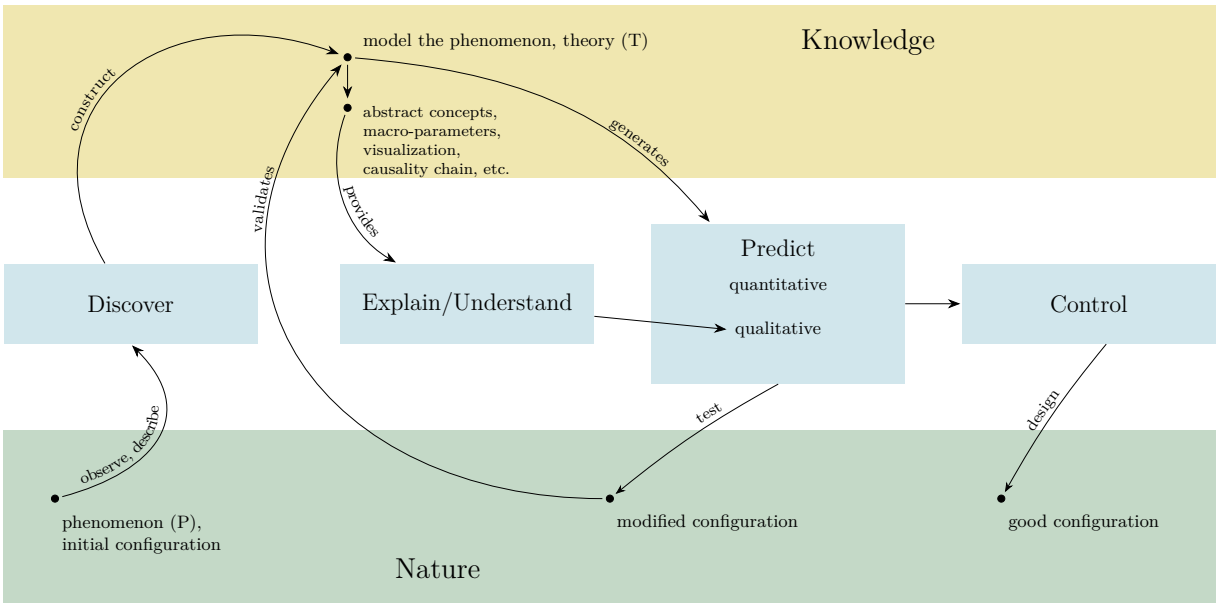

Figure 9.1 Research from an engineering point of view, from the discovery of a phenomenon to the control, leading to the design of a good configuration (this is fig. 1.5, repeated here for convenience).

In our approach, we constructed a mathematical model mainly to achieve scientific understanding of the self-oscillations in the SBPHP. We found that most aspects of the model describe well the experiment: the momentum balance on the liquid plug, the energy balance on the vapor bubble (isothermal condition usually applies), the ideal gas law and the friction expression (either Poiseuille or oscillating flow). With regards to the phase-change however, the model does not fully match the experiment. In order to make the SBPHP start, we had to introduce a capillary. This meant that the assumption of local phase-change was not valid in our experiment. Thus, the model from which we derive our results differs from the experimental device. Nonetheless, the model captures most of the physics and important aspects of the phase-change, enabling us to understand the phenomenon

very well at a qualitative level. Some quantitative prediction are however out of reach. In the space of all configurations, the phase-change can be varied significantly by engineering the internal walls. In our approach, the goal was not to produce quantitative predictions for the specific configuration considered in the experiment but to reach an understanding general enough to guide us in the exploration of the configuration space, in order to find a configuration which leads to a good performance. We could highlight the importance of the instability mechanism and of the nonlinearities on the startup, the amplitude and the power output for SOFHE. We could also gave important guidelines on how to control those by controlling the phase-change and the viscous friction. Those conclusions are general enough to apply to most configurations.

Chapter 3. Why it oscillates and what leads to the startup.
Starting from the *observation* that the liquid plug can oscillate, we asked where those oscillations comes from. A mathematical model was *constructed*, the model was linearized and an analytical solution was found. We found that the force produced by the pressure difference on the liquid plug includes a restoring force $\widetilde{F_{\mathcal{V}}}$, produced by the compression-expansion of the vapor (change of volume). We showed that the oscillations are *explained* by the interplay of the compression-expansion of the vapor acting as a spring and the liquid plug acting as a mass, leading to a spring-mass system (resonator). We *predicted* an oscillating frequency for the startup. Our approach complements existing work on the subject in the literature: we show that this analysis is still valid in the presence of phase-change, under some conditions (phase-change in anti-phase with position and $\sigma - \zeta_f$ small). We then *tested* experimentally the frequency prediction for a range of relevant parameters (those experiments were carried on by Thomas Monin) and found good agreements between the theory and the experiment, which *validated* the spring-mass system. We can predict the frequency both qualitatively and quantitatively. We find that we can *control* the frequency very well.

Starting from the *observation* that oscillations can increase during the startup, we also asked what *explains* the startup. The model constructed also includes the phase-change. We found that the force produced by the pressure difference on the liquid plug also includes a positive feedback force $\widetilde{F_m}$, due to the variations of mass of the vapor. Those variations of mass come from the evaporation and condensation as the liquid plug oscillates between the heat source and the heat sink. We *explained* the startup as produced by the interplay of the phase-change leading to a positive feedback force and the viscous friction between the liquid and the walls, acting as a dissipative force. The equilibrium becomes unstable and the startup occurs when the phase-change coefficient (σ) is increased above the

friction coefficient (ζ_f). This can be neatly expressed by a new dimensionless instability number, $\Pi = \sigma/\zeta_f$, with the startup occurring when Π is increased above 1. The number Π is analogous to other instability numbers such as the Rayleigh number (Ra) for the Rayleigh–Bénard instability. Based on Π, we *predicted* that the startup can be triggered by increasing the axial thermal gradient, reducing the external pressure or decreasing the phase-change thermal resistance (among other parameters). We *validated* the instability mechanism by confirming that the phase-change does positive work while viscous friction does negative work and by confirming the effects on the startup of the parameters mentioned above. We have reached a good level of *control* over the oscillation startup. Although we do not fully understand how to control the phase-change in the experiment, we now know that the instability can be controlled by controlling the magnitude of the phase-change component in anti-phase with the position, producing a positive feedback force.

Additional original contributions presented here include: 1) the first ever use of a capillary as a controllable wicking structure (*discovery*), which allow to greatly increase the oscillations amplitude, 2) experimental measurements during the startup (position, pressure, mass of vapor, friction, etc.), 3) a theoretical expression of the friction force in an oscillating regime which is validated experimentally and 4) an energy analysis approach which can be used to study the effect of phase-change and friction in a very general way, both theoretically and experimentally.

This work was published in Physical Review Fluids [112].

Chapter 4. What leads to the steady-state regime.
We started with experimental *observations*. We reused the experimental measurements of the startup, showing the initial growth of amplitude and the subsequent saturation, as the system reaches an oscillating steady-state regime. We showed that, in a phase-space representation, the system approaches a closed loop (a limit cycle, corresponding to the oscillating steady-state regime). The goal here was to consider a simple mathematical *model* describing this phenomenon and to use it to better *understand* what leads to the saturation of the amplitude, why there is such a limit cycle and how we can control it. We considered the model presented in chapter 3. We showed by comparing the analytical solution of the linearized equation and the numerical resolution of the nonlinear equations that the saturation and the limit cycle are due to nonlinearities. We then proceeded to obtain an approximate analytical solution of the nonlinear equations, using center manifold reduction followed by the normal form reduction technique. This solution shows that, during the startup, the growth and subsequent saturation of the amplitude is *explained* by the

interplay of the instability mechanism and a limiting mechanism, due to the nonlinearities. We then proved mathematically the existence of the limit cycle, created by a Poincaré-Andronov-Hopf bifurcation. Finally, we *predicted* the oscillations amplitude. We studied how to *control* the oscillations amplitude on the limit cycle. We showed that the amplitude can be increased by increasing the instability and by decreasing the nonlinearities. More specifically, this entails that the amplitude can be increased by increasing the phase-change and decreasing the friction. We studied how phase-change and friction impact the oscillations amplitude quantitatively, using numerical continuation. Consequences for the design of PHP and SOFHE were discussed.

This work complements an earlier conference publication on the role of nonlinearities [111]. A preliminary version of this work was published as a conference paper [113] which led to a manuscript now accepted by the Nonlinear Dynamics Journal [114].

Chapter 5. Accurate solution for the steady-state.
The approximate analytical solution obtained in chapter 4 is only valid for small oscillations amplitude. This chapter is about building better theoretical tools to describe and understand the oscillations amplitude in the model. I obtained accurate analytical and semi-analytical solutions, valid across the whole range of the parameters. First, I tracked the limit cycle using numerical continuation and examined the spectral diagram of the solution across a large range of the parameters. I then applied the averaging method, for each nonlinearities individually, without approximating the vector field by a Taylor series. Doing so, I was able to obtain an extremely accurate analytical solution for the dynamics, for the phase-change nonlinearity. For the pressure nonlinearity, the averaging solution, is unable to reproduce the harmonics in the solution. Thus, I suggested a modified solution, based on the averaging form but written as an infinite series, which turns out to be extremely accurate as well. The parameters of this modified solution are obtained by fitting the solution to numerical continuation results. For both nonlinearities, I observed that, as the amplitude increases, harmonics develop in the solution due to the nonlinearities. I also found that to increase the amplitude, one should first increase the instability and then decrease the nonlinearities. I expect this general statement to be valid for any nonlinearities. The two analytical solutions obtained here were used to study the energy harvesting in chapter 6.

Chapter 6. How an energy harvesting device behaves.
In this chapter, we answered the question of how an energy harvesting device (SOFHE) would behave. We added a load (a dissipative force representing a velocity-damped transducer) to the model described in chapter 3. We adapted the solution obtained in chapter 5

such that we get a very accurate analytical solution describing the dynamics (amplitude, frequency) and the power output as well as the efficiency. We showed how the power output behaves as a function of the load: the power follows an asymmetrical bell shape curve with no power at no load, a maximum power at an optimal load value and no power again at a maximum load value. At that maximum value, the load creates enough dissipation to kill the self-oscillations. Those qualitative *predictions* were validated in experiments [58]. Our model enables us to *explain* the behavior. We then show how the power output can be increased by increasing the phase-change and by decreasing the viscous friction (*control*). We also studied the efficiency and showed that it also follows an asymmetrical bell shape curve. We discussed the consequences of our analysis with regards to the design of SOFHE. We also discussed how the behavior we observe in this self-oscillating harvester differs qualitatively from forced oscillating harvesters.

Early work on the subject led a to a conference paper [111]. This work was later on submitted as a journal publication to Applied Thermal Engineering.

Chapter 7. Energy persective.
In this chapter, we revisited the startup, the saturation of the amplitude and the power output from an energy viewpoint. We started with the theoretical model. We first showed how, during the startup, the work done by phase-change is greater than the (negative) work done by friction, such that a positive net energy is injected into the system at each oscillations, leading to a growth in the energy of the resonator and in the oscillations amplitude. We can visually see that the effect of the nonlinearity is to reduce the work done by phase-change compared to its linear value. The consequence is that the friction work eventually catches up with the phase-change and the system reaches a steady-state. We then showed how controlling the instability (related to the slopes at the origin of the phase-change and viscous friction works) and the nonlinearities (the deviation from the linear work) could lead to greater oscillations amplitude. With regards to the power output, we showed that the same strategies also led to greater power. We subsequently looked at experimental data for the startup and the power output. We found qualitatively the same behavior than in the theoretical model. Based on our model, we obtained an expression allowing an indirect measure of the load coefficient, useful to analyze experimental data. Overall, we find that one needs to increase the work done by phase-change and reduce the work done by friction in order to increase the oscillations amplitude or the power output.

Our approach here enables great simplification of the problem. We can discuss the phenomenon solely in terms of the average energy of the resonator $\overline{E_r}$, the average work rate done by phase-change ($\overline{\dot{W}}_m$) and done by friction ($\overline{\dot{W}}_f$). This way of thinking is also

very general: regardless of how complicated the phase-change is, what matters is $\overline{\dot{W}}_m$, the average work rate over a cycle. Our conclusions on the role of $\overline{\dot{W}}_m$ and $\overline{\dot{W}}_f$ are general.

This chapter was prepared as a manuscript for a new submission to Applied Thermal Engineering.

Few notes on scientific understanding

In our approach, understanding was achieved by various means. Whenever possible, simple analytical formulas were obtained from which the effect of the parameters on the dynamics could be deduced. We reduced the large number of parameters to only few macro-parameters (ω_n, σ, T_{HL}, ζ_f) which have dynamical relevance. Indeed they are related to abstract concepts we introduced to describe the dynamics (resonator, instability mechanism, limiting mechanism). Those concepts capture distinct aspects of the dynamics (oscillation, startup, steady-state). One can think of the impact of the configuration in terms of those concepts and of the macro-parameters to predict the behavior of the phenomenon qualitatively. In section 1.3.1, I described scientific understanding from a geometrical point of view fig. 1.6). We were able to obtain such a representation in terms of the macro-parameters for the behavior (fig. 3.4), the oscillations amplitude (fig. 4.9) and the maximum power output (figs. 7.15 and 7.16). Finally, by adopting an energy point of view, we were able to describe the dynamics in a very concise and general manner, in terms of the average energy of the resonator $\overline{E_r}$ and the average work rate done by phase-change ($\overline{\dot{W}}_m$) and by friction ($\overline{\dot{W}}_f$).

Other scientific contributions

In this thesis, I had the opportunity to contribute to other scientific publications on the SBPHP self-oscillations, including the work of Thomas Monin to demonstrate energy harvesting with SOFHE [78, 75], the work of Nooshin Karami to study the thermodynamic cycle and the mechanical power output [57, 58] and the work of Alihossein Nikkhah on testing the oscillating friction expression numerically [1].

9.2 Further Research

From our model, we find that the phase-change can have a significant impact on the oscillations amplitude and the power output. This was also confirmed experimentally, by using a capillary to promote the formation of a thin liquid film to enhance phase-change. I suspect however that it should be possible to go much further by better controlling the phase-change. One must control both the magnitude and the timing of the phase-change. To be more accurate, we really want to control the overall waveform of the phase-change since we should not be limited to sinusoidal behavior. What we need to do is to control the

phase-change in order to maximize the overall average work rate done by phase-change, $\overline{\dot{W}}_m$. From a theoretical point of view, an interesting question is: is there an optimal phase-change profile? From an experimental point of view the required level of control could be achieve using microfabrication. One can use a silicon wafer as one of the walls and build on the surface an array of small pillars around which thin liquid films will form, leading to much higher overall phase-change rate. By tuning the geometry of those pillars (location, size, density, etc.), we may be able to control the phase-change waveform and ajust it to maximize the average work rate done by phase-change. As a guiding tool, it could be helpful to look at the instantaneous work done by phase-change at each point of the cycle. My colleague Nooshin Karami is currently investigating microfabrication approaches to control the phase-change.

For SOFHE, my work focused mostly on the engine, but another crucial component is the electromechanical transducer. There is a lot to be done in the design of the transducer and its implementation. Once we get a good enough engine and a good enough transducer, one should build a SOFHE for an actual application.

APPENDIX A

Appendix to Chapter 3

A.1 Theoretical Additional Informations and Results

A.1.1 Energy Conservation for the Vapor Bubble

In this section, we consider the vapor control volume (see fig. 3.2a) and derive its energy conservation equation (3.2). While doing so, we will have to consider the distribution of pressure P_g, temperature T_g, and vapor density ρ_g in the vapor. In fig. A.1 we show how those should looks like qualitatively. Those quantities oscillates over time, but their profile is qualitatively similar at each time. We now discuss how those profiles are obtained. As discussed in section 3.2.1, it is appropriate to consider saturation conditions at the meniscus. The pressure P_g is given as a function of the mass m_g temperature T_g and volume of vapor $\mathcal{V}_g$ by the ideal gas law (3.3). Since pressure information propagates much faster than the liquid column oscillations, pressure will tend to be homogeneous, so $P_{g,sat} = P_g$; the pressure dictates the saturation conditions. The temperature of the vapor is $T_g = T_{g,sat}$ at the meniscus (given as a function of P_g by the Clausius-Clapeyron relation (3.8)). Away from the meniscus, heat exchange between the wall and the vapor leads to $T_g > T_{g,sat}$; the vapor is superheated. In the isothermal hypothesis, we assume that heat exchange between the wall and the vapor are fast enough such that T_g is kept constant in time. In the adiabatic hypothesis, we assume this heat exchange to be slow enough such that it can be neglected, so T_g will depend on the compression and expansion of the vapor bubble during the oscillations. Finally, the vapor density ρ_g distribution is given as a function of pressure and temperature by the ideal gas law.

We start with the energy conservation for a general control volume [35]

$$\sum \dot{E} = \frac{d}{dt}\left(\int_{C\mathcal{V}} e\rho \; d\mathcal{V}\right) + \int_{CS} e\rho(\mathbf{V_r}\cdot\mathbf{n})dA, \tag{A.1}$$

where $\sum \dot{E}$ is the total rate of energy transfer applied to the control volume, e is the specific energy (energy per unit of mass), $d\mathcal{V}$ is an elemental volume, dA is an elemental surface on the control surface, $\boldsymbol{V_r}$ is the velocity of the fluid relative to the control surface ($\boldsymbol{V_r} = \boldsymbol{V} - \boldsymbol{V_s}$, where $\boldsymbol{V}$ and $\boldsymbol{V_s}$ are the velocities relative to the referential of the fluid and of the control surface, respectively) and $\boldsymbol{n}$ is a normal unit vector oriented outward from the control surface.

We first expand the total rate of energy transfer $\sum \dot{E}$ and obtain the expression below. The total rate of energy transfer includes the effect of the pressure applied by the meniscus control volume, the heat exchange rate between the vapor and the walls $\dot{Q}_g$, and the volumic forces (gravity). We neglect the gravity on the vapor. We note that the pressure applied by the meniscus (from the liquid plug) on the vapor is $P_{g,sat}$. Also, the velocity of

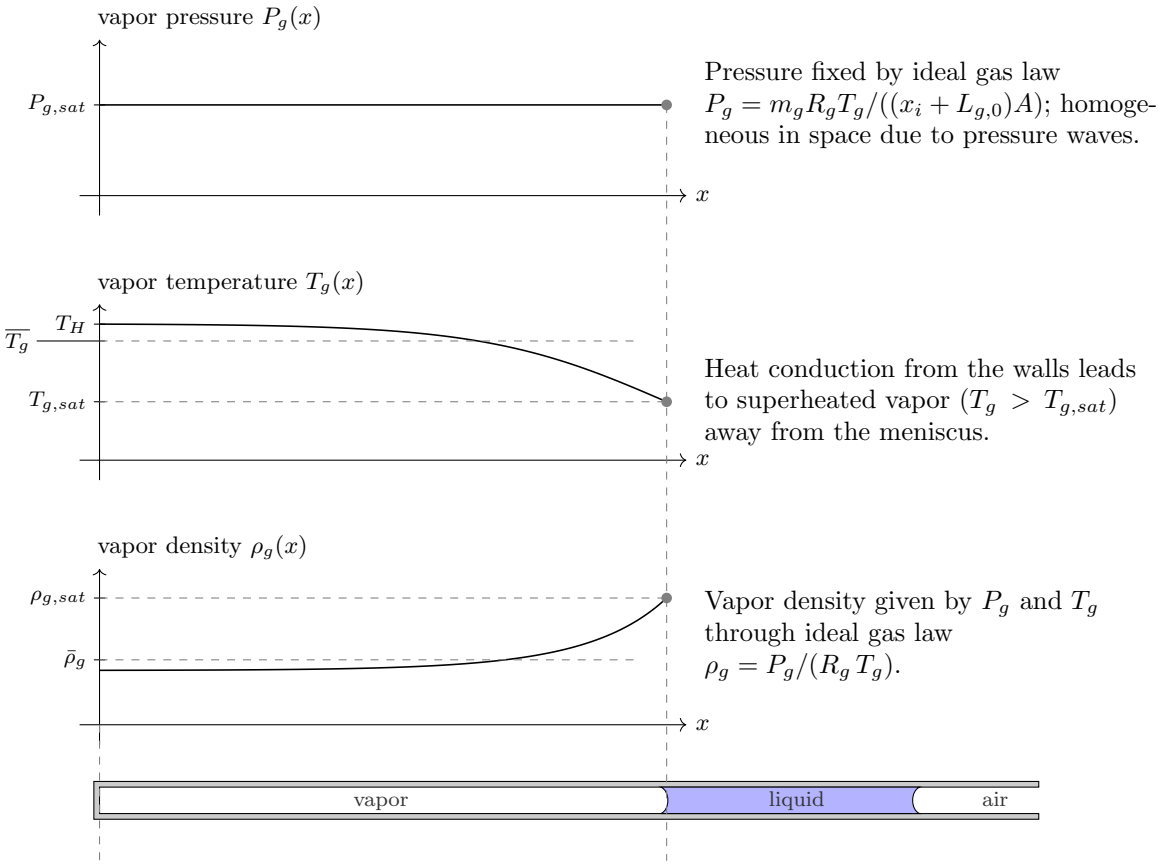

Figure A.1 Qualitative representation of the pressure P_g, temperature T_g, and density ρ_g distributions in the vapor bubble along x.

the vapor V_g at the meniscus can be rewritten as $\bar{V}_{r,g} + V_s$ with the relative velocity related to phase change: $\bar{V}_{r,g} = -\dot{m}_g/(\rho_{g,sat}\, A)$ and the velocity of the control surface being the velocity of the meniscus $V_s = \dot{x}_i$. For $\sum \dot{E}$ we obtain

$$\sum \dot{E} = -P_{g,sat} V_g A + \dot{Q}_g = -P_{g,sat} A \left(\frac{-\dot{m}_g}{\rho_{g,sat}\, A} + \dot{x}_i \right) + \dot{Q}_g,$$

leading to

$$\sum \dot{E} = \left(\frac{\dot{m}_g\, P_{g,sat}}{\rho_{g,sat}} \right) - (P_{g,sat} A\, \dot{x}_i) + \dot{Q}_g. \tag{A.2}$$

We then simplify the second term on the right-hand side of the energy conservation (A.1) which represents the rate of energy exchange due to mass flow across the boundaries of the control volume. The only transfer of mass occurs at the meniscus. We can integrate by considering an average velocity $\bar{V}_{r,g}$ where the subscript *out* means in the outward direction (from the vapor toward the meniscus control volume). The velocity $\bar{V}_{r,g}$ (positive in the direction of the liquid plug) can be rewritten as a function of the mass flow rate leading

to the evaporation (liquid to vapor) $\dot{m}_g$ as $\bar{V}_{r,g} = -\dot{m}_g/\rho_g A$. We get that

$$\int_{CS} e\rho(\mathbf{V_r}\cdot\mathbf{n})dA = \int_{meniscus} \rho_g e_g(\mathbf{V_r}\cdot\mathbf{n})dA \;=\; \left(\rho_g e_g A\bar{V}_{r,g}\right)_{out} \;=\; -\dot{m}_g\, e_{g,out}. \quad \text{(A.3)}$$

The energy conservation can be rewritten as

$$\left(\frac{\dot{m}_g\, P_{g,sat}}{\rho_{g,sat}}\right) - (P_{g,sat} A\,\dot{x}_i) + \dot{Q}_g = \frac{d}{dt}\left(\int_{CV} e_g\rho_g d\mathcal{V}\right) - \dot{m}_g\, e_{g,out}. \quad \text{(A.4)}$$

The specific energy e is the sum of the internal energy $\hat{u}$, the kinetic energy $\frac{1}{2}V^2$, and the potential energy gz. Here we neglect the gravitational potential energy of the vapor. We can rewrite the energy conservation as

$$\left(\frac{\dot{m}_g\, P_{g,sat}}{\rho_{g,sat}}\right) - (P_{g,sat} A\,\dot{x}_i) + \dot{Q}_g = \frac{d}{dt}\int_{CV} \rho_g\left(\hat{u}_g + \frac{1}{2}{V_g}^2\right)d\mathcal{V} - \left(\hat{u}_g + \frac{1}{2}{V_g}^2\right)_{out}\dot{m}_g. \quad \text{(A.5)}$$

The vapor kinetic energy has been previously neglected [126, 20]. We can justify this assumption by an estimation of the magnitude of those terms. We would like to verify that $\frac{1}{2}{V_g}^2 \ll \hat{u}_g$, and solving for V_g, we obtain $V_g \ll \sqrt{2\,\hat{u}_g}$. To compute $\hat{u}_g$, we use the constitutive relation $d\hat{u}_g \approx c_v\, dT_g$. Assuming c_v mostly constant on the desired range and assuming that the vapor is an ideal gas, we have that $\hat{u}_g \approx c_v\, T_g$. For the water vapor, $c_v = 1.41\,\mathrm{kJ/kgK}$. Considering $T_g = 373\,\mathrm{K}$ we get: $\sqrt{2\,\hat{u}_g} \sim 1026\,\mathrm{m/s}$. For oscillations of an amplitude of 1 cm at 25 Hz, the velocity is approximately 0.5 m/s which is 0.05% of 1026 m/s. Neglecting the kinetic energy is therefore justified. We obtain

$$\left(\frac{\dot{m}_g\, P_{g,sat}}{\rho_{g,sat}}\right) - (P_{g,sat} A\,\dot{x}_i) + \dot{Q}_g = \frac{d}{dt}\int_{CV} \rho_g\,\hat{u}_g d\mathcal{V} - \hat{u}_{g,out}\,\dot{m}_g. \quad \text{(A.6)}$$

We can simplify this equation with some constitutive relations. We consider the vapor as an ideal gas, $P_{g,sat} = \rho_g\, R_g\, T_{g,sat} = \rho_g\,(c_p - c_v)\,T_{g,sat}$, and also, as mentioned before, take $\hat{u}_g = c_v\, T_g$. We get

$$\dot{m}_g\,(c_p - c_v)\,T_{g,sat} - P_{g,sat} A\dot{x}_i + \dot{Q}_g = \frac{d}{dt}\int_{CV} \rho_g\, c_v\, T_g\; d\mathcal{V} - c_v\, T_{g,sat}\;\dot{m}_g.$$

Let us now simplify the first term on the right-hand side, which represents the rate of change of the energy in the vapor. We first perform the integral by considering the averaged quantities $\bar{\rho_g}$, $\bar{c_v}$, and $\overline{T}_g$. We then assume $\bar{c_v}$ constant and use the relation $\mathcal{V}_g = m_g/\bar{\rho_g}$:

$$\frac{d}{dt}\int_{CV} \rho_g\, c_v\, T_g\; d\mathcal{V} = \frac{d}{dt}\left(\bar{\rho_g}\;\bar{c_v}\;\overline{T}_g\;\mathcal{V}_g\right) = \bar{c_v}\;\frac{d}{dt}\left(m_g\;\overline{T}_g\right).$$

We then distribute the derivative

$$\frac{d}{dt}\int_{CV} \rho_g\, c_v\, T_g\; d\mathcal{V} = \bar{c_v}\, m_g\, \dot{\overline{T}}_g + \bar{c_v}\, \dot{m}_g\, \overline{T}_g.$$

Substitution in the energy equation and rearranging gives

$$\bar{c_v}\, m_g\, \dot{\overline{T}}_g + \bar{c_v}\, \dot{m}_g\, \overline{T}_g - \cancel{c_v\, T_{g,sat}\, \dot{m}_g} = \dot{m}_g\, c_p\, T_{g,sat} - \cancel{\dot{m}_g\, c_v\, T_{g,sat}} - P_{g,sat} A \dot{x}_i + \dot{Q}_g$$

Finally, rearranging once again leads to the following equation, which describes the evolution of the vapor temperature $\overline{T}_g$:

$$\bar{c_v}\, m_g\, \dot{\overline{T}}_g = \left(c_p\, T_{g,sat} - \bar{c_v}\, \overline{T}_g\right)\, \dot{m}_g - P_{g,sat} A \dot{x}_i + \dot{Q}_g. \tag{A.7}$$

Equation (3.2) in the main text corresponds to eq. (A.7) after solving for $\dot{\overline{T}}_g$ and dropping the overbars. Note that taking $T_{g,sat} = T_g$ and $\rho_g = \rho_{g,sat}$ in eq. (A.7) leads to the expression commonly used in the literature. In contrast to [126, 20, 85], the above description takes into account the fact that the meniscus is at saturation ($T_{g,sat} \neq T_g$). We assume that the meniscus remains at saturation due to the phase change but that the bulk of the vapor may differ from the saturation condition (the vapor is typically superheated).

A.1.2 Friction in an Oscillating Regime

In this section we show how to derive the friction force for a fluid of infinite length subjected to an oscillating pressure gradient in a circular pipe, given by eq. (3.9b). First, we briefly explain how one can derive the velocity profile in appendix A.1.2, as described by White [123]. We then show how to derive the friction force as a function of the pressure gradient from the velocity profile in appendix A.1.2.

Oscillating Velocity Profile

In this section we show how to derive the velocity profile for the case of interest (see White [123, sec.3-4.2 Pipe Flow Due to Oscillating Pressure Gradient, p.135] for more details). Navier-Stokes equations reduce to the partial differential equation

$$\rho \frac{\partial u}{\partial t} = -\frac{dp}{dx} + \mu\left(\frac{\partial^2 u}{\partial r^2} + \frac{1}{r}\frac{\partial u}{\partial r}\right). \tag{A.8}$$

We consider a sinusoidal pressure gradient written as a complex exponential

$$\frac{dp}{dx} \equiv -\rho K e^{i\omega t}, \tag{A.9}$$

with $e^{i\omega t} = \cos(\omega t) + i\sin(\omega t)$. The solution of eq. (A.8) for the velocity profile is given by the following, after substitution of the pressure gradient dp/dx, considering the no-slip condition ($u\,(r_0, t) = 0$, where r_0 is the tube radius) and neglecting the transient behavior,

with J_0 a Bessel function of the first kind

$$u = \frac{K}{i\omega}\, e^{i\omega t}\left[1 - \frac{J_0\left(r\sqrt{-i\omega/\nu}\right)}{J_0\left(r_0\sqrt{-i\omega/\nu}\right)}\right]. \tag{A.10}$$

This solution was first found by Sexl [102]. Dimensionless quantities are now introduced [1]:

$$\widetilde{r} \equiv \frac{r}{r_0}, \qquad \widetilde{u} \equiv \frac{u}{u_{max}} \quad \text{with}: \; u_{max} = \frac{K{r_0}^2}{4\nu}, \qquad \mathrm{Re}_\omega \equiv \frac{\omega {r_0}^2}{\nu}. \tag{A.11}$$

The Bessel function makes the solution difficult to study, but it is possible to get simpler expressions by considering series approximations. One reaches the two approximations for low Re_ω and high Re_ω, respectively,

$$\widetilde{u} \approx \left(1-\widetilde{r}^2\right)\cos(\omega t) + \tfrac{1}{16}\mathrm{Re}_\omega\left(\widetilde{r}^4 + 4\widetilde{r}^2 - 5\right)\sin(\omega t) + \mathcal{O}\left(\mathrm{Re}_\omega^2\right) \qquad \text{for} \mathrm{Re}_\omega < 4, \tag{A.12a}$$

$$\widetilde{u} \approx \frac{4}{\mathrm{Re}_\omega}\left[\sin(\omega t) - \frac{e^{-B}}{\sqrt{\widetilde{r}}}\,\sin(\omega t - B)\right] + \mathcal{O}\left(\mathrm{Re}_\omega^{-2}\right) \qquad \text{for} \mathrm{Re}_\omega > 4, \tag{A.12b}$$

with $B \equiv (1-\widetilde{r})\sqrt{\mathrm{Re}_\omega/2}$. The first term in eq. (A.12a) corresponds to a quasistatic Poiseuille flow, with the velocity in phase with the pressure gradient. Poiseuille flow is therefore a good approximation for Re_ω sufficiently small. The second term in eq. (A.12a) adds a small delay and reduces the velocity at $\widetilde{r} = 0$. At higher Re_ω, the velocity profile given by eq. (A.12b) exhibits Richardson's annular effect, where the flow near the wall moves at a certain velocity but the core moves at another velocity, possibly opposite.

Oscillating Friction Force

Given the velocity profiles we now want to derive the friction force. The shear stress at the wall $\tau_{rx}|_{r=r_0}$, considering no velocity in the radial direction, is ([35, p.823])

$$\tau_{rx}|_{r=r_0} = \mu\varepsilon_{rx}|_{r=r_0} = \mu\frac{\partial u}{\partial r}\bigg|_{r=r_0} = \mu\frac{u_{max}}{r_0}\,\frac{\partial \widetilde{u}}{\partial \widetilde{r}}\bigg|_{\widetilde{r}=1}. \tag{A.13}$$

The friction is then

$$F_f = \int_0^L 2\pi r_0 \cdot \tau_{rx}|_{r=r_0}\, dx = 2\pi\mu\, L\, u_{max} \cdot \frac{\partial \widetilde{u}}{\partial \widetilde{r}}\bigg|_{\tilde{r}=1}. \tag{A.14}$$

We now need to substitute the solution for the velocity profile $\widetilde{u}$ in F_f. For $\mathrm{Re}_\omega \ll 4$, the velocity profile corresponds to a quasistatic Poiseuille flow, so the corresponding friction force equation (3.9a) can be used. For $\mathrm{Re}_\omega < 4$, improvements to the Poiseuille friction

1. Note a small typographical error in $u_{max} = Kr_0/4\nu$ in [123]; it should read $u_{max} = Kr_0{}^2/4\nu$ (see [123, Eq.(3-34), p.116])

approximation could be obtain by considering eq. (A.12a). Here we will only derive F_f for high Re_ω. We get the expression for the derivative of the velocity profile (A.12b) evaluated at the wall

$$\left.\frac{\partial \widetilde{u}}{\partial \widetilde{r}}\right|_{\tilde{r}=1} = -\frac{1}{\mathrm{Re}_\omega}\left[\sqrt{8\mathrm{Re}_\omega}\cos(\omega t) + \left(\sqrt{8\mathrm{Re}_\omega} - 2\right)\sin(\omega t)\right] \quad \text{for} \mathrm{Re}_\omega > 4, \tag{A.15}$$

leading to the expression for the friction force F_f,

$$F_f = -\frac{2\pi\mu\, L\, u_{max}}{\mathrm{Re}_\omega}\left[\sqrt{8\mathrm{Re}_\omega}\cos(\omega t) + \left(\sqrt{8\mathrm{Re}_\omega} - 2\right)\sin(\omega t)\right] \quad \text{for} \mathrm{Re}_\omega > 4. \tag{A.16}$$

Now, instead of assuming a pressure gradient of fixed amplitude expressed as an explicit function of time, we would like to express it in terms of the state of the system, by the ideal gas law (3.3). First, we express $\cos(\omega t)$ in terms of dp/dx from eq. (A.9). Then, assuming a sinusoidal pressure gradient of slowly varying amplitude (relative to the oscillation's period), we consider $dp/dx = (\hat{P}_e - P_g)/L_\ell$, with P_g given by the ideal gas law. We get the following expression for $\cos(\omega t)$, with $\Delta P_g \equiv P_g - P_{g,0} = P_g - \hat{P}_e$

$$\cos(\omega t) = -\frac{1}{\rho K}\,\Re\left(\frac{dp}{dx}\right) = -\frac{1}{\rho K}\,\frac{\hat{P}_e - P_g}{L_\ell} = \frac{\Delta P_g}{\rho K L_\ell}. \tag{A.17}$$

We express $\sin(\omega t)$ in terms of ΔP_g by using the time derivative of $\cos(\omega t)$:

$$\sin(\omega t) = -\frac{1}{\omega}\,\frac{d\,\cos(\omega t)}{dt} = -\frac{1}{\omega}\,\frac{d}{dt}\left(\frac{\Delta P_g}{\rho K L_\ell}\right) = -\frac{1}{\omega\rho K L_\ell}\,\frac{d\,\Delta P_g}{dt}. \tag{A.18}$$

Substitution of those expressions for $\cos(\omega t)$ and $\sin(\omega t)$ in F_f gives

$$F_f = -\frac{2\pi\mu\, L_\ell\, u_{max}}{\mathrm{Re}_\omega}\left[\sqrt{8\mathrm{Re}_\omega}\left(\frac{1}{\rho K L_\ell}\,\Delta P_g\right) - \left(\sqrt{8\mathrm{Re}_\omega} - 2\right)\frac{1}{\omega\rho K L_\ell}\,\frac{d\,\Delta P_g}{dt}\right].$$

With $u_{max} = K{r_0}^2/4\nu$ we make the following simplifications

$$F_f = -\frac{2\pi\cancel{\mu}\,\cancel{L_\ell}}{\mathrm{Re}_\omega}\,\frac{\cancel{K\rho}\,{r_0}^2}{4\cancel{\mu}}\,\frac{1}{\cancel{\rho K L_\ell}}\left[\sqrt{8\mathrm{Re}_\omega}\,\Delta P_g - \left(\sqrt{8\mathrm{Re}_\omega} - 2\right)\frac{1}{\omega}\,\frac{d\,\Delta P_g}{dt}\right],$$

$$F_f = -\frac{A}{2\,\mathrm{Re}_\omega}\left[\sqrt{8\mathrm{Re}_\omega}\,\Delta P_g - \left(\sqrt{8\mathrm{Re}_\omega} - 2\right)\frac{1}{\omega}\,\frac{d\,\Delta P_g}{dt}\right]$$

and finally get the expression for the friction force in terms of ΔP_g,

$$F_f = -\sqrt{\frac{2}{\mathrm{Re}_\omega}}\,\Delta P_g\,A + \frac{1}{\omega}\left(\sqrt{\frac{2}{\mathrm{Re}_\omega}} - \frac{1}{\mathrm{Re}_\omega}\right)\Delta\dot{P}_g\,A. \tag{A.19}$$

In the linear solution (see appendix A.1.3), the dimensionless quantity $\zeta_{f\omega} = \sqrt{1/(2\mathrm{Re}_\omega)}$ appears as a damping coefficient, analogous to ζ_f for the Poiseuille flow case. We can choose to express F_f in terms of $\zeta_{f\omega}$ instead of Re_ω:

$$F_f = -\zeta_{f\omega}\,\Delta P_g\,A + \frac{1}{\omega}\left(\zeta_{f\omega} - 2\zeta_{f\omega}^2\right)\Delta\dot{P}_g\,A. \tag{A.20}$$

Note that we do not know the angular frequency ω in advance. Assuming $\omega \approx \omega_n$ should be a good first approximation.

A.1.3 Differential Equations and Linear Solution

The mechanical equilibrium (3.1), the evaporation rate (3.7) and the gas temperature rate of change (3.2) are given in dimensionless form in, respectively,

$$\ddot{\widetilde{x}}_i = \widetilde{\Delta P_g} + \widetilde{F_f}, \tag{A.21a}$$

$$\frac{d\,\widetilde{\Delta m_g}}{d\tau} = \dot{\widetilde{\Delta m_g}} = \widetilde{T_{HL}}\,\arctan\left[\,-\left|\widetilde{T'_{wc}}\right|\,(\widetilde{x}_i - \widetilde{x_c})\,\right] + \widetilde{C_{th}} - \left(\frac{T_{g,0}}{m_{g,0}\;\omega_n\;H_v R_{th}}\right)\;\widetilde{\Delta T}_{g,sat}, \tag{A.21b}$$

$$\begin{aligned}\frac{d\,\widetilde{\Delta T_g}}{d\tau} = \dot{\widetilde{\Delta T_g}} &= \frac{\gamma_{th}\,\left(\widetilde{\Delta T}_{g,sat} + \widetilde{T}_{g,sat,0}\right) - \left(1 + \widetilde{\Delta T_g}\right)}{1 + \widetilde{\Delta m_g}}\;\dot{\widetilde{\Delta m_g}} \\ &+ \frac{(1-\gamma_{th})\left(1 + \widetilde{\Delta P_g}\right)\;\dot{\widetilde{x}}_i}{1 + \widetilde{\Delta m_g}} + \frac{\dot{\widetilde{Q}}_g}{1 + \widetilde{\Delta m_g}}.\end{aligned} \tag{A.21c}$$

Equation (A.21c) takes into account the heat transfer $\dot{\widetilde{Q}}_g$ between the tube wall and the vapor. However, instead of deriving an expression for $\dot{\widetilde{Q}}_g$, we only consider two special cases, one where the vapor is isothermal ($\dot{\widetilde{Q}}_g$ compensates the other terms such that $\dot{\widetilde{T}}_g(\tau) = 0$) and a second case where there is no heat exchange between the vapor and the surroundings ($\dot{\widetilde{Q}}_g = 0$). The dimensionless expression of the variation of pressure $\widetilde{\Delta P_g}$ is given by

$$\widetilde{\Delta P_g} = \underbrace{-\left(\frac{1}{1+\widetilde{x}_i}\right)\widetilde{x}_i}_{\widetilde{F_\mathcal{V}}}\;\underbrace{+\left(\frac{1+\widetilde{\Delta m_g}}{1+\widetilde{x}_i}\right)\widetilde{\Delta T_g}}_{\widetilde{F_T}}\;\underbrace{+\left(\frac{1}{1+\widetilde{x}_i}\right)\widetilde{\Delta m_g}}_{\widetilde{F_m}}. \tag{A.22a}$$

The dimensionless expressions of friction and variations of temperature saturation are given by, respectively,

$$\dot{\widetilde{\Delta P_g}} = -\left(\frac{\left(1+\widetilde{\Delta m_g}\right)\,\left(1+\widetilde{\Delta T_g}\right)}{\left(1+\widetilde{x_i}\right)^2}\right)\,\dot{\widetilde{x}}_i + \left(\frac{1+\widetilde{\Delta m_g}}{1+\widetilde{x_i}}\right)\,\dot{\widetilde{\Delta T_g}} + \left(\frac{1+\widetilde{\Delta T_g}}{1+\widetilde{x_i}}\right)\,\dot{\widetilde{\Delta m_g}}, \tag{A.22b}$$

$$\widetilde{F_f} = \begin{cases} -2\,\zeta_f\,\dot{\widetilde{x}}_i & \text{(Poiseuille flow, } \mathrm{Re}_\omega \ll 4\text{)} \\ -\sqrt{\frac{2}{\mathrm{Re}_\omega}}\,\widetilde{\Delta P_g} + \frac{1}{\widetilde{\omega}}\,\left(\sqrt{\frac{2}{\mathrm{Re}_\omega}} - \frac{1}{\mathrm{Re}_\omega}\right)\dot{\widetilde{\Delta P_g}} & \text{(oscillating flow, } 4 < \mathrm{Re}_\omega < 2000\text{)}, \end{cases} \tag{A.22c}$$

$$\widetilde{\Delta T}_{g,sat} = \frac{H_v\,\widetilde{T}_{g,sat,0}}{H_v - R_g\,T_{g,0}\,\widetilde{T}_{g,sat,0}\,\ln\left[\widetilde{\Delta P_g}+1\right]} - \widetilde{T}_{g,sat,0}. \tag{A.22d}$$

The dimensionless variables and parameters are given by, respectively.

$$\tau \equiv \omega_n\,t, \tag{A.23a}$$

$$\widetilde{x_i} \equiv \frac{x_i}{L_{g,0}}, \tag{A.23b}$$

$$\widetilde{\Delta m_g} \equiv \frac{\Delta m_g}{m_{g,0}}, \tag{A.23c}$$

$$\widetilde{\Delta T_g} \equiv \frac{\Delta T_g}{T_{g,0}}, \tag{A.23d}$$

$$\widetilde{\Delta T}_{g,sat} \equiv \frac{\Delta T_{g,sat}}{T_{g,0}}, \tag{A.23e}$$

$$\widetilde{T}_{g,sat,0} \equiv \frac{T_{g,sat,0}}{T_{g,0}}, \tag{A.23f}$$

$$\widetilde{\Delta P_g} \equiv \frac{\Delta P_g}{P_{g,0}}, \tag{A.23g}$$

$$\widetilde{F_f} \equiv \frac{F_f}{P_{g,0}\,A}; \tag{A.23h}$$

$$\zeta_f \equiv -\frac{c}{2\,m_\ell\;\omega_n}, \tag{A.24a}$$

$$\zeta_{f\omega} \equiv \sqrt{\frac{1}{2\,\mathrm{Re}_\omega}} = \sqrt{\frac{\mu}{2\,\rho_\ell\,\omega\,R^2}} = \frac{1}{\sqrt{\widetilde{\omega}}}\;\zeta_{f\omega_n}, \tag{A.24b}$$

$$\zeta_{f\omega_n} \equiv= \sqrt{\frac{\mu}{2\,\rho_\ell\,\omega_n\,R^2}}, \tag{A.24c}$$

$$\widetilde{\dot{Q}_g} \equiv \frac{\dot{Q}_g}{c_v\,\omega_n\,m_{g,0}\,T_{g,0}}, \tag{A.24d}$$

$$\widetilde{T_{HL}} \equiv \left(\frac{1}{\pi\;\omega_n m_{g,0}\,H_v\,R_{th}}\right)\;T_{HL}, \tag{A.24e}$$

$$\left|\widetilde{T'_{wc}}\right| \equiv \left(\frac{\pi\;L_{g,0}}{T_{HL}}\right)\;|T'_{wc}|, \tag{A.24f}$$

$$\widetilde{x_c} \equiv \left(\frac{1}{L_{g,0}}\right)\;x_c, \tag{A.24g}$$

$$\widetilde{C_{th}} \equiv \frac{\frac{1}{2}\,(T_H + T_L) - T_{g,sat,0}}{m_{g,0}\,\omega_n\;H_v R_{th}}, \tag{A.24h}$$

$$\widetilde{\varepsilon} \equiv \frac{R_g\;{T_{g,0}}^2\;\widetilde{T}^{\,2}_{g,sat,0}}{2\;m_{g,0}\;\omega_n\;{H_v}^2 R_{th}}. \tag{A.24i}$$

Linearization of eq. (A.21) leads to the following equations written in matrix form:

$$\dot{\boldsymbol{q}} = \boldsymbol{A}\,\boldsymbol{q} \qquad \text{with } \boldsymbol{q} = \begin{pmatrix} \widetilde{x_i} \\ \widetilde{\dot{x}_i} \\ \widetilde{\Delta m_g} \\ \widetilde{\Delta T_g} \end{pmatrix}; \tag{A.25a}$$

$$\boldsymbol{A} = \begin{pmatrix} 0 & 1 & 0 & 0 \\ A_{21} & A_{22} & A_{23} & A_{24} \\ -2\;(\widetilde{\sigma} - \widetilde{\varepsilon}) & 0 & -2\,\widetilde{\varepsilon} & -2\,\widetilde{\varepsilon} \\ -2\,C_{\gamma T}\;(\widetilde{\sigma} - \widetilde{\varepsilon}) & (1 - \gamma_{th}) & -2\,C_{\gamma T}\,\widetilde{\varepsilon} & -2\,C_{\gamma T}\,\widetilde{\varepsilon} \end{pmatrix}; \tag{A.25b}$$

$$\begin{aligned} A_{21} &= -1 + 2\,\zeta_{f\omega} - 4/\widetilde{\omega}\;(C_{\gamma T} + 1)\;(\widetilde{\sigma} - \widetilde{\varepsilon})\left(\zeta_{f\omega} - {\zeta_{f\omega}}^2\right), \\ A_{22} &= -2\,\gamma_{th}/\widetilde{\omega}\;\left(\zeta_{f\omega} - {\zeta_{f\omega}}^2\right), \\ A_{23} &= 1 - 2\,\zeta_{f\omega} - 4\,\widetilde{\varepsilon}/\widetilde{\omega}\;(C_{\gamma T} + 1)\;\left(\zeta_{f\omega} - {\zeta_{f\omega}}^2\right), \\ A_{24} &= 1 - 2\,\zeta_{f\omega} - 4\,\widetilde{\varepsilon}/\widetilde{\omega}\;(C_{\gamma T} + 1)\;\left(\zeta_{f\omega} - {\zeta_{f\omega}}^2\right); \end{aligned} \tag{A.25c}$$

$$A_{21} = -1, A_{22} = -2\,\zeta_f, A_{23} = 1, A_{24} = 1. \tag{A.25d}$$

The variables which must be solved are the elements of a vector $\boldsymbol{q}$. In the matrix $\boldsymbol{A}$, the second row is given by eq. (A.25c) in the case of the oscillating friction and by eq. (A.25d) for the Poiseuille friction. The parameter $C_{\gamma T}$ is used for compactness with the definition $C_{\gamma T} \equiv \gamma_{th}\, \widetilde{T}_{g,sat,0} - 1$. The coefficient $\widetilde{\varepsilon}$ (eq. (A.24i)) expresses a rate of phase change due to variations of saturation temperature (only appears because $\widetilde{\Delta T}_{g,sat}$ is taken into account) and is therefore referred to as the dynamic saturation temperature coefficient.

The basic case assumes constant saturation temperature and constant vapor temperature, so $\widetilde{\Delta T}_{g,sat} = \widetilde{\varepsilon} = \widetilde{\Delta T_g} = 0$ and friction from the Poiseuille flow is taken into account. We get $\dot{\boldsymbol{q}} = \boldsymbol{A}\,\boldsymbol{q}$, with $\boldsymbol{q}$ and $\boldsymbol{A}$ defined by

$$\boldsymbol{q} = \begin{pmatrix} \widetilde{x_i} \\ \dot{\widetilde{x_i}} \\ \widetilde{\Delta m_g} \end{pmatrix}, \quad \boldsymbol{A} = \begin{pmatrix} 0 & 1 & 0 \\ -1 & -2\,\zeta_f & 1 \\ -2\,\widetilde{\sigma} & 0 & 0 \end{pmatrix}. \tag{A.26}$$

The basic case is solved first. Then the general case is solved.

Solution of the Basic Case

In order to solve eq. (A.26), we must find the eigenvalues and eigenvectors of the matrix $\boldsymbol{A}$. The eigenvalues λ must satisfy the condition $\det(\boldsymbol{A} - \lambda \boldsymbol{I})$, where $\boldsymbol{I}$ is the identify matrix. This condition leads to a characteristic cubic polynomial which is solved [50, 120] for λ (eq. (A.27a)). Here w is a primitive cube root of unity, p and b are the coefficients of the depressed cubic, d is the discriminant, and C_λ is a cubic root:

$$\lambda_n = -\frac{2}{3}\,\zeta_f \;+\; w^{n-1}\, C_\lambda - \frac{p}{3\, w^{n-1}\, C_\lambda} \quad \text{with } n = 1, 2, 3, \tag{A.27a}$$

$$w \equiv e^{2\pi i/3} = -\tfrac{1}{2} + \tfrac{1}{2}\sqrt{-3}, \tag{A.27b}$$

$$p \equiv 1 - \tfrac{4}{3}{\zeta_f}^2, \tag{A.27c}$$

$$b \equiv 2\widetilde{\sigma} - \tfrac{2}{3}\,\zeta_f + \tfrac{16}{27}\,{\zeta_f}^3, \tag{A.27d}$$

$$d = -4p^3 - 27b^2, \tag{A.27e}$$

$$C_\lambda \equiv \sqrt[3]{-\tfrac{1}{2}\,b + \tfrac{1}{2}\sqrt{-\tfrac{1}{27}\,d}}. \tag{A.27f}$$

Depending on the sign of the discriminant d, there are either three distinct real roots ($d > 0$), multiple real roots ($d = 0$), or one real root and two complex conjugate roots ($d < 0$). Oscillations occur only when $d < 0$. Provided all roots are distinct ($d \neq 0$), the general solution for the cubic is given by

$$\boldsymbol{q} = c_1 \boldsymbol{v_1}\, e^{\lambda_1 \tau} + c_2 \boldsymbol{v_2}\, e^{\lambda_2 \tau} + c_3 \boldsymbol{v_3}\, e^{\lambda_3 \tau}, \tag{A.28}$$

where the λ are given by eq. (A.27a) and the $\boldsymbol{v}$ are eigenvectors. The eigenvectors can be found by the condition $(\boldsymbol{A} - \lambda \boldsymbol{I})\,\boldsymbol{v} = \boldsymbol{0}$. The eigenvectors can be written as functions of

the eigenvalues as given by

$$\boldsymbol{v_n} = \begin{pmatrix} -\dfrac{1}{2\,\widetilde{\sigma}}\,\lambda_n \\ -\dfrac{1}{2\,\widetilde{\sigma}}\,(\lambda_n)^2 \\ 1 \end{pmatrix} \qquad \text{with} \quad n = 1, 2, 3. \tag{A.29}$$

We now need to find the constants c. These constants are fixed by the initial conditions. They can be found by setting $\tau = 0$ in the solution (A.28) and solving for the c. We do not provide the result explicitly here because of the length of the expressions. The solution (A.28) is now completed.

In the case where there are oscillations ($d < 0$), the solution eq. (A.28) can be rewritten in a more meaningful way. If we ensure that the real root of C_λ is taken, λ_1 is the real root and $\lambda_{2,3}$ are the complex conjugates. The solution can then be written as

$$q_n = a_{n,1}\; e^{\lambda_1 \tau} + a_{n,2}\, \sin\left(\widetilde{\omega}\tau + \varphi_n\right) \cdot e^{\widetilde{\alpha}\tau}, \tag{A.30a}$$

where $n = 1, 2, 3$ and $a_{n,1}$, $a_{n,2}$ and φ_n are constants fixed by the initial conditions. The growth rate $\widetilde{\alpha}$ and the dimensionless angular frequency $\widetilde{\omega}$ are defined as the real part and the imaginary part of the complex conjugate, such that $\lambda_{2,3} = \widetilde{\alpha} \pm i\widetilde{\omega}$:

$$\widetilde{\omega} = \|\Im[\lambda_{2,3}]\| = \tfrac{\sqrt{3}}{2}\,\left|C_\lambda + \frac{p}{3\,C_\lambda}\right|, \tag{A.30b}$$

$$\widetilde{\alpha} = \Re[\lambda_{2,3}] = -\frac{2}{3}\,\zeta_f\; - \frac{1}{2}\,C_\lambda + \frac{p}{6\,C_\lambda}, \tag{A.30c}$$

$$a_{n,1} = c_1\, v_{n,1}, \tag{A.30d}$$

$$a_{n,2} = \sqrt{4\; c_2\, c_3\, v_{n,2}\, v_{n,3}}, \tag{A.30e}$$

$$\tan\left(\varphi_n\right) = \frac{c_2\, v_{n,2} + c_3\, v_{n,3}}{i\,\left(c_2\, v_{n,2} - c_3\, v_{n,3}\right)}. \tag{A.30f}$$

Note that one must be careful when computing the phase φ by making sure that the arctangent function covers $0 : 2\pi$ (by using the function atan2 on usual software).

Once substitutions are made, the discriminant d , the growth rate of the real root λ_1, the growth rate of the oscillations $\widetilde{\alpha}$, and the angular frequency $\widetilde{\omega}$ are functions of $\widetilde{\sigma}$ and ζ_f only. They can be represented by surfaces as shown in fig. A.2. There are no oscillations in the lower right corner, since the discriminant is positive as shown in fig. A.2a. Oscillations of q_n grow if $\widetilde{\alpha} > 0$, the stability threshold occuring at $\widetilde{\alpha} = 0$. As one can anticipate from fig. A.2c, solving $\widetilde{\alpha} = 0$ for $\widetilde{\sigma}$ gives $\widetilde{\sigma} = \zeta_f$; the system is unstable when $\widetilde{\sigma} > \zeta_f$. The instability number Π is defined as the ratio between the phase-change coefficient and the dissipation coefficient $\Pi = \widetilde{\sigma}/\zeta_f$. The system is unstable when the phase change is greater than the dissipation, when $\Pi > 1$. Considering the dimensionless angular frequency,

eq. (A.30b) gives $\widetilde{\omega} = 1$ (the dimensional frequency is ω_n) for the line $\widetilde{\sigma} = \zeta_f$. In the upper part for $\widetilde{\sigma} > \zeta_f$, however, the frequency increases.

Although exact, the expressions for the eigenvalues and for $\widetilde{\alpha}$ and $\widetilde{\omega}$ are difficult to analyze. Those are all nonlinear algebraic functions of $\widetilde{\sigma}$ and ζ_f. Since $\widetilde{\sigma}$ and ζ_f are usually small, it is useful to linearize the eigenvalues around $\widetilde{\sigma} = \zeta_f = 0$. We get the following approximations for the roots:

$$\lambda_1 \approx -2\,\widetilde{\sigma}, \tag{A.31a}$$

$$\lambda_{2,3} \approx (\widetilde{\sigma} - \zeta_f) \pm i. \tag{A.31b}$$

The growth rate and the dimensionless angular frequency can be approximated as

$$\widetilde{\alpha} \approx \widetilde{\sigma} - \zeta_f = \zeta_f\,(\Pi - 1)\,, \tag{A.32a}$$

$$\widetilde{\omega} \approx 1. \tag{A.32b}$$

These expressions are much simpler. The phase change $\widetilde{\sigma}$ acts as feedback and the friction ζ_f acts as dissipation. The solution in the main text (3.14) is based on eqs. (A.30a) and (A.32). The linearized expressions of $\widetilde{\alpha}$ and $\widetilde{\omega}$ are good approximations in the lower left corner of fig. A.2c and fig. A.2d and exact on the line $\widetilde{\sigma} = \zeta_f$. We can see the deviations from the linearized formulas in these figures. Beyond the linearized approximation, we see that actually the friction ζ_f influences the growth rate and that the phase change $\widetilde{\sigma}$ influences the frequency. These effects are significant only for high values of $\widetilde{\sigma}$ or ζ_f however.

Solution of the General Case

The general case includes secondary effects which are not required to produce self-oscillations, but provide a more accurate physical representation of the problem. Variation of saturation temperature $\widetilde{\Delta T_{g,sat}}$, variation of vapor temperature $\widetilde{\Delta T_g}$, and friction in an oscillating regime (expressed by the coefficient $\zeta_{f\omega}$) are taken into account. The solution of eq. (A.25) is given by

$$\boldsymbol{q} = c_0 \boldsymbol{v_0}\, e^{\lambda_0 \tau} + c_1 \boldsymbol{v_1}\, e^{\lambda_1 \tau} + c_2 \boldsymbol{v_2}\, e^{\lambda_2 \tau} + c_3 \boldsymbol{v_3}\, e^{\lambda_3 \tau}, \tag{A.33}$$

in the case where all eigenvalues are distinct.

The eigenvalues can be found similarly to the basic case. Here, however, a quartic characteristic polynomial must be solved [50, 121]. The first eigenvalue is null $\lambda_0 = 0$ and the first term in the solution of $\boldsymbol{q}$ is therefore a constant. For $\lambda_{1,2,3}$, we only give the linearized values (for small $\widetilde{\sigma}$, $\widetilde{\varepsilon}$, and $\zeta_{f\omega}$),

$$\lambda_0 = 0, \tag{A.34a}$$

$$\lambda_1 \approx -\,2\,\widetilde{T}_{g,sat,0}\,\widetilde{\sigma}, \tag{A.34b}$$

$$\lambda_{2,3} \approx \widetilde{T}_{g,sat,0}\,(\widetilde{\sigma} - \gamma_{th}\,\widetilde{\varepsilon}) - \sqrt{\gamma_{th}}\,\zeta_{f\omega} \pm\ i\ \sqrt{\gamma_{th}}\,(1 - \zeta_{f\omega})\,. \tag{A.34c}$$

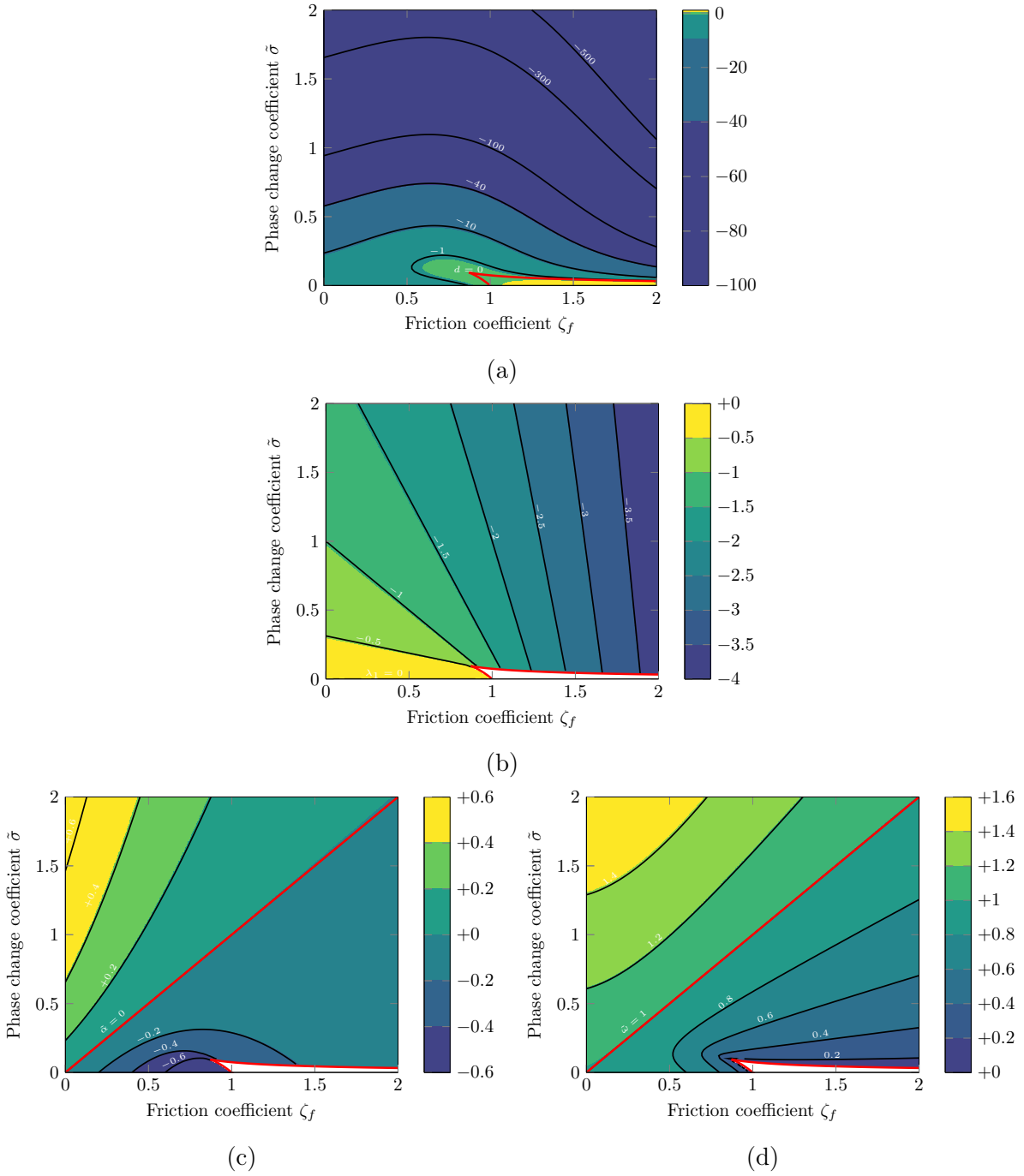

Figure A.2 (a) discriminant d (with $d < 0$ required for complex conjugate roots), (b) dimensionless growth of the real root λ_1, (eq. (A.27a)), (c) growth rate of the oscillations $\widetilde{\alpha}$ (eq. (A.30c)), and (d) dimensionless angular frequency $\widetilde{\omega}$ (eq. (A.30b)) as surfaces, along $\widetilde{\sigma}$ and ζ_f.

In the case where there are oscillations (such as when $\widetilde{\sigma}$, $\widetilde{\varepsilon}$, and $\zeta_{f\omega}$ are small), the solution can be rewritten as

$$q_n = a_{n,0} + a_{n,1}\, e^{\lambda_1 \tau} + a_{n,2} \sin\left(\widetilde{\omega}\tau + \varphi_n\right) \cdot e^{\widetilde{\alpha}\tau}. \tag{A.35}$$

The roots $\lambda_{2,3}$ are the complex conjugates and are responsible for the oscillations (growing or not). The real part $\widetilde{\alpha}$ is the growth rate and the imaginary part $\widetilde{\omega}$ is the angular frequency. Their linearized expressions are given by

$$\lambda_1 \approx -2\,\widetilde{T}_{g,sat,0}\,\widetilde{\sigma}, \tag{A.36a}$$

$$\lambda_{2,3} \approx \widetilde{\alpha} \;\pm\; i\,\widetilde{\omega}, \tag{A.36b}$$

$$\widetilde{\omega} \approx \sqrt{\gamma_{th}}\,(1 - \zeta_{f\omega})\,, \tag{A.36c}$$

$$\widetilde{\alpha} = \widetilde{T}_{g,sat,0}\,(\widetilde{\sigma} - \gamma_{th}\;\widetilde{\varepsilon}) - \sqrt{\gamma_{th}}\,\zeta_{f\omega} \tag{A.36d}$$

$$= \sqrt{\gamma_{th}}\,\zeta_{f\omega}\,(\Pi - 1)\,, \tag{A.36e}$$

$$\Pi \equiv \frac{\widetilde{T}_{g,sat,0}\;(\widetilde{\sigma} - \gamma_{th}\,\widetilde{\varepsilon})}{\sqrt{\gamma_{th}}\,\zeta_{f\omega}} = \left(1 - \frac{\gamma_{th}\,\widetilde{\varepsilon}}{\widetilde{\sigma}}\right)\;\Pi_\sigma, \tag{A.36f}$$

$$\Pi_\sigma \equiv \frac{\widetilde{T}_{g,sat,0}\;\widetilde{\sigma}}{\sqrt{\gamma_{th}}\,\zeta_{f\omega}}$$

$$\approx \sqrt[4]{\frac{{\rho_\ell}^3\;L_\ell L_{g,0}}{4\,\mu^2\,{\gamma_{th}}^2}}\;\frac{R_g\,T_{g,sat,0}\left|T'_{w,0}\right|}{\pi\,R\,H_v\,R_{th}\;\;{\hat{P}_e}^{5/4}}, \tag{A.36g}$$

$$\frac{\gamma_{th}\,\widetilde{\varepsilon}}{\widetilde{\sigma}} = \frac{\gamma_{th}\;{R_g\;T_{g,sat,0}}^2}{L_{g,0}\,H_v\left|T'_{w,0}\right|}. \tag{A.36h}$$

It is worth mentioning that eq. (A.36c) is actually not an explicit equation for $\widetilde{\omega}$. Indeed, $\zeta_{f\omega}$ is itself a function of $\widetilde{\omega}$ as given by eq. (A.24b). For $\zeta_{f\omega}$ small, however, we can assume that $\zeta_{f\omega} \sim \zeta_{f\omega_n}$, where $\zeta_{f\omega_n}$ (eq. (A.24c)) is based on ω_n and is thus known.

Similarly to the basic case, the system oscillates at a dimensionless frequency $\widetilde{\omega}$ with an instability threshold depending on a new formulation of the number Π given by eq. (A.36f). The importance of the variations of saturation temperature can be evaluated by the ratio $\gamma_{th}\,\widetilde{\varepsilon}/\widetilde{\sigma}$. The effect is negligible if $\gamma_{th}\,\widetilde{\varepsilon}/\widetilde{\sigma} \ll 1$ and Π then reduces to Π_σ. The oscillating friction is proportional to $\zeta_{f\omega}$. Increasing $\zeta_{f\omega}$ decreases Π_σ and stabilizes the system, just like for the Poiseuille friction. For the case studied in section 3.5, $\mathrm{Re}_\omega \approx 133$ so oscillating friction applies, $\zeta_f \approx 0.03$, $\zeta_{f\omega} \approx 0.06$, and $\zeta_{f\omega}/\zeta_f \approx 2$. In this case, the oscillating friction is greater than the Poiseuille friction. The oscillating friction, contrary to the Poiseuille friction, also reduces the frequency of the oscillations. In the case studied, this is a small effect.

In the case where there is no direct heat transfer between the wall and the vapor ($\dot{\widetilde{Q}}_g = 0$), referred to as adiabatic, the temperature of vapor varies according to the pressure. This introduces the heat capacity ratio γ_{th} and the dimensionless saturation temperature at equilibrium $\widetilde{T}_{g,sat,0}$ ($\widetilde{T}_{g,sat,0} = T_{g,sat,0}/T_{g,0} \;<\; 1$) in the solution and in Π. The variations of

T_g produce a change of pressure resulting in the force component $\widetilde{F_T}$. This force is partly opposite to the position, stiffening the spring and increasing the frequency by a factor $\sqrt{\gamma_{th}}$, and partly opposite to the velocity, stabilizing the oscillations as seen in Π. For a heat source at 150 °C and the system at atmospheric pressure, the factor $\widetilde{T}_{g,sat,0}/\sqrt{\gamma_{th}} = 0.76$ and Π_σ is reduced by 25%. The γ_{th} factor appears in $\gamma_{th}\,\widetilde{\varepsilon}/\widetilde{\sigma}$ and in Π_σ because both the saturation temperature and the oscillating friction are functions of the pressure difference which is a function of the temperature. For the given solution, the isothermal case can be found by setting $\gamma_{th} = \widetilde{T}_{g,sat,0} = 1$.

Variations of saturation temperature during the oscillations (dynamic effect) affects the phase change by the dynamic saturation temperature coefficient $\widetilde{\varepsilon}$ as seen in the third row of eq. (A.25b). Increasing $\widetilde{\varepsilon}$ increases the ratio $\gamma_{th}\,\widetilde{\varepsilon}/\widetilde{\sigma}$, which in turns decreases Π. The variations of saturation temperature therefore have a stabilizing effect. This is because those variations decrease the absolute temperature difference $\|T_w - T_{g,sat}\|$ and thus decrease the phase change (see eqs. (3.4) and (A.25b)).Also, a change of the saturation temperature at equilibrium $\widetilde{T}_{g,sat,0}$ (static effect) changes the thermal gradient at equilibrium in Π_σ, according to eq. (3.6) for our assumed arctangent wall temperature profile. This can increase or decrease the instability depending on the value of $\widetilde{T}_{g,sat,0}$ and on the wall temperature profile.

Gravity changes $\hat{P}_e$ in Π and has the same effect as the external pressure P_e on the instability. An angle θ of 90° increases $\hat{P}_e$ and stabilizes the system. An angle θ of −90°, on the contrary, decreases $\hat{P}_e$ and destabilizes the system. This analysis does not consider the effect of gravity on the thermal resistance. A secondary effect of $\hat{P}_e$ is to change $T_{g,sat,0}$ (eq. (3.8)), thus possibly changing the thermal gradient at equilibrium.

A.2 Experimental Additional Informations and Results

A.2.1 Details on the Instability Experiment

In this section we provide more details to section 3.5 on how quantities are derived from the position and pressure measurements. The position of the meniscus x_i is measured via a high-speed camera. We use an in-house code to detect the meniscus edge from the video. The motion has small discretization steps (20 µm) due to the pixels in the frames. This only represents around 0.1% of the final amplitude. However, when computing the derivatives $\dot{x}_i$ and $\ddot{x}_i$, those small steps lead to noise (high-frequency noise is amplified by the derivatives). To avoid this problem, we use a fit (smoothing splines) to obtain a position signal x_i identical to the original one, except for the steps which are averaged out. Deriving this signal gives velocity $\dot{x}_i$ and acceleration $\ddot{x}_i$ signals with very little noise. We also use a fit for the pressure, although the original signal is extremely accurate.

To extract the mass of vapor m_g, we simply solve the ideal gas law (3.3) for the mass of vapor, obtaining

$$m_g = \frac{P_g\,\mathcal{V}_g}{R_g\,T_g} = \frac{P_g \cdot (x_i + L_{g,0})\;A}{R_g\,T_g}. \tag{A.37}$$

In this equation, the position x_i and the pressure P_g are directly measured (importantly, measurements are synchronized in time). As discussed in section 3.5.2, simple heat transfer estimation shows that T_g is very much constant, so we assume that T_g equals the temperature of the evaporator, which is measured by a thermocouple. All quantities in eq. (A.37) are known, so the mass of vapor can be obtained. The evaporation rate $\dot{m}_g$ is obtained simply by deriving in time.

The friction force $\widetilde{F_f}$ is obtained by solving the momentum balance (3.1) for F_f, leading to

$$F_f = m_\ell \, \ddot{x}_i - \left(P_g - \hat{P}_e \right) A \tag{A.38}$$

All quantities are known in this equation, so the friction force can be obtained. The signal has some noise at very small amplitude (see fig. 3.8) since it is very sensitive to the noise in x_i (because it involves the second derivative $\ddot{x}_i$), which is more significant at very small amplitude.

In section 3.5.2, we provided an approximate value for $\widetilde{\sigma}$. It was obtained from the linear equation $\dot{\widetilde{\Delta m_g}} \approx -2\,\widetilde{\sigma}\,\widetilde{x_i}$ (eq. (3.12b)). We consider the first harmonics of $\dot{\widetilde{\Delta m_g}}$ and $\widetilde{x_i}$. The ratio of the harmonics amplitudes, divided by -2, gives $\widetilde{\sigma}$. The relation $\dot{\widetilde{\Delta m_g}} \approx -2\,\widetilde{\sigma}\,\widetilde{x_i}$ assumes that $\dot{\widetilde{\Delta m_g}}$ and $\widetilde{x_i}$ are in phase, but there actually is a small phase shift in the experiment. To take this into account, we actually only take the component in phase with the position of the first harmonic of $\dot{\widetilde{\Delta m_g}}$ and not the full $\dot{\widetilde{\Delta m_g}}$. The small component in phase with the velocity does not contribute to the positive feedback (it leads to an inertial force). Said differently, the coefficient $\widetilde{\sigma}$ defines the proportionality of the component of $\dot{\widetilde{\Delta m_g}}$ in phase with the position and not the velocity. The method is only valid when the dynamics is linear, so $\widetilde{\sigma}$ must be extracted early enough in the startup so that the oscillation amplitude is small enough that nonlinearities are negligible. This leads to some uncertainty in the extracted value of $\widetilde{\sigma}$. We note that another technique to extract $\widetilde{\sigma}$ would be to fit an exponential to the amplitude growth (at the beginning of the startup, where nonlinearities are not yet taking place so the growth has not yet saturated). From the exponential, $\widetilde{\alpha}$ can be extracted (see eq. (3.14)).Then $\widetilde{\sigma}$ is found given $\widetilde{\alpha} \approx \widetilde{\sigma} - \zeta_f$. Both techniques gives similar results in our experiment.

A.2.2 Validation of the Mechanical Resonator Representation

The experimental setup for the validation of the mechanical resonator is shown in fig. A.3. A glass tube open on one side is used as a SBPHP. Sliding the tube in or out of the heat source changes $L_{g,0}$, the size of the vapor bubble at equilibrium. The tube is heated at the closed end by an evaporator, a reservoir filled with glycerin maintained at a temperature T_H. The two ends of the evaporator are closed with PDMS plugs. A capillary is inserted in the SBPHP tube to enhance the phase change and reduce the threshold temperature T_H for self-oscillations. The temperature T_H is measured by a thermocouple (Omega 5TC-TT-K-30-36) and the heater (Omega Lux heater CSH-1011001/120) is driven by a heater controller (RKC Instrument REX-C100), limited by a voltage regulator. A pressure relief valve, not shown in the figure, prevents overpressurization of the glycerin. Outside the

evaporator, the tube is connected to a pressure sensor (Omega PX26-005DV), for frequency measurements. The resonator is characterized by a natural frequency. To validate that the oscillations in the SBPHP are explained by the coupling of a gas spring and the liquid column mass, we can test the angular frequency ω_n prediction (3.15e). In eq. (3.15e), two parameters L_ℓ and $L_{g,0}$ can be easily controlled. We measured the frequency for a range of those two parameters.

The predicted frequency matches well with the experimental results for the range of lengths tested, as shown in figs. A.4a and A.4b. These results are considered to be strong evidence of the existence of a mechanical resonator due to the coupling between the liquid mass and $F_\mathcal{V}$, the spring effect due to a change of pressure from a change of volume of the vapor. Still, the theory slightly underpredicts the frequency in figure A.4a. The theoretical expression considered is based on several hypotheses such as small $\widetilde{\sigma}$ and ζ_f (Poiseuille flow) and does not take into account the nonlinearities of eq. (A.21).

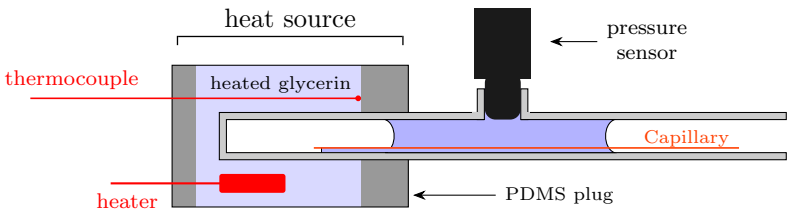

Figure A.3 Schematic of the experimental setup for variations of $L_{g,0}$, not to scale.

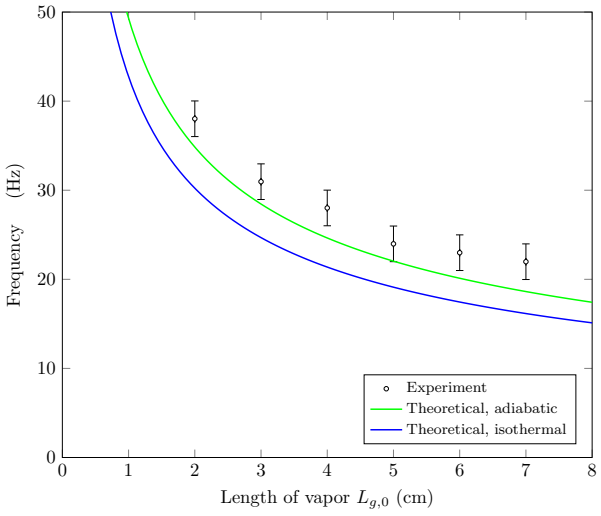

(a)

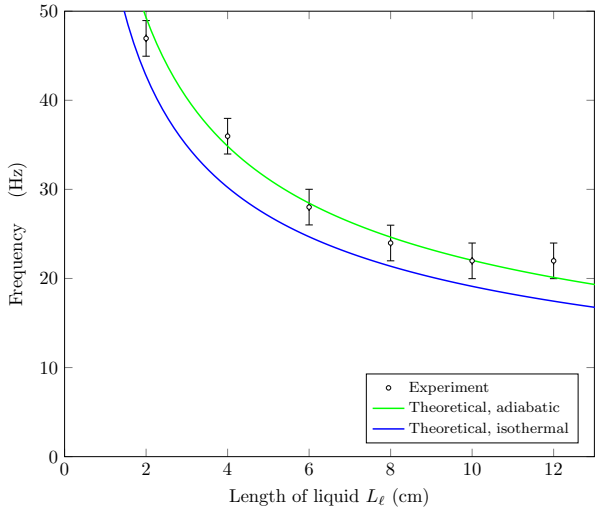

(b)

Figure A.4 Experimental validation of the frequency for ranges of (a) vapor length $L_{g,0}$ (fixed liquid length $L_\ell = 14\,\text{cm}$) and (b) liquid length L_ℓ (fixed vapor length $L_{g,0} = 7\,\text{cm}$).

APPENDIX B

Appendix to Chapter 4

B.1 Detailed Procedure to Derive the Normal Form

In this appendix, we show how to derive the normal form vector field for r and θ (eq. (4.17)) from the vector field for q_1, q_2 and q_3 (eq. (4.14)). We first use the center manifold reduction to reduce the three-dimensional system to a two-dimensional one (appendix B.1.1). We then reduce the two-dimensional system to its normal form, which we can solve analytically (appendix B.1.2). The solution is provided for new phase-space variables z_1 and z_2, related to the original one (q_1, q_2 and q_3) through a series of transformations. In appendix B.1.3, we make the inverse transformation and provide the analytical solution for q_1, q_2 and q_3. Our procedure is mainly based on Wiggins [124]. See Rand [91] for an introduction and Moon and Rand [82] for an example of the technique. Because the procedure involves lengthy manipulations, it is best handled using an analytical software. The Matlab code used for this purpose is made available in supplementary materials in the article. In the following, we will not include the full explicit expressions of some of the quantities in the intermediary steps, please refer to the code for those.

B.1.1 Center Manifold Reduction

We start from eq. (4.14), but replace σ by the bifurcation parameter δ, using $\sigma = \delta + \zeta_f$ and resulting in

$$\dot{q}_1 = q_2, \tag{B.1a}$$

$$\dot{q}_2 = \left[1 - c_P \left(\frac{q_1}{1+q_1}\right)\right](-q_1 + q_3) - 2\,\zeta_f\; q_2, \tag{B.1b}$$

$$\begin{aligned}\dot{q}_3 = {} & -2\,(\delta+\zeta_f)\,(1-c_T)\;q_1 \\ & + c_T\,T_{HL}\left(\arctan\left[-\left(\frac{2\,(\delta+\zeta_f)}{T_{HL}\cos^2[\psi/2]}\right)q_1 - \tan\left[\frac{\psi}{2}\right]\right] + \frac{\psi}{2}\right).\end{aligned} \tag{B.1c}$$

To apply the center manifold reduction technique, we need the real part of the complex conjugate eigenvalues to be 0. Here however, the real part of the complex conjugate eigenvalues can be positive or negative, if $\delta \neq 0$ (see section 4.2.2). Fortunately, we can transform the system to satisfy the center manifold requirement by a clever trick [124, p.251]: we define δ as a new phase-space variable and add the following differential equation to the system,

$$\dot{\delta} = 0, \tag{B.1d}$$

which defines δ as a constant. Because δ is a phase-space variable, the quantities δq_1 are now nonlinear. Thus, δ will not appear in the linear part and will not contribute

to the eigenvalues anymore. The real part of the complex-conjugate eigenvalues will be 0 (we will show that in the following). The new phase-space given by eq. (B.1) is four-dimensional. As a compact notation, we define the vector of phase-space variables $\boldsymbol{x}$ as $\boldsymbol{x} \equiv [q_1, q_2, q_3, \delta]^T$ and eq. (B.1) becomes $\dot{\boldsymbol{x}} = \boldsymbol{f}(\boldsymbol{x})$, where $\boldsymbol{f}$ is the vector field.

Standard Form

Before making the reduction, we must transform the system into a standard form. To do so, we first split the vector field as

$$\dot{\boldsymbol{x}} = \boldsymbol{f}\,(\boldsymbol{x}) = A\boldsymbol{x} + \boldsymbol{F}(\boldsymbol{x}), \tag{B.2}$$

where $A\boldsymbol{x}$ is the linear part and $\boldsymbol{F}(\boldsymbol{x})$ is the nonlinear part. The matrix A is given by

$$A = \mathrm{D}\boldsymbol{f}(\boldsymbol{0}) = \begin{bmatrix} 0 & 1 & 0 & 0 \\ -1 & -2\zeta_f & 1 & 0 \\ -2\zeta_f & 0 & 0 & 0 \\ 0 & 0 & 0 & 0 \end{bmatrix}, \tag{B.3}$$

where $\mathrm{D}\boldsymbol{f}(\boldsymbol{0})$ is the Jacobian of the vector field evaluated at the equilibrium $\boldsymbol{x} = \boldsymbol{0}$ (this is the linearization of the vector field). The nonlinear part is given by $\boldsymbol{F}(\boldsymbol{x}) = \boldsymbol{f}(\boldsymbol{x}) - A\boldsymbol{x}$. We have that $\boldsymbol{F}(\boldsymbol{0}) = \boldsymbol{0}$ and $\mathrm{D}\boldsymbol{F}(\boldsymbol{0}) = \boldsymbol{0}$. For small $\boldsymbol{x}$, $\boldsymbol{F}(\boldsymbol{x})$ is small and the system is weakly nonlinear.

The eigenvalues of A are: $\lambda_1 = 0$, $\lambda_2 = -i$, $\lambda_3 = i$ and $\lambda_4 = -2\zeta_f$. We see here that we indeed have the real part of complex-conjugate eigenvalues $\lambda_{2,3}$ being 0. The corresponding eigenvectors are the columns of the matrix

$$V = \begin{bmatrix} 0 & i & -i & 1 \\ 0 & 1 & 1 & -2\zeta_f \\ 0 & 2\zeta_f & 2\zeta_f & 1 \\ 1 & 0 & 0 & 0 \end{bmatrix}. \tag{B.4}$$

The standard form we seek requires the linear part to be in a block diagonal form [124, p.37], in the Jordan canonical form more specifically. To reach that form, we use a linear transformation given by a matrix T_a. For A having distinct real eigenvalues λ_j with corresponding eigenvectors $\boldsymbol{v_j}$ and distinct complex eigenvalues $\lambda_j = a_j + i\,b_j$ and $\bar{\lambda}_j = a_j - i\,b_j$ with corresponding complex eigenvectors $\boldsymbol{w_j} = \boldsymbol{u_j} + i\,\boldsymbol{v}_j$ and $\bar{\boldsymbol{w}}_{\boldsymbol{j}} = \boldsymbol{u_j} - i\,\boldsymbol{v}_j$, with $j = k+1, ..., n$, the matrix T_a is given by $T_a = [\boldsymbol{v_1}, \boldsymbol{u_1}, \ldots, \boldsymbol{v_n}, \boldsymbol{u_n}]$ (see Perko [88, p.39,28,154,108] for details). Given the eigenvectors eq. (B.4), we obtain, for T_a and its inverse ${T_a}^{-1}$ (with $\kappa \equiv 1/(1 + 4{\zeta_f}^2)$),

$$T_a = \begin{bmatrix} 0 & -1 & 0 & 1 \\ 0 & 0 & 1 & -2\zeta_f \\ 0 & 0 & 2\zeta_f & 1 \\ 1 & 0 & 0 & 0 \end{bmatrix} \quad \text{and} \quad {T_a}^{-1} = \begin{bmatrix} 0 & 0 & 0 & 1 \\ -1 & -2\kappa\,\zeta_f & \kappa & 0 \\ 0 & \kappa & 2\kappa\zeta_f & 0 \\ 0 & -2\kappa\,\zeta_f & \kappa & 0 \end{bmatrix}. \tag{B.5}$$

We apply this transformation to the vector of phase-space variable $\boldsymbol{x}$ and obtain a transformed vector of phase-space variables, we have

$$\boldsymbol{y} = {T_a}^{-1}\boldsymbol{x} = \begin{bmatrix} y_1 \\ y_2 \\ y_3 \\ y_4 \end{bmatrix} = \begin{bmatrix} \delta \\ \kappa \ \left(-q_1 + q_3 - 2\zeta_f q_2 - 4{\zeta_f}^2 q_1\right) \\ \kappa \ (q_2 + 2\zeta_f q_3) \\ \kappa \ (q_3 - 2\zeta_f q_2) \end{bmatrix} \tag{B.6}$$

and

$$\boldsymbol{x} = T_a\boldsymbol{y} = \begin{bmatrix} q_1 \\ q_2 \\ q_3 \\ \delta \end{bmatrix} = \begin{bmatrix} -y_2 + y_4 \\ y_3 - 2\zeta_f \, y_4 \\ 2\zeta_f \, y_3 + y_4 \\ y_1 \end{bmatrix}. \tag{B.7}$$

Substitution of $\boldsymbol{x} = T_a\boldsymbol{y}$ into the system $\dot{\boldsymbol{x}} = A\boldsymbol{x} + \boldsymbol{F}(\boldsymbol{x})$ (eq. (B.2)) leads to

$$\dot{\boldsymbol{y}} = \boldsymbol{g}\,(\boldsymbol{y}) = J \ \boldsymbol{y} \ + \boldsymbol{G}(\boldsymbol{y}), \tag{B.8}$$

where J is the matrix ${T_a}^{-1} A \, T_a$ and $\boldsymbol{G}(\boldsymbol{y}) = {T_a}^{-1}\boldsymbol{F}(T_a\boldsymbol{y})$. The matrix J is given by

$$J = {T_a}^{-1} A \, T_a = \begin{bmatrix} 0 & 0 & 0 & 0 \\ 0 & 0 & -1 & 0 \\ 0 & 1 & 0 & 0 \\ 0 & 0 & 0 & -2\zeta_f \end{bmatrix}. \tag{B.9}$$

We can split eq. (B.8) into three rows as

$$\dot{\boldsymbol{y}} = \begin{bmatrix} \dot{\boldsymbol{y}}_p \\ \dot{\boldsymbol{y}}_c \\ \dot{\boldsymbol{y}}_s \end{bmatrix} = \begin{bmatrix} 0 & 0 & 0 \\ 0 & J_c & 0 \\ 0 & 0 & J_s \end{bmatrix} \begin{bmatrix} \boldsymbol{y}_p \\ \boldsymbol{y}_c \\ \boldsymbol{y}_s \end{bmatrix} + \begin{bmatrix} \boldsymbol{0} \\ \boldsymbol{G}_c(\boldsymbol{y}_c, \boldsymbol{y}_p, \boldsymbol{y}_s) \\ \boldsymbol{G}_s(\boldsymbol{y}_c, \boldsymbol{y}_p, \boldsymbol{y}_s) \end{bmatrix}, \tag{B.10}$$

where

$$J_c = \begin{bmatrix} 0 & -1 \\ 1 & 0 \end{bmatrix} \quad \text{and} \quad J_s = -2\zeta_f. \tag{B.11}$$

In eq. (B.10), the first row having variable $\boldsymbol{y}_p = \delta$, corresponds to a *parameter* subsystem, the second row having variables $\boldsymbol{y}_c = [y_2, y_3]^T$ corresponds to a *center* subsystem since its eigenvalues are complex conjugate eigenvalues with 0 real parts and the third row having variable $\boldsymbol{y}_s = y_4$, corresponds to a *stable* subsystem since its eigenvalue is real and negative. The parameter, center and stable directions are linearly uncoupled from one another. We have that $\boldsymbol{G}_c = \boldsymbol{0}$, $\boldsymbol{G}_s = \boldsymbol{0}$, $\mathrm{D}\boldsymbol{G}_c = \boldsymbol{0}$ and $\mathrm{D}\boldsymbol{G}_s = \boldsymbol{0}$. eq. (B.10) is the standard form required to apply the Center manifold theorem.

Center Manifold Reduction

There exists a center manifold for the system eq. (B.10) defined locally by

$$W^c_{loc}(\mathbf{0}) = \{(\boldsymbol{y}_c, \boldsymbol{y}_p, \boldsymbol{y}_s) \in \mathbb{R}^c \times \mathbb{R}^p \times \mathbb{R}^s \mid \boldsymbol{y}_s = \boldsymbol{h}(\boldsymbol{y}_c, \boldsymbol{y}_p), \\ |\boldsymbol{y}_c| < \gamma_c,\ |\boldsymbol{y}_p| < \gamma_p,\ \boldsymbol{h}(\mathbf{0},\mathbf{0}) = \mathbf{0},\ \mathrm{D}\boldsymbol{h}(\mathbf{0},\mathbf{0}) = \mathbf{0},\} \quad \text{(B.12)}$$

for γ_c and γ_p sufficiently small [124, Sec. 18.2, p.251]. The center manifold is a three-dimensional surface in the four-dimensional phase-space. Sufficiently close to the origin $\boldsymbol{y} = \mathbf{0}$, "small amplitude periodic orbits are contained in the center manifold" [124, p.247]. Consequently, we will be able to consider only the dynamics in the center manifold and thus reduce the dimensionality of the system. In eq. (B.12), we have that $\boldsymbol{y}_s = y_4 = h(\boldsymbol{y}_c, \boldsymbol{y}_p)$, the stable direction is reduced to a function h of $\boldsymbol{y}_c = [y_2, y_3]^T$ and $\boldsymbol{y}_p = y_1 = \delta$. It is common to approximate h by a power expansion, we have

$$y_4 \approx h, \qquad \text{with}: \ h = c_1\, y_1^2 + c_2\, y_1 y_2 + c_3\, y_1 y_3 + c_4\, y_2^2 + c_5\, y_2 y_3 + c_6\, y_3^2. \quad \text{(B.13)}$$

We now must find the coefficients c_j. For $W^c_{loc}(0)$ to be a center manifold, h must satisfy the differential equations of the system. By substitution of $y_4 = h(\delta, y_2, y_3)$ in eq. (B.8), we find that h must satisfy the following quasilinear partial differential equation [124, p.252]

$$\mathcal{N}(h(\boldsymbol{y}_c, \boldsymbol{y}_p)) \equiv \mathrm{D}_{\boldsymbol{y}_c} h(\boldsymbol{y}_c, \boldsymbol{y}_p) \cdot \boldsymbol{g}_c(\boldsymbol{y}_c, h(\boldsymbol{y}_c, \boldsymbol{y}_p), \boldsymbol{y}_p) - \boldsymbol{g}_s(\boldsymbol{y}_c, h(\boldsymbol{y}_c, \boldsymbol{y}_p), \boldsymbol{y}_p) = 0. \quad \text{(B.14)}$$

Collecting terms of like powers, we obtain 6 algebraic equations which we solve for the 6 c's, leading to

$$c_1 = 0, \quad \text{(B.15a)}$$

$$c_2 = \frac{4}{\left(1 + 4{\zeta_f}^2\right)^2}, \quad \text{(B.15b)}$$

$$c_3 = \frac{2}{\left(1 + 4{\zeta_f}^2\right)^2}, \quad \text{(B.15c)}$$

$$c_4 = \frac{-T_{HL}\, c_P + 2\zeta_f\, \tan[\psi/2] \left(1 + 2{\zeta_f}^2\right) c_T}{2T_{HL}\left(1 + 5{\zeta_f}^2 + 4{\zeta_f}^4\right)}, \quad \text{(B.15d)}$$

$$c_5 = \frac{-\zeta_f T_{HL}\left(1 + 2{\zeta_f}^2\right) c_P + 2{\zeta_f}^2\, \tan[\psi/2]\, c_T}{T_{HL}\left(1 + 5{\zeta_f}^2 + 4{\zeta_f}^4\right)}, \quad \text{(B.15e)}$$

$$c_6 = \frac{-T_{HL}\left(1 + 2{\zeta_f}^2\right) c_P + 2\zeta_f\, \tan[\psi/2]\, c_T}{2T_{HL}\left(1 + 5{\zeta_f}^2 + 4{\zeta_f}^4\right)}. \quad \text{(B.15f)}$$

By substitution of $\boldsymbol{y}_s = y_4 = h(\delta, y_2, y_3)$ in system eq. (B.10), the center subsystem becomes

$$\dot{\boldsymbol{y}}_c = \boldsymbol{g}_c = J_c \boldsymbol{y}_c + \boldsymbol{G}_c(\boldsymbol{y}_c, \boldsymbol{y}_p, \boldsymbol{h}(\boldsymbol{y}_c, \boldsymbol{y}_p)) \qquad \text{with:} \qquad J_c = \begin{bmatrix} 0 & -1 \\ 1 & 0 \end{bmatrix}, \tag{B.16a}$$

where $\boldsymbol{y}_c = [y_2, y_3]^T$ and $\boldsymbol{G}_c$ is a complicated function of y_2 y_3 and δ. This system is now completely decoupled from the stable subsystem (does not depend on $\boldsymbol{y_s}$ at all). The parameter subsystem equation is again

$$\dot{\delta} = 0. \tag{B.16b}$$

eq. (B.16) is a three-dimensional phase-space (with variables y_2, y_3 and δ). However, since $\dot{\delta} = 0$, the motion on the plane $y_2 - y_3$ is invariant (remains on the plane), so knowing the value δ is enough to predict the motion on the plane $y_2 - y_3$. The dynamics is thus effectively two-dimensional and is given by eq. (B.16a). Properties of the dynamics in the plane $y_2 - y_3$ can change as the *height* δ changes. In fact, we will find that a Hopf bifurcation occurs at $\delta = 0$.

B.1.2 Normal Form

Now that we have a two-dimensional system eq. (B.16a), we can use the normal form reduction technique to obtain an approximative solution for it. In normal form, we want the instability to be captured in the linear part, we want δ to appear in the linear part [124, Eq.(19.2.1,19.2.3), p.278,279]. Unfortunately, we purposefully removed δ from the linear part to apply the center manifold reduction. We can bring δ back by splitting the vector field $\boldsymbol{g}_c$ in eq. (B.16) again, but without taking δ as a phase-space variable. Doing so, we get

$$\dot{\boldsymbol{y}}_c = \boldsymbol{g}_c(\boldsymbol{y}_c) = B\boldsymbol{y}_c + \boldsymbol{H}(\boldsymbol{y}_c), \tag{B.17}$$

where $B = \mathrm{D}_{\boldsymbol{y}_c} \boldsymbol{g}_c(\boldsymbol{0})$ is the Jacobian of $\boldsymbol{g}_c$ evaluated at the fixed point $\boldsymbol{y}_c = \boldsymbol{0}$. Also, $\boldsymbol{H} = \boldsymbol{g}_c - B\boldsymbol{y}_c$, $\boldsymbol{H} \in C^1(E)$, $\boldsymbol{H}(\boldsymbol{0}) = \boldsymbol{0}$ and $\mathrm{D}\boldsymbol{H}(\boldsymbol{0}) = \boldsymbol{0}$. As desired, the eigenvalues of B now depend on δ. However, B is not in the Jordan canonical form, so we must perform a linear transformation again, similarly to what was done in appendix B.1.1.

Standard Form for Complex Conjugate Eigenvalues

Here, we transform eq. (B.17) in its standard form, such that the linear part is in a Jordan canonical form. To do so, we must perform a linear transformation through the multiplication of a matrix T_b. To find such matrix, we first Taylor expand B for small δ. We find

$$B = \begin{bmatrix} 0 & -1 \\ 1 & 0 \end{bmatrix} + \frac{2\delta}{1 + 4{\zeta_f}^2} \begin{bmatrix} 1 & 0 \\ 2\zeta_f & 0 \end{bmatrix} + \mathcal{O}(\delta^2). \tag{B.18}$$

Considering the truncated expression of B above, we compute the trace $\mathrm{tr}(B)$ and the determinant $\det(B)$. Assuming the discriminant $\mathrm{tr}(B)^2 - 4\det(B) < 0$ (true for either

small $|\delta|$ or $\delta > 0$), the eigenvalues are complex conjugates given by $\lambda = \alpha + i\omega$ and $\bar{\lambda} = \alpha - i\omega$ with the real part $\alpha = \frac{1}{2}\,\mathrm{tr}(B)$ and the imaginary part $\omega = \frac{1}{2}\sqrt{\mathrm{tr}(B)^2 - 4\det(B)}$. Taylor expansion of α and ω in terms of δ leads to:

$$\alpha = \frac{\delta}{1 + 4{\zeta_f}^2} + \mathcal{O}(\delta^2), \qquad \text{and} \qquad \omega = 1 + \left(\frac{2\zeta_f}{1 + 4{\zeta_f}^2}\right)\delta + \mathcal{O}(\delta^2). \tag{B.19}$$

The eigenvectors corresponding to the eigenvalues λ and $\bar{\lambda}$ are $\boldsymbol{w} = \boldsymbol{u} + i\,\boldsymbol{v}$, and $\bar{\boldsymbol{w}} = \boldsymbol{u} - i\,\boldsymbol{v}$ respectively, with

$$\boldsymbol{u} = \begin{bmatrix} \dfrac{\alpha - b_{22}}{b_{21}} \\ 1 \end{bmatrix} \qquad \text{and} \qquad \boldsymbol{v} = \begin{bmatrix} \dfrac{\omega}{b_{21}} \\ 0 \end{bmatrix}, \tag{B.20}$$

where the b_{ij} are the elements of the truncated matrix B (eq. (B.18)). From those, we build the transformation matrix as:

$$T_b = [\boldsymbol{v}, \boldsymbol{u}]\,. \tag{B.21}$$

Introducing a new phase-space vector of variables $\boldsymbol{z}$ with $\boldsymbol{y}_c = T_b\boldsymbol{z}$, eq. (B.17) is transformed into

$$\dot{\boldsymbol{z}} = \boldsymbol{k}\,(\boldsymbol{z}) = J_B\ \boldsymbol{z}\ + \boldsymbol{K}(\boldsymbol{z}), \tag{B.22}$$

where $\boldsymbol{k}(\boldsymbol{z})$ is a new vector field, $J_B = {T_b}^{-1} B\, T_b$ and $\boldsymbol{K}(\boldsymbol{z}) = {T_b}^{-1}\boldsymbol{H}(T_b\boldsymbol{z})$. eq. (B.22) is the required form to apply normal form reduction (requirement specified in [124, 197/,148/]). Indeed, we have that the linear part J_B satisfies

$$J_B = \begin{bmatrix} \alpha & -\omega \\ \omega & \alpha \end{bmatrix} + \mathcal{O}(\delta^2), \tag{B.23}$$

so J_B is in the Jordan canonical form at first order approximation. Also the vector field $\boldsymbol{k}$ is C^r with $r \geqslant 5$, centered at the fixed point of interest such that $\boldsymbol{k}\,(\boldsymbol{z} = \boldsymbol{0}, \delta = 0) = \boldsymbol{0}$ and finally, $\alpha(\delta = 0) = 0$ and $\omega(\delta = 0) \neq 0$.

Normal Form Reduction

One can reduce eq. (B.22) to its normal form by third order Taylor expansion of the vector field and successive transformations (see Wiggins [124, Eq.(20.2.7) p.379, p.279] for details), leading to

$$\dot{z}_1 = \alpha(\delta)z_1 - \omega(\delta)z_2 + (a(\delta)z_1 - b(\delta)z_2)\ \left(z_1^2 + z_2^2\right) + \mathcal{O}(|z_1|^5, |z_2|^5), \tag{B.24a}$$

$$\dot{z}_2 = \omega(\delta)z_1 + \alpha(\delta)z_2 + (b(\delta)z_1 + a(\delta)z_2)\ \left(z_1^2 + z_2^2\right) + \mathcal{O}(|z_1|^5, |z_2|^5), \tag{B.24b}$$

where a and b are given by the normal form procedure. eq. (B.24) correspond to eq. (4.15) in the main text. We care especially about the amplitude of the oscillations, so it makes sense to introduce polar coordinates with $z_1 = r\cos(\theta)$ and $z_2 = r\sin(\theta)$, where r is the amplitude and θ is the phase. Introducing those into eq. (B.24) leads to

$$\dot{r} = \alpha(\delta)r + a(\delta)r^3 + \mathcal{O}(r^5), \tag{B.25a}$$
$$\dot{\theta} = \omega(\delta) + b(\delta)r^2 + \mathcal{O}(r^4), \tag{B.25b}$$

which are differential equations for r and θ. Because we study this system close to the bifurcation (close to $\delta = 0$), it makes sense to simplify eq. (B.25) by Taylor expanding its coefficients in terms of δ. We get

$$\dot{r} = d\delta r + a_0 r^3 + \mathcal{O}(\delta^2 r, \delta r^3, r^5), \tag{B.26a}$$
$$\dot{\theta} = \omega_0 + c\delta + b_0 r^2 + \mathcal{O}(\delta^2, \delta r^2, r^4), \tag{B.26b}$$

which is the desired normal form (corresponds to eq. (4.17) in the main text). The parameters d, ω_0 and c are given by (see supplementary material and Wiggins [124])

$$d \equiv \frac{1}{1 + 4{\zeta_f}^2}, \tag{B.27a}$$
$$\omega_0 \equiv 1, \tag{B.27b}$$
$$c = \frac{2\zeta_f}{1 + 4{\zeta_f}^2}. \tag{B.27c}$$

The expression of b_0 will not be needed but can be found through the normal form procedure [40]. Finally a_0 is given by

$$a_0 = a_{0,T} + a_{0,PT} + a_{0,P}, \tag{B.28a}$$

with

$$a_{0,T} \equiv \left(\frac{-2{\zeta_f}^3 \left(1 + {\zeta_f}^2 \cos\left[\psi\right]\right)}{{T_{HL}}^2 (1 + \cos\left[\psi\right]) \left(1 + {\zeta_f}^2\right) \left(1 + 4{\zeta_f}^2\right)} \right) c_T, \tag{B.28b}$$
$$a_{0,PT} \equiv \left(\frac{{\zeta_f}^2 \sin\left[\psi\right] \left(3 + 4{\zeta_f}^2\right)}{4T_{HL} \left(1 + \cos\left[\psi\right]\right) \left(1 + {\zeta_f}^2\right) \left(1 + 4{\zeta_f}^2\right)} \right) c_P c_T, \tag{B.28c}$$
$$a_{0,P} \equiv \left(\frac{-\zeta_f}{8\left(1 + {\zeta_f}^2\right)} \right) c_P, \tag{B.28d}$$

which corresponds to eq. (4.19) in the main text.

B.1.3 Solution in the q Variables (Back Transformation)

We now would like to know what is the analytical solution for the original variables q_1, q_2 and q_3. To obtain it, we must make the inverse transformations, going from $\boldsymbol{z}$ to $\boldsymbol{y_c}$ (normal form) to $\boldsymbol{y}$ (center manifold reduction) to $\boldsymbol{x}$ (standard form) to $\boldsymbol{q}$ (which is easy). Refer to previous sections to reproduce the following results.

First, we have that $\boldsymbol{y}_c = T_b\boldsymbol{z}$. Then, we can obtain $\boldsymbol{y}$ from $\boldsymbol{y}_c$ based on the following, where we used row vectors $[1,0]$ and $[0,1]$ to select $y_{c,1}$ and $y_{c,2}$ respectively:

$$\boldsymbol{y} = \begin{bmatrix} y_1 \\ y_2 \\ y_3 \\ y_4 \end{bmatrix} = \begin{bmatrix} \delta \\ y_{c,1} \\ y_{c,2} \\ h(\delta, y_{c,1}, y_{c,2}) \end{bmatrix} = \begin{bmatrix} \delta \\ [1,0]\cdot T_b\boldsymbol{z} \\ [0,1]\cdot T_b\boldsymbol{z} \\ h(\delta, [1,0]\cdot T_b\boldsymbol{z}, [0,1]\cdot T_b\boldsymbol{z}) \end{bmatrix}.$$

We then obtain $\boldsymbol{x}$ from $\boldsymbol{y}$ (based on eq. (B.7))

$$\boldsymbol{x} = T_a\boldsymbol{y} = \begin{bmatrix} -y_2 + y_4 \\ y_3 - 2\zeta_f\, y_4 \\ 2\zeta_f\, y_3 + y_4 \\ y_1 \end{bmatrix} = \begin{bmatrix} -[1,0]\cdot T_b\boldsymbol{z} + h(\delta, z_1, z_2) \\ [0,1]\cdot T_b\boldsymbol{z} - 2\zeta_f\, h(\delta, z_1, z_2) \\ 2\zeta_f\, [0,1]\cdot T_b\boldsymbol{z} + h(\delta, z_1, z_2) \\ \delta \end{bmatrix}.$$

$\boldsymbol{q}$ simply corresponds to the first three elements of $\boldsymbol{x}$, we have

$$\boldsymbol{q} = \begin{bmatrix} q_1 \\ q_2 \\ q_3 \end{bmatrix} = \begin{bmatrix} -[1,0]\cdot T_b\boldsymbol{z} + h(\delta, z_1, z_2) \\ [0,1]\cdot T_b\boldsymbol{z} - 2\zeta_f\, h(\delta, z_1, z_2) \\ 2\zeta_f\, [0,1]\cdot T_b\boldsymbol{z} + h(\delta, z_1, z_2) \end{bmatrix}, \tag{B.29}$$

where h is given by the following (based on eq. (B.13) with $y_1 = \delta$)

$$h(\delta, z_1, z_2) = c_1\,\delta^2 + c_2\,\delta y_2(\boldsymbol{z}) + c_3\,\delta y_3(\boldsymbol{z}) + c_4\,y_2(\boldsymbol{z})^2 + c_5\,y_2(\boldsymbol{z})y_3(\boldsymbol{z}) + c_6\,y_3(\boldsymbol{z})^2, \tag{B.30}$$

with $y_2(\boldsymbol{z}) = [1,0]\cdot T_b\boldsymbol{z}$ and $y_3(\boldsymbol{z}) = [0,1]\cdot T_b\boldsymbol{z}$.

Now, because the solutions are $z_1 = r\cos(\theta)$ and $z_2 = r\sin(\theta)$, the quantities $[n,m]\cdot T_b\boldsymbol{z}$ are linear combinations of sines and cosines. Thus, we can write each q_i (with $i = 1,2,3$) as Fourier series with terms up to second-order harmonics (these being produced by the terms $c_4{y_2}^2$, $c_5y_2y_3$ and $c_6{y_3}^2$). We have

$$q_i = \tfrac{1}{2}\,a_{i0} + a_{i1}\cos(\theta) + b_{i1}\sin(\theta) + a_{i2}\cos(2\theta) + b_{i2}\sin(2\theta), \tag{B.31a}$$

with the coefficients computed as usual when dealing with Fourier series:

$$a_{i0} = \frac{1}{\pi}\int_{-\pi}^{\pi} q_i(\bar{r},\theta)\ d\theta \tag{B.31b}$$

$$a_{ik} = \frac{1}{\pi}\int_{-\pi}^{\pi} q_i(\bar{r},\theta)\cos(k\theta)\ d\theta \tag{B.31c}$$

$$b_{ik} = \frac{1}{\pi}\int_{-\pi}^{\pi} q_i(\bar{r},\theta)\sin(k\theta)\ d\theta \tag{B.31d}$$

Because we care mostly about the amplitude of each terms, it make sense to rewrite this Fourier series in an amplitude-phase form as

$$q_i = \frac{A_{i0}}{2} + \sum_{k=1}^{n} A_{ij}\sin\left(k\theta + \varphi_{ik}\right) \tag{B.32a}$$

with the following coefficients:

$$A_{i0} = a_{i0} \tag{B.32b}$$

$$A_{ik} = \sqrt{{a_{ik}}^2 + {b_{ik}}^2} \tag{B.32c}$$

$$\varphi_{ik} = \mathrm{atan2}\left(a_{ik}, b_{ik}\right) \tag{B.32d}$$

Using Taylor expansions in terms of δ and ζ_f we obtain the following

$$A_{10} = \left(\frac{c_P T_{HL} - 2c_T\zeta_f \tan\left[\psi/2\right]}{T_{HL}}\right) r^2 \qquad + \mathcal{O}(\delta^2, {\zeta_f}^2, \delta\zeta_f), \tag{B.33a}$$

$$A_{11} = r \qquad + \mathcal{O}(\delta^2, {\zeta_f}^2, \delta\zeta_f), \tag{B.33b}$$

$$A_{12} = \frac{(\delta+\zeta_f)\left(c_P T_{HL} - 2c_T\zeta_f\tan\left[\psi/2\right]\right)}{2T_{HL}}\, r^2 \quad + \mathcal{O}(\delta^2, {\zeta_f}^2, \delta\zeta_f), \tag{B.33c}$$

which led to the approximations given by eq. (4.20), where we also considered $\psi = 0$.

B.2 Effect of Deviation of the Equilibrium from the Inflexion Point (ψ)

In the main text, we discussed the dynamics based on the vector field $\dot{r} = d\delta r + a_0 r^3$ (eq. (4.17a)) for $a_0 < 0$. In section 4.3.3, we showed that we indeed have $a_0 < 0$, if we assume $\psi = 0$. In this appendix, we investigate the general case, where $\psi \neq 0$. We first described how we obtained the evaporation rate equation and how we introduced ψ (see appendix B.2.1). We then explain what ψ means (a measure of the deviation of the equilibrium relative to the inflexion point of the wall temperature profile) and evaluate what values it can take, depending on $T_{g,sat,0}$, T_H and T_L (appendix B.2.2). We then evaluate the sign of a_0, as a function of ψ and other parameters (appendix B.2.3). Although we expect to have $a_0 < 0$ in typical conditions, we find that we can indeed have $a_0 > 0$ for large enough ψ. Finally, we study what the dynamics looks like when $a_0 > 0$ (appendix B.2.4).

B.2.1 Derivation of the Evaporation Rate Expression, With the Deviation Parameter ψ

Here, we describe the original expression from the evaporation rate from Tessier-Poirier et al. [112] (appendix B.2.1) and show how we obtain the new expression used here, which introduce ψ (appendix B.2.1).

Expression of the Evaporation Rate

The dimensionless evaporation rate $\dot{q}_3$ was derived in Tessier-Poirier et al. [112, Eq.(10b) p.10] as (we adapted the nomenclature to match the one used in the main text)

$$\dot{q}_3 = T_{HL} \arctan\left[-\left|\widetilde{T'_{wc}}\right| (q_1 - \widetilde{x_c}) \right] + \widetilde{C_{th}}. \tag{B.34}$$

In eq. (B.34), the parameters are the phase-change limit T_{HL}, the dimensionless wall axial temperature gradient at the inflexion point $\left|\widetilde{T'_{wc}}\right|$, the dimensionless position of the inflexion point relative to the equilibrium $\widetilde{x_c}$ and $\widetilde{C_{th}}$, a constant which represents the evaporation rate when the meniscus is at the inflexion point, when $q_1 = \widetilde{x_c}$. Those parameters are defined as

$$T_{HL} \equiv \frac{T_H - T_L}{\pi\ m_{g,0}\,\omega_n\ H_v\,R_{th}}, \tag{B.35a}$$

$$\left|\widetilde{T'_{wc}}\right| \equiv \left(\frac{\pi\ L_{g,0}}{T_{HL}}\right)\ |T'_{wc}|, \text{ where } |T'_{wc}| = \left.\frac{-dT_w}{dx}\right|_{x=x_c}, \tag{B.35b}$$

$$\widetilde{x_c} \equiv \left(\frac{1}{L_{g,0}}\right)\ x_c, \text{ where } x_c = \left(\frac{T_H - T_L}{\pi\,|T'_{wc}|}\right)\ \tan\left[\frac{\pi\left(T_{g,sat,0} - \frac{1}{2}\left(T_H + T_L\right)\right)}{T_H - T_L}\right], \tag{B.35c}$$

$$\widetilde{C_{th}} \equiv \frac{\frac{1}{2}\left(T_H + T_L\right) - T_{g,sat,0}}{m_{g,0}\,\omega_n\ H_v R_{th}}. \tag{B.35d}$$

The dimensionless axial temperature gradient at the equilibrium $\left|T'_{w,0}\right|$ is an important parameter, which can be expressed as a function of the gradient at the inflexion point as

$$\left|T'_{w,0}\right| \equiv \left.\frac{-dT_w}{dx}\right|_{x=0} = \frac{|T'_{wc}|}{1+\tan^2\left[\pi\left(T_{g,sat,0}-T_{w,avg}\right)/\left(T_H-T_L\right)\right]}. \tag{B.36}$$

Finally, note that linearization of eq. (B.34) leads to $\dot{q}_3 = -2\,\sigma\,q_1$ (eq. (4.9c)) where

$$\sigma \equiv \frac{1}{2}\,\frac{T_{HL}\left|\widetilde{T'_{wc}}\right|}{1+\left(\widetilde{x_c}\left|\widetilde{T'_{wc}}\right|\right)^2} = \frac{L_{g,0}\,\left|T'_{w,0}\right|}{2\,m_{g,0}\,\omega_n\,H_v\,R_{th}}, \tag{B.37}$$

the last equality involving dimensional quantities, obtained by substitution.

New Form for the Evaporation Rate

Here, we will show how to transform eq. (B.34) into the form given by eq. (4.7c). We prefer this latter form because it involves less parameters and those are easier to study. Setting $\dot{q}_3 = 0$, we find that

$$\left|\widetilde{T'_{wc}}\right|\widetilde{x_c} = \tan[-\widetilde{C_{th}}/T_{HL}] \tag{B.38}$$

Substitution of this into the equation for $\dot{q}_3$ eliminates the parameter $\widetilde{x_c}$, we have

$$\dot{q}_3 = T_{HL}\left(\arctan\left[-\left|\widetilde{T'_{wc}}\right|q_1 - \tan\left[\frac{\widetilde{C_{th}}}{T_{HL}}\right]\right] + \frac{\widetilde{C_{th}}}{T_{HL}}\right).$$

In a_0 (eq. (B.28)), the quantity $\widetilde{C_{th}}$ only appears in the ratio $2\widetilde{C_{th}}/T_{HL}$, as argument of cosine and sine functions. It therefore makes sense to define the quantity $\psi \equiv 2\widetilde{C_{th}}/T_{HL}$, which we use to eliminate $\widetilde{C_{th}}$, leading to

$$\dot{q}_3 = T_{HL}\left(\arctan\left[-\left|\widetilde{T'_{wc}}\right|q_1 - \tan\left[\frac{\psi}{2}\right]\right] + \frac{\psi}{2}\right).$$

Knowing that $\left|\widetilde{T'_{wc}}\right|$ is ultimately expressed in phase-change coefficient σ when the equation is linearized to $\dot{q}_3 = -2\,\sigma\,q_1$, it makes sense to replace it right away with σ. Substitution of $\left|\widetilde{T'_{wc}}\right|\widetilde{x_c} = -\tan[\psi/2]$ in eq. (B.37) gives

$$\sigma = \frac{1}{2}\,\frac{T_{HL}\left|\widetilde{T'_{wc}}\right|}{1+\tan^2[\psi/2]} = \tfrac{1}{2}\,\cos^2[\psi/2]\;T_{HL}\left|\widetilde{T'_{wc}}\right|, \tag{B.39}$$

where we use the trigonometric identity $1+\tan^2\theta = \sec^2\theta = 1/\cos^2\theta$. Solving eq. (B.39) for $\left|\widetilde{T'_{wc}}\right|$, we get $\left|\widetilde{T'_{wc}}\right| = 2\sigma/T_{HL}\,(\cos^2[\psi/2])$. Substitution of the results in the $\dot{q}_3$ equation

above, we obtain

$$\dot{q}_3 = T_{HL} \arctan\left[-\left(\frac{2\sigma}{T_{HL}\cos^2\left[\psi/2\right]}\right) q_1 - \tan\left[\frac{\psi}{2}\right]\right] + \frac{\psi}{2} T_{HL}, \tag{B.40}$$

which is eq. (4.7c) in the main text.

B.2.2 Studying the ψ Expression

In appendix B.2.2, we explain what ψ means physically. We also derive an expression of ψ in terms of $T_{g,sat,0}$, T_H and T_L. In B.2.2, we evaluate what values ψ can take.

ψ as a Measure of the Deviation of the Equilibrium from the Inflexion Point

Both $\widetilde{x_c}$ and $\widetilde{C_{th}}$ are dimensionless measures of the deviation of the equilibrium relative to the inflexion point. This is obvious for $\widetilde{x_c}$, since x_c is directly the distance between the equilibrium and the inflexion point. The quantity $\widetilde{C_{th}}$ is also a measure of the deviation since it is proportional to $\frac{1}{2}(T_H + T_L) - T_{g,sat,0}$, where $\frac{1}{2}(T_H + T_L)$ is the temperature at the inflexion point and where $T_{g,sat,0}$ is the saturation temperature, which is the temperature at the equilibrium (where $\dot{q}_3 = 0$). Thus, $\widetilde{C_{th}} \neq 0$ only when the equilibrium is away from the inflexion point, when $T_{g,sat,0} \neq \frac{1}{2}(T_H + T_L)$. In fact, we see from eq. (B.35c) that x_c is also expressed as a function of $\frac{1}{2}(T_H + T_L) - T_{g,sat,0}$. Now, the new quantity ψ, which we use to eliminate both $\widetilde{x_c}$ and $\widetilde{C_{th}}$, also expresses the deviation of the equilibrium relative to the inflexion point. Given $\psi = 2\widetilde{C_{th}}/T_{HL}$, ψ is also proportional to $\frac{1}{2}(T_H + T_L) - T_{g,sat,0}$ and the conclusions for $\widetilde{C_{th}}$ above also hold for ψ.

Let's now express ψ as a function of the temperature T_H, T_L and $T_{g,sat,0}$. Starting from $\psi \equiv 2\widetilde{C_{th}}/T_{HL}$, after substitution of $\widetilde{C_{th}}$ (eq. (B.35d)) and T_{HL} (eq. (B.35a)), we get

$$\psi = \frac{2\pi}{(T_H - T_L)} \left(\frac{T_H + T_L}{2} - T_{g,sat,0}\right).$$

Additional manipulations leads to

$$\psi = \pi \left(\frac{T_H + T_L}{T_H - T_L} - \frac{2\,T_{g,sat,0}}{T_H - T_L}\right),$$

where ψ depends on three parameters, T_H, T_L and $T_{g,sat,0}$. Dividing numerator and denominator of each terms by T_H, we obtain

$$\psi = \pi \left(\frac{1 + T_L/T_H}{1 - T_L/T_H} - \frac{2\,T_{g,sat,0}/T_H}{1 - T_L/T_H}\right) \qquad \text{with: } 0 < \left(\frac{T_L}{T_H}\right) < \left(\frac{T_{g,sat,0}}{T_H}\right) < 1 \tag{B.41}$$

which now depends only on two groups of parameters, the ratios T_L/T_H and $T_{g,sat,0}/T_H$. The inequalities above are obtained by considering that $0 < T_L < T_{g,sat,0} < T_H$ (and temperature expressed in kelvin so always positive). The equation (B.41) for ψ corresponds to eq. (4.8c) in the main text.

Values ψ Takes, as Function of $T_{g,sat,0}$, T_H and T_L

We now want to investigate what values can ψ take. We will find that ψ ranges between $-\pi$ (when $T_{g,sat,0} = T_H$, the equilibrium is as far as possible in the heat source region) and $+\pi$ (when $T_{g,sat,0} = T_L$, the equilibrium is as far as possible in the heat sink region).

fig. B.1 shows ψ/π values as a surface along the ratios T_L/T_H and $T_{g,sat,0}/T_H$. Given the inequalities $0 < T_L < T_{g,sat,0} < T_H$, we have boundaries in fig. B.1. First, the condition $T_{g,sat,0} = T_H$ (the equilibrium is far into the heat source) gives the boundary $T_{g,sat,0}/T_H = 1$ which is a straight horizontal line in fig. B.1, and we find that $\psi = -1$ (eq. (B.41)) there. Second, the condition $T_{g,sat,0} = T_L$ (the equilibrium is far into the heat sink) gives the boundary $T_{g,sat,0}/T_H = T_L/T_H$ which gives the diagonal line in fig. B.1, and we find that $\psi = +1$ (eq. (B.41)) there. The inequalities $0 < T_L/T_H < 1$ and $0 < T_{g,sat,0}/T_H < 1$ (eq. (B.41)) close the surface in fig. B.1.

It is useful to define an additional line corresponding to the case where the equilibrium is perfectly centered on the inflexion point ($x_c = 0$). We then have $T_{g,sat,0} = (T_H + T_L)/2$ and one can easily verify that $\psi = 0$ as expected, from eq. (B.41). Also, dividing $T_{g,sat,0} = (T_H + T_L)/2$ by T_H, we find that

$$(T_{g,sat,0}/T_H) = \tfrac{1}{2}\,(T_L/T_H) + \tfrac{1}{2} \qquad \text{for } \psi = +\pi/2, \tag{B.42}$$

which corresponds to a function of the form $y = mx + b$ in the graph fig. B.1. Additional isolines (for constant ψ values) can be added to the graph by solving eq. (4.8c) for $T_{g,sat,0}/T_H$, we obtain

$$\frac{T_{g,sat,0}}{T_H} = \left(\frac{1 + (\psi/\pi)}{2}\right)\frac{T_L}{T_H} + \frac{1 - (\psi/\pi)}{2}, \tag{B.43}$$

which clearly produce isolines of the form $y = mx + b$ in fig. B.1. For $\psi = \pm\pi/2$, we have

$$(T_{g,sat,0}/T_H) = \tfrac{3}{4}\,(T_L/T_H) + \tfrac{1}{4} \qquad \text{for } \psi = +\pi/2, \tag{B.44a}$$
$$(T_{g,sat,0}/T_H) = \tfrac{1}{4}\,(T_L/T_H) + \tfrac{3}{4} \qquad \text{for } \psi = +\pi/2, \tag{B.44b}$$

which are also shown in fig. B.1.

B.2.3 Sign of a_0

Here, we evaluate the sign of a_0 in the general case where $\psi \neq 0$. First, consider the phase-change nonlinearity only (appendix B.2.3). For the pressure nonlinearity only, a_0 does not depend on ψ and we have $a_0 < 0$ always. We then study the sign of a_0 for both nonlinearities (appendix B.2.3).

Phase-Change Nonlinearity

For the phase-change nonlinearity only ($c_P = 0$, $c_T = 1$) we have $a_0 = a_{0,T}$ (eq. (B.28)). We clearly have from eq. (B.28) that $a_{0,T} > 0$ only if $1 + {\zeta_f}^2 \cos[\psi] < 0$ [1]. Two necessary conditions for having $a_{0,T} > 0$ are having $\zeta_f > 1$ (however, ζ_f is usually much smaller than

1. The $1 + \cos[\psi]$ in the denominator does not change the sign of $a_{0,T}$ because $\cos[\psi] > -1$, since $T_{g,sat,0} < T_H$

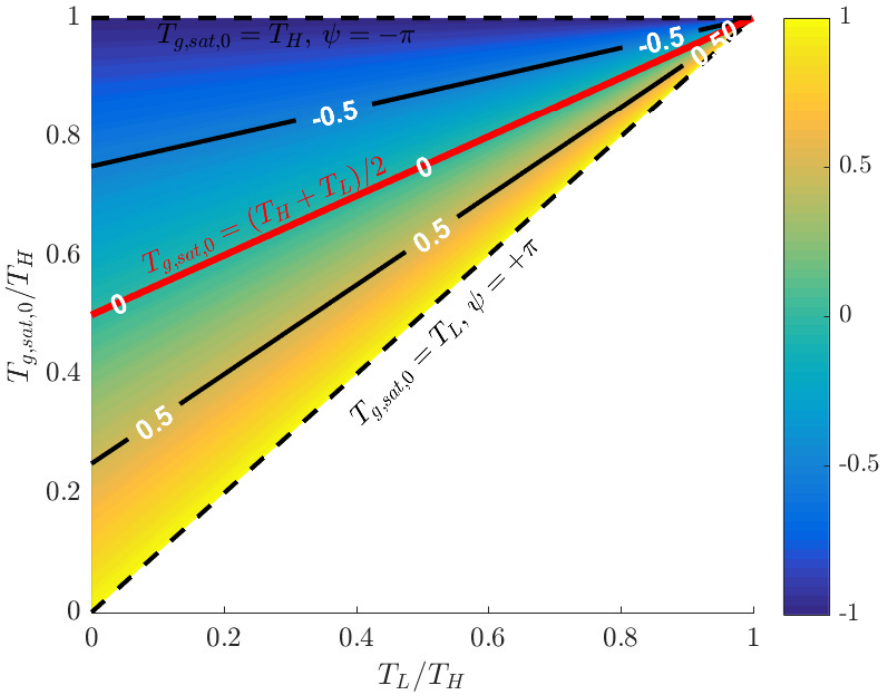

Figure B.1 (Color online). ψ/π as a surface function of parameters T_L/T_H and $T_{g,sat,0}/T_H$; The lower right corner is not allowed because we must have $T_{g,sat,0} > T_L$; we find that $-1 < (\psi/\pi) < +1$.

one) and having either $\psi < -\pi/2$ or $\psi > +\pi/2$, so that the equilibrium is far enough from the inflexion point. Solving $1 + {\zeta_f}^2 \cos[\psi] = 0$ gives the curves [2] $\zeta_f = +\sqrt{-1/\cos[\psi]}$ where $a_{0,T} = 0$ and which delimits regions of different signs for $a_{0,T}$. Those boundaries are the same whatever the value of T_{HL} is.

We plot those curves in fig. B.2, with ζ_f and ψ as the axis. The region in the center corresponds to $a_{0,T} < 0$. There are two regions where $a_{0,T} > 0$ in the top corners, delimited by the curves $\zeta_f = +\sqrt{-1/\cos[\psi]}$.

Pressure and Phase-Change Nonlinearities

We now compute the boundaries $a_0 = 0$ for both pressure and phase-change nonlinearities ($c_P = 1$, $c_T = 1$) numerically. We find that they now depend on the value of T_{HL} (see fig. B.3). From eq. (B.28), we see that $a_{0,T} \propto 1/{T_{HL}}^2$, $a_{P,T} \propto 1/T_{HL}$ and $a_{0,P}$ is not a function of T_{HL}. Thus, for very small T_{HL}, the term $a_{0,T}$ dominates and the boundaries (fig. B.3a) look very much like the one for the phase-change only (fig. B.2). As we increase T_{HL}, the boundaries move, the region for $a_0 > 0$ in the left corner moves to the right, the one on the right corner moves to the left and a new one appears in the bottom right (see fig. B.3a to B.3c). The two regions for $a_0 > 0$ in the right eventually merge (fig. B.3c to B.3d). As T_{HL} is further increase, the $a_{0,P}$ terms starts to dominate, so the regions where $a_0 > 0$ must eventually disappear. This is what we observe as both regions for $a_0 > 0$

2. the solution $\zeta_f = -\sqrt{-1/\cos[\psi]}$ is discarded, since $\zeta_f > 0$.

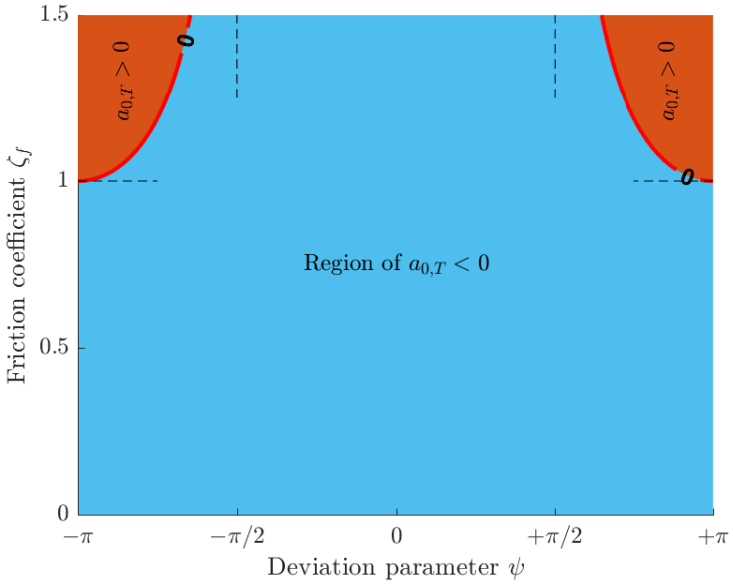

Figure B.2 (Color online). Boundaries for $a_{0,T} = 0$ (eq. (B.28)); $a_{0,T} < 0$ in the blue region and $a_{0,T} > 0$ in the orange region.

move out of the graph (fig. B.3d to B.3f). The region for $a_0 < 0$ eventually takes all the available space for large T_{HL}.

B.2.4 Dynamics for $a_0 > 0$

Let's now discuss how the dynamics is affected by having a positive term a_0 in the vector field $\dot{r} = d\delta r + a_0 r^3$ (eq. (4.17a)). For $a_0 < 0$, the function $\dot{r}(r)$ was bending downwards. Now, for $a_0 > 0$, the function $\dot{r}(r)$ curves upwards (see fig. B.4a), the nonlinearities are not saturating, but instead, tends to increase $\dot{r}$. The stability of the equilibrium point at $r = 0$ is still controlled by δ. Although the slope at $r = 0$ is given by $d\delta$, the sign of the slope only depends on δ because $d > 0$ always (so $d\delta > 0$ and $\delta > 0$ means the same thing as well as $d\delta < 0$ and $\delta < 0$). For $d\delta > 0$, the amplitude grows faster than the linear case ($\dot{r}$ is larger for $a_0 > 0$) and without bounds, the system never reaches a limit cycle. For $d\delta < 0$, the equilibrium is stable, but an unstable fixed point (corresponding to a unstable limit cycle in either the z_i or the q_i variables) exists at $r = r_{LC}$. For $r < r_{LC}$, the amplitude decreases toward $r = 0$ and for $r > r_{LC}$, increases without bounds. As δ goes from positive to negative, the unstable limit cycle is created, a process called a subcritical Poincaré-Andronov-Hopf bifurcation.

Now, we have to keep in mind that the full vector field also includes higher order terms ($\mathcal{O}(r^5)$, see eq. (B.26)). The equilibrium stability is still controlled by δ. The truncated form $\dot{r} = d\delta r + a_0 r^3$ is sufficient to predict the limit cycle bifurcation but higher order terms are however required to predict the dynamics further. In fig. B.4b, we show how the vector fields $\dot{r}$ can look like when a negative quintic term is included. At small r, the vector fields looks like fig. B.4a, but differs qualitatively for larger r. At $d\delta$ negative and large enough, there is only a stable equilibrium (see $\dot{r} = -3r + r^3 - 0.2r^5$ curve). At $d\delta$ negative but small enough, there is one unstable limit cycle but also one larger stable limit cycle, due to the quintic term (see curve $\dot{r} = -r + r^3 - 0.2r^5$). At positive $d\delta$, there is now

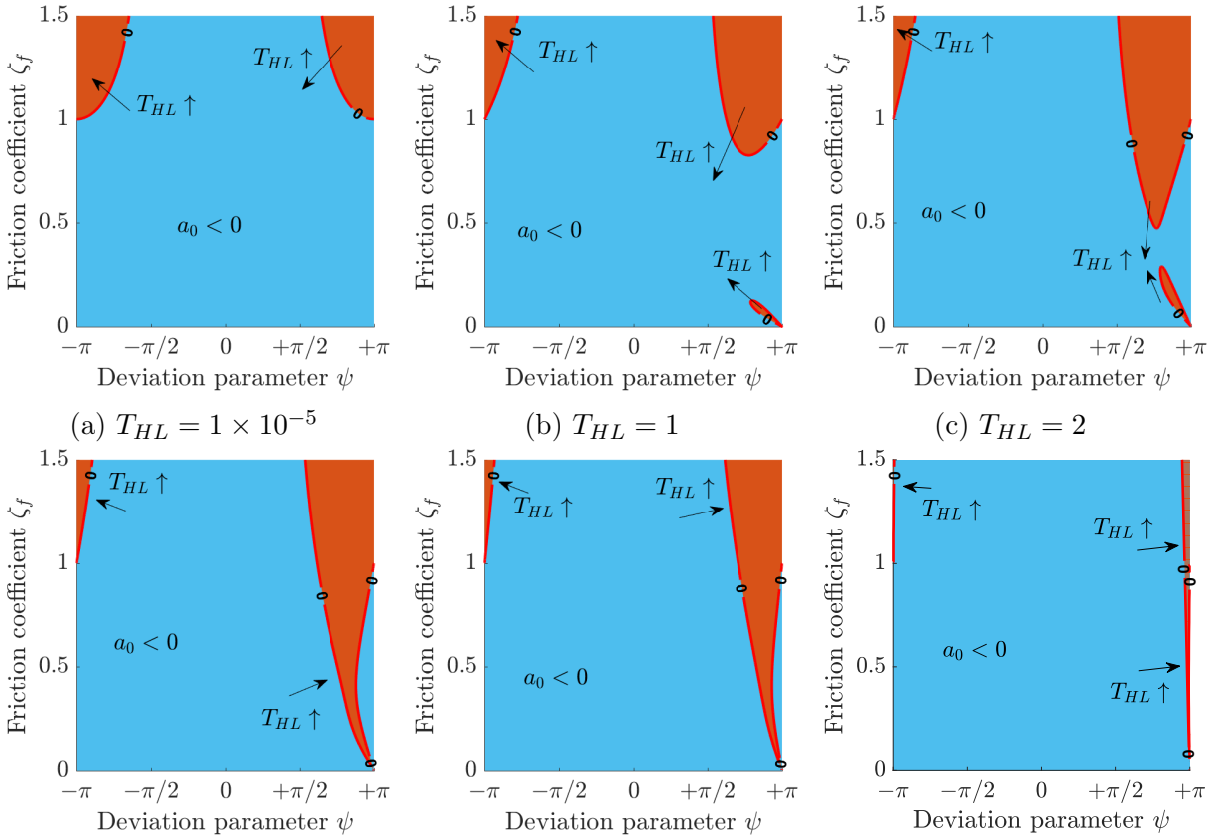

(a) $T_{HL} = 1 \times 10^{-5}$ (b) $T_{HL} = 1$ (c) $T_{HL} = 2$

(d) $T_{HL} = 3$ (e) $T_{HL} = 5$ (f) $T_{HL} = 50$

Figure B.3 (Color online). Boundaries for $a_0 = 0$ (eq. (B.28)), for both pressure and phase-change nonlinearities ($c_P = 1$, $c_T = 1$), are computed numerically for increasing T_{HL} for (a) to (f); $a_0 < 0$ in the blue region and $a_0 > 0$ in the orange region.

only one large stable limit cycle (see curve $\dot{r} = r + r^3 - 0.2r^5$). Thus, adding a quintic term may prevent the amplitude from growing without bounds, by creating a stable limit cycle surrounding the unstable limit cycle. Let's note that there is still the creation of an unstable limit cycle as δ becomes negative, through a subcritical Poincaré-Andronov-Hopf bifurcation. However there is an additional, global, bifurcation that can occur. For $d\delta$ negative and sufficiently small (curve $\dot{r} = -3r + r^3 - 0.2r^5$), increasing $d\delta$ leads to the creation of an unstable limit cycle and a larger stable limit cycle (curve $\dot{r} = -r + r^3 - 0.2r^5$). This process is called a a saddle-node bifurcation of cycles (see Strogatz [107, Subcritical Hopf Bifurcation p.251, Saddle-node Bifurcation of Cycles p.261]).

The behavior we observe numerically for $a_0 > 0$ qualitatively corresponds to the behavior with a negative quintic term described above. fig. B.5 shows numerical simulations of eq. (4.14) for various initial conditions. In fig. B.5a, $d\delta$ is small and negative, the dynamics suggest the existence of a stable equilibrium, an unstable limit cycle and a larger stable limit cycle, just like the curve $\dot{r} = -r + r^3 - 0.2r^5$ in fig. B.4b. In fig. B.5b, $d\delta$ is positive,

the dynamics suggest the existence of a unstable equilibrium, and one large and stable limit cycle, just like the curve $\dot{r} = r + r^3 - 0.2r^5$ in fig. B.4b.

Let's now provide a few final remarks on the vector field with a negative quintic term as shown in fig. B.4b. If the system behaves as the curve $\dot{r} = -r+r^3-0.2r^5$, the unstable limit cycle acts as a barrier: self-oscillations are possible even though the equilibrium is stable, but an initial push beyond the unstable limit cycle is needed. Also, the system described by the vector field with a negative quintic term has an hysteresis: as $d\delta$ is increased above 0, large oscillations starts (given a small perturbation) but can only be turned off by bringing $d\delta$ below some negative value. The described behavior with a negative quintic term could be made possible by other nonlinearities than the one considered in this paper. For example, having a phase-change which suddenly increases when the amplitude is large enough could produce such behavior.

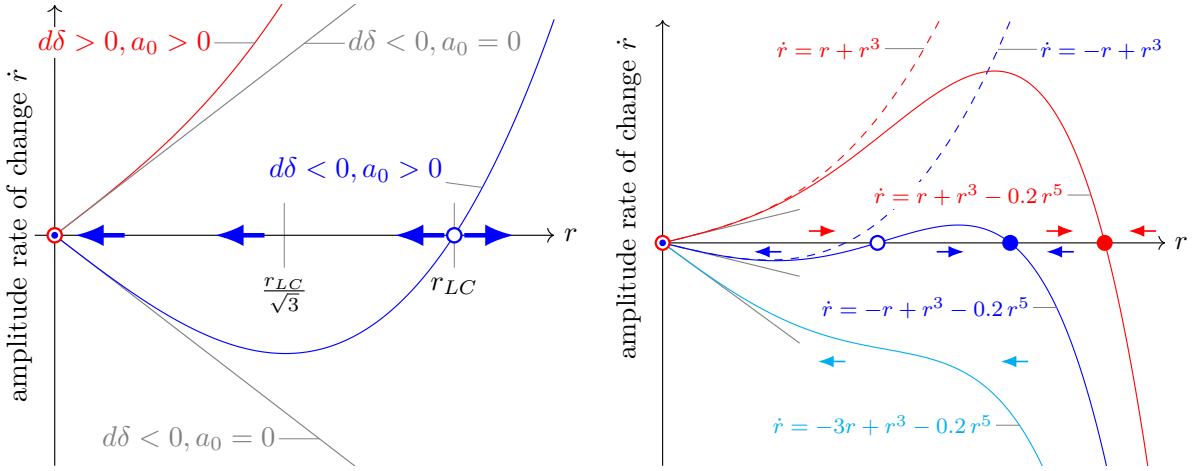

(a) (b)

Figure B.4 (Color online). (a)Vector field $\dot{r}(r)$ from $\dot{r} = d\delta r + a_0 r^3$ (eq. (4.17a)), for $a_0 = 0$ or $a_0 > 0$. For $d\delta > 0$ and $a_0 > 0$, the amplitude grows faster than in the linear case and do not saturate. For $d\delta < 0$ and $a_0 > 0$, an unstable fixed point exists at $r = r_{LC}$, which corresponds to an unstable (repulsive) limit cycle in the z_1 and z_2 variables. (b) Vector fields $\dot{r}(r)$ including a negative cubic term; a stable limit cycle may exists.

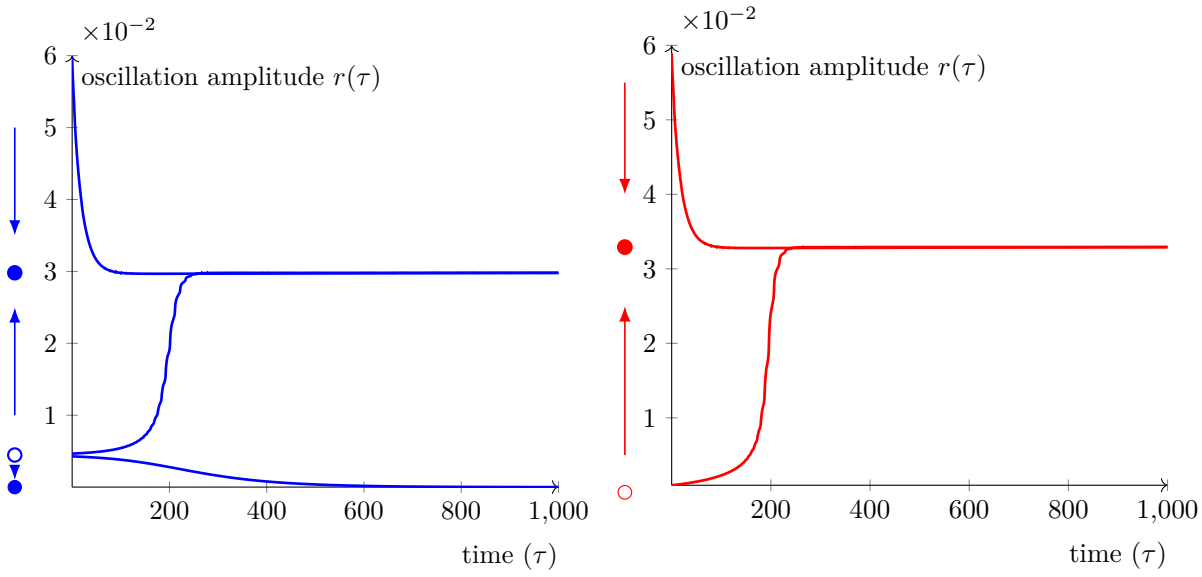

(a) $\Pi = 0.95$ (b) $\Pi = 1.05$

Figure B.5 (Color online). Oscillation amplitude r (based on the amplitude in q_1) from numerical simulations of eq. (4.14), for various initial conditions and for $c_P = c_T = 1$, $\zeta_f = 1.5$, $T_{HL} = 0.1$ and $\psi = 0.9\pi$. The results show similar behavior as in fig. B.4b. (a) $\Pi = 0.95$ (so $d\delta = -0.0231$), for $r(\tau = 0)$ small enough r decreases toward 0, but for $r(\tau = 0)$ large enough, r increases or decreases towards a constant value. This suggests the existence of a small unstable limit cycle surrounded by a larger stable limit cycle. (b) $\Pi = 1.05$ (so $d\delta = +0.0231$), r increases or decreases towards a constant value. This suggests the existence of a stable limit cycle.

APPENDIX C

Appendix to Chapter 5

Here, we perform averaging on the system of eq. (5.1), for the phase-change nonlinearity only, so $c_P = 0$ and $c_T = 1$. The goal is to obtain a solution valid everywhere. The following steps are carried on in a Matlab program. The averaging technique we used here is mostly based on [51, 17, 91].

C.1 System of Equations

Starting with eq. (5.1), the system is in the form:

$$\begin{aligned}\dot{q}_1 &= f_1(q_1, q_2, q_3),\\ \dot{q}_2 &= f_2(q_1, q_2, q_3),\\ \dot{q}_3 &= f_3(q_1, q_2, q_3),\end{aligned}$$

In Matlab:

```
%% Variables and system of equations
```

⋮

```
f(1,:) = q2;
f(2,:) = ( 1-cP*(q1/(1+q1)) )*(-q1+q3) - 2*zf*q2;
f(3,:) = -2*s*(1-cT)*q1 +...
    cT*Thl*( atan( -(2*s/(Thl*cos(psi/2)^2))*q1 - tan(psi/2) ) + psi/2);
f=subs(f,[q1,q2,q3],[x1,x2,x3]);
```

We then assume $\psi = 0$, and $c_P = 0$, $c_T = 1$ (phase-change nonlinearity only). We also replace the parameter σ by δ and adds $\dot{\delta} = 0$ as a 4th differential equation (δ now being considered an additional phase-space variable; trick for center manifold reduction).

```
% psi=0 for now :
f=simplify(subs(f,psi,0));

% Set cp and ct as following, for now :
f=simplify(subs(f,[cP,cT],[0,1]));
warning('we fix cP and cT for now');input('')
%%%%%%%%%%%%%%%%%%%%%%%%%%%%%%%%%%%%%%%%%%%%%%%%%%%%%%%%%%%%%%%%%%%%%%%%%%%%%%%

% We add d as a new phase-space variable.

f=subs(f,s,d+zf);
```

```
% We add d(d)/dt as new equation with the following new line in
% the vector field :

f(4,:) = 0;
```

C.2 Alignment Along the Eigenbasis

We perform a linear transformation such that we obtain a new system, aligned with the eigenbasis.

```
%% Standard form

q = [q1;q2;q3];

% We first compute the Jacobian. The vector of phase-space variables is :
% xx = [q1;q2;q3;d] ;
xx = [x1;x2;x3;d] ;

% The jacobian is :
Df = simplify( jacobian(f,xx) )

% Evaluated at the equilibrium (which is 0) :
Df0 = simplify(subs(Df,xx,zeros(size(xx))))

% We have the system dx/dt = f(x) = Ax + F(x) with :
A = Df0;
F = simplify(f-A*xx);

% We verify that F(0)=0 and DF(0)=0 :
F0  = simplify(subs(F,xx,zeros(length(xx),1)));
DF  = simplify( jacobian(F,xx) );
DF0 = simplify(subs(DF,xx,zeros(length(xx),1)));

% We now need to find the eigenvalues and eigenvectors of A. To this end,
% we use the built-in function eig.
syms L1 L2 L3
L = eig(A);

[eigvecA, eigvalA,eigindA] = eig(A)
eigvec = eigvecA;

% Scaling of the eigenvectors.
% Eigenvectors are defined up to a constant factor. We therefore have the
% freedom to multiply each eigenvectors by some non-zero constant.

bMat = diag([1,2*zf,2*zf,1]);% For Basic
```

```
eigvec = eigvecA*bMat;

%%%%%%%%%%%%%%%%%%%%%%%%%%%%%%%
% We find the eigenvector corresponding to positive imaginary part (this
    is
% how the matrix P is defined, with L(j)=a(j)+ i b(j).

imagPosInd = find(simplify(sum(eigvalA,1)==1i));
if length(imagPosInd)~=1; error('assume one and only one +1i'); end

% Transformation T (Eq.2.21 p.17/124 and Eq.4.4 p.32/124)
assume([ 0 < zf, in(zf, 'real'), zf < 1, in(d, 'real')]);
Ta = [eigvec(:,1),imag(eigvec(:,imagPosInd)),real(eigvec(:,imagPosInd)),
    eigvec(:,4)]
Tainv = inv(Ta);

%%%%%%%%%%%%%%%%%%%%%%%%%%%%%%%



% Validation of the T transformation
J = simplify(Tainv*A*Ta)

% Validate eigenvalues and eigenvectors of J
[eigJvec, eigJval,eigJind] = eig(J)

% We now apply the T Transformation to F also.
syms y1 y2 y3 y4
yy = [y1;y2;y3;y4] ;
x_y = Ta*yy;

y_x = simplify(Tainv*xx)
G_x = simplify(Tainv*F)
G_y = simplify(subs(G_x,xx,x_y))
g   = J*yy + G_y

% Inspection (J and eigJval) gives us the following :
pline = [1]; %   parameters lines
cline = [2,3]; % center lines (excluding parameters lines)
sline = [4]; %   stable lines

yp = yy(pline)

% rotational part :
yc = yy(cline)
yc_x = y_x(cline)
```

```
Jc = J(cline,cline)
Gc = G_y(cline)
gc = Jc*yc + Gc;

% stable part :
ys = yy(sline)
ys_x = y_x(sline)
Js = J(sline,sline)
Gs = G_y(sline)
gs = Js*ys + Gs;

% Validate eigenvalues and eigenvectors of Jc
[eigJcvec, eigJcval,eigJcind] = eig(Jc)
% real parts of the eigenvalues effectively == 0.

% We verify that Gc(0)=0,Gs(0)=0, DGc(0)=0 and DGs(0)=0.

Gc0  = simplify(subs(Gc,yy,zeros(length(yy),1)));
Gs0  = simplify(subs(Gs,yy,zeros(length(yy),1)));
DGc  = simplify( jacobian(Gc,yc) );
DGc0 = simplify(subs(DGc,yy,zeros(length(yy),1)));
DGs  = simplify( jacobian(Gs,ys) );
DGs0 = simplify(subs(DGs,yy,zeros(length(yy),1)));
```

We get a system of the following form:

$$\dot{y}_{c,1} = g_{c,1}(\delta = y_1, y_{c,1} = y_2, y_{c,2} = y_3, y_s = y_4) \tag{C.1}$$
$$\dot{y}_{c,2} = g_{c,2}(\delta = y_1, y_{c,1} = y_2, y_{c,2} = y_3, y_s = y_4) \tag{C.2}$$
$$\dot{y}_s = g_s(\delta = y_1, y_{c,1} = y_2, y_{c,2} = y_3, y_s = y_4) \tag{C.3}$$

The third dimension y_s is linearly stable (decreases towards 0 for the linearized system). We cannot simply take $y_s = 0$ for the nonlinear system, a priori, though.

C.3 Center Manifold Reduction

So, we use center manifold reduction here, to obtain an approximation h of y_s, with h a function of δ, $y_{c,1}$ and $y_{c,2}$. This allow to reduce the system to only two dimensions, while ensuring that the topology is preserved. We must first obtain the expression for h.

```
% We must now find the values of the coefficient. For this, we can use
% Taylor expansions (see CenterManifold_NormalForm_PTNL_V2B). Here, we
% instead taylor expand N and use the function coeffs to solve for the
% prefactors of each powers.

cvec2  = [c1,c2,c3,c4,c5,c6];
N2tay = simplify(taylor(N2,[y1,y2,y3],[0,0,0],'Order',3));
```

```
[N2prefactors,N2powers] = coeffs(N2tay,[y1,y2,y3]);
cStruct2S = solve(N2prefactors==0,cvec2);

% We now convert the structure cStruct2S into a vector cvec2S
names = fieldnames(cStruct2S);
for ii=1:length(names)
eval(['cvec2S(ii)=cStruct2S.' names{ii} ';']);
end
```

However, in order to apply averaging, we will prefer to avoid using this approximation and simply take $h = 0$. As explained later one, we will find that taking $h = 0$ is simpler, more accurate and preserves the topology of the system, for the specific case studied. So, in order to control the value of h, we multiply each coefficients by a new parameter c_h. For $c_h = 1$, h is given by the approximation obtained by the center manifold reduction while, for $c_h = 0$, we simply have $h = 0$.

```
% introducing a coefficient to control h or h=0. ch=1 or ch=0.
% We do it here instead of in h, because finding the c's would cancel ch
% (because the c's are found to match N...)
syms ch
cvec2S = ch*cvec2S;
%%%%%%%%%%%%%%%%%%%%%%%%%%%%%%%%%%%%%%%%%%%%%%%%%%%%%%%%%%%%%%%%%%%%%%%%%%%%%%%
% Substitution in h gives hS :
% hS = simplify(subs(h,[c1,c2,c3,c4,c5,c6],[c1S,c2S,c3S,c4S,c5S,c6S]));
h2S = simplify(subs(h2,cvec2,cvec2S));
```

The next step is to substitute y_s by h in the vector field.

```
%% 2D equations
% We can now obtain a reduced velocity-field. We substitute h in the first
% two equations of Dy. Those two equations a 2D velocity-field for y1 and
% y2.

% The center manifold definition gives ys = h(yc,yp). This can be used to
% in the vector field of yc which is now independent of the others. We
   also
% replace yp=y1 by its expression, the parameter d.
Gc_h = simplify(subs(Gc,ys,h2));
Gc_h = simplify(subs(Gc_h,y1,y_x(1))); % y1->d
Gc_h = simplify(subs(Gc_h,cvec2,cvec2S));

gc_h = simplify(subs(gc,ys,h2));
gc_h = simplify(subs(gc_h,y1,y_x(1))); % y1->d
gc_h = simplify(subs(gc_h,cvec2,cvec2S));
```

We get a now two-dimensional system of the following form:

$$\dot{y}_{c,1} = g_{c,1}(\delta, y_{c,1}, y_{c,2}, y_s = h(\delta, y_{c,1}, y_{c,2}))$$
$$\dot{y}_{c,2} = g_{c,2}(\delta, y_{c,1}, y_{c,2}, y_s = h(\delta, y_{c,1}, y_{c,2}))$$

C.4 Transformation into Polar Coordinates

We now introduce the following definitions:

$$\begin{bmatrix} y_{c,1} \\ y_{c,2} \end{bmatrix} = \begin{bmatrix} r\ \cos(\theta) \\ r\ \sin(\theta) \end{bmatrix} \tag{C.4}$$

Such that the variables $y_{c,1}$ and $y_{c,2}$ are replaced by the variables r and θ. There are two ways to think about the above transformation, and both will be useful.

1) Solution of the linear system.
Equation (C.4), where $\theta = \omega\tau + \varphi$, with r and φ constants defined by the initial conditions, is actually the solution of $\dot{\boldsymbol{y}}_c = \boldsymbol{g}_c$ once linearized (Jordan form). Thus, simply taking r and φ as now function of time as a solution of the nonlinear case is the method of variations of parameters. One than have to solve for $r(\tau)$ and $\varphi(\tau)$ (one may consider θ as the variable instead of φ and solve for $\theta(\tau)$ first, then solve for $\varphi(\tau)$ given $\theta = \omega\tau + \varphi$).

2) Change of coordinates, from cartesian to polar.
In our case, we care mostly about the oscillations amplitude. Thus, eq. (C.4) is simply a transformation from cartesian coordinates $(y_{c,1}, y_{c,2})$ to polar coordinates (r, θ), where r is the oscillations amplitude. Thus, we note that no approximations have been made yet. The system is 2D and was defined by a point in phase-space given by cartesian coordinates $(x = y_{c,1}, y = y_{c,2})$. We can define that point location exactly by polar coordinates instead. Of course, since we have a dynamical system, that point will move in time. This means that r and θ must be allowed to be functions of time τ in general. The movement of the point is given by the differential equations. The differential equations in cartesian coordinates can be transformed into polar coordinates leading to:

$$\begin{bmatrix} \dot{r} \\ \dot{\theta} \end{bmatrix} = \begin{bmatrix} +\cos(\theta) & +\sin(\theta) \\ -\frac{1}{r}\sin(\theta) & +\frac{1}{r}\cos(\theta) \end{bmatrix} \begin{bmatrix} \dot{y}_{c,1}\,(y_{c,1} = r\ \cos(\theta), y_{c,2} = r\ \sin(\theta)) \\ \dot{y}_{c,2}\,(y_{c,1} = r\ \cos(\theta), y_{c,2} = r\ \sin(\theta)) \end{bmatrix} \tag{C.5}$$

Those differential equations describes how the amplitude r and the angle θ vary over time. One now wish to find the solution of the system, meaning expressions for $r(\tau)$ and $\theta(\tau)$ in terms of the parameters and the independent variable τ. We do not yet have this solution.

Those operations are carried on in the Matlab program:

```
%% Polar coordinates and epsilon scaling
% we have rdot = R(...), theta and ydot = Y(...).
syms r th

% substitution, which gc_h (from CM reduction)
```

```
gr_rth = subs(gc_h,[yc(1),yc(2)],[r*cos(th),r*sin(th)]);

% Vector rdot; thetadot
rthdot = [cos(th) , sin(th) ; -1/r*sin(th) , +1/r*cos(th)] * gr_rth;
```

C.4.1 Introduction of a Small Parameter ε

Periodic averaging applies to system of the form $\dot{\boldsymbol{x}} = \varepsilon \boldsymbol{f}(\boldsymbol{x}, t)$, for $\varepsilon \ll 1$ and where $\boldsymbol{f}$ is T-periodic in t. Averaging works well here because the variables $\boldsymbol{x}$ vary slowly compared to the fast T time scale. Problems of the form $\dot{\boldsymbol{x}} = \boldsymbol{f}^0(\boldsymbol{x}, t) + \varepsilon \boldsymbol{f}^{[1]}(\boldsymbol{x}, t)$, $\boldsymbol{x}(t_0) = \boldsymbol{a}$, where $\boldsymbol{f}^0$ is the linear part and the ε term is a perturbation can be brought in the required form $\dot{\boldsymbol{x}} = \varepsilon \boldsymbol{f}(\boldsymbol{x}, t)$ given the appropriate transformation.

In our case however, there is no parameter chosen as ε already, but we can introduce a ε as done by Chow and Mallet-Paret [17, p.4,12]. To do so, for a given parameter or variable x, we will make the substitution $x = \varepsilon\, x^\star$, so x can be considered small by assuming ε small and $x^\star$ as $\mathcal{O}(1)$.

So, in our case, we recall that having r a constant and $\theta = \omega\tau + \varphi$ with ω a constant, so $\dot{r} = 0$ and $\dot{\theta} = \omega$, means that the system is linear (see discussion above). So, we would like to have $\dot{r} = \mathcal{O}(\varepsilon)$ and $\dot{\theta} = \Omega(\tau) = \omega + \mathcal{O}(\varepsilon)$ in which case we have a perturbation of the linear case. Also, this means that r and Ω (and φ) vary slowly compared to the oscillations time scale.

In order to have the amplitude varying slowly, it make sense to consider a small δ (recall that the linear solution is proportional to $e^{\delta\tau}$, for δ small, so the amplitude vary slowly for δ small), so we introduce $\delta = \varepsilon\, \delta^\star$, where ε is small and $\delta^\star$ is $\mathcal{O}(1)$. Doing so, we get $\dot{r} = \mathcal{O}(1) + \mathcal{O}(\varepsilon)$, so $\dot{r} \neq 0$ for $\varepsilon = 0$. Thus, assuming δ small is not enough.

```
% Only considering de small is not enough:
% simplify(taylor(subs(rthdot,[d],ep*de),ep,'Order',1))
% simplify(subs(subs(rthdot,[d],ep*de),ep,0))
```

We then also consider small amplitude r, so $r = \varepsilon r^\star$. So, we have the following substitutions:

$$\delta = \varepsilon \delta^\star \tag{C.6a}$$

$$r = \varepsilon r^\star \tag{C.6b}$$

which transforms the following differential equations (where R and Ω are the vector fields):

$$\begin{bmatrix} \dot{r} \\ \dot{\theta} \end{bmatrix} = \begin{bmatrix} R(d, r, \theta) \\ \Omega(d, r, \theta) \end{bmatrix} \tag{C.7}$$

into:

$$\begin{bmatrix} \dot{r^\star} \\ \dot{\theta} \end{bmatrix} = \begin{bmatrix} R^\star(\varepsilon, \delta^\star, r^\star, \theta) \\ \Omega^\star(\varepsilon, \delta^\star, r^\star, \theta) \end{bmatrix}, \text{ with: } \begin{bmatrix} R^\star \\ \Omega^\star \end{bmatrix} = \begin{bmatrix} \frac{1}{\varepsilon} R(\delta \to \varepsilon\delta^\star, r \to \varepsilon r^\star, \theta) \\ \Omega(\delta \to \varepsilon\delta^\star, r \to \varepsilon r^\star, \theta) \end{bmatrix} \tag{C.8}$$

In Matlab:

```
% with r=ep*rS, d=ep*dS,
% and dr/dt= ep*drS/dt -> drS/dt=(1/ep)*dr/dt and....
% we have :
rthdote = diag([1/ep,1])*subs(rthdot,[r,d],ep*[rS,dS]);
rthdote = collect(rthdote,ep);% collect seems needed to cancel the
   epsilons

% Verification for averaging:
% For small ep, we have rdot=O(ep) and thetadot=1+O(ep).
collect(simplify(taylor(rthdote,ep,'Order',2)),ep)
% gives:
% ((de*re*(cos(2*th) + 2*zf*sin(2*th) + 1))/(4*zf^2 + 1))*ep
% ((2*de*zf - de*sin(2*th) + 2*de*zf*cos(2*th))/(4*zf^2 + 1))*ep + 1

% for ep=0, we have rdot=0, thetadot=1.
simplify(limit(rthdote,ep,0,'right')) %gives [0;1]
```

We find that a Taylor expansion of the vector field in terms of ε (equivalent to considering both δ and r small) leads to (following Chow and Mallet-Paret [17] notation):

$$\begin{bmatrix} \dot{r^\star} \\ \dot{\theta} \end{bmatrix} = \begin{bmatrix} \varepsilon R_1^\star(\delta^\star, r^\star, \theta) + \mathcal{O}(\varepsilon^2) \\ \omega + \varepsilon\Omega_1^\star(\delta^\star, r^\star, \theta) + \mathcal{O}(\varepsilon^2) \end{bmatrix}, \quad \text{with: } \omega = \Omega^\star(\varepsilon = 0) = 1. \tag{C.9}$$

So $\dot{r^\star}$ is small, order ε, meaning $r^\star$ vary slowly. However, we have that $\dot{\theta}$ is not small (unsurprisingly, because the angle θ should vary at a rate ω for $\varepsilon = 0$), so we do not strictly speaking have a system $\dot{\boldsymbol{x}} = \varepsilon f(\boldsymbol{x}, t)$. One way to view this problem is as averaging over angles [1], in which case the system as it is can be averaged without any modifications. Another way is to consider that $\theta = \omega\tau + \varphi$. We have that ω is the angular frequency when $\varepsilon = 0$, so $\omega = \Omega(\varepsilon = 0)$ which gives $\omega = 1$ here. So, $\dot{\theta} = \omega + \dot{\varphi}$, and:

$$\dot{\varphi} = \dot{\theta} - \omega = \Omega^\star - \omega = \Omega^\star - 1 \tag{C.10a}$$

leading to, after Taylor expansion,

$$\dot{\varphi} = \varepsilon\Omega_1^\star(\delta^\star, r^\star, \theta) + \mathcal{O}(\varepsilon^2) \tag{C.10b}$$

1. See Sanders [101] and Jan A. Sanders et al. [51, p.157]. Sanders [101] requires Ω bounded away from zero, which makes total sense, T must be large enough so that r varies slowly compared to the oscillations period.

which means that φ does vary slowly. Thus, a simple change of variable from (r, θ) to (r, φ) does lead to:

$$\begin{bmatrix} \dot{r^\star} \\ \dot{\varphi} \end{bmatrix} = \begin{bmatrix} R^\star(\varepsilon, \delta^\star, r^\star, \theta = \omega\tau + \varphi) + \mathcal{O}(\varepsilon^2) \\ -\omega + \Omega^\star(\varepsilon, \delta^\star, r^\star, \theta = \omega\tau + \varphi) + \mathcal{O}(\varepsilon^2) \end{bmatrix} \tag{C.11a}$$

amenable to averaging, since it has the Taylor expansion:

$$\begin{bmatrix} \dot{r^\star} \\ \dot{\varphi} \end{bmatrix} = \begin{bmatrix} \varepsilon R_1^\star(\delta^\star, r^\star, \theta = \omega\tau + \varphi) + \mathcal{O}(\varepsilon^2) \\ \varepsilon \Omega_1^\star(\delta^\star, r^\star, \theta = \omega\tau + \varphi) + \mathcal{O}(\varepsilon^2) \end{bmatrix} \tag{C.11b}$$

Finally, note that the system $[\dot{r^\star}; \dot{\varphi}] = [0; 0]$ for $\varepsilon = 0$. The system is linear for $\varepsilon = 0$ and eq. (C.4) is the solution.

C.5 Center Manifold Correction to the Vector Field

The center manifold reduction changes the vector field due to the h term. It will be helpful to make that correction explicit. We can write:

$$\dot{r^\star} = \underbrace{\dot{r^\star}(c_h = 0)}_{\text{full vector field, but with } h=0} + \underbrace{\left[\dot{r^\star} - \dot{r^\star}(c_h = 0) \right]}_{\text{3D correction, to be Taylor expanded}}$$

Thus, eq. (C.8) is transformed into:

$$\begin{bmatrix} \dot{r^\star} \\ \dot{\theta} \end{bmatrix} = \begin{bmatrix} R^\star(\varepsilon, \delta^\star, r^\star, \theta) \\ \Omega^\star(\varepsilon, \delta^\star, r^\star, \theta) \end{bmatrix} = \begin{bmatrix} R^\star_{h=0}(\varepsilon, \delta^\star, r^\star, \theta) \\ \Omega^\star_{h=0}(\varepsilon, \delta^\star, r^\star, \theta) \end{bmatrix} + \begin{bmatrix} R^\star_{Corr}(\varepsilon, \delta^\star, r^\star, \theta) \\ \Omega^\star_{Corr}(\varepsilon, \delta^\star, r^\star, \theta) \end{bmatrix} \tag{C.12a}$$

where:

$$R^\star_{h=0}(\varepsilon, \delta^\star, r^\star, \theta) = R^\star(\varepsilon, \delta^\star, r^\star, \theta, c_h \to 0) \tag{C.12b}$$
$$\Omega^\star_{h=0}(\varepsilon, \delta^\star, r^\star, \theta) = \Omega^\star(\varepsilon, \delta^\star, r^\star, \theta, c_h \to 0) \tag{C.12c}$$
$$R^\star_{Corr}(\varepsilon, \delta^\star, r^\star, \theta) = R^\star(\varepsilon, \delta^\star, r^\star, \theta, c_h) - R^\star(\varepsilon, \delta^\star, r^\star, \theta, c_h \to 0) \tag{C.12d}$$
$$\Omega^\star_{Corr}(\varepsilon, \delta^\star, r^\star, \theta) = \Omega^\star(\varepsilon, \delta^\star, r^\star, \theta, c_h) - \Omega^\star(\varepsilon, \delta^\star, r^\star, \theta, c_h \to 0) \tag{C.12e}$$

The correction is what ensures topological equivalence of the vector field near the bifurcation point $\delta = y_{c,1} = y_{c,2} = 0$. By making the correction explicit, we will be able to study how it impacts the vector field. We will find that, in our case, it can be neglected (this as to be proven, in some case the correction changes the vector field qualitatively). We will show how we use the correction more specifically in appendix C.7.

In Matlab:

```
%% Split for averaging (based on notes)

% based on rdot = rdot(h=0) + [rdot - rdot(h=0)].
```

```
% the term in brackets is the 3D correction, which can safely be Taylor
% expanded without losing too much in accuracy.

% Vector field with h=0 (tangent approx):
rdote_h0 = simplify(subs(rthdote(1),ch,0),'Seconds',5);
% 3D correction (from CM reduction), to be Taylor expanded
warningi('Make sure the Taylor expansion order is sufficient');
% Should match normal form (we need r^3 at least)
rdote_Corr = subs(rthdote(1)-rdote_h0,ch,1);
rdote_Corr = simplify(taylor(rdote_Corr,ep,'Order',3),'Seconds',5) %
   Taylor expansion in ep
% Vector field with 3D correction
rdote = rdote_h0 + rdote_Corr;

% Full vector field (3D correction not splitted and not Taylor expanded)
rdote_Full = subs(rthdote(1),ch,1); %no Taylor expansion of the correction
```

C.6 Averaging

We now wish to perform the averaging per se. First, note that for the following, averaging a T-periodic function $g(t)$ is defined as:

$$\bar{g} = \langle g \rangle = \frac{1}{T} \int_0^T g(s)\, ds \tag{C.13}$$

Equation (C.12) is a system of two coupled, first-order, nonlinear differential equations. These are still too complicated to be solved. The goal here is to decoupled those equations, to make them easier to study (and solve, possibly). One way to do so is to restrict our analysis to the amplitude averaged over a cycle, $\bar{r}$. Starting from eq. (C.12),

$$\dot{r^\star} = R^\star(\varepsilon, \delta^\star, r^\star, \theta) \tag{C.14}$$

We average the left-hand side and the right-hand side, leading to:

$$\dot{\overline{r^\star}} = \frac{1}{2\pi} \int_0^{2\pi} R^\star(\varepsilon, \delta^\star, r^\star, s)\, ds \tag{C.15}$$

given that derivative and averaging are commutative (See Strogatz). Once the integration is made, we see that the vector field will no longer depends on θ explicitly (now decoupled from $\dot{\theta}$). The equation above is exact, no approximations have been made so far (beside CMR). However, in carrying the integration, we would need to take into account that $r^\star$ is actually a function of θ, which is problematic, since we do not have the solution for $r^\star$ yet. Fortunately, we know that $R^\star = \mathcal{O}(\varepsilon)$, which means that r vary slowly compared to the fast $\mathcal{O}(1)$ time scale of the oscillations and thus, should not vary too much over one cycle. In fact, for $\varepsilon = 0$, we know that $r^\star$ is a constant. We can thus make the assumption $r^\star = \overline{r^\star} + \mathcal{O}(\varepsilon)$, so the variable $\overline{r^\star}$ will be taken as constant over the integration. We get:

$$\dot{\overline{r^\star}} = \frac{1}{2\pi}\int_0^{2\pi} R^\star(\varepsilon, \delta^\star, \overline{r^\star}, s)\, ds \quad + \mathcal{O}(\varepsilon^2) \tag{C.16}$$

which can be integrated, leading to a first-order nonlinear differential equation for $\overline{r^\star}$. The error $\mathcal{O}(\varepsilon^2)$ is obtained by an asymptotic analysis. The asymptotic analysis (averaging theorem) uses a near-identity and applies to the Taylor expanded vector field (see **??**). The asymptotic analysis is valid for $\varepsilon \to 0$, in which case $R^\star$ reduces to its Taylor expansion. If the asymptotic analysis is useful to evaluate the error, we can apply the averaging to the full $R^\star$ as above, and not just its Taylor expansion. We find that taking the full $R^\star$ produces a result valid for very large ε, which is not the case with the Taylor expansion. The validity beyond ε small is not guaranteed by the averaging process, but it seems true nonetheless.

Now, let's consider the angular frequency. Starting from eq. (C.12), we have:

$$\dot{\theta} = \Omega^\star(\varepsilon, \delta^\star, r^\star, \theta) \tag{C.17}$$

Or, alternatively, we can use the phase as described above with:

$$\dot{\varphi} = \Omega^\star - \omega \tag{C.18}$$

where $\omega = 1$. Clearly, we cannot consider an averaged θ, because θ varies on the full trigonometric circle on a given cycle. However, we can consider an averaged φ, since $\dot{\varphi} = \Omega^\star - \omega = \mathcal{O}(\varepsilon)$, so φ is relatively constant over one cycle. Thus, from

$$\dot{\varphi} = \Omega^\star - \omega$$

We average the left-hand side and the right-hand side, leading to:

$$\dot{\bar{\varphi}} = \frac{1}{2\pi}\int_0^{2\pi} -\omega + \Omega^\star(\varepsilon, \delta^\star, r^\star, \theta \to s)\; ds$$

where no approximations have been considered so far. Given that ω is a constant:

$$\dot{\bar{\varphi}} = -\omega + \frac{1}{2\pi}\int_0^{2\pi} \Omega^\star(\varepsilon, \delta^\star, r^\star, \theta \to s)\, ds \tag{C.19}$$

We cannot carry the integration right away, because $r^\star$ is actually a function of the independent variable. Fortunately, as for $\dot{r^\star}$, we can make the assumption $r^\star = \overline{r^\star} + \mathcal{O}(\varepsilon)$, so the variable $\overline{r^\star}$ will be taken as constant over the integration. We get:

$$\dot{\bar{\varphi}} = -\omega + \frac{1}{2\pi}\int_0^{2\pi} \Omega^\star(\varepsilon, \delta^\star, \overline{r^\star}, \theta \to s)\, ds \quad + \mathcal{O}(\varepsilon^2) \tag{C.20}$$

Going back to $\dot{\theta}$, given $\dot{\theta} = \Omega^\star = \omega + \dot{\varphi}$, we can write $\dot{\theta} = \omega + \dot{\bar{\varphi}} + \mathcal{O}(\varepsilon^2)$:

$$\dot{\theta} = \frac{1}{2\pi}\int_0^{2\pi} \Omega^\star(\varepsilon, \delta^\star, \overline{r^\star}, \theta \to s)\, ds \quad + \mathcal{O}(\varepsilon^2) \tag{C.21}$$

Thus, averaging gives us the following new system of equations:

$$\begin{bmatrix} \dot{\overline{r^\star}} \\ \dot{\theta} \end{bmatrix} = \begin{bmatrix} \langle\, R^\star(\varepsilon, \delta^\star, \overline{r^\star}, \theta)\,\rangle_\theta \\ \langle\, \Omega^\star(\varepsilon, \delta^\star, \overline{r^\star}, \theta)\,\rangle_\theta \end{bmatrix} + \begin{bmatrix} \mathcal{O}(\varepsilon^2) \\ \mathcal{O}(\varepsilon^2) \end{bmatrix} \tag{C.22a}$$

which can be rewritten as follow, if we make the correction explicit as in eq. (C.12):

$$\begin{bmatrix} \dot{\overline{r^\star}} \\ \dot{\theta} \end{bmatrix} = \begin{bmatrix} \langle\, R^\star_{h=0}(\varepsilon, \delta^\star, \overline{r^\star}, \theta)\,\rangle_\theta \\ \langle\, \Omega^\star_{h=0}(\varepsilon, \delta^\star, r^\star, \theta)\,\rangle_\theta \end{bmatrix} + \begin{bmatrix} \langle\, R^\star_{Corr}(\varepsilon, \delta^\star, \overline{r^\star}, \theta)\,\rangle_\theta \\ \langle\, \Omega^\star_{Corr}(\varepsilon, \delta^\star, \overline{r^\star}, \theta)\,\rangle_\theta \end{bmatrix} + \begin{bmatrix} \mathcal{O}(\varepsilon^2) \\ \mathcal{O}(\varepsilon^2) \end{bmatrix} \tag{C.22b}$$

Thus, we can averaged the $h = 0$ term and the correction term separately.

In Matlab, we proceed as follow. A function `avgmatch` was built to apply integral results from Mathematica.

```
%% Averaging with avgmatch
% We perform the integration with avgmatch. We will average rdote_h0 and
% rdote_Corr independently.

% Very importantly, we use expand 'sincos' to make trigonometric terms
% appear, which will be recognized by the function avgmatch.
rdote_h0   = combine(expand(rdote_h0),'sincos');
rdote_Corr = combine(expand(rdote_Corr),'sincos');

% We then use children to split in terms to be integrated.
rdote_h0_Childs   = children(rdote_h0);
rdote_Corr_Childs = children(rdote_Corr);

whos rdote_h0_Childs rdote_Corr_Childs

% Averaging using avgmatch :
[rdote_h0_Avg, rdote_h0_Childs_Avg] = avgmatchSb(rdote_h0_Childs);%
    avgmatchS
```

```
[rdote_Corr_Avg, rdote_Corr_Childs_Avg] = avgmatchSb(rdote_Corr_Childs);%
    avgmatchS

% Simplification
rdote_h0_Avg = simplify(rdote_h0_Avg);
rdote_Corr_Avg = simplify(rdote_Corr_Avg);
rdote_Avg = rdote_h0_Avg+rdote_Corr_Avg; %based on correction obviously
```

C.7 Asymptotic expansion and Testing Topological Equivalence

Here, we consider a expansion of the vector field in terms of ε, valid for small enough ε. We will find that we obtain the same vector field as from the normal form approach, which is great.

We will also use the expansion in terms of ε to verify the effect of the correction for the 3D vector field introduced in appendix C.5. Somewhat surprisingly, I found that the Taylored Correction gets larger as r increases and actually *decreases the quality* of the prediction (numerically). After all, the correction is only required to be accurate near the bifurcation point. Also, I found that the vector field without the correction is actually extremely accurate. So, it would be great if we could justify neglecting the correction. We will do exactly that here using the ε expanded vector field. We will show here that the correction can safely be neglected while preserving the topological equivalence.

We proceed in Matlab:

```
%% Asymptotic approximation and Verification of Topological Equivalence
% We consider expansions in terms of ep. We use that to test if we can
% neglect the 3D correction and also, to compare to normal form results.

% Taylor expansion
rdote_h0_AvgTay   = simplify(taylor(rdote_h0_Avg,ep,'Order',3),'Seconds'
    ,5);
rdote_Corr_AvgTay = simplify(taylor(rdote_Corr_Avg,ep,'Order',3),'Seconds'
    ,5);

% Coefficients in terms of re (possibly do it in terms of ep)
[rdote_h0_AvgTay_co,rdote_h0_AvgTay_te]=coeffs(rdote_h0_AvgTay,rS,'All');
rdote_h0_AvgTay_co = simplify(fliplr(rdote_h0_AvgTay_co));
    rdote_h0_AvgTay_te = fliplr(rdote_h0_AvgTay_te);
[rdote_Corr_AvgTay_co,rdote_Corr_AvgTay_te]=coeffs(rdote_Corr_AvgTay,rS,'
    All');
rdote_Corr_AvgTay_co = simplify(fliplr(rdote_Corr_AvgTay_co));
    rdote_Corr_AvgTay_te = fliplr(rdote_Corr_AvgTay_te);

% padding zeros so that length=4. e.g.:[x]->[x,0,0,0]
```

```
% e.g.: useful to access rdote_Corr_AvgTay_co(2), even if it is 0.
rdote_h0_AvgTay_co=[rdote_h0_AvgTay_co,zeros(1,4-length(rdote_h0_AvgTay_co
    ))];
rdote_Corr_AvgTay_co=[rdote_Corr_AvgTay_co,zeros(1,4-length(
    rdote_Corr_AvgTay_co))];

% Check for the linear quantity (d*delta*rS):
% using <'Order',1,'OrderMode','relative'> allows to automatically select
% the leading order in epsilon (the others can be discarded).
taylor(rdote_h0_AvgTay_co(2), ep, 'Order', 1, 'OrderMode', 'relative')
taylor(rdote_Corr_AvgTay_co(2), ep, 'Order', 1, 'OrderMode', 'relative')
% We find that the h0 is O(ep) and the correction is O(ep^2), so the
% correction can safely be discarded for that term.
ddS = taylor(rdote_h0_AvgTay_co(2)+rdote_Corr_AvgTay_co(2), ep, 'Order',
    1, 'OrderMode', 'relative')

% Check for the nonlinear term (a0*rS^3) :
taylor(rdote_h0_AvgTay_co(4), ep, 'Order', 1, 'OrderMode', 'relative')
taylor(rdote_Corr_AvgTay_co(4), ep, 'Order', 1, 'OrderMode', 'relative')
% We find that the correction term is 0, so it obviously has no effect.
a0S = taylor(rdote_h0_AvgTay_co(4)+rdote_Corr_AvgTay_co(4), ep, 'Order',
    1, 'OrderMode', 'relative')

% Note that the analysis above is valid because the Taylor expansion for
% rdote_Corr was sufficient, see where we considered:
% rdote_Corr = simplify(taylor(rdote_Corr,ep,'Order',3),'Seconds',5) %
    Taylor expansion in r
% So, having Order 3 expansion in ep is ok, it leads to term O(ep^2) which
% are smaller than the larger terms in rdote_h0_AvgTay_co.

% we have an equation of the following form:
% d(rS)/dt = ddS*rS + a0S*rS^3
% To compare to normal form, we must remove the epsilon scaling. We have:
% r=ep*rS => rS=r/ep,
% Substitution in the equation above gives:
% (1/ep) d(r)/dt = ddS*(1/ep)*r + a0S*(1/ep^3)*r^3
%        d(r)/dt = ddS*r + (a0S/ep^2)*r^3
% Which is analog to (from normal form) :
%        d(r)/dt = dd*r  + a0*r^3
%
% We thus have:
% dd=ddS and a0= a0S/ep^2.
%
% Given those relations and given d=ep*dS => dS=d/ep, we have:
dd = simplify(subs(ddS,dS,d/ep)); % = d/(4*zf^2 + 1)
```

```
a0 = simplify(subs(a0S/ep^2,dS,d/ep)); % = -zf^3/(Thl^2*(4*zf^2 + 1))

% which are exactly the same results as obtained from normal forms with
% psi=0.
```

We have that Taylor expansion of the averaged vector field $\dot{\overline{r^\star}}$ from eq. (C.22) in terms of ε, and ordering in terms of $r^\star$ is given by:

$$\dot{\overline{r^\star}} = \langle\, R^\star_{h=0}(\varepsilon, \delta^\star, \overline{r^\star}, \theta)\,\rangle_\theta \;+\; \langle\, R^\star_{Corr}(\varepsilon, \delta^\star, \overline{r^\star}, \theta)\,\rangle_\theta \;+ \mathcal{O}(\varepsilon^2) \tag{C.23a}$$

with the following results from Taylor expansion:

$$\langle\, R^\star_{h=0}(\varepsilon, \delta^\star, \overline{r^\star}, \theta)\,\rangle_\theta = \left(\frac{\varepsilon\delta^\star}{1+4{\zeta_f}^2}\right) \quad r^\star + \left(-\frac{\varepsilon^2{\zeta_f}^3}{{T_{HL}}^2\left(1+4{\zeta_f}^2\right)}\right) r^{\star 3} \quad + \mathcal{O}(\varepsilon^3) \tag{C.23b}$$

$$\langle\, R^\star_{Corr}(\varepsilon, \delta^\star, \overline{r^\star}, \theta)\,\rangle_\theta = \left(\frac{-8\varepsilon^2\zeta_f\delta^{\star 2}}{\left(1+4{\zeta_f}^2\right)^3}\right) r^\star + \quad \left(0\right) \quad r^{\star 3} \quad + \mathcal{O}(\varepsilon^3) \tag{C.23c}$$

We do not care so much about $\dot{\theta}$, because we have the $\dot{\theta} = \omega$ for $\varepsilon = 0$ and the correction will not change that.

In order to make an analogy to the normal forms, we can rewrite this results as:

$$\dot{r^\star} = d\delta^\star \; r^\star \;+\; a_0^\star \; r^{\star 3} \tag{C.24a}$$

where $d\delta^\star$ is:

$$d\delta^\star = \underbrace{\frac{\varepsilon\delta^\star}{1+4{\zeta_f}^2}}_{\text{from } h=0} + \underbrace{\frac{-8\varepsilon^2\zeta_f\delta^{\star 2}}{\left(1+4{\zeta_f}^2\right)^3}}_{\text{3D (CMR) correction}} \tag{C.24b}$$

Thus, given that the $h = 0$ term is $\mathcal{O}(\varepsilon)$ and that the correction is $\mathcal{O}(\varepsilon^2)$, the correction can be neglected in $d\delta^\star$. $a_0^\star$ is given by:

$$a_0^\star = \underbrace{-\frac{\varepsilon^2{\zeta_f}^3}{{T_{HL}}^2\left(1+4{\zeta_f}^2\right)}}_{\text{from } h=0} + \underbrace{0}_{\text{3D (CMR) correction}} \tag{C.24c}$$

with no correction term on $a_0^\star$ from CMR. We thus have that the CMR correction can be neglected in the $\dot{r^\star}$ vector field, in the asymptotic expansion ($\varepsilon \to 0$). The topology of the system is preserved even with $h = 0$.

Let's now compare our results to the normal form. Given that the normal form is expressed as $\dot{r} = d\delta r + a_0 r^3$, we must remove the ε scaling in the averaging, with $r = \varepsilon r^\star \Rightarrow r^\star = r/\varepsilon$, leading to:

$$\begin{aligned} \dot{r^\star} &= d\delta^\star \; r^\star &&+ \; a_0^\star \; r^{\star 3} \\ \left(\frac{1}{\varepsilon}\right)\dot{r} &= d\delta^\star \; \left(\frac{r}{\varepsilon}\right) &&+ \; a_0^\star \; \left(\frac{r}{\varepsilon}\right)^3 \\ \dot{r} &= d\delta^\star \; r &&+ \; \left(\frac{a_0^\star}{\varepsilon^2}\right) \; r^3 \end{aligned}$$

which is analogous to the normal form vector field:

$$\dot{r} = d\delta \; r \qquad + \; a_0 \; r^3 \tag{C.25a}$$

Equating the coefficients, we have $d\delta = d\delta^\star$ and $a_0 = a_0^\star/\varepsilon^2$. Given the leading order definitions for $d\delta^\star$ and $a_0^\star$ above, and given $\delta = \varepsilon\delta^\star \Rightarrow \delta^\star = \delta/\varepsilon$, we get:

$$d\delta = d\delta^\star = \frac{\delta}{1 + 4{\zeta_f}^2} \tag{C.25b}$$

$$a_0 = \frac{a_0^\star}{\varepsilon^2} = -\frac{{\zeta_f}^3}{{T_{HL}}^2\left(1 + 4{\zeta_f}^2\right)} \tag{C.25c}$$

which is exactly the result obtained in normal forms, for $\psi = 0$ (see chapter 4). Thus we validated that we obtain the same $\dot{r}$ vector field in the asymptotic expansion from normal forms and averaging.

C.8 Solving for the Limit Cycle

Starting from the averaged, non-Taylor expanded, vector field eq. (C.22),

$$\begin{bmatrix} \dot{\overline{r^\star}} \\ \dot{\theta} \end{bmatrix} = \begin{bmatrix} \langle\, R^\star_{h=0}(\varepsilon, \delta^\star, \overline{r^\star}, \theta)\,\rangle_\theta \\ \langle\, \Omega^\star_{h=0}(\varepsilon, \delta^\star, r^\star, \theta)\,\rangle_\theta \end{bmatrix} + \begin{bmatrix} \langle\, R^\star_{Corr}(\varepsilon, \delta^\star, \overline{r^\star}, \theta)\,\rangle_\theta \\ \langle\, \Omega^\star_{Corr}(\varepsilon, \delta^\star, \overline{r^\star}, \theta)\,\rangle_\theta \end{bmatrix} + \begin{bmatrix} \mathcal{O}(\varepsilon^2) \\ \mathcal{O}(\varepsilon^2) \end{bmatrix} \tag{C.26a}$$

we found that the correction is negligible in the asymptotic limit and thus, the vector field $h = 0$ preserves the topology of the full 3D system. We can safely neglect the correction, leading to the simplified, approximate system:

$$\begin{bmatrix} \dot{\overline{r^\star}} \\ \dot{\theta} \end{bmatrix} = \begin{bmatrix} \langle\, R^\star_{h=0}(\varepsilon, \delta^\star, \overline{r^\star}, \theta)\,\rangle_\theta \\ \langle\, \Omega^\star_{h=0}(\varepsilon, \delta^\star, r^\star, \theta)\,\rangle_\theta \end{bmatrix} \tag{C.27a}$$

where we also truncated the error term.

C.8.1 Solving for the Limit Cycle Amplitude

Now, we are interested in solving for the limit cycle. On the limit cycle, we have $\dot{\overline{r^\star}} = 0$, so we can solve:

$$\langle\, R^\star_{h=0}(\varepsilon, \delta^\star, \overline{r^\star}, \theta)\,\rangle_\theta = 0 \tag{C.28}$$

for $\overline{r^\star}$. We get the following three solutions:

$$\overline{r^\star} = \{0\ ,\ +r^\star_{LC}\ ,\ -r^\star_{LC}\} \quad \text{with: } r^\star_{LC} \equiv \frac{1}{\varepsilon}\frac{T_{HL}}{\zeta_f}\frac{\sqrt{\varepsilon\delta^\star\,(\zeta_f + \varepsilon\delta^\star)}}{\zeta_f\,(\zeta_f + \varepsilon\delta^\star)} \tag{C.29}$$

with $\overline{r^\star} = 0$ being the fixed point (equilibrium), the solution $\overline{r^\star} = +r^\star_{LC} > 0$ being the limit cycle amplitude and the solution $\overline{r^\star} = -r^\star_{LC} < 0$ being a non-physical solution.

We used the ε scaling in the approach above to verify the order of various terms, but we now would prefer to express the final result without it. From eq. (C.6), we have $\bar{r} = \varepsilon\overline{r^\star}$ and $\delta = \varepsilon\delta^\star \Rightarrow \delta^\star = \delta/\varepsilon$, leading to:

$$r_{LC} = \frac{T_{HL}}{\zeta_f}\frac{\sqrt{\delta\,(\delta + \zeta_f)}}{\delta + \zeta_f} \tag{C.30}$$

We would also prefer to replace δ by Π, with $\delta = \zeta_f\,(\Pi - 1)$, leading to:

$$r_{LC} = \frac{T_{HL}}{\zeta_f}\sqrt{\frac{\Pi - 1}{\Pi}} \tag{C.31}$$

which is our final result. We prefer the Π form because it shows that the square root only depends on a single parameter, the ratio σ/ζ_f.

in Matlab:

```
%% Solving the averaging vector field for the amplitude
% We now solve rdote_h0_Avg for the fixed points. We are especially
% interested in the limit cycle solution.

rSLC = simplify(solve(rdote_h0_Avg==0,rS)) % symvar(rdote_h0_Avg)

% The amplitude is expressed in the epsilon scaling. We would like to
% remove the epsilon scaling to go back to the original variables and
% parameters. We have:
%
% rLC =ep*rSLC and d=ep*dS=>dS=d/ep,
%
% leading to:

rLC = simplify(subs(ep*rSLC,dS,d/ep))
```

```
% which gives:
%                                          0
%   (Thl*(d*(d + zf))^(1/2))/(zf*(d + zf))
%  -(Thl*(d*(d + zf))^(1/2))/(zf*(d + zf))

%Now, with the substitution d=zf*(Pi-1), we have:
rLC = simplify(subs(rLC,d,zf*(Pi-1)))
% rLC = simplify(subs(subs(ep*rSLC,[ep,dS],[d,1]),d,zf*(Pi-1)))

% which gives:
%                                      0
%   (Thl*(Pi - 1)^(1/2))/(Pi^(1/2)*zf)
%  -(Thl*(Pi - 1)^(1/2))/(Pi^(1/2)*zf)
```

C.8.2 Solving for the Limit Cycle Angular Frequency

Starting from eq. (C.27), we substitute $r^\star$ by r_{LC} given above,

$$\dot{\theta} = \bar{\Omega}^\star_{h=0}(\varepsilon, \delta^\star, \overline{r^\star} \to r^\star_{LC})$$

leading to simply:

$$\dot{\theta} = 1 \quad \text{on the limit cycle, for } \overline{r^\star} \to r^\star_{LC}. \tag{C.32}$$

in Matlab (where the averaging of $\Omega^\star_{h=0}$ is included):

```
%% Solving the angular frequency

% Averaging the vector field
thdot_h0 = children(combine(expand( simplify(subs(rthdote(2),ch,0)) ),'
    sincos'));
[thdot_h0_Avg, thdot_h0_Childs_Avg] = avgmatchSb(thdot_h0);

% Solving for the Limit Cycle
assumeAlso(d>0);
thdotLC_rS = simplify(subs(thdot_h0_Avg,rS,rSLC(2)))
thdotLC  = simplify(subs(thdotLC_rS,dS,d/ep))

% which simplify gives: 1.
```

APPENDIX D

Appendix to Chapter 6

D.1 Energy Harvesting from the Linear Forced Oscillator

In this appendix, we analyze the energy harvesting from a linear forced oscillator, such that it can be compared to energy harvesting from self-oscillations. The linear forced oscillator is represented as:

$$m\ddot{x} + c\dot{x} + kx = F_0 \cos(\omega t) \tag{D.1}$$

With $c = c_f + c_L$, where c_f is the friction coefficient and c_L the harvesting coefficient. We now make this equation dimensionless, with a characteristic time $1/\omega_n$, given $\omega_n = \sqrt{k/m}$ the angular frequency and with a characteristic length F_0/k, leading to:

$$\frac{d^2\, q}{d\, \tau^2} + 2\zeta \frac{d\, q}{d\, \tau} + q = \cos\left(\Omega\ \tau\right) \tag{D.2}$$

Where $q = x/(F_0/k)$ is the dimensionless position, $\tau = \omega_n t$ is the dimensionless time, $\zeta = c/(2\sqrt{km})$ is the damping ratio and $\Omega = \omega/\omega_n$ is the dimensionless forcing frequency. Also, the damping coefficient ζ includes both the friction and the harvesting, with $\zeta = \zeta_f + \zeta_L$, where ζ_f and ζ_L are dimensionless coefficients for friction and harvesting, respectively. Equation (D.2) is often called the *universal oscillator equation*. The steady-state solution of eq. (D.2) is [64]:

$$q(\tau) = a\cos(\Omega\tau) + b\sin(\Omega\tau) = A\cos\left(\Omega\tau + \varphi\right) \tag{D.3a}$$

with:

$$a = \frac{1-\Omega^2}{\left(1-\Omega^2\right)^2 + 4\Omega^2\zeta^2},\ b = \frac{2\zeta\Omega}{\left(1-\Omega^2\right)^2 + 4\Omega^2\zeta^2} \tag{D.3b}$$

and the amplitude $A = \sqrt{a^2+b^2}$ is:

$$A = \frac{1}{\sqrt{\left(1-\Omega^2\right)^2 + 4\Omega^2\zeta^2}} \tag{D.3c}$$

The amplitude A is shown in fig. D.1a as a function of the dimensionless forcing frequency Ω. The maximum occurs at $\Omega = \sqrt{1-2\zeta^2}$, so the dimensional forcing frequency at the maximum amplitude is $\omega = \sqrt{1-2\zeta^2}\omega_n$. This is called *practical resonance* [64, p.90].

D.1.1 Power Output

The dimensionless [1] power is $\overline{\dot{W}}_h = \zeta_L \, \Omega^2 \, A^2$, leading to:

$$\overline{\dot{W}}_h = \frac{\zeta_L \, \Omega^2}{\left(1-\Omega^2\right)^2 + 4\Omega^2 \left(\zeta_f + \zeta_L\right)^2} \tag{D.4}$$

The power $\overline{\dot{W}}_h$ as a function of the dimensionless forcing frequency Ω is shown in fig. D.1b. Using a derivative test, we find that the power reaches a maximum at $\Omega = \Omega_{\text{Opt}}$, with:

$$\Omega_{\text{Opt}} = 1 \tag{D.5a}$$

corresponding to $\omega = \omega_n$. We note that Ω maximizing the power is not exactly the same as the one maximizing the power. At $\Omega = \Omega_{\text{Opt}} = 1$, the amplitude is:

$$A(\Omega = \Omega_{\text{Opt}}) = \frac{1}{2\left(\zeta_f + \zeta_L\right)} \tag{D.5b}$$

and the maximum power is:

$$\overline{\dot{W}}_h(\Omega = \Omega_{\text{Opt}}) = \frac{\zeta_L}{4\left(\zeta_f + \zeta_L\right)^2} \tag{D.5c}$$

The amplitude A and the power $\overline{\dot{W}}_h$, at $\Omega = 1$ (eq. (D.5)), are shown as function of the harvesting coefficient in eq. (D.5). The amplitude decreases monotonically as a function of ζ_L. On the other hand, the power reaches a maximum at $\zeta_L = \zeta_f$. This is known as *impedance matching*, which is a result of the *maximum power transfer theorem*. The maximum power there is:

$$\overline{\dot{W}}_{h,max} = \frac{1}{16\zeta_f} \tag{D.6}$$

Thus, the power can be increased furthermore by decreasing the friction coefficient ζ_f. Note that this latter expression does not hold for $\zeta_f = 0$ however, so the power is not infinite at $\zeta_f = 0$.

D.1.2 Efficiency

In the linear forced oscillator, some energy is injected in the system by the forcing term. Over a cycle the energy is the work $W_{\text{Forcing,Cycle}}$. The energy harvested over a cycle is the

1. The dimensional power is obtained by $\left(\omega_n {F_0}^2/k\right) \overline{\dot{W}}_h$.

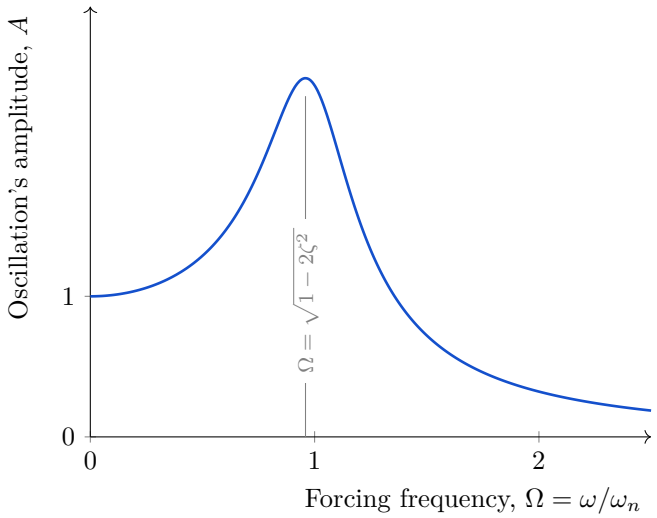

(a)

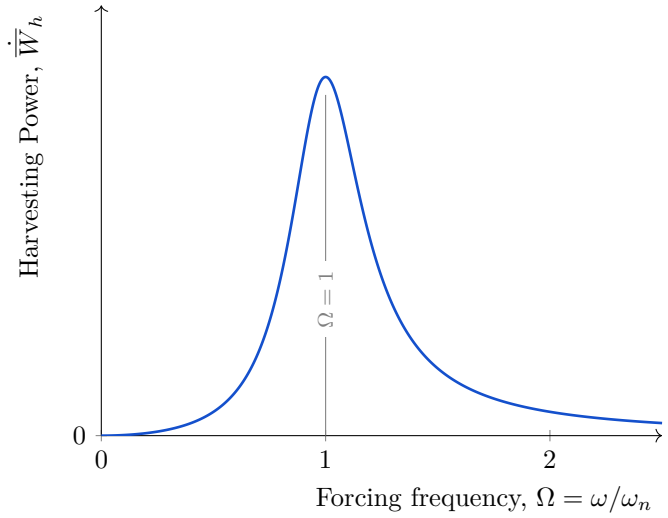

(b)

Figure D.1 Curves evaluated for $\zeta_f = \zeta_L = 0.10$. (a) Amplitude A as a function of the dimensionless forcing frequency Ω; there is a maximum (practical resonance) at $\Omega = \sqrt{1-2\zeta^2}$. (b) Power $\dot{\overline{W}}_h$ as a function of the dimensionless forcing frequency Ω; there is a maximum at exactly $\Omega = 1$.

work $W_{\text{h,Cycle}}$. The efficiency is, after simplifications:

$$\eta = \frac{W_{\text{h,Cycle}}}{W_{\text{Forcing,Cycle}}} = \frac{\zeta_L}{\zeta_L + \zeta_f} = \frac{1}{1 + (\zeta_f/\zeta_L)} \tag{D.7}$$

The efficiency η does not depend on the forcing frequency Ω. The efficiency increases as ζ_f decreases and ζ_L increases. For either $\zeta_f \to 0$ or $\zeta_L \to +\infty$, the efficiency approaches 1. In fig. D.3, we show both the efficiency and the power as a function of ζ_L. We see that

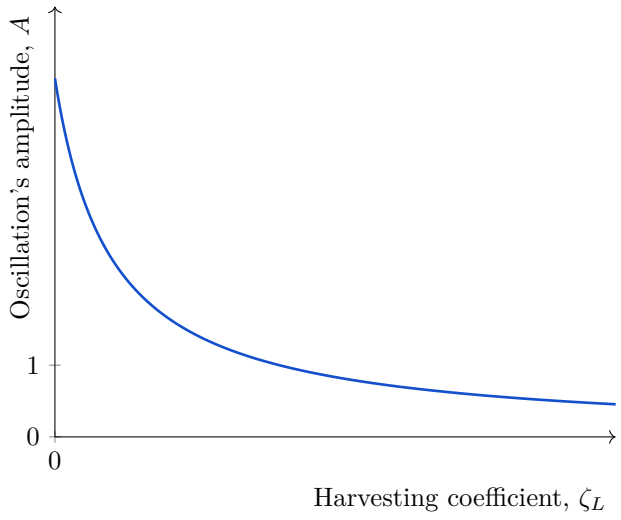

(a)

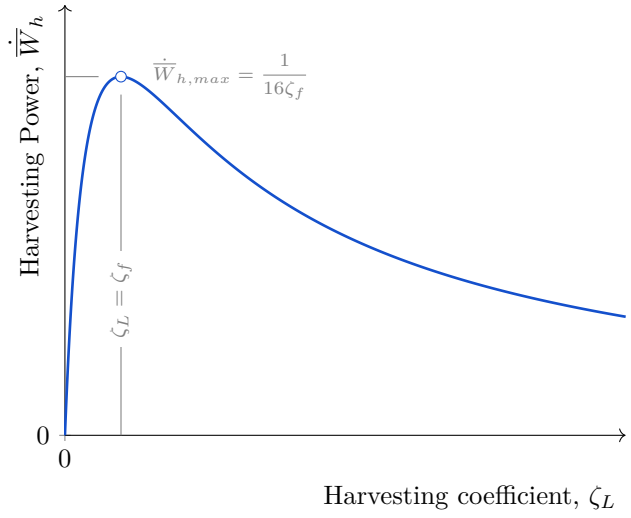

(b)

Figure D.2 Curves evaluated for $\zeta_f = \zeta_L = 0.10$. (a) Amplitude A at $\Omega = 1$ as a function of the harvesting coefficient ζ_L; the amplitude is progressively decreasing. (b) Power $\overline{\dot{W}}_h$ at $\Omega = 1$ as a function of the harvesting coefficient ζ_L; there is a maximum at $\zeta_L = \zeta_f$.

the power reaches a maximum value at $\zeta_L = \zeta_f$, but the efficiency keeps increasing as ζ_L increase. Thus, the conditions for maximum power and maximum efficiency differ.

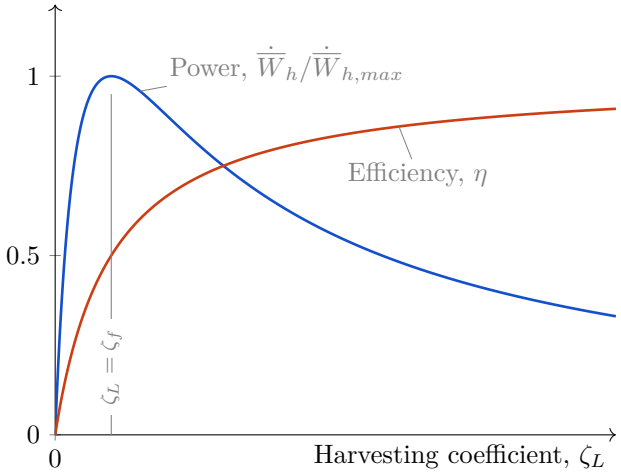

Figure D.3 Power and efficiency as a function of ζ_L; whereas the power is maximal at $\zeta_L = \zeta_f$, the efficiency approaches a maximum for $\zeta_L \to +\infty$.

LIST OF REFERENCES

[1] A. Nikkhah, A. Tessier-Poirier, N. Karami, O. Abouali, and L.G. Frechette. Investigation of the Liquid Plug Friction Force in the Self-Oscillating Fluidic Heat Engine (SOFHE). In *2019 19th International Conference on Micro and Nanotechnology for Power Generation and Energy Conversion Applications (PowerMEMS)*, pages 1–7, December 2019. doi: 10.1109/PowerMEMS49317.2019.92321106939.

[2] A. Abdelkefi, A. H. Nayfeh, and M. R. Hajj. Design of piezoaeroelastic energy harvesters. *Nonlinear Dynamics*, 68(4):519–530, June 2012. ISSN 1573-269X. doi: 10.1007/s11071-011-0233-x.

[3] Hisateru Akachi. Structure of micro-heat pipe, June 1993. Patent number : 5 219 020.

[4] Massimo Alioto, editor. *Enabling the Internet of Things: From Integrated Circuits to Integrated Systems*. Springer International Publishing, 2017. ISBN 978-3-319-51480-2. doi: 10.1007/978-3-319-51482-6.

[5] X. Amandolese, S. Michelin, and M. Choquel. Low speed flutter and limit cycle oscillations of a two-degree-of-freedom flat plate in a wind tunnel. *Journal of Fluids and Structures*, 43:244–255, November 2013. ISSN 0889-9746. doi: 10.1016/j.jfluidstructs.2013.09.002.

[6] G. O. Antoine, E. de Langre, and S. Michelin. Optimal energy harvesting from vortex-induced vibrations of cables. *Proceedings of the Royal Society A: Mathematical, Physical and Engineering Sciences*, 472(2195):20160583, November 2016. doi: 10.1098/rspa.2016.0583. Publisher: Royal Society.

[7] Philippe Aubin, Brian D'Entremont, Filippo Cataldo, Jackson B. Marcinichen, Raffaele L. Amalfi, and John R. Thome. Numerical Simulations of Pulsating Heat Pipes, Part 1: Modeling. In *2019 18th IEEE Intersociety Conference on Thermal and Thermomechanical Phenomena in Electronic Systems (ITherm)*, pages 232–242, May 2019.

[8] H. K. Bardaweel, M. J. Anderson, R. F. Richards, and C. D. Richards. Optimization of the dynamic and thermal performance of a resonant micro heat engine. *J. Micromech. Microeng.*, 18(10):104014, September 2008. ISSN 0960-1317. doi: 10.1088/0960-1317/18/10/104014. Publisher: IOP Publishing.

[9] S P Beeby, M J Tudor, and N M White. Energy harvesting vibration sources for microsystems applications. *Meas. Sci. Technol.*, 17(12):R175–R195, December 2006. ISSN 0957-0233, 1361-6501. doi: 10.1088/0957-0233/17/12/R01.

[10] Amin Bibo, Gang Li, and Mohammed F. Daqaq. Electromechanical Modeling and Normal Form Analysis of an Aeroelastic Micro-Power Generator. *Journal of Intelligent Material Systems and Structures*, 22(6):577–592, April 2011. ISSN 1045-389X. doi: 10.1177/1045389X11400929.

[11] Henri Bénard. Les tourbillons cellulaires dans une nappe liquide. *Revue Générale des Sciences Pures et Appliquées*, 11:1261–1271, 1309–1328, 1900.

[12] Henri Bénard. *Les tourbillons cellulaires dans une nappe liquide propageant de la chaleur par convection: en régime permanent.* Gauthier-Villars, 1901.

[13] J. Boswell, C. Wilson, D. Pounds, and B. Drolen. Recent advances in oscillating heat pipes for passive electronics thermal management. In *2018 34th Thermal Measurement, Modeling Management Symposium (SEMI-THERM)*, pages 37–41, March 2018. doi: 10.1109/SEMI-THERM.2018.8357350.

[14] Nancy Cartwright and Ernan McMullin. How the Laws of Physics Lie. *American Journal of Physics*, 52(5):474–476, May 1984. ISSN 0002-9505. doi: 10.1119/1.13641.

[15] Yunus Cengel and Michael Boles. *Thermodynamics: An Engineering Approach.* McGraw-Hill Science/Engineering/Math, January 2010.

[16] J. H. Cho, L. W. Weiss, C. D. Richards, D. F. Bahr, and R. F. Richards. Power production by a dynamic micro heat engine with an integrated thermal switch. *J. Micromech. Microeng.*, 17(9):S217–S223, August 2007. ISSN 0960-1317. doi: 10.1088/0960-1317/17/9/S02. Publisher: IOP Publishing.

[17] Shui-Nee Chow and John Mallet-Paret. Integral averaging and bifurcation. *Journal of Differential Equations*, 26(1):112–159, October 1977. ISSN 0022-0396.

[18] V. T. Coppola and R. H. Rand. Averaging using elliptic functions: approximation of limit cycles. *Acta Mechanica*, 81(3-4):125–142, September 1990. ISSN 0001-5970, 1619-6937. doi: 10.1007/BF01176982.

[19] Creative Commons. Creative Commons — Attribution 3.0 Unported — CC BY 3.0, 2021. URL https://creativecommons.org/licenses/by/3.0/.

[20] S. P. Das, V. S. Nikolayev, F. Lefevre, B. Pottier, S. Khandekar, and J. Bonjour. Thermally induced two-phase oscillating flow inside a capillary tube. *International Journal of Heat and Mass Transfer*, 53(19–20):3905–3913, September 2010. ISSN 0017-9310. doi: 10.1016/j.ijheatmasstransfer.2010.05.009.

[21] Henk W. De Regt and Dennis Dieks. A Contextual Approach to Scientific Understanding. *Synthese*, 144(1):137–170, March 2005. ISSN 1573-0964.

[22] Brian P. d'Entremont and John R. Thome. A Numerical Study of Pulsating Heat Pipe Performance. In *Proceedings of the ASME 2015 International Technical Conference and Exhibition on Packaging and Integration of Electronic and Photonic Microsystems (InterPACK2015)*. American Society of Mechanical Engineers Digital Collection, November 2015.

[23] A. Dhooge, W. Govaerts, Yu. A. Kuznetsov, H. G.E. Meijer, and B. Sautois. New features of the software MatCont for bifurcation analysis of dynamical systems. *Mathematical and Computer Modelling of Dynamical Systems*, 14(2):147–175, April

2008. ISSN 1387-3954. doi: 10.1080/13873950701742754. MatCont available on https://sourceforge.net/projects/matcont/.

[24] Olivier Doaré, Sébastien Michelin, Miguel Pineirua, and Yifan Xia. Flow Energy Harvesting With Piezoelectric Flags. In *Proceedings of the ASME 2014 33rd International Conference on Ocean, Offshore and Arctic Engineering*, volume 9A of *Ocean Renewable Energy*. American Society of Mechanical Engineers Digital Collection, June 2014.

[25] Robert T. Dobson. Theoretical and experimental modelling of an open oscillatory heat pipe including gravity. *International Journal of Thermal Sciences*, 43(2):113–119, February 2004. ISSN 1290-0729. doi: 10.1016/j.ijthermalsci.2003.05.003.

[26] Robert T. Dobson. An open oscillatory heat pipe water pump. *Applied Thermal Engineering*, 25(4):603–621, March 2005. ISSN 1359-4311. doi: 10.1016/j.applthermaleng.2004.07.005.

[27] Robert T. Dobson and TM Harms. Lumped parameter analysis of closed and open oscillatory heat pipes. In *Proceedings of the 11th International heat pipe Conference*, pages 137–142. Japan, 1999.

[28] P. G. Drazin. *Introduction to Hydrodynamic Stability*. Cambridge University Press, September 2002. ISBN 978-0-521-00965-2.

[29] A. Erturk, W. G. R. Vieira, C. De Marqui, and D. J. Inman. On the energy harvesting potential of piezoaeroelastic systems. *Appl. Phys. Lett.*, 96(18):184103, May 2010. ISSN 0003-6951. doi: 10.1063/1.3427405. Publisher: American Institute of Physics.

[30] Amir Faghri. Heat pipes: Review, opportunities and challenges. *Frontiers in Heat Pipes*, 5(1), April 2014. ISSN 2155-658X.

[31] Richard P. Feynman, Robert B. Leighton, and Matthew L. Sands. *The Feynman lectures on physics*. Addison-Wesley, Reading, Mass., 1963. URL https://www.feynmanlectures.caltech.edu/index.html.

[32] I. Finnie and Rane L. Curl. On the Functioning of a Familiar Non-Linear Thermodynamic Oscillator. In *Proc. Internat. Union of Theor. and Appl. Mech.*, volume 3, pages 486–497, 1963.

[33] I. Finnie and Rane L. Curl. Physics in a Toy Boat. *American Journal of Physics*, April 1963.

[34] L. Fourgeaud, E. Ercolani, J. Duplat, P. Gully, and V. S. Nikolayev. Evaporation-driven dewetting of a liquid film. *Phys. Rev. Fluids*, 1(4):041901, August 2016. doi: 10.1103/PhysRevFluids.1.041901.

[35] Frank White. *Fluid Mechanics*. MgGraw-Hill Education, eight edition, January 2015.

[36] Lex Fridman. John Hopfield: Physics View of the Mind and Neurobiology | Lex Fridman Podcast #76, 2020. URL https://www.youtube.com/watch?v=DKyzcbNr8WE.

[37] Roman Frigg and Stephan Hartmann. Models in Science. In Edward N. Zalta, editor, *The Stanford Encyclopedia of Philosophy*. Metaphysics Research Lab, Stanford University, spring 2020 edition, 2020. URL https://plato.stanford.edu/archives/spr2020/entries/models-science/.

[38] Nikhilesh Ghanta and Arvind Pattamatta. Modeling of compressible phase-change heat transfer in a Taylor-Bubble with application to pulsating heat pipe (PHP). *Numerical Heat Transfer, Part A: Applications*, 69(12):1355–1375, June 2016. ISSN 1040-7782.

[39] Manfred Groll and Sameer Khandekar. State of the Art on Pulsating Heat Pipes. In *Proceedings of the ASME 2004 2nd International Conference on Microchannels and Minichannels*, pages 33–44. American Society of Mechanical Engineers Digital Collection, December 2008. doi: 10.1115/ICMM2004-2318. URL https://asmedigitalcollection-asme-org.ezproxy.usherbrooke.ca/ICNMM/proceedings/ICMM2004/41642/33/304865.

[40] John Guckenheimer and Philip Holmes. *Nonlinear Oscillations, Dynamical Systems, and Bifurcations of Vector Fields*. Springer Science & Business Media, November 2013. ISBN 978-1-4612-1140-2.

[41] P. Gully, F. Bonnet, Vadim S. Nikolayev, N. Luchier, and T. Q. Tran. EVALUATION OF THE VAPOR THERMODYNAMIC STATE IN PHP. *Heat Pipe Science and Technology, An International Journal*, 5(1-4), 2014. ISSN 2151-7975, 2151-7991. doi: 10.1615/HeatPipeScieTech.v5.i1-4.410. Publisher: Begel House Inc.

[42] Tingting Hao, Xuehu Ma, Zhong Lan, Nan Li, and Yuzhe Zhao. Effects of Superhydrophobic and Superhydrophilic Surfaces on Heat Transfer and Oscillating Motion of an Oscillating Heat Pipe. *Journal of Heat Transfer*, 136(8), May 2014. ISSN 0022-1481.

[43] Tingting Hao, Xuehu Ma, Zhong Lan, Nan Li, Yuzhe Zhao, and Hongbin Ma. Effects of hydrophilic surface on heat transfer performance and oscillating motion for an oscillating heat pipe. *International Journal of Heat and Mass Transfer*, 72:50–65, May 2014. ISSN 0017-9310.

[44] Werner Heisenberg. The physical content of quantum kinematics and mechanics. In John Archibald Wheeler and Wojciech Hubert Zurek, editors, *Quantum theory and measurement*, Princeton Series in physics. Princeton University Press, Princeton, New-jersey, 1983. ISBN 0-691-08315-0 978-0-691-08315-5.

[45] G M Homsy. Viscous Fingering in Porous Media. *Annual Review of Fluid Mechanics*, 19(1):271–311, 1987. doi: 10.1146/annurev.fl.19.010187.001415.

[46] T. Huesgen and P. Woias. A novel self-starting MEMS-heat engine for thermal energy harvesting. In *2010 IEEE 23rd International Conference on Micro Electro Mechanical Systems (MEMS)*, pages 1179–1182, January 2010. doi: 10.1109/MEMSYS.2010.5442422. ISSN: 1084-6999.

[47] T. Huesgen, J. Ruhhammer, G. Biancuzzi, and P. Woias. Detailed study of a micro heat engine for thermal energy harvesting. *J. Micromech. Microeng.*, 20(10):104004, September 2010. ISSN 0960-1317. doi: 10.1088/0960-1317/20/10/104004. Publisher: IOP Publishing.

[48] iNEMI. iNEMI ROADMAP IDENTIFIES TRENDS IMPACTING ELECTRONICS THERMAL MANAGEMENT, April 2016. URL https://www.electronics-cooling.com/2016/04/inemi-roadmap-identifies-trends-impacting-electronics-thermal-management/.

[49] ITRS. 2015 International Technology Roadmap for Semiconductors (ITRS). Technical report, Semiconductor Industry Association, 2015.

[50] Nathan Jacobson. *Basic Algebra I: Second Edition*. Dover Publications, 1985.

[51] Jan A. Sanders, Ferdinand Verhulst, and James Murdock. *Averaging Methods in Nonlinear Dynamical Systems*, volume 59 of *Applied Mathematical Sciences*. Springer New York, New York, NY, 2007. ISBN 978-0-387-48916-2.

[52] Alejandro Jenkins. Self-oscillation. *Physics Reports*, 525(2):167–222, April 2013. ISSN 0370-1573. doi: 10.1016/j.physrep.2012.10.007.

[53] John Archibald Wheeler and Wojciech Hubert Zurek. *Quantum theory and measurement*. Princeton Series in physics. Princeton University Press, Princeton, New-jersey, 1983. ISBN 0-691-08315-0 978-0-691-08315-5.

[54] Nicola Jones. How to stop data centres from gobbling up the world's electricity. *Nature*, 561(7722):163–166, September 2018. doi: 10.1038/d41586-018-06610-y.

[55] Soohwan Jun and Sung Jin Kim. Experimental study on a criterion for normal operation of pulsating heat pipes in a horizontal orientation. *International Journal of Heat and Mass Transfer*, 137:1064–1075, July 2019. ISSN 0017-9310.

[56] Chuljae Jung and Sung Jin Kim. Effects of oscillation amplitudes on heat transfer mechanisms of pulsating heat pipes. *International Journal of Heat and Mass Transfer*, 165:120642, February 2021. ISSN 0017-9310. doi: 10.1016/j.ijheatmasstransfer.2020.120642.

[57] Nooshin Karami, A Tessier-Poirier, E Léveillé, T Monin, F Formosa, and L G Fréchette. Thermodynamic Cycle of a Self-Oscillating Fluidic Heat Engine (SOFHE) for Thermal Energy Harvesting. In *Proceedings of the International Symposium on Oscillating/Pulsating Heat Pipes 2019*, page 4, Daejeon, Korea, 2019.

[58] Nooshin Karami, Albert Tessier-Poirier, Étienne Léveillé, Thomas Monin, Fabien Formosa, and Luc G. Fréchette. Experimental Characterization of the Thermody-

namic Cycle of a Self-Oscillating Fluidic Heat Engine (SOFHE) for Thermal Energy Harvesting. *Applied Thermal Engineering (Under review process)*, 2021. Under review process.

[59] Sameer Khandekar and Manfred Groll. An insight into thermo-hydrodynamic coupling in closed loop pulsating heat pipes. *International Journal of Thermal Sciences*, 43(1):13–20, January 2004. ISSN 1290-0729. doi: 10.1016/S1290-0729(03)00100-5. URL http://www.sciencedirect.com/science/article/pii/S1290072903001005.

[60] Sameer Khandekar, Nicolas Dollinger, and Manfred Groll. Understanding operational regimes of closed loop pulsating heat pipes: an experimental study. *Applied Thermal Engineering*, 23(6):707–719, April 2003. ISSN 1359-4311. doi: 10.1016/S1359-4311(02)00237-5. URL https://www.sciencedirect.com/science/article/pii/S1359431102002375.

[61] Sameer Khandekar, Pradipta K. Panigrahi, Frédéric Lefèvre, and Jocelyn Bonjour. Local hydrodynamics of flow in a pulsating heat pipe: A review. *Frontiers in Heat Pipes*, 1(2), November 2010. ISSN 2155-658X. doi: 10.5098/fhp.v1.2.3003.

[62] Wookyoung Kim and Sung Jin Kim. Effect of reentrant cavities on the thermal performance of a pulsating heat pipe. *Applied Thermal Engineering*, 133:61–69, March 2018. ISSN 1359-4311. doi: 10.1016/j.applthermaleng.2018.01.027.

[63] Jonathan G. Koomey. Worldwide electricity used in data centers. *Environmental Research Letters*, 3(3):034008, 2008. ISSN 1748-9326. doi: 10.1088/1748-9326/3/3/034008.

[64] Erwin Kreyszig. *Advanced Engineering Mathematics*. John Wiley & Sons, December 2010. ISBN 978-0-470-45836-5.

[65] Thomas S. Kuhn. *The structure of scientific revolutions*. International encyclopedia of unified science ; v. 2, no. 2. University of Chicago Press, Chicago, [2d ed., enl.]. edition, 1970. ISBN 0-226-45803-2 978-0-226-45803-8.

[66] Yuri Kuznetsov. *Elements of Applied Bifurcation Theory*. Springer Science & Business Media, September 1998. ISBN 978-0-387-98382-0.

[67] Zirong Lin, Shuangfeng Wang, Ryo. Shirakashi, and L. Winston Zhang. Simulation of a miniature oscillating heat pipe in bottom heating mode using CFD with unsteady modeling. *International Journal of Heat and Mass Transfer*, 57(2):642–656, February 2013. ISSN 0017-9310.

[68] É. Léveillé, G. Mirshekari, S. Monfray, T. Skotnicki, and L.G. Fréchette. A Microfluidic Heat Engine Based on Explosive Evaporation. In *Proceedings of the 12th International Workshop on Micro and Nanotechnology for Power Generation and Energy Conversion Applications (PowerMEMS 2012)*, Atlanta, Georgia, USA, 2012.

[69] H. B. Ma, M. A. Hanlon, and C. L. Chen. An investigation of oscillating motions in a miniature pulsating heat pipe. *Microfluid Nanofluid*, 2(2):171–179, December 2005. ISSN 1613-4982, 1613-4990. doi: 10.1007/s10404-005-0061-8.

[70] Hongbin Ma. *Oscillating Heat Pipes*. Springer, May 2015. ISBN 978-1-4939-2504-9.

[71] Mauro Mameli, Marco Marengo, and Sameer Khandekar. Local heat transfer measurement and thermo-fluid characterization of a pulsating heat pipe. *International Journal of Thermal Sciences*, 75:140–152, January 2014. ISSN 1290-0729. doi: 10.1016/j.ijthermalsci.2013.07.025.

[72] Marco Marengo and Vadim S. Nikolayev. Pulsating Heat Pipes: Experimental Analysis, Design and Applications. In *Encyclopedia of Two-Phase Heat Transfer and Flow IV*, pages 1–62. WORLD SCIENTIFIC, May 2018. ISBN 978-981-323-439-0.

[73] P.D. Mitcheson, T.C. Green, E.M. Yeatman, and A.S. Holmes. Architectures for vibration-driven micropower generators. *Journal of Microelectromechanical Systems*, 13(3):429–440, June 2004. ISSN 1941-0158. doi: 10.1109/JMEMS.2004.830151. Conference Name: Journal of Microelectromechanical Systems.

[74] Masayoshi Miura, Takao Nagasaki, and Yu Ito. Experimental investigation of heat transport with oscillating liquid column in pulsating heat pipe using forced oscillation system. *International Journal of Heat and Mass Transfer*, 106:997–1004, March 2017. ISSN 0017-9310. doi: 10.1016/j.ijheatmasstransfer.2016.10.069.

[75] T. Monin, A. Tessier-Poirier, A. Amnache, T. Skotnicki, S. Monfray, F. Formosa, and L.G. Frechette. DEMONSTRATION OF A MICROFABRICATED SELF-OSCILLATING FLUIDIC HEAT ENGINE (SOFHE). In *2018 Solid-State, Actuators, and Microsystems Workshop Technical Digest*, pages 368–369, Hilton Head, South Carolina, USA, May 2018. Transducer Research Foundation. ISBN 978-1-940470-03-0. doi: 10.31438/trf.hh2018.104.

[76] Thomas Monin. *Études de systèmes thermo-fluidiques auto-oscillants pour des applications de récupération d'énergie thermique*. PhD thesis, Université Grenoble - Alpes et Université de Sherbrooke, November 2017.

[77] Thomas Monin, Albert Tessier-Poirier, Étienne Léveillé, Alexandre Juneau-Fecteau, Fabien Formosa, Stéphane Monfray, Thomas Skotnicki, and Luc G. Fréchette. Validation expérimentale du comportement d'un caloduc élémentaire décrit comme un résonateur mécanique excité par la thermique. In *CIFQ 2015*, Sherbrooke, June 2015.

[78] Thomas Monin, Albert Tessier-Poirier, Étienne Léveillé, Alexandre Juneau-Fecteau, T. Skotnicki, Fabien Formosa, Stéphane Monfray, and Luc G. Fréchette. First experimental demonstration of a Self-Oscillating Fluidic Heat Engine (SOFHE) with piezoelectric power generation. *J. Phys.: Conf. Ser.*, 773(1):012039, 2016. ISSN 1742-6596.

[79] J. G. Monroe, E. S. Vasquez, Z. S. Aspin, K. B. Walters, M. J. Berg, and S. M. Thompson. Electromagnetic induction by ferrofluid in an oscillating heat pipe. *Appl. Phys. Lett.*, 106(26):263901, June 2015. ISSN 0003-6951. doi: 10.1063/1.4923400. Publisher: American Institute of Physics.

[80] J. G. Monroe, M. Bhandari, J. Fairley, O. J. Myers, N. Shamsaei, and S. M. Thompson. Energy harvesting via thermo-piezoelectric transduction within a heated capillary. *Appl. Phys. Lett.*, 111(4):043902, July 2017. ISSN 0003-6951. doi: 10.1063/1.4996235. Publisher: American Institute of Physics.

[81] J. Gabriel Monroe, Omar T. Ibrahim, Scott M. Thompson, and Nima Shamsaei. Energy harvesting via fluidic agitation of a magnet within an oscillating heat pipe. *Applied Thermal Engineering*, 129:884–892, January 2018. ISSN 1359-4311.

[82] F.C. Moon and Richard H. Rand. Parametric Stiffness Control of Flexible Structures. In G. Rodriguez, editor, *JPL Proceedings of the Workshop on Identification and Control of Flexible Space Structures*, volume 2, California Institute of Technology, Pasadena, California, April 1985. JPL Publication.

[83] Reza Nemati and Mohammad Behshad Shafii. Advanced heat transfer analysis of a U-shaped pulsating heat pipe considering evaporative liquid film trailing from its liquid slug. *Applied Thermal Engineering*, 138:475–489, June 2018. ISSN 1359-4311.

[84] Vadim S. Nikolayev. Oscillatory instability of the gas–liquid meniscus in a capillary under the imposed temperature difference. *International Journal of Heat and Mass Transfer*, 64:313–321, September 2013. ISSN 0017-9310. doi: 10.1016/j.ijheatmass transfer.2013.04.043.

[85] Vadim S. Nikolayev. Effect of tube heat conduction on the single branch pulsating heat pipe start-up. *International Journal of Heat and Mass Transfer*, 95:477–487, April 2016. ISSN 0017-9310. doi: 10.1016/j.ijheatmasstransfer.2015.12.016.

[86] Vadim S. Nikolayev. Physical principles and state-of-the-art of modeling of the pulsating heat pipe: A review. *Applied Thermal Engineering*, page 117111, May 2021. ISSN 1359-4311. doi: 10.1016/j.applthermaleng.2021.117111. URL https://www.sciencedirect.com/science/article/pii/S1359431121005512.

[87] Vadim S. Nikolayev and Marco Marengo. Pulsating Heat Pipes: Basics of Functioning and Modeling. In *Encyclopedia of Two-Phase Heat Transfer and Flow IV*, pages 63–139. WORLD SCIENTIFIC, May 2018. ISBN 978-981-323-439-0.

[88] Lawrence Perko. *Differential Equations and Dynamical Systems*. Springer Science & Business Media, February 2008. ISBN 978-0-387-95116-4.

[89] J. L. Plawsky, A. G. Fedorov, S. V. Garimella, H. B. Ma, S. C. Maroo, L. Chen, and Y. Nam. Nano- and Microstructures for Thin-Film Evaporation—A Review. *Nanoscale and Microscale Thermophysical Engineering*, 18(3):251–269, July 2014. ISSN 1556-7265. doi: 10.1080/15567265.2013.878419.

[90] Jian Qu, Xiaojun Li, Qian Wang, Feng Liu, and Hongxin Guo. Heat transfer characteristics of micro-grooved oscillating heat pipes. *Experimental Thermal and Fluid Science*, 85:75–84, July 2017. ISSN 0894-1777.

[91] Richard H. Rand. *Lecture Notes on Nonlinear Vibrations*. The Internet-First University Press, May 2012. URL http://ecommons.cornell.edu/handle/1813/28989.

[92] Manoj Rao, Frédéric Lefèvre, Sameer Khandekar, and Jocelyn Bonjour. Understanding transport mechanism of a self-sustained thermally driven oscillating two-phase system in a capillary tube. *International Journal of Heat and Mass Transfer*, 65:451–459, October 2013. ISSN 0017-9310. doi: 10.1016/j.ijheatmasstransfer.2013.05.067.

[93] Manoj Rao, Frédéric Lefèvre, Sameer Khandekar, and Jocelyn Bonjour. Heat and mass transfer mechanisms of a self-sustained thermally driven oscillating liquid–vapour meniscus. *International Journal of Heat and Mass Transfer*, 86:519–530, July 2015. ISSN 0017-9310. doi: 10.1016/j.ijheatmasstransfer.2015.03.015.

[94] Rayleigh. The Explanation of Certain Acoustical Phenomena. *Nature*, 18(455), July 1878. ISSN 1476-4687. doi: 10.1038/018319a0.

[95] John William Strutt Baron Rayleigh. *The Theory of Sound*. Macmillan, 1896.

[96] Lord Rayleigh. On convection currents in a horizontal layer of fluid, when the higher temperature is on the under side. *The London, Edinburgh, and Dublin Philosophical Magazine and Journal of Science*, 32(192), December 1916. ISSN 1941-5982. doi: 10.1080/14786441608635602.

[97] Osborne Reynolds. An experimental investigation of the circumstances which determine whether the motion of water shall be direct or sinuous, and of the law of resistance in parallel channels. *Proceedings of the Royal Society of London*, 35(224-226):84–99, January 1883. doi: 10.1098/rspl.1883.0018. Publisher: Royal Society.

[98] P. L. Rijke. Notice of a new method of causing a vibration of the air contained in a tube open at both ends. *The London, Edinburgh, and Dublin Philosophical Magazine and Journal of Science*, 17(116), June 1859. ISSN 1941-5982. doi: 10.1080/14786445908642701.

[99] Gautier Rouaze, Jackson B. Marcinichen, Filippo Cataldo, Philippe Aubin, and John R. Thome. Simulation and experimental validation of pulsating heat pipes. *Applied Thermal Engineering*, page 117271, June 2021. ISSN 1359-4311.

[100] Philip Geoffrey Saffman and Geoffrey Ingram Taylor. The penetration of a fluid into a porous medium or Hele-Shaw cell containing a more viscous liquid. *Proceedings of the Royal Society of London. Series A. Mathematical and Physical Sciences*, 245 (1242):312–329, June 1958. doi: 10.1098/rspa.1958.0085. Publisher: Royal Society.

[101] Jan A. Sanders. Averaging. *Scholarpedia*, 1(11):1760, November 2006. ISSN 1941-6016. doi: 10.4249/scholarpedia.1760. URL http://www.scholarpedia.org/article/Averaging.

[102] Theodor Sexl. Über den von E. G. Richardson entdeckten "annulareffekt". *Z. Physik*, 61(5):349–362, May 1930. ISSN 0044-3328. doi: 10.1007/BF01340631.

[103] Mohammad B. Shafii, Amir Faghri, and Yuwen Zhang. Thermal Modeling of Unlooped and Looped Pulsating Heat Pipes. *Journal of Heat Transfer*, 123(6):1159–1172, May 2001. ISSN 0022-1481. doi: 10.1115/1.1409266.

[104] Qingchen Shen, Chao Chang, Peng Tao, Ziyang Ning, Shujian Rong, Yanming Liu, Chengyi Song, Jianbo Wu, Wen Shang, and Tao Deng. Waste heat recovery in an oscillating heat pipe using interfacial electrical double layers. *Appl. Phys. Lett.*, 112(24):243903, June 2018. ISSN 0003-6951. doi: 10.1063/1.5033347. Publisher: American Institute of Physics.

[105] Giulia Spinato, Navid Borhani, and John R. Thome. Understanding the self-sustained oscillating two-phase flow motion in a closed loop pulsating heat pipe. *Energy*, 2015. ISSN 0360-5442.

[106] Giulia Spinato, Navid Borhani, and John R. Thome. Operational regimes in a closed loop pulsating heat pipe. *International Journal of Thermal Sciences*, 102: 78–88, April 2016. ISSN 1290-0729. doi: 10.1016/j.ijthermalsci.2015.11.006.

[107] Steven Henry Strogatz. *Nonlinear Dynamics and Chaos: With Applications to Physics, Biology, Chemistry, and Engineering*. Westview Press, 1994. ISBN 0-7382-0453-6.

[108] Sujesha Sudevalayam and Purushottam Kulkarni. Energy Harvesting Sensor Nodes: Survey and Implications. *IEEE Communications Surveys Tutorials*, 13(3):443–461, 2011. ISSN 2373-745X.

[109] Harald Sundmaeker, Patrick Guillemin, Peter Friess, and Sylvie Woelfflé. *Vision and Challenges for Realising the Internet of Things*. Cluster of European Research Projects on the Internet of Things (CERP-IoT), Brussels, March 2010.

[110] G. I. Taylor. Stability of a Viscous Liquid Contained between Two Rotating Cylinders. *Philosophical Transactions of the Royal Society of London. Series A, Containing Papers of a Mathematical or Physical Character*, 223:289–343, January 1923. ISSN 0264-3952.

[111] Albert Tessier-Poirier, T. Monin, E. Léveillé, F. Formosa, S. Monfray, and L. G. Fréchette. Influence of nonlinearities on the power output of the Self-Oscillating Fluidic Heat Engine (SOFHE). *J. Phys.: Conf. Ser.*, 773(1):012113, 2016. ISSN 1742-6596.

[112] Albert Tessier-Poirier, Thomas Monin, Étienne Léveillé, Stéphane Monfray, Fabien Formosa, and Luc G. Fréchette. How evaporation and condensation lead to self-oscillations in the single-branch pulsating heat pipe. *Phys. Rev. Fluids*, 4(10):103901, October 2019.

[113] Albert Tessier-Poirier, Richard H. Rand, and Luc G. Fréchette. What Limits the Oscillations Amplitude of the Single-Branch Pulsating Heat Pipe. In *Proceedings*

of the International Symposium on Oscillating/Pulsating Heat Pipes 2019, Daejeon, Korea, September 2019.

[114] Albert Tessier-Poirier, Richard H. Rand, and Luc G. Fréchette. What limits the oscillations' amplitude in the single-branch pulsating heat pipe. *Nonlinear Dynamics*, January 2022. ISSN 1573-269X. doi: 10.1007/s11071-021-07188-3.

[115] Theodore Theodorsen. General Theory of Aerodynamic Instability and the Mechanism of Flutter. Technical Report NACA-TR-496, National Advisory Committee for Aeronautics (NACA), 1935.

[116] Theodore Theodorsen and I. E. Garrick. Mechanism of Flutter A Theoretical and Experimental Investigation of the Flutter Problem. Technical Report NACA-TR-685, National Advisory Committee for Aeronautics (NACA), January 1940.

[117] Van P Carey. *Liquid Vapor Phase Change Phenomena: An Introduction to the Thermophysics of Vaporization and Condensation Processes in Heat Transfer Equipment, Second Edition*. Taylor & Francis Group, November 2007.

[118] Jiansheng Wang, He Ma, and Qiang Zhu. Effects of the evaporator and condenser length on the performance of pulsating heat pipes. *Applied Thermal Engineering*, 91:1018–1025, December 2015. ISSN 1359-4311.

[119] Jiansheng Wang, He Ma, Qiang Zhu, Yiwei Dong, and Kaihong Yue. Numerical and experimental investigation of pulsating heat pipes with corrugated configuration. *Applied Thermal Engineering*, 102:158–166, June 2016. ISSN 1359-4311.

[120] Eric W. Weisstein. "cubic Formula." from mathworld–a wolfram web resource, 2016. URL http://mathworld.wolfram.com/CubicFormula.html.

[121] Eric W. Weisstein. "quartic Equation." from mathworld–a wolfram web resource, 2017. URL http://mathworld.wolfram.com/QuarticEquation.html.

[122] S Whalen, M Thompson, D Bahr, C Richards, and R Richards. Design, fabrication and testing of the P3 micro heat engine. *Sensors and Actuators A: Physical*, 104(3): 290–298, May 2003. ISSN 0924-4247. doi: 10.1016/S0924-4247(03)00032-3.

[123] Frank M. White. *Viscous Fluid Flow*. McGraw-Hill, 1991. ISBN 978-0-07-100995-9.

[124] Stephen Wiggins. *Introduction to Applied Nonlinear Dynamical Systems and Chaos*. Springer, 2003.

[125] D. Zabek, J. Taylor, V. Ayel, Y. Bertin, C. Romestant, and C. R. Bowen. A novel pyroelectric generator utilising naturally driven temperature fluctuations from oscillating heat pipes for waste heat recovery and thermal energy harvesting. *Journal of Applied Physics*, 120(2):024505, July 2016. ISSN 0021-8979. doi: 10.1063/1.4958338. Publisher: American Institute of Physics.

[126] Yuwen Zhang and Amir Faghri. Heat transfer in a pulsating heat pipe with open end. *International Journal of Heat and Mass Transfer*, 45(4):755–764, February 2002. ISSN 0017-9310. doi: 10.1016/S0017-9310(01)00203-4.

[127] Yuwen Zhang and Amir Faghri. Advances and Unsolved Issues in Pulsating Heat Pipes. *Heat Transfer Engineering*, 29(1):20–44, 2008. ISSN 0145-7632. doi: 10.1080/01457630701677114.

[128] Yuwen Zhang, A. Faghri, and M. B. Shafii. Analysis of liquid–vapor pulsating flow in a U-shaped miniature tube. *International Journal of Heat and Mass Transfer*, 45 (12):2501–2508, June 2002. ISSN 0017-9310.

[129] Z. Jon Zuo, Mark T. North, and Lee Ray. Combined pulsating and capillary heat pipe mechanism for cooling of high heat flux electronics. *ASME*, 364:237–244, 1999.

[130] Z.J. Zuo, M.T. North, and K.L. Wert. High heat flux heat pipe mechanism for cooling of electronics. *IEEE Transactions on Components and Packaging Technologies*, 24 (2):220–225, June 2001. ISSN 1521-3331. doi: 10.1109/6144.926386.